Technical Basis Document No. 10: Unsaturated Zone Transport

Revision 1

CONTENTS

CONTENTS (Continued)

FIGURES

FIGURES (Continued)

TABLES

INTENTIONALLY LEFT BLANK

ACRONYMS

AECL   Atomic Energy of Canada, Limited

DFBA   difluorobenzoic acid
DOE   U.S. Department of Energy

ECRB   Enhanced Characterization of the Repository Block
ESF   Exploratory Studies Facility

KTI   Key Technical Issue

LANL   Los Alamos National Laboratory
LA   license application

NRC   U.S. Nuclear Regulatory Commission

PFBA   pentafluorobenzoic acid

TH   thermal-hydrologic
THC   thermal-hydrologic-chemical
THM   thermal-hydrologic-mechanical
TSPA   total system performance assessment
TSPA-LA   total system performance assessment for the license application

INTENTIONALLY LEFT BLANK

1. INTRODUCTION

1.1 OVERVIEW

This technical basis document provides a summary of the conceptual understanding of the general issues affecting transport of radioactive solute and colloidal species through the unsaturated zone of Yucca Mountain and an evaluation of the relative importance of controlling factors and conditions. The postclosure performance of the repository is determined in part by the ability of radionuclides escaping from the waste packages to reach the water table. This document is one in a series that is being prepared for each component of the repository system relevant to predicting its likely postclosure performance. The relationship of radionuclide transport to the other components is illustrated in Figure 1-1. Radionuclide transport is affected by the processes that will be described in *Technical Basis Document No. 1: Climate and Infiltration*, *Technical Basis Document No. 2: Unsaturated Zone Flow*, *Technical Basis Document No. 3: Water Seeping into Drifts*, *CSNF Waste Form Degradation: Summary Abstraction* (BSC 2003a, Section 4), and *Technical Basis Document No. 9: Engineered Barrier System Transport*. The amount and rate of radionuclide arrival at the water table after potential releases from the repository has a direct impact on downstream components of the Yucca Mountain system (i.e., on transport in the saturated zone underneath Yucca Mountain and possible later appearance in the biosphere).

The information presented in this document, along with the associated references, provides a framework for the radionuclide-transport-related studies supporting the ongoing development of the postclosure safety analysis to be included in the license application (LA).

1.2 PURPOSE AND SCOPE

The purpose of this document is to provide an overview of the current understanding of radionuclide transport through the unsaturated zone to the saturated zone, including a summary description of transport modeling activities. Transport modeling and analysis are performed to evaluate the attributes of the unsaturated zone as a natural barrier. This document presents the technical basis for addressing transport-related Key Technical Issue (KTI) agreements between the U.S. Nuclear Regulatory Commission (NRC) and the U.S. Department of Energy (DOE). Detailed responses to these transport-related KTI agreements are provided in Appendices A to C (Table 1-1).
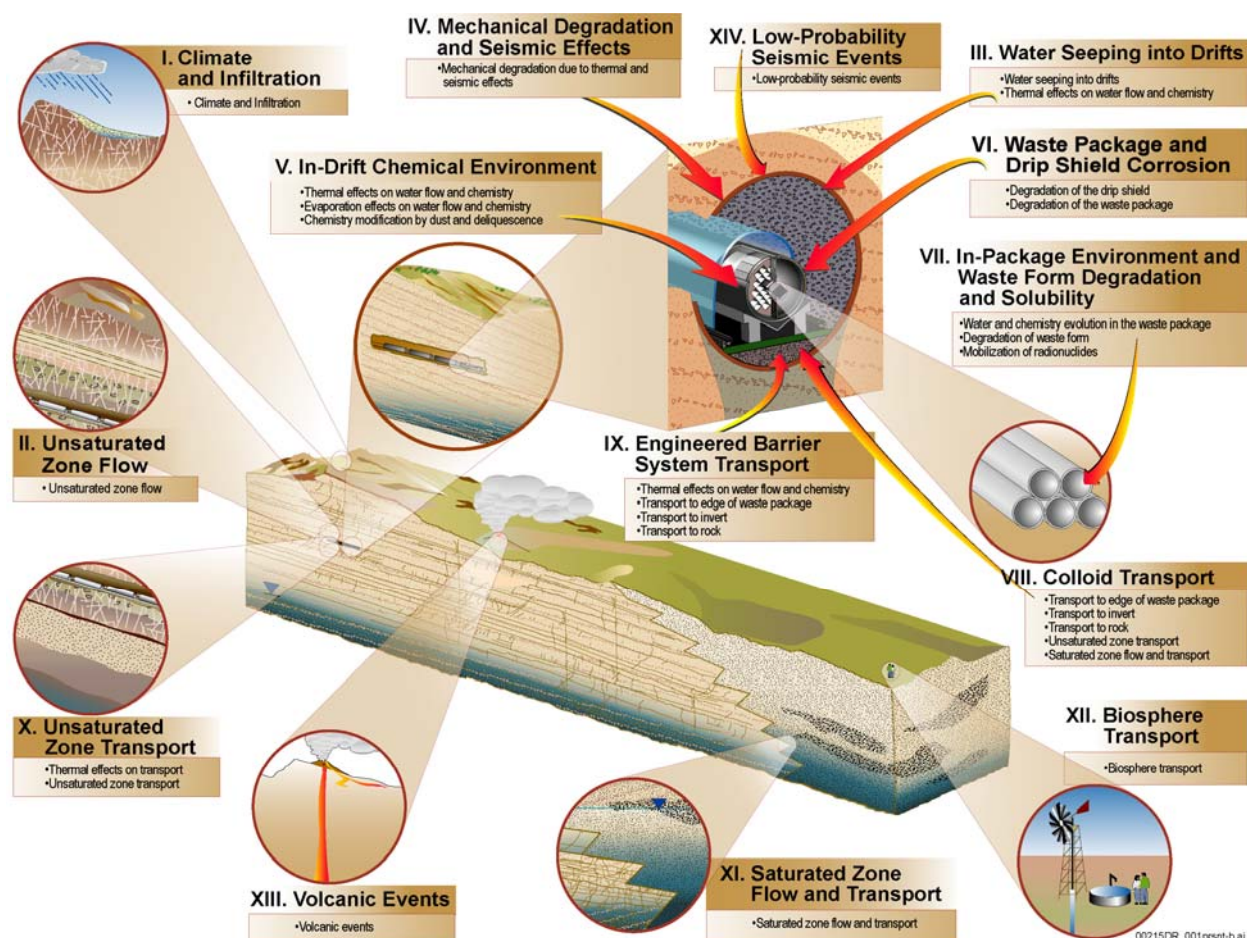
Figure 1-1. Components of the Postclosure Technical Basis for the License Application

Table 1-1. Transport-Related Key Technical Issues Addressed in Appendices

KTI ID	Short Description	Appendix
RT 1.02	Provide analog radionuclide data from the tracer tests for Calico Hills at Busted Butte	A
RT 3.01	Importance of transport through fault zones below the repository	B
RT 3.04	Relative importance of hydrogeologic units beneath the repository	B
RT 3.10	Provide data from analog tracers used at Busted Butte	A
TSPAI 3.28	Confidence in the active-fracture continuum concept in the transport model	C
TSPAI 3.29	Integration of the active fracture model with matrix diffusion in the transport model	C

Radionuclide transport processes are qualitatively described in Section 2. These processes include solute advection and dispersion, colloidal transport, and retardation mechanisms, such as sorption and matrix diffusion. The properties of the radionuclide species are also discussed, including radioactive daughter products and diffusion coefficients. The relationship of unsaturated zone radionuclide transport to other components of the repository system and radionuclide transport processes is described in Section 3.

Section 4 contains a discussion of laboratory data and field tests that provide parameters for radionuclide transport simulation and evidence supporting the conceptual model for unsaturated zone transport.

Section 5 covers the development of models for unsaturated zone transport, including descriptions of how the other system components (e.g., the effects of climate, the unsaturated zone flow) are incorporated into the radionuclide transport model. This section also discusses the conceptualization and simplifications used in model development, as well as transport model calibration and confidence building.

The predictive simulations are summarized in Section 6. The consideration of model uncertainties is also discussed.

The transport abstraction for total system performance assessment (TSPA) is presented in Section 7.

Summary and conclusions are presented in Section 8.

1.3 NOTE REGARDING THE STATUS OF SUPPORTING TECHNICAL INFORMATION

This document was prepared using the most current information available at the time of its development. This technical basis document and its appendices providing Key Technical Issue agreement responses were prepared using preliminary or draft information and reflect the status of the Yucca Mountain Project's scientific and design bases at the time of submittal. In some cases, this involved the use of draft analysis and model reports and other draft references whose contents may change with time. Information that evolves through subsequent revisions of analysis and model reports and other references will be reflected in the LA as the approved analyses of record at the time of LA submittal. Consequently, the Project will not routinely update either this technical basis document or its Key Technical Issue agreement appendices to reflect changes in the supporting references prior to submittal of the LA.

INTENTIONALLY LEFT BLANK

2. RADIONUCLIDES AND TRANSPORT PROCESSES

Water from precipitation percolating through Yucca Mountain is the dominant agent determining corrosion of engineered barriers and waste packages, waste dissolution, and radionuclide transport from the repository to the accessible environment. The flow of water, and subsequent transport of radionuclides, is determined by the characteristics of unsaturated zone geology. The amount and rate of radionuclides released from waste packages, and subsequently transported through the unsaturated zone to the water table, are key factors determining the long-term safety of the repository system at Yucca Mountain.

Subsurface formations in the unsaturated zone consist of heterogeneous layers of anisotropic, fractured volcanic tuffs with alternating welded and nonwelded ash-flow and ash-fall deposits. The welded units are generally denser, harder, and more intensely fractured than the nonwelded units. The major geologic units of the unsaturated zone beneath Yucca Mountain, from top to bottom, are the volcanic tuff formations of the Paintbrush (Tp) Group, the Calico Hills Formation (Tac), and the Crater Flat (Tc) Group. The lithostratigraphic nomenclature divides the Paintbrush Group into the Tiva Canyon (Tpc), Yucca Mountain (Tpy), Pah Canyon (Tpp), and Topopah Spring (Tpt) tuffs. The Crater Flat Group is divided into the Prow Pass (Tcp), Bullfrog (Tcb), and Tram tuffs (Tct). For purposes of hydrogeologic studies, a separate hydrogeologic nomenclature was developed based on the degree of welding and hydrologic property distributions (CRWMS M&O 2000, Tables 4.7-1 and 8.10-1).

The major hydrogeologic units are divided into the Tiva Canyon welded (TCw), the Paintbrush nonwelded (PTn) (consisting primarily of the Yucca Mountain and Pah Canyon members and the interbedded tuffs), the Topopah Spring welded (TSw), the Calico Hills nonwelded (CHn), and the Crater Flat undifferentiated (CFu) units. Based on the hydrogeologic properties of the lithostratigraphic units, Flint (1998) developed a detailed hydrogeologic stratigraphy for use in numerical flow and transport modeling. This correlation between the lithostratigraphic units, hydrogeologic units, and corresponding unsaturated zone flow and transport model layers can be found in *Technical Basis Document No. 3: Water Seeping into Drifts*, and more details are available in *UZ Flow Models and Submodels* (BSC 2003b, Section 6.1.1). A summary indicating the correlation between the three different classification systems of the unsaturated zone subsurface is presented in Table 2-1. Note that there is not necessarily one-to-one mapping of the lithostratigraphic units to the flow and transport model layers because geologically dissimilar media can have very similar hydrogeologic behavior.

The conceptual model for water flow through the unsaturated zone, developed from extensive field measurements and modeling studies, is shown in Figure 2-1. This model illustrates the geologic control over the flow of water through the unsaturated zone and is the basis for modeling radionuclide transport. Infiltrating water flows through the densely fractured Tiva Canyon welded (TCw) unit mainly through fractures. Within the more porous Paintbrush nonwelded (PTn) unit, most of the water flows through the matrix, where the high storage capacity promotes the dampening of infiltration pulses. Small amounts of flowing water preferentially pass through faults that cut through this unit.

The repository lies within the Topopah Spring welded (TSw) unit. Here water flow may become focused into fewer fractures as it approaches the repository horizon, affecting seepage rates into

the repository drift and the number of waste packages that are contacted by water. The transport time of radionuclides to the water table will be determined largely by the flow paths (indicated in the figure), the relative dominance of fracture and matrix flow, and the mineralogy of the units.

Table 2-1.　Major Hydrogeologic Units, Lithostratigraphy, Unsaturated Zone Model Layer, and Hydrogeologic Unit Correlation

Major Hydrogeologic Units[a]	Lithostratigraphic Nomenclature[b]	Hydrogeologic Unit[c]	Unsaturated Zone Flow Model Layer[d]
Tiva Canyon welded (TCw)	Tpcr	CCR, CUC	tcw11
	Tpcp	CUL, CW	tcw12
	TpcLD		
	Tpcpv3	CMW	tcw13
	Tpcpv2		
Paintbrush nonwelded (PTn)	Tpcpv1	CNW	ptn21
	Tpbt4	BT4	ptn22
	Tpy (Yucca)	TPY	ptn23
		BT3	ptn24
	Tpbt3		
	Tpp (Pah)	TPP	ptn25
	Tpbt2	BT2	ptn26
	Tptrv3		
	Tptrv2		
Topopah Spring welded (TSw)	Tptrv1	TC	tsw31
	Tptrn	TR	tsw32
	Tptrl, Tptf	TUL	tsw33
	Tptpul, RHHtop		
	Tptpmn	TMN	tsw34
	Tptpll	TLL	tsw35
	Tptpln	TM2 (upper 2/3 of Tptpln)	tsw36
		TM1 (lower 1/3 of Tptpln)	tsw37
	Tptpv3	PV3	tsw38
	Tptpv2	PV2	tsw39 (vitric, zeolitic)

Table 2-1. Major Hydrogeologic Units, Lithostratigraphy, and Unsaturated Zone Model Layer, and Hydrogeologic Unit Correlation (Continued)

Major Hydrogeologic Units[a]	Lithostratigraphic Nomenclature[b]	Hydrogeologic Unit[c]	Unsaturated Zone Flow Model Layer[d]
Calico Hills nonwelded (CHn)	Tptpv1	BT1 or BT1a (altered)	ch1 (vitric, zeolitic)
	Tpbt1		
	Tac (Calico)	CHV (vitric) or CHZ (zeolitic)	ch2 (vitric, zeolitic)
			ch3 (vitric, zeolitic)
			ch4 (vitric, zeolitic)
			ch5 (vitric, zeolitic)
	Tacbt (Calicobt)	BT	ch6 (vitric, zeolitic)
	Tcpuv (Prowuv)	PP4 (zeolitic)	pp4
	Tcpuc (Prowuc)	PP3 (devitrified)	pp3
	Tcpmd (Prowmd)	PP2 (devitrified)	pp2
	Tcplc (Prowlc)		
	Tcplv (Prowlv)	PP1 (zeolitic)	pp1
	Tcpbt (Prowbt)		
	Tcbuv (Bullfroguv)		
Crater Flat undifferentiated (CFu)	Tcbuc (Bullfroguc)	BF3 (welded)	bf3
	Tcbmd (Bullfrogmd)		
	Tcblc (Bullfroglc)		
	Tcblv (Bullfroglv)	BF2 (nonwelded)	bf2
	Tcbbt (Bullfrogbt)		
	Tctuv (Tramuv)		
	Tctuc (Tramuc)	Not Available	tr3
	Tctmd (Trammd)		
	Tctlc (Tramlc)		
	Tctlv (Tramlv)	Not Available	tr2
	Tctbt (Trambt) and below		

Source: Simmons 2004, Table 7-1.

NOTE: [a] Modified from Montazer and Wilson 1984, Table 1.
   [b] BSC 2002.
   [c] Flint 1998.
   [d] BSC 2003c.
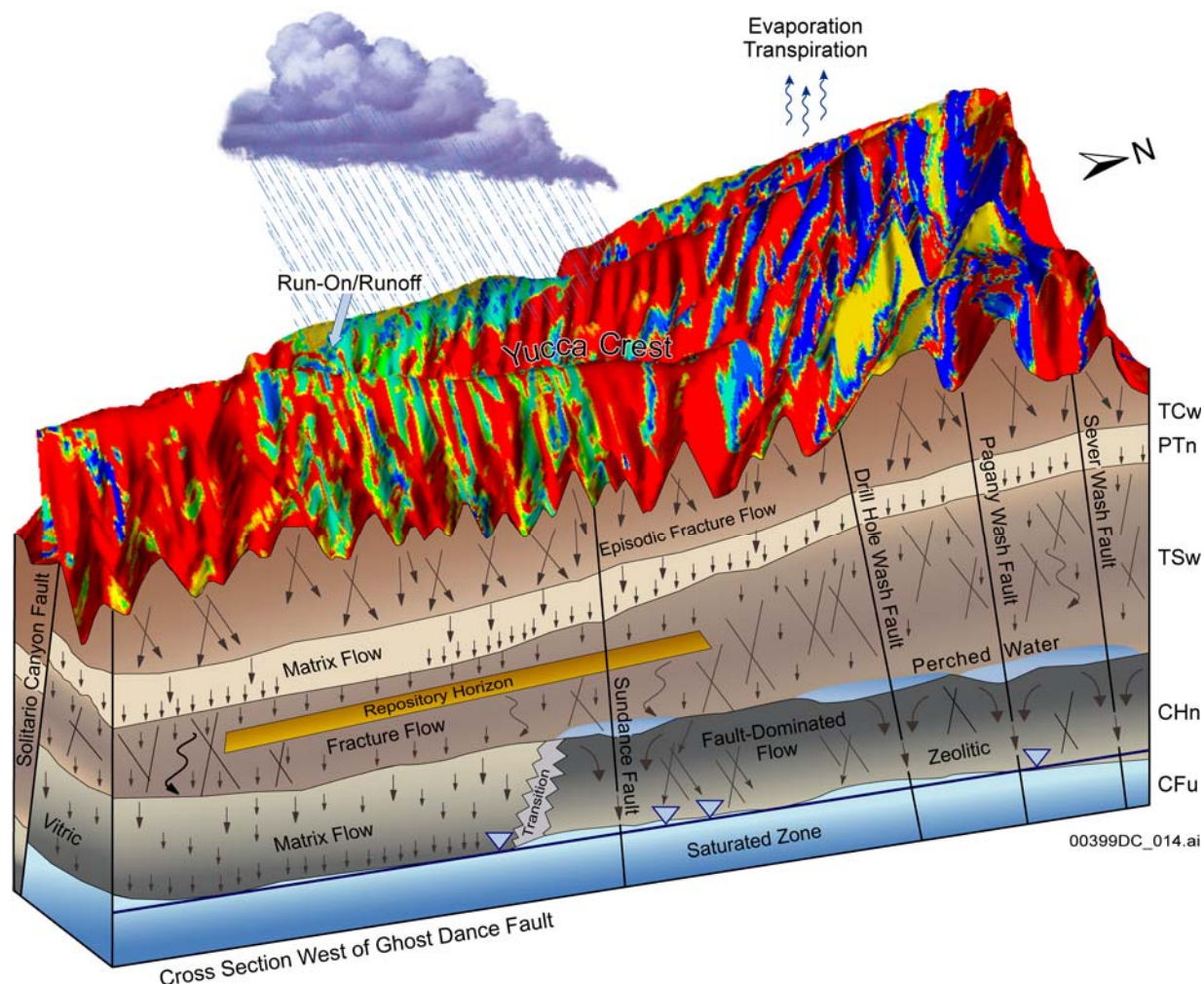
NOTE: Lithostratigraphic nomenclature, hydrogeologic units, and unsaturated zone flow model layers are listed in Table 2-1.

Figure 2-1. Overall Water Flow Behavior in the Unsaturated Zone, Including the Relative Importance of Fracture and Matrix Flow Components in the Major Hydrogeologic Units

The main hydrogeologic units below the repository are the Calico Hills nonwelded (CHn) and Crater Flat undifferentiated (CFu) units. Both of these units have vitric and zeolitic components that differ in their degree of hydrothermal alteration and subsequent hydrologic properties. The major vitric layers in the CHn (CHv) are in the southern half of the area below the repository. These units have relatively high matrix porosity, low fracture density, and permeability that is [JO1]similar in the fractures and in the matrix. Given the small fracture volumes in these units, a large fraction of the flow occurs through the matrix. The zeolitic rocks have low matrix permeability and some fracture permeability; consequently, a relatively small amount of water may flow through the zeolitic units, with most of the water flowing laterally in perched water bodies and then vertically down faults. Section 3.2 contains a more detailed discussion of unsaturated zone flow and its relationship to transport.

Figure 2-2 illustrates the processes affecting the fate and transport of radionuclides from the repository horizon. These processes are described in detail later in this section. Both solute and

colloidal forms of radionuclides are considered. The important transport processes include advection through the fractures and matrix, dispersion and diffusion within the matrix, sorption, and radioactive decay accounting for the different properties of daughter products. This section continues with descriptions of the various forms of radionuclides considered in transport modeling, followed by discussions of the different transport processes.
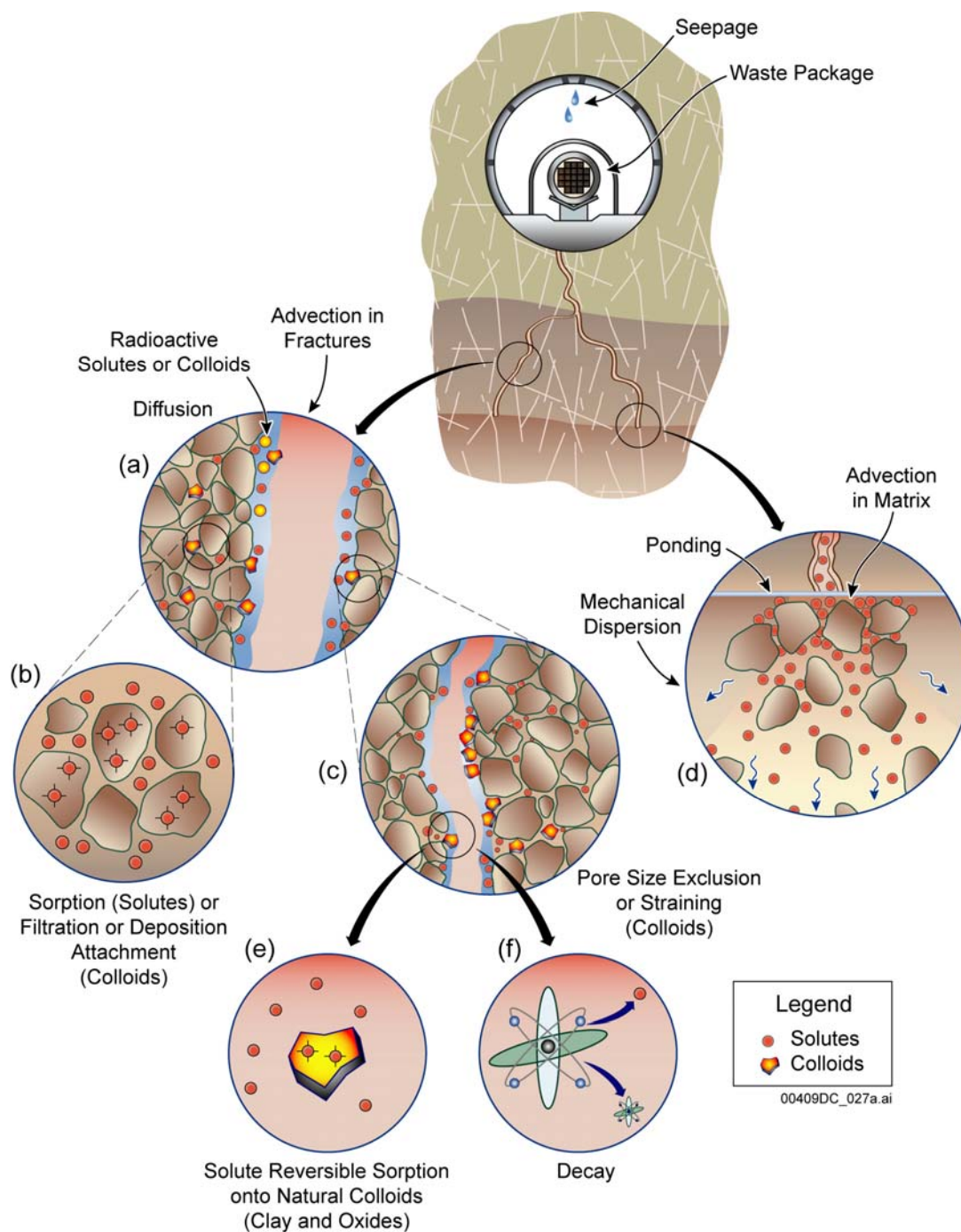
Figure 2-2. Processes Affecting Transport of Radionuclides

2.1   RADIONUCLIDES RELEASED INTO THE UNSATURATED ZONE

Radionuclides considered in the studies of unsaturated zone transport were selected to represent the species known to occur in substantial concentrations in the radioactive wastes (either as parents or as daughter products of decay).   These radionuclides cover the range of transport properties (sorption and diffusion) and half-lives of all representative species listed in Section 5 (in Table 5-2).   Because of radioactive decay, the transport of both the parent and daughter products must be accounted for (Figure 2-2f). Daughter products with long half--lives are especially important for performance assessment.   Since daughter products may have significantly different transport behavior than parent radionuclides, the migration and fate of all the important members of the decay chain must be considered.

In addition, radionuclides may be transported through the unsaturated zone in two different forms: radioactive solutes (which are radionuclides dissolved in water) and radioactive colloids.

Figure 2-3 depicts the classification of colloids according to their origin and characteristics (BSC 2003d, Section 6.3.1).   In Class I colloids, the entire nonaqueous component of the colloidal particle is radioactive.   This class includes true or intrinsic colloids (e.g., plutonium(IV), which are generated from a solute when its concentration exceeds its solubility (Saltelli et al. 1984). Class I colloids also include waste-form colloids, which are produced from the nucleation of colloids from waste-form dissolution and from spallation of colloid-sized waste from alteration products.   Waste-form colloids are believed to be one of the most significant contributors to radionuclide transport in the unsaturated zone (BSC 2003d, Section 6.3.1).

Class II represents natural colloids, called pseudocolloids, onto which actinides are irreversibly sorbed.   Pseudocolloids can be inorganic (e.g., clay, iron oxyhydroxides, silica) or organic (e.g., microbes and humic acids) (Ibaraki and Sudicky 1995, p. 2945) and include all colloidal particles that are neither true colloids nor waste-form colloids.   For Class II colloids, radionuclide sorption is, by definition, either irreversible or incorporated into the colloidal structure (e.g., by co-precipitation of radionuclides).   Only a portion of the colloidal particle (usually a very small one) is radioactive.   In this class of colloids, the actinide remains confined onto the colloid and does not exchange mass with its surroundings (i.e., the liquid phase or adjacent colloids).

Class III includes radioactive pseudocolloids in which actinides are reversibly sorbed onto the underlying natural colloid.   As in Class II colloids, only a small portion of the colloidal particle is radioactive.   However, for Class III colloids, the actinide portion is not confined to the colloid but can exchange mass with its surroundings (i.e., the liquid phase or adjacent colloids).
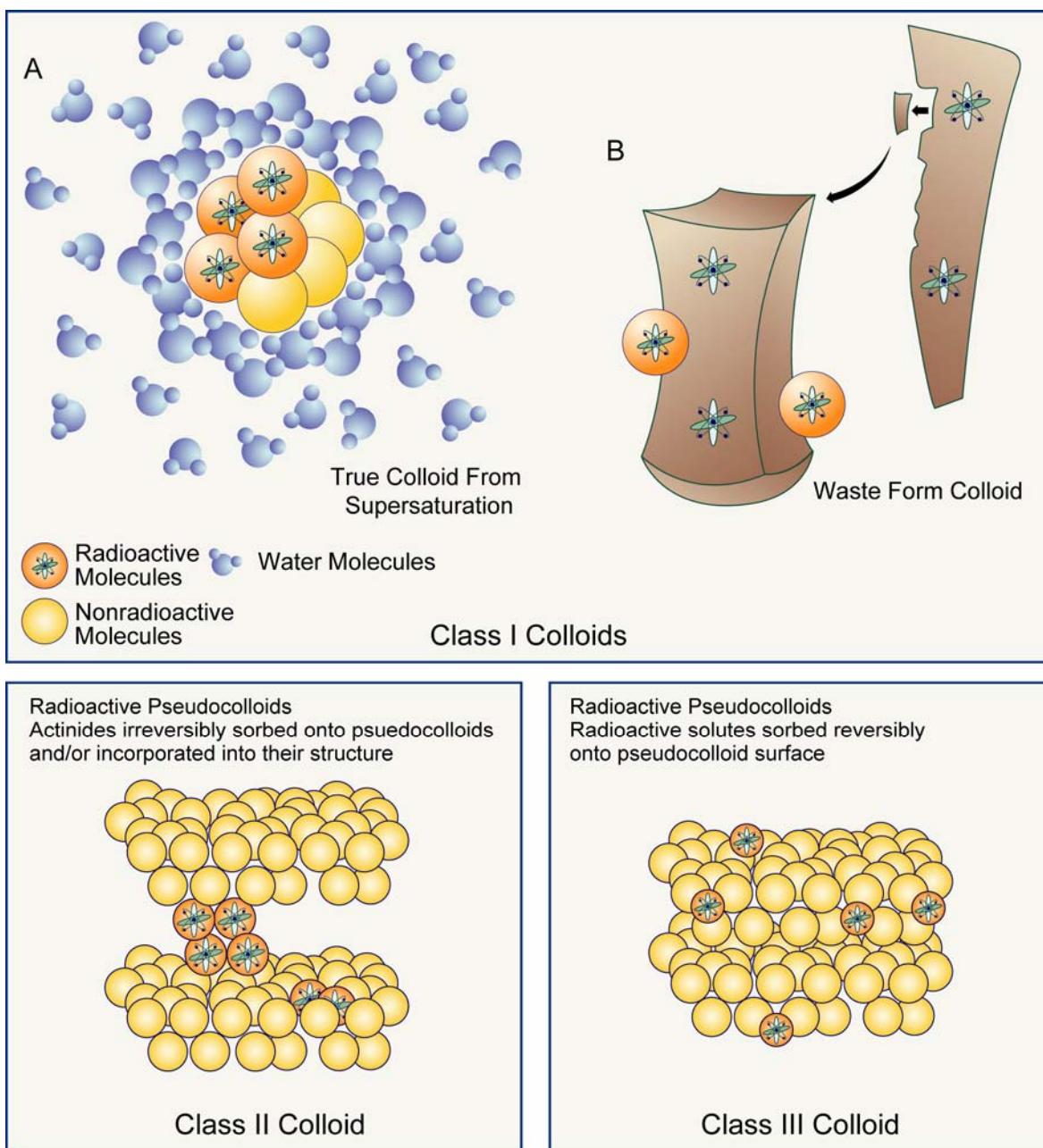
Figure 2-3. Colloid Type and Origin

The fate of radioactive colloids is a far more complex and less understood process compared to solutes because of the possible effects of daughter product generation on colloids and the resulting transport properties. It is not known if colloidal size changes when the daughter product is ejected (e.g., due to recoil during alpha decay) or under what conditions the daughter will remain a part of the colloid. The size of pseudocolloids is unlikely to change due to radioactive decay. However, it is not known if the daughter products will remain sorbed or if they will be ejected into the liquid phase. The problem is further complicated by colloid generation, flocculation, and instability, which affect daughter distribution and partitioning in a complex manner (BSC 2003e, Section 6.18).

2.2   DESCRIPTION OF TRANSPORT PROCESSES

2.2.1   Advective and Dispersive Transport

Water flowing through the unsaturated zone can transport radionuclides from the emplacement location to the water table (Figure 2-1). Fracture flow is expected to be the dominant transport mechanism in most hydrogeologic units except for the vitric CHv unit and perched water zone because of high fracture permeability compared to matrix permeability, limited fracture pore volumes, limited fracture–matrix contact areas, and short contact times between the radionuclide–carrying liquid phase and the rock matrix (Figure 2-2a). Fracture-dominated advective transport is expected to lead to the earliest arrivals at the water table due to fast water flow and because the aforementioned factors can adversely affect the two main retardation mechanisms: (1) matrix diffusion and (2) immobilization by means of solute sorption onto or colloid filtration by the matrix (BSC 2003e, Section 6). While advective flow is predominantly downward in response to gravity some lateral advection is also expected in response to lateral flow diversion at the boundaries of hydrogeologic units that have sharp contrasts in their hydraulic properties (BSC 2003b, Section 6.2.2). Flow diversion may also occur in the perched-water bodies of the unsaturated zone. Laterally diverted flow ultimately finds a pathway to the water table through other more permeable zones, such as faults or connecting fractures.

Mechanical dispersion arises from localized velocity variations and, combined with diffusion, constitutes hydrodynamic dispersion (Figure 2-2d). Longitudinal dispersion (i.e., dispersion in the direction of flow) may result in earlier arrivals of smaller concentrations of radionuclides at the water table ahead of the mean concentration front. However, dispersion is not expected to play a significant role in radionuclide transport in the system dominated by fracture flow. Additionally, dispersion effects are small because matrix diffusion spreads the arrivals of radionuclides more significantly compared to spreading by mechanical dispersion. Finally, the repository emplacement area is very broad (approximately 5,000 m by 2,000 m) relative to the distance to the water table (about 300 m); this configuration has been shown to minimize lateral dispersion effects (BSC 2003b, Section 6.7.1).

Based on the results of inverse modeling (BSC 2003f), the calibrated properties indicated that, in the vitric CHv units, matrix flow dominates because of similar permeability of fractures and matrix (Figure 2-1) and the low fracture volumes. This, combined with the high matrix pore volume, results in much slower transport velocities in addition to larger water–rock contact areas and longer radionuclide–matrix contact times (BSC 2003e, Section 6).

2.2.2   Matrix Diffusion

The diffusion of radioactive solutes and colloids into the rock matrix is an important retardation mechanism controlling the radionuclide transfer between the fractures and the rock matrix; it is the only significant retardation mechanism for nonsorbing solutes, such as ^{99}Tc (Figure 2-2a). In the process of matrix diffusion, radionuclides move into the matrix, where water flow is slow and where sorption or filtration (Sections 2.2.2 and 2.2.4) are much more likely to occur because of greater contact areas and times between water and rock (Figure 2-2b). Matrix diffusion removes some radionuclides from the flowing fractures, thus slowing radionuclide transport through the fractures. Diffusive flux within the matrix of a given species is a function of its

molecular properties (e.g., electric charge, size, and diffusion coefficient), its concentration gradient, and other properties, such as temperature, the matrix pore structure, and water saturation of the pore space (BSC 2003e, Section 6.2).

In general, matrix diffusion is less for colloids than for solutes, because the large size of the colloids: (1) reduces the colloid diffusion coefficient; (2) reduces the number of colloids entering the matrix because of pore size exclusion; and (3) enhances advection by guiding the colloids to the center of the fracture pores where velocities are higher than the average water velocity (Figure 2-2c) (Ibaraki and Sudicky 1995, p. 2948).

2.2.3 Sorption

Sorption describes a combination of chemical and physical interactions between dissolved radionuclides and the rock matrix. Sorption removes a portion of the dissolved species from the mobile liquid phase and transfers it to the solid phase. The solid phase includes both the immobile rock matrix and mobile (Figure 2-2b) or immobile (Figure 2-2e) colloids. If the solid phase is immobile, sorption results in larger concentration gradients between the sorption sites and the bulk matrix, thereby enhancing diffusive fluxes between fractures and matrix and reducing the rate of solute transport.

The sorption behavior of radionuclides is usually described by the distribution coefficient (K_d), which quantifies the partitioning of radionuclides between the solid and aqueous phases. At the same temperature, repetitive experiments with different concentration of solutes can construct a family of points forming a linear equilibrium isotherm, based on which the K_d can be estimated for the solutes of interest. The K_d values for Yucca Mountain studies are obtained from laboratory batch experiments using crushed tuffs with a particle size of 75 to 500 μm (BSC 2003e, Attachment I) contacted with groundwater (or simulated groundwater) representative of the site, spiked with one or more of the elements of interest. Sorption experiments have been carried out as a function of time, element concentration, atmospheric composition, particle size, and temperature. In some cases, the solids remaining from sorption experiments were contacted with unspiked groundwater in desorption experiments. The sorption and desorption experiments together provide information on the equilibration rates of the forward and backward sorption reactions (see Section 4.1).

The primary controls on sorption behavior in the unsaturated zone flow system include the nature of mineral surfaces in the rock units contacted by the flowing water, the pore-water and perched water chemistry, the specific sorption mechanisms for each radionuclide, the concentrations of the various radionuclides in water, and their speciation and redox state.

Effective K_d values obtained from batch experiments involving high concentration solutions will tend to underestimate the field K_d values if the expected field concentrations are low and nonlinear or kinetic sorption prevails (BSC 2003e, Section 6.1.2.3). Conversely, batch experiments using crushed rock samples may overestimate the K_d values (compared to intact rock samples and for the same solute concentration) if kinetic effects are involved and the contact time is short. Even though procedures were used to minimize the inclusion of fines, crushing of the material creates new contact surfaces and increases the radionuclide accessibility to pores that may not contribute to sorption on intact rocks. The difference in the K_d estimates

from the two sample types vanishes for sufficiently long contact times. The deterministic approach in the Yucca Mountain studies tends to underestimate the K_d values because it involves an averaging of K_d values obtained from experiments using both low and high solution concentrations, while the release concentrations from the repository are expected to be low. The underestimation of K_d values produces an earlier arrival prediction of radionuclide mass to the water table.

2.2.4   Colloid Transport

Colloid filtration is categorized into two processes: (1) physical-chemical deposition and (2) straining. Colloid deposition onto rock surfaces as water flows through its pores (Figure 2-2b) is commonly assumed to occur in two steps: (1) transport of colloids to matrix surfaces by Brownian diffusion, interception, or gravitational sedimentation (i.e., colloid-matrix collision); and (2) attachment of colloids to matrix surfaces. The fraction of collisions resulting in attachment is called the attachment efficiency and is strongly influenced by interparticle forces between colloids and matrix surfaces, such as van der Waals and electric double-layer interactions, steric stabilization, and hydrodynamic forces (Kretzschmar et al. 1995, p. 435). Kretzschmar et al. (1997, p. 1129) demonstrated that colloid deposition generally follows a first-order kinetic rate law, and they experimentally determined the corresponding collision efficiencies. Once attached, colloid detachment is generally slow, and attachment can appear to be irreversible.

Colloid straining (Figure 2-2c) can also affect the distribution and transport of colloids. Straining mechanisms can be classified according to the relative size of the colloid as conventional straining (if the colloid is larger than the pore throat diameter or the fracture aperture, pore size exclusion accounted for in the study of colloid transport in Section 6), and film straining (if the colloid is larger than the thickness of the adsorbed water film coating the grains of the rock) (Wan and Tokunaga 1997, p. 2413). McGraw and Kaplan (1997, p. 5.2) found a very strong dependence of filtration on the colloid size under unsaturated conditions. Colloid removal increased exponentially with colloid size, and the decrease in colloid mobility at low volumetric water contents was attributed to resistance due to friction (as the colloids were dragged along the sand grains). Wan and Tokunaga (1997, pp. 2413 and 2419) found that if the water saturation of the pore space is lower than a critical saturation value, colloids can only move in the thin film of water that lines the grain boundaries. Colloid retardation increased as the ratio of the water film thickness to the colloid diameter decreased.

Two classes of colloids, Class I and Class II (Section 2.1), were considered in the transport study (BSC 2003e, Section 6.18). Class I includes true colloids and waste form colloids, in which the entire non-aqueous component of the colloid is composed of the radioactive substance. Those were taken to have the properties of PuO_2 and are subject to radioactive decay. Note that the assumption of PuO_2 colloids indicates that radioactivity follows the decay of [239]Pu. This does not affect their overall transport behavior (a strong function of size) or limit the validity of observations. Additionally, the Class I colloid size and density were considered invariable during the simulation. This stipulation means that matrix diffusion does not increase in response to a smaller colloid diameter and colloid filtration (the parameters of which are based on the actinide mass per unit volume) does not decrease due to lower concentrations. In both colloidal classes considered in this study, four different colloid sizes were considered (see Section 6.2).

3. RELATIONSHIP OF RADIONUCLIDE TRANSPORT TO OTHER COMPONENTS OF THE REPOSITORY SYSTEM

Unsaturated zone transport processes are impacted by various components of the repository system. Precipitation and near-surface processes determine the infiltration of water to the unsaturated zone (Figure 2-1). The water that percolates below the root zone (i.e., net infiltration) follows pathways that are (among other factors) determined by the geology of Yucca Mountain. As infiltration approaches the repository horizon, flow is focused into fewer fractures. Even though there is a lack of field evidence to show the flow focusing, ^{36}Cl data (Fabryka-Martin et al. 1996) and field observation (Wang et al. 1998) show that there are discrete flow features through fractures. The percolation flux distribution affects the fraction of waste emplacement drifts encountering seepage, the seepage rate, and thus potential water–waste contact. Flow through the engineered barrier system within the repository impacts water–waste contact and provides the source term for radionuclide transport. Flow diversion around the drifts creates a shadow zone below the repository, which determines the transfer mechanism and release rates of radionuclides from the waste emplacement drifts to the natural system, and thus affects the nature of the radionuclide source term for transport through the unsaturated zone. Figure 2-1 also shows other hydrologic features that impact radionuclide transport below the repository, including perched water and the distinctly different flow patterns through the northern and southern portions of the Calico Hills unit.

The unsaturated zone flow model and its submodels are developed to simulate past, present, and future hydrogeologic, geothermal, and geochemical conditions and processes within the Yucca Mountain unsaturated zone to support various TSPA-LA activities. A detailed analysis of simulated percolation fluxes at the repository level and at the water table was conducted for nominal simulation scenarios of unsaturated zone flow fields (BSC 2003b). Flow modeling for the unsaturated zone has indicated whether fracture or matrix flow dominates in a given hydrogeologic unit. With this understanding, the relative importance of various radionuclide transport processes and the potential of the unsaturated zone for retarding the transport of radionuclides to the water table can be evaluated. Finally, the unsaturated zone transport predictions provide the source terms for saturated zone predictions of transport to the accessible environment.

The repository-system components that relate to radionuclide transport are described in Figure 1-1. These components include climate and infiltration, unsaturated zone flow, the engineered barrier system, and saturated zone transport and are summarized in the following sections. Technical basis documents for each component provide additional detailed information. The effects of thermal loading and the engineered barrier system in the vicinity of the repository are discussed in the current document. The interaction among repository-system components with radionuclide transport processes is a key part of synthesizing information for the development of transport models and is discussed in more detail in Section 5.

3.1 CLIMATE AND INFILTRATION

Climatic conditions play a critical role in transport. They are key for estimating the net infiltration and deep percolation in the unsaturated zone, and ultimately in estimating groundwater flux. Under a wetter climatic regime, the increased precipitation leads to increased

water percolation through the unsaturated zone and the repository, resulting in faster water flow and earlier radionuclide arrivals at the water table. With faster flow, transport is accelerated by the decreased travel and contact times that limit radionuclide retardation by the unsaturated zone.

Forecasting of climatic conditions at Yucca Mountain indicates that the present-day climate persists for 400 to 600 years, followed by a warmer and much wetter monsoon climate for 900 to 1,400 years (USGS 2001, Table 2, p. 67). This monsoon climate is followed by a cooler and wetter glacial transition climate for the remaining 8,000 to 8,700 years (USGS 2001, Table 2, p. 67).

Maps of steady-state net infiltration for the present-day, monsoon, and glacial transition climate states over the Yucca Mountain region were prepared from numerical simulations (Figure 3-1). These include lower-bound, mean, and upper-bound conditions for each of these climatic states. The distributions of infiltration indicated by the maps were then used to calculate space- and time-averaged steady-state infiltration rates for each of the climate scenarios (USGS 2003, Section 6.4 and 6.11).

The concept behind numerical simulations of net infiltration is based on the solution of the water balance, plug-flow equation using the INFIL V2.0 numerical code. For each of the watersheds, the INFIL code performs daily simulations of net infiltration over all model cells, using the calculations of the evapotranspiration rate and surface runoff/run-on. The main types of data used for numerical modeling of infiltration rate include the precipitation and temperature records, the water storage capacity of the root zone, the field capacity of soils, and hydraulic conductivity of the soil and bedrock.

Results of field and modeling investigations over the Yucca Mountain region (USGS 2003, Section 6.11) show that the net infiltration rate varies greatly in space and time depending on storm amplitudes, duration, and frequencies. In very wet years, infiltration pulses to the unsaturated zone of Yucca Mountain may occur over a relatively short time period (Bodvarsson et al. 1999, p. 10). Where the soil thickness decreases and bedrock crops out, net infiltration increases because fast preferential flow through rock fractures exceeds the depth of evapotranspiration (Flint and Flint 1995, p. 14). Spatial and temporal variability in net infiltration at Yucca Mountain are caused by episodic storm and precipitation events (Hevesi et al. 1994) as well as the heterogeneous nature of the topsoil layer and topography. Near-surface infiltration data (USGS 2003, Section 6.11) suggest that significant infiltration occurs only every few years. In very wet years, infiltration increases to hundreds of millimeters per year during a relatively short time.

Climatic conditions and infiltration at Yucca Mountain and their impact on the repository system behavior are discussed in detail in *Technical Basis Document No. 1: Climate and Infiltration*.
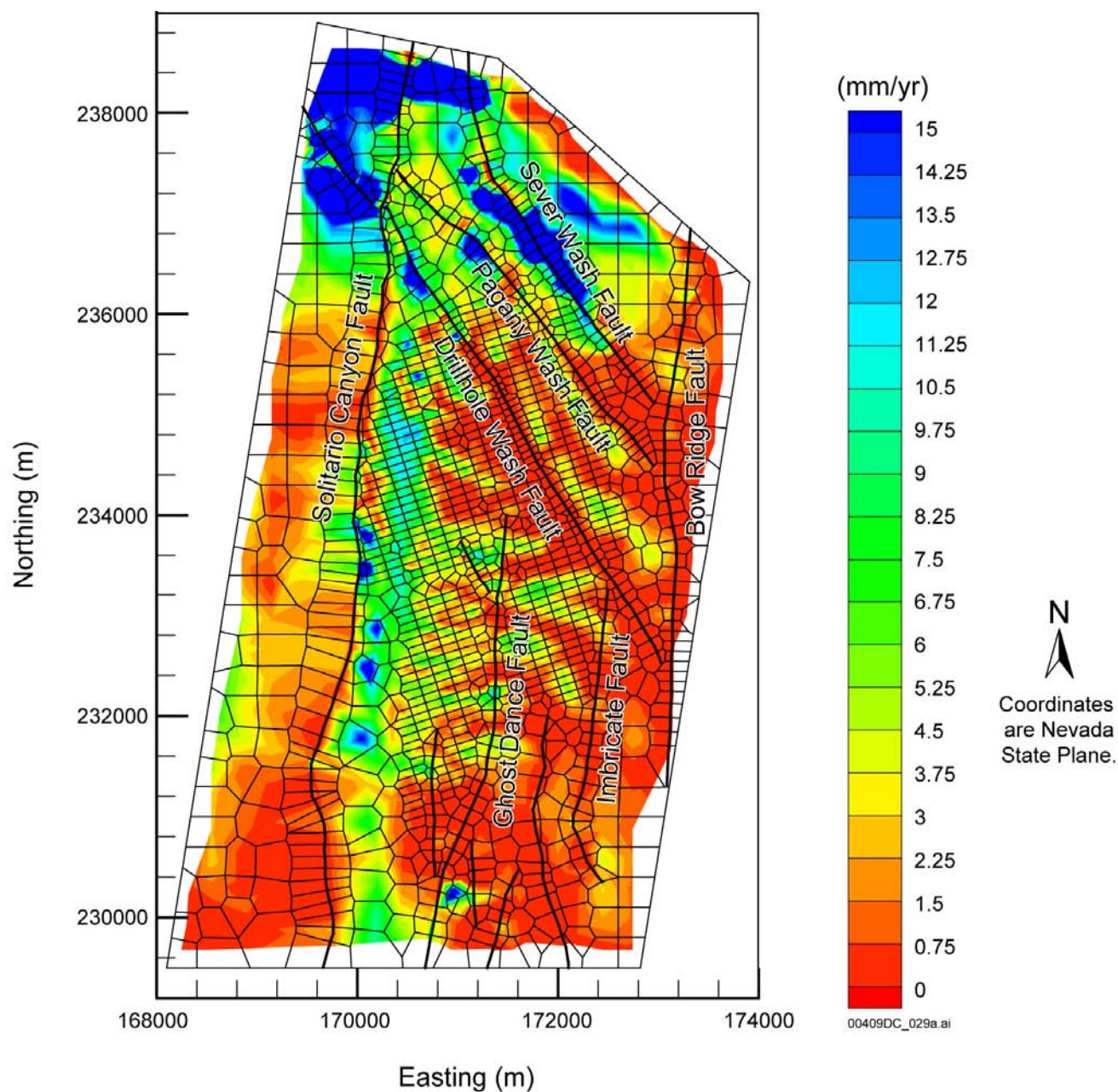
Source: DTN: GS000308311221.005.

NOTE: The TSPA-LA model grid is presented in Section 5, Figure 5-1.

Figure 3-1. Plan View of Net Infiltration Distributed over the Three-Dimensional Unsaturated Zone TSPA-LA Model Grid for the Present-Day (Base-Case) Mean Infiltration Scenario

3.2 UNSATURATED ZONE FLOW

Accurate determination of the relative importance of fracture and matrix flow components is especially important for chemical transport processes. Flow in fractures is typically much faster than flow in the matrix, leading to much shorter transport times for radionuclides and other chemicals in fractures compared to the matrix. The characteristic flow behavior in each of the major hydrogeologic units shown in Figure 2-1 is supported by extensive field observations or modeling studies. In general, flow is primarily fracture-dominated in the densely welded and intensely fractured TCw and TSw hydrogeologic units and matrix-dominated in the nonwelded, less intensely fractured PTn unit, where flow is damped. This conceptual understanding was the basis for the development of the site-scale unsaturated zone flow model.

The high density of interconnected fractures and low matrix permeabilities in the TCw unit (BSC 2003g, Sections 6.1 and 6.2) are considered to give rise to significant water flow in fractures and limited matrix imbibition (water flow from fractures to the matrix). Thus, episodic infiltration pulses are expected to move rapidly through fracture networks, with little attenuation by the matrix. The relatively high matrix permeabilities and porosities and low fracture densities of the PTn unit (BSC 2003g, Sections 6.1 and 6.2) should convert the predominant fracture flow in the TCw to dominant matrix flow within the PTn (BSC 2003b, Section 6.2.2). The dominance of matrix flow and the relatively large storage capacity of the matrix (resulting from its high porosity and low saturation) give the PTn significant capacity to attenuate infiltration pulses.

Faults and geological structures may cut through the entire PTn unit at some locations, leading to fast flow paths when the localized tuff matrix is not dry enough to imbibe water flowing in the fractures. However, recent modeling studies support the existence of lateral flow within the PTn (BSC 2003b, Section 6.6.3). These modeling results show that this lateral flow pattern through the PTn has a large impact on percolation flux distribution in the repository horizon. These percolation fluxes and their distributions at the repository level indicated that there exists a certain amount of large-scale lateral flow or diversion by the PTn unit.

The repository resides within the TSw hydrogeologic unit. The spatially and temporally damped fluxes from the PTn flow into the fractures of the TSw, where the flow becomes focused into fewer fractures or faults as it approaches the repository horizon because of lower fracture density (BSC 2003g, Section 6.1.2). Flow focusing and flow channelization in the fractures may affect seepage rates into repository drifts and thus the number of waste packages potentially contacted by water. Field evidence at Yucca Mountain suggests that preferential flow pathways may exist in the unsaturated rocks of Yucca Mountain. Preferential flow pathways are in part supported by elevated levels of ^{36}Cl, attributed to atmospheric nuclear tests conducted in the 1950s and 1960s, which have been reported at several locations in the Exploratory Studies Facility (ESF) (Fabryka-Martin et al. 1996, Section 9). Focusing flow along these preferential paths or well-connected fracture networks plays an important role in controlling patterns of percolation through highly fractured tuffs, such as the TSw unit, and have a direct impact on seepage into drifts (BSC 2001a, Section 6.4.2).

Flow behavior below the repository is especially important for predicting radionuclide transport from the repository horizon to the water table because transport paths follow the pattern of water flow. The main hydrogeologic units below the repository are the CHn and CFu units. Both of

these units have vitric and zeolitic components that differ in their degree of hydrothermal alteration and subsequent hydrological properties. The zeolitic rocks have low matrix permeability and some fracture permeability; consequently, a relatively small amount of water may flow through the zeolitic units, with most of the water flowing laterally in perched water bodies and then vertically down faults (BSC 2003b, Section 6.6.3).

Perched water zones have been reported in a number of boreholes within the lower portion of the TSw unit and within the upper portion of the CHn unit (BSC 2003b, Section 6.2.2). These perched-water bodies were found primarily in the northern part of the repository area, where lower-permeability, sparsely fractured zeolitic rock units predominate. The occurrence of perched water suggests that certain layers of the lower TSw (e.g., the basal vitrophyre) and the upper zeolitic CHn serve as barriers to vertical flow. On the other hand, the vitric units have relatively high matrix porosity, and a matrix permeability that is similar to their fracture permeability. Because of (1) the permeability parity in the matrix and in the fractures and (2) the limited volume of the fractures (compared to the matrix), simulation results indicate that matrix flow dominates in these vitric units (BSC 2003h). Test results within the CHn at the Busted Butte underground facility show that water flow and radionuclide transport occur mainly within the matrix of the CHn, implying that fracture flow is limited in this unit (BSC 2003h).

The extent of fracture–matrix interaction is a key factor in determining flow and transport processes in the unsaturated zone. Fracture–matrix interaction refers to flow and transport (or mass exchange) between fractures and the matrix. Because of their different hydrologic properties, distinct flow and transport behavior occurs in each component. Modeling results and field observations show limited fracture–matrix interaction in welded units at Yucca Mountain (BSC 2003b, Section 6.6.3). Fingering flow in fractures in unsaturated fractured rocks is believed to be a major reason for limiting fracture–matrix interaction. To incorporate the effects of fingering flow into modeling of flow and transport in unsaturated fractured rocks, the active fracture model was developed by Liu et al. (1998, pp. 2633 to 2646), as documented in *Analyses of Hydrologic Properties Data* (BSC 2003g, Section 6.6). In the model, only a fraction of connected fractures are considered to conduct liquid water as a result of fingering flow at a fracture network scale and within individual fractures.

Major faults may have the potential to significantly affect the flow processes at Yucca Mountain. A fault is considered to serve as a localized, fast-flow conduit for liquid water, especially below the repository. Low-permeability layers (or perched water zones) at the base of the TSw and in the CHn may laterally divert a considerable amount of flow to major faults, which may focus flow downward to the water table. However, it is also possible that alteration within or along faults in the CHn and CFu reduces their permeability, increasing water travel times from the TSw to the water table. Nevertheless, to be conservative, faults below the repository have been treated as localized fast-flow paths in the current unsaturated zone flow model (BSC 2003b, Section 6.1.1).

The site-scale unsaturated zone flow model (BSC 2003b) has been developed, calibrated, and verified based on the geology of the site and field observations. The unsaturated zone flow model is a three-dimensional dual-permeability model. A variety of data (including matrix saturation and water potential data, pneumatic data, perched-water data, temperature data, and geochemical data) has been used for calibrating and confirming the model. Confidence in the

model is increased through comparison against a substantial amount of field data not used for model calibration. These confidence building activities include checking for consistency between modeling results with hydrologic data, geochemical data, and data collected from in situ tests. Effects of thermal processes and the resultant coupled processes on unsaturated zone flow are also treated. The site-scale unsaturated zone flow model generates unsaturated zone flow fields used directly in TSPA analyses.

Unsaturated zone flow and its relevance for the repository system behavior are discussed in detail in *Technical Basis Document No. 2: Unsaturated Zone Flow*.

3.3 SHADOW ZONE

Diversion of percolating water around a waste emplacement drift results in an environment of greatly diminished flow inside the drift compared to the adjacent undisturbed formation. In such an environment, diffusion is practically the only radionuclide transport mechanism to the surrounding rock. Because of the relatively large water content of the matrix in comparison with the fractures, diffusive releases from waste emplacement drifts are strongly partitioned to the matrix. Under these conditions, transport times to the water table increase by orders of magnitude compared to fracture release (BSC 2003i, Section 6.3). Simulation results show that transport is dominated by matrix advection and that most of the radionuclide mass is retained within the matrix at breakthrough at the water table. Consequently, the effects of the drift shadow on transport extend into the saturated zone.

The effects of variations in the flow field and fracture–matrix interaction in the vicinity of a waste emplacement drift, and sensitivity to the corresponding parameters, were investigated by (BSC 2003i). These simulations indicated that, when radionuclides were released into the rock matrix, transport was not significantly affected when flow beneath the emplacement drift was substantially reduced.

Sensitivity calculations have shown that the main effect of the drift shadow on transport is that radionuclide transport is initiated in the matrix (BSC 2003i, Section 6.3). This leads to slow transport through the unsaturated zone because transport is largely confined to the low-permeability matrix. Contrary to the effects on flow, the impact of the drift shadow on transport is not significant when the radionuclides are released into the matrix. Varying degrees of fracture–matrix interaction in the dual-permeability model used in these simulations (BSC 2003i) are shown to have a significant influence on transport in the drift shadow.

3.4 SATURATED ZONE TRANSPORT

The radionuclides that enter the saturated zone are expected to be retarded over a spatial and temporal scale that is dependent on the degradation modes and rates of the engineered barriers. For example, it is possible that the engineered barriers fail either over a broad temporal scale (ranging from thousands to hundreds of thousands of years) due to natural degradation processes, or over a relatively short time interval associated with a low-probability disruptive event, such as a large seismic event or a volcanic event. The spatial scale over which radionuclides enter the saturated zone may be: (1) relatively confined to an area near vertically below each degraded waste package sits (for cases where flow is predominantly vertical through the unsaturated zone);

(2) concentrated at locations where the bulk of the unsaturated groundwater flow intersects the water table; or (3) dispersed over a significant fraction of the total repository footprint of several square kilometers. Uncertainty in the timing and spatial extent of the radionuclides that enter the saturated zone is addressed by considering a range of locations and combining the advective-dispersive transport times within the saturated zone to those times when radionuclides are predicted to reach the saturated zone. This abstraction process is described in *SZ Flow and Transport Model Abstraction* (BSC 2003j).

Saturated zone flow and transport processes are represented by different conceptual and numerical models, including models of groundwater flow at the regional and site scale and models of radionuclide transport. The bases of these models are derived from site-specific in situ observations, as well as field and laboratory tests to determine the relevant parameter values used in these models.

The most likely pathway for radionuclides to reach the accessible environment is through the uppermost groundwater aquifers below the repository. These aquifers, collectively referred to as the saturated zone, delay the transport of radionuclides to the accessible environment and reduce the concentration of radionuclides before they reach the accessible environment. Delay in the release of radionuclides to the accessible environment allows radioactive decay to diminish the mass of radionuclides that are ultimately released. Dilution of radionuclide concentrations in the groundwater used by the potential receptor occurs during transport and in the process of extracting groundwater from wells. The key processes that affect the performance of this barrier include advection, sorption, diffusion (in particular matrix diffusion), hydrodynamic dispersion, decay and ingrowth, and filtration of colloids carrying radionuclides.

Analyses conducted using the saturated zone transport model indicate that the saturated zone is expected to provide significant retardation to the transport of radionuclides to the accessible environment within the 10,000-year period of regulatory concern for the repository at Yucca Mountain. The expected behavior of the saturated zone system is to delay the transport of sorbing radionuclides and radionuclides associated with colloids for many thousands of years, even under wetter climatic conditions in the future. Nonsorbing radionuclides are expected to be delayed for hundreds of years during transport in the saturated zone.

Flow and transport processes in the saturated zone are discussed in detail in *Technical Basis Document No. 11: Saturated Zone Flow and Transport*.

3.5 TEMPERATURE EFFECT ON TRANSPORT

The effects of higher temperature on transport are described by its potential impact on flow (the vehicle of advective transport), and on the magnitude of the main transport parameters. The discussion in the ensuing section indicates that large-scale thermally induced alteration of the hydrologic properties (and, consequently, of large-scale advective transport) of the unsaturated zone is expected to be minimal. However, higher temperatures in the immediate vicinity of the repository can have a drying effect that significantly affects transport by distorting the flow field, enlarging the shadow zone, and leading to reduced releases. Temperature has an effect on the magnitude of the transport parameters.

3.5.1 Effect on Large-Scale Flow and Advective Transport

Because radionuclide transport is controlled by water flow through the unsaturated zone, the thermal effects on flow will affect transport. The mountain-scale thermal-hydrologic (TH), thermal-hydrologic-chemical (THC), and thermal-hydrologic-mechanical (THM) process models were developed to assess mountain-scale hydrologic, chemical, and mechanical changes and to predict unsaturated zone flow behavior in response to heat release by radioactive decay of radioactive waste. The three-dimensional TH model predicts that in a ventilated repository, heating will have, in general, only a limited impact on far-field flow fields, with thermally enhanced flux zones not extending 30 m beyond the repository. Without ventilation, on the other hand, thermally impacted flux zones extend as far as 100 m from the repository.

Mineral dissolution and precipitation leading to changes in hydrologic properties may affect the percolation flux to the repository horizon, impacting seepage into and flow below the repository, which will impact radionuclide transport in the unsaturated zone. The results of the THC simulations (BSC 2003k, Section 6.4.4) indicate that mineral precipitation/dissolution will not significantly affect the hydrologic properties and the percolation flux compared to the effects caused by TH processes alone. Changes to water chemistry, mineralogy, and hydrologic properties in the ambient temperature regions are minimal over the 10,000 years of the simulation.

The mountain-scale THM model is capable of assessing the magnitude and distribution of changes in hydrologic properties and of analyzing the impact of such changes on the large-scale vertical percolation flux through the repository horizon (BSC 2003l, Section 6.5). The result shows that maximum THM-induced changes in hydrologic properties occur at around 1,000 years after waste emplacement, when average temperature in the mountain reaches maximum values. THM-induced changes in large-scale hydrologic properties have no significant impact on the vertical percolation flux through the repository horizon. The implication of these results is that if radionuclide releases begin 2,000 years or later after the waste package emplacement in the repository, temperature effects on flow and advective transport will be negligible.

3.5.2 Effects on Transport in the Shadow Zone

In the shadow zone below the drift (Figure 3-2a), the transport of radioactive solutes is retarded because of the reduced water saturations (BSC 2003m, Section 6.7). The heat generated by the decaying radioactive waste can significantly accentuate this condition by further reducing water saturations and possibly leading to dryout regions in the vicinity of the waste emplacement drifts. Low water saturations reduce water velocities in the shadow zone (into which water moves mainly in response to capillary pressure differentials) and significantly lowers diffusive fluxes across the fracture–matrix interfaces.

The effect of the shadow zone on the transport of colloids is expected to be far more significant, because advective fluxes are low, and diffusive fluxes (the only mechanism capable of transporting radionuclides past the boundaries of the shadow zone) are depressed, because the colloid diffusion coefficient is generally orders of magnitude lower than the molecular diffusion coefficient of solutes.

3.5.3 Effects on the Magnitude of the Transport Parameters

The transport parameters and processes that can be affected by a temperature increase are: (1) the diffusion coefficient D_0 of the dissolved or colloidal species; (2) the sorption parameters of the dissolved species or the filtration parameters of the suspended colloid; (3) the near-field hydrology and the extent and behavior of the shadow zone; and (4) the ambient hydrologic and chemical conditions, which can contribute to thermal alteration of the rock near the repository. These temperature-related consequences are depicted in Figure 3-2.
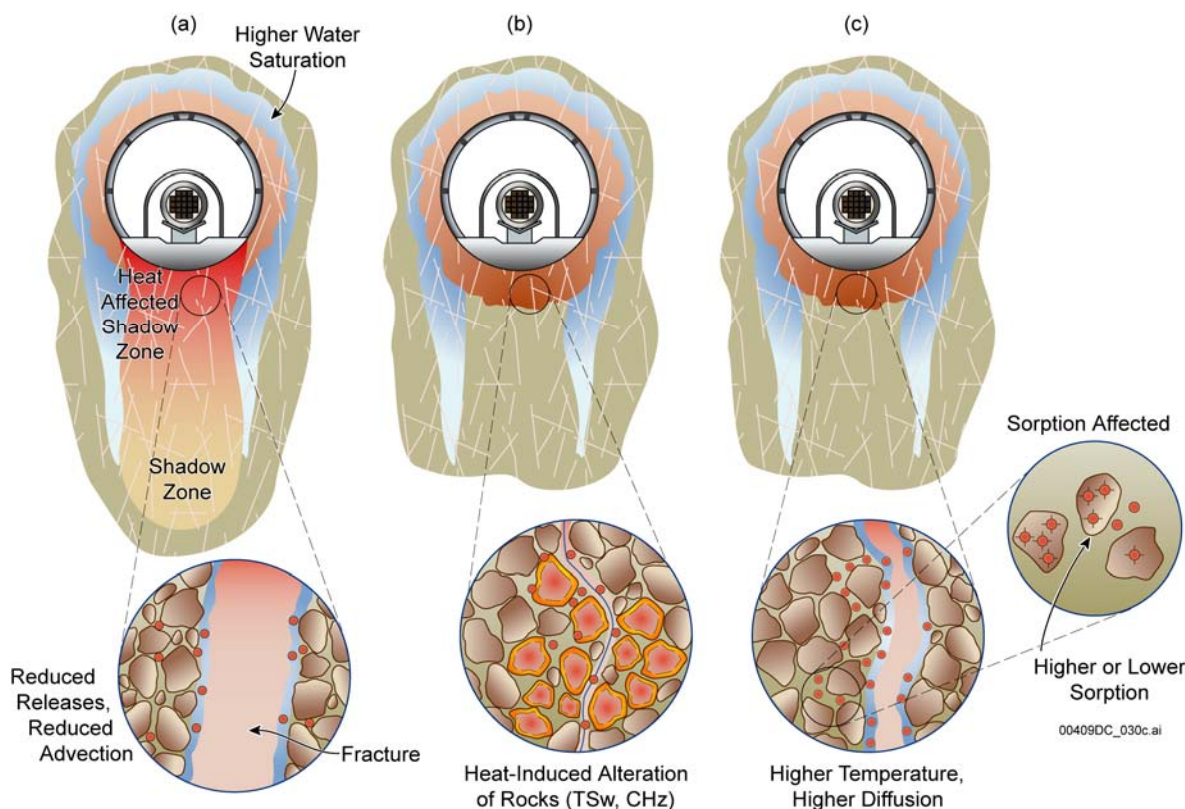
Figure 3-2. Effects of Heat and the Engineered Barrier System on Transport Processes for Solutes and Colloids in the Shadow Zone

3.5.3.1 Temperature Effects on Diffusion

Ambient temperature at the repository horizon at Yucca Mountain is about 25°C, and the maximum temperature at which boiling of the fracture and pore fluids will occur ranges from 95°C to 110°C. Temperature enhances diffusion by increasing Brownian motion (Figure 3-2c). This effect is quantified by an increase in the D_0 of radionuclides. Based on a relationship proposed by Robin et al. (1987, pp. 1105 to 1106), an increase in temperature from 20°C (at the top of the unsaturated zone domain) to 30°C (at the water table) leads to an increase of D_0 by about 30%. The effect is stronger when considering the temperature changes induced by waste-generated heat.

3.5.3.2   Temperature Effects on Sorption and Filtration

The effect of temperature on sorption is less clear. Temperature increases generally lead to an increased K_d, the value of which depends on the species involved, the nature of the sorbing substrate, the composition of the aqueous phase, and the assumed sorption mechanism (Figure 3-2c). The critical parameter defining the temperature dependence of K_d is the enthalpy of sorption, ΔH_r, which is usually relatively small in magnitude. Changes in the degree of sorption between ambient temperature at the repository horizon at Yucca Mountain, about 25°C, and the maximum temperature at which boiling of the fracture and pore fluids will occur, 95°C to 110°C, will be relatively small (by about a factor of 10, depending on the radionuclide species under consideration), when compared to the estimated ranges of sorption coefficients (see Table 5-1). For strontium, europium, and uranium(VI), K_d increases 1.6 to 3.8 times due to temperature increases from 25°C to 95°C (BSC 2003n).

When modeling solute radionuclide transport in the near field, it can be assumed within experimental error that the K_d values of all cited radionuclides are not temperature dependent. This simplifying assumption can be considered conservative because, for most species, the mean value of ΔH_r is small and likely within the limits of uncertainty imposed by the uncertainties of other model parameters. Laboratory studies (BSC 2003n) confirmed the validity of this approach over a wide range of radionuclides.

Colloid filtration (deposition) generally follows a kinetic process (BSC 2003e, Sections 6.2.3 and 6.16.2). An increase in temperature increases the forward filtration coefficient, κ^+, indicating an increase in the filtration (i.e., deposition) rate (BSC 2003e, Equation 6-31). There is no information on the effect of temperature on the backward filtration coefficient, κ^-.

3.5.3.3   Temperature Effects on the Sorptive Properties of the Host Rock

Higher temperatures may thermally alter the devitrified and zeolitic layers below the repository horizon, affecting the sorption of radionuclides (Figure 3-2b). Significant changes in the sorptive properties of the host rocks and zeolites are predicted to occur under the thermal, hydrologic, and geochemical conditions prevailing during the thermal perturbation caused by waste emplacement (BSC 2003o). In the Calico Hills Formation, the dominant zeolitic zone underlying the repository horizon, the temperature is expected to rise to about 70°C and about 15 vol % of the clinoptilolite is predicted to alter to more stable secondary feldspars and stellerite. Partial dehydration of the clinoptilolite may occur (Carey and Bish 1996; 1997). However, the expected temperature excursion would be insufficient to alter coexisting opal-CT to quartz. Opal-CT maintains a high silica activity in the system and curtails alteration of the zeolites to more stable, but less sorptive phases (Duffy 1993a; 1993b). Despite current modeling uncertainties relating to the persistence of zeolites, the determination that sorption coefficients of given radionuclides have temperature dependencies, as discussed above, remains a valid basis for predicting radionuclide behavior at Yucca Mountain.

It has been determined that coupled THC processes will be inconsequential because the duration and magnitude of the thermal pulse and kinetic factors affecting the metastabilities of extant phases are too small to cause significant alteration and the water fluxes are not sufficiently large to dissolve and redeposit significant quantities of the minerals (BSC 2003k, Section 7.3). The

inherent stability of zeolites under the geochemical and hydrologic conditions prevailing during the thermal perturbation due to waste emplacement is such that no significant changes in the sorptive properties of the host rocks and zeolites are expected during this period. Thus, it can be concluded that there is no need to account for zeolitic alterations in the simulations. For the radionuclides with temperature dependent K_d values, a simple modification of the sorption coefficient would be sufficient to account for the radionuclide sorptive behavior of the rock matrix at Yucca Mountain.

INTENTIONALLY LEFT BLANK

4. LABORATORY MEASUREMENTS AND FIELD OBSERVATIONS

4.1 LABORATORY SORPTION MEASUREMENTS

Measurements of the sorption distribution coefficient, K_d, in the unsaturated zone rocks are critical in the determination of sorption-induced retardation of radionuclide transport. All modeling predictions of radionuclide fate and transport through the unsaturated zone are based on these measurements.

This section provides the bases for the derivation of sorption coefficients and their probable ranges used in the unsaturated zone transport calculations (BSC 2003e). The sorption coefficient data on which the distributions are based are obtained in laboratory experiments in which crushed rock samples from the Yucca Mountain site are contacted with groundwater (or simulated groundwater) representative of the site and spiked with one or more of the elements of interest. Sorption experiments have been carried out as a function of time, element concentration, atmospheric composition, particle size, and temperature. In some cases, the solids remaining from sorption experiments were contacted with unspiked groundwater in desorption experiments. The sorption and desorption experiments together provide information on the equilibration rates of the forward and backward sorption reactions. For elements that sorb primarily through surface complexation reactions, the experimental data are augmented with the results of calculations using PHREEQC V2.3 (BSC 2001b). The inputs for the calculations include groundwater compositions, surface areas, binding constants for the elements of interest, and thermodynamic data for solution species. These calculations provide a basis for interpolation and extrapolation of the experimentally derived sorption coefficient data set.

The primary controls on sorption behavior of the elements of interest in the unsaturated zone flow system include the detailed characteristics of mineral surfaces in the rock units through which water flows from the repository to the saturated zone. It also includes the detailed chemistry of pore waters and perched waters in the unsaturated zone along flow paths, the sorption behavior of each element, and their concentrations in the groundwater. These parameters are discussed in the following sections.

There are three dominant rock types in the unsaturated zone along potential flow paths from the repository to the saturated zone: devitrified tuff, zeolitic tuff, and vitric tuff (BSC 2003c, Section 6). Devitrified tuff is composed primarily of silica (quartz and cristobalite) and alkali feldspar. It may also contain trace amounts of mica, hematite, calcite, tridymite, kaolinite, and hornblende, as well as minor amounts (less than 25%) of smectite and/or zeolite. For the purpose of this analysis, sorption coefficient distributions for devitrified tuff are based on data obtained from samples that are composed primarily of silica phases and feldspar with only trace amounts of other phases. Sorption coefficient distributions for zeolitic tuff are taken exclusively from samples that contain more than 50% zeolite, with the balance made up of clay, silica phases, alkali feldspar, and/or glass. Zeolitic tuffs have significantly higher surface areas compared to other tuffs (Triay et al. 1996, p. 62). For vitric tuffs, sorption coefficient distributions are based on samples that contain more than 50% glass, with the remainder composed predominantly of feldspar, silica phases, zeolites, and clay.

Sorption coefficients for the radionuclides of interest can be a function of the concentrations of the radionuclides present in solution. In most cases, experiments were carried out over a range of concentrations up to the solubility limit. Above the solubility limit, a solid phase incorporating the element of interest is precipitated out of solution. Therefore, the concentration of an element in solution cannot rise much higher than the solubility limit. Because experiments have been carried out at concentrations up to the solubility limit for most elements of interest, the experimental results and the probability distributions derived from them include this dependency. The only element for which the experimental concentrations did not approach the solubility limit was cesium, which has a very high solubility in Yucca Mountain waters (BSC 2003p, Section 6.17); cesium concentrations in Yucca Mountain groundwaters will not have a solubility limitation (BSC 2003p, p. I-27)

In the unsaturated zone, two rather distinct water types exist in the ambient system. One is perched water and the other is pore water. Perched water is generally more dilute than pore water. The J-13 (water from the main supply well for activities) and UE-25 p#1 (groundwater obtained from Paleozoic carbonate rocks at depth beneath Yucca Mountain) waters were used in sorption experiments as end-member compositions intended to bracket the impact of water composition on sorption coefficients. The two selected waters bracket the chemical composition of pore water and perched water found in the unsaturated zone. Because water from the UE-25 p#1 well was not available to the experimental program at all times, synthetic p#1 water was developed. Bicarbonate concentration in the synthetic groundwater was similar to that found in UE-25 p#1. It was used primarily in experiments with uranium, neptunium, and plutonium because the solution and sorption behavior of these elements is sensitive to the bicarbonate and carbonate concentrations in solution.

The derivation of sorption coefficient probability distributions for the elements of interest on the major rock types in Yucca Mountain involves both an evaluation of available experimental data and sorption modeling (BSC 2003e, Attachment I). Figure 4-1 shows an example of experimental and modeling results with significant variations in the sorption coefficients. The radionuclides of interest are divided into three groups of radionuclides. For the first group, including americium, neptunium, protactinium, plutonium, thorium, and uranium, experimental data are used to evaluate the impact of radionuclide concentrations, sorption kinetics, and variations in water chemistry on sorption coefficients. Surface complexation modeling is used to further evaluate the impact of variations in water chemistry and surface area on sorption coefficients. The surface complexation models used in this analysis are based on the code PHREEQC V2.3 (BSC 2001b). The impact of variations in pH on neptunium coefficients on devitrified tuffs is shown in Figure 4-1. The amount of scatter in the experimental data shows that the neptunium sorption coefficient depends very little on pH. PHREEQC surface complexation model curves reflect the equilibrium values of neptunium sorption coefficients on devitrified tuff (BSC 2003e, Attachment I).
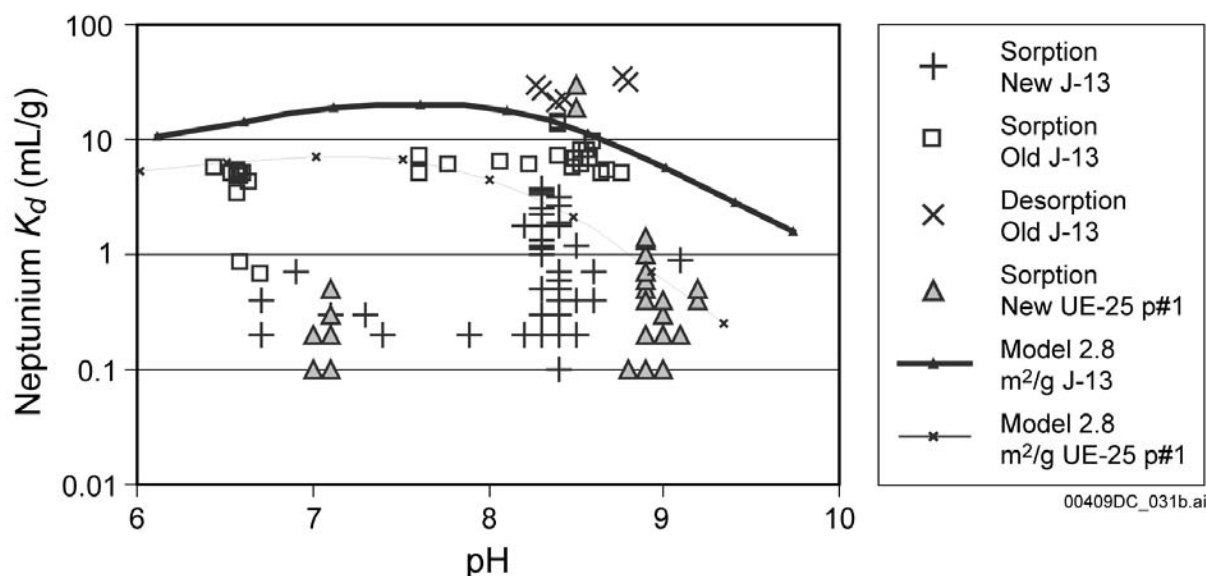
Source: BSC 2003e, Figure I-20.

NOTE: PHREEQC model results for J-13 and synthetic UE-25 p#1 waters are also plotted.

Figure 4-1. Neptunium Sorption Coefficient on Devitrified Tuff in J-13 and Synthetic UE-25 p#1 Waters versus Solution pH in Sorption (Forward) and Desorption (Backward) Experiments

In the second group of elements, including cesium, radium, and strontium, the ranges of sorption coefficient values for the major rock types are derived directly from the available experimental data and the ranges for environmental variables expected in the transport system. Although it would be preferable to have a theoretical model to evaluate the impact of variations in water chemistry and rock chemistry on sorption coefficients for these radionuclides, sufficient data are not available to properly constrain such a model. For the third group, including carbon, iodine, and technetium, the sorption coefficient is set to zero in volcanic rocks and in alluvium.

On the basis of the experimental and modeling results, the probability distribution function can be cumulative lognormal or truncated normal distributions. The distributions were constrained by pH, Eh, water chemistry, rock composition and surface area, and radionuclide concentration (see Section 5.3.2, Table 5-1, for K_ds in the rocks of the unsaturated zone). In general, the approach used in derivation of the distributions tended to underestimate the range and median or expected value. This conservative approach was taken because of the potential scaling uncertainties in the application of these distributions to transport calculations at Yucca Mountain.

4.2 FIELD TESTS AND OBSERVATIONS

Field tests were vital in the understanding of the processes and phenomena occurring during transport through the unsaturated zone. Even more importantly, they provided the basis for confidence building and validation of the numerical models used to predict the long-term fate and transport of radionuclides following potential releases at the repository.

A summary of field experiments designed to investigate transport is presented in this section. These tests include the Busted Butte test series, the Alcove 8–Niche 3 test, and the Alcove 1 test.

For the Alcove 1 test, numerical simulation and prediction were also presented here to provide implications of these field test results to model developments for the site-scale transport modeling.

Transport tests that have been conducted up to now (and which are discussed here) involve length scales ranging from a few meters to a maximum of 30 m, and the time scale of these experiments does not exceed 2 years. There is a gap in the upper ranges of both the spatial and the temporal test scales, and a larger mountain-scale test or series of tests is practically infeasible. This gap impedes the application of the knowledge gained from the current set of field tests to the validation and support of the mountain-scale transport model. Nevertheless, the available test results are useful in establishing the basic conceptual framework of transport and for forming the basis for extension to large-scale transport.

4.2.1 Busted Butte Test Series

The Busted Butte unsaturated zone transport test was a long-term experiment conducted in Busted Butte near Yucca Mountain (BSC 2003h, Section 6.13) to investigate flow and transport issues in the unsaturated zone process models for Yucca Mountain.

The Busted Butte test facility is located in Area 25 of the Nevada Test Site, approximately 160 km northwest of Las Vegas, Nevada, and 8 km southeast of the repository area. The site was selected because of the presence of a readily accessible exposure of the Topopah Spring Tuff and the Calico Hills Formation, and the similarity of these units to those beneath the repository horizon (see Figure 4-2). The test facility consists of an underground excavation along a hydrogeologic contact between the TSw unit and the CHn unit. This contact is comprised of the nonwelded portion of the basal vitrophyre of the Topopah Spring Tuff. The study of the TSw–CHn interface is important because of the significant role that the vitric layers of the CHn unit play in radionuclide retardation (BSC 2003e, Section 6.10).

The test proceeded in two phases, each differing in design, purpose, and experimental scales, among other factors. A detailed description of the tests can be found in *Unsaturated Zone and Saturated Zone Transport Properties* (BSC 2001c, Section 6.8; BSC 2003h, Section 6.13). The first phase, including test Phases 1A and 1B, was designed as a scoping study to assist in design and analysis of Phase 2 and as a short-term experiment aimed at providing initial transport data on a fracture near an interface. The second phase incorporated a larger region than Phase 1, with a broader, more complex scope for tracer injection, monitoring, and collection.

4.2.1.1 Phase 1A Test

The Phase 1A Test was located in the CHn unit spanning both the geologic Calico Hills Formation (Tac) and the nonwelded subzone of the lowermost Topopah Spring Tuff (Tptpv1 in the lithostratigraphic units (BSC 2002); ch1v in the unsaturated zone hydrogeologic model layer (BSC 2003e). It involved the injection of nonreactive tracers into the Tptpv1 and the subsequent flow and transport in the Tptpv1 and Tac layers. It was a noninstrumented or blind test, consisting of four single-point injection boreholes. All Phase 1 boreholes were 2 m long and 10 cm in diameter.
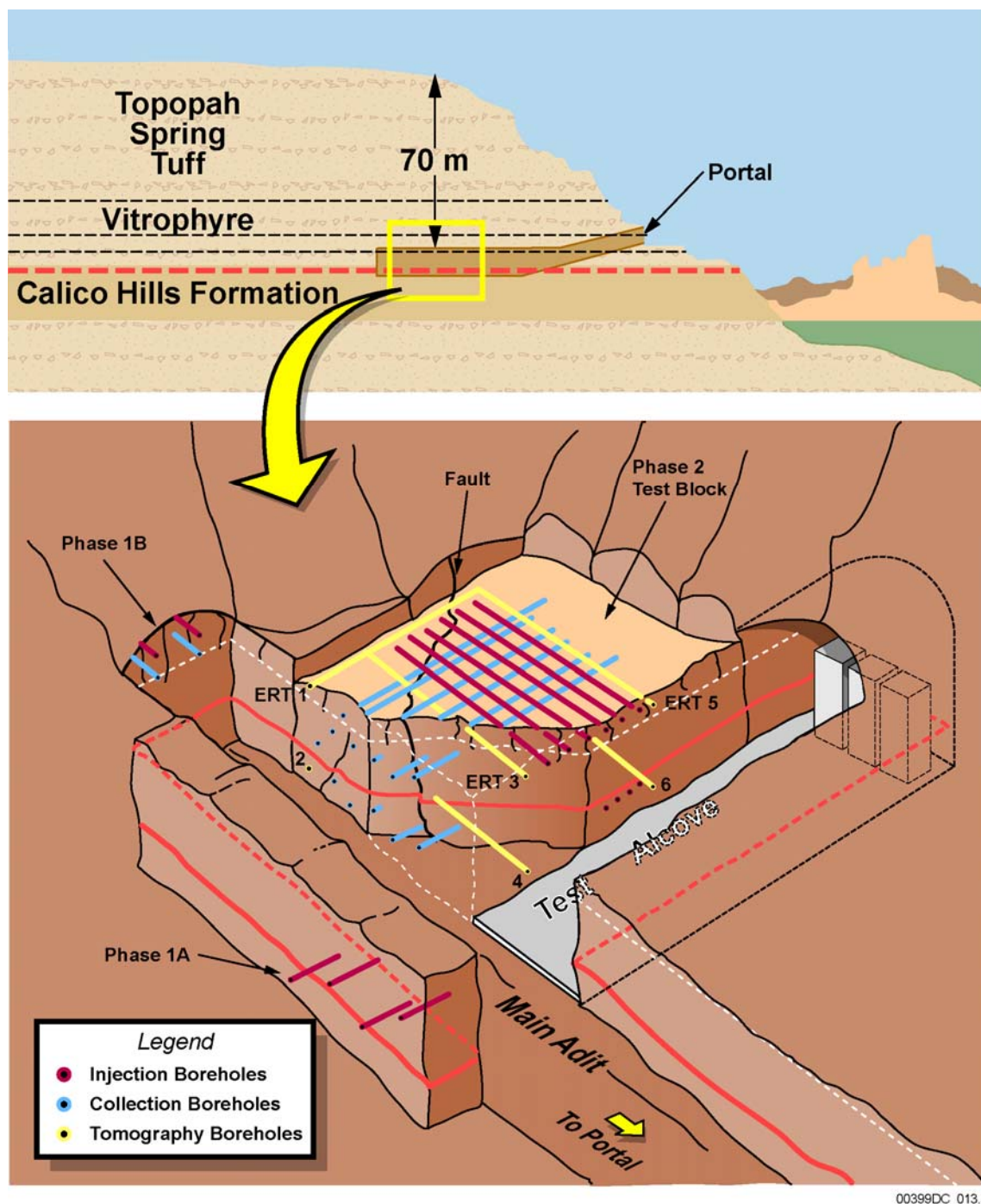
Source: BSC 2003h, Figure 6.13.1-1.

NOTE: This schematic of the Busted Butte unsaturated zone transport test shows the relative locations of the different experiment phases and borehole locations. Figure not drawn to scale. ERT = electrical resistivity tomography.

Figure 4-2. Busted Butte Unsaturated Zone Transport Test

Tracers were injected continuously for 286 days at rates of 1 mL/hr (boreholes 2 and 4) and 10 mL/hr (boreholes 1 and 3). The injected species included a mixture of conservative (nonsorbing) tracers (bromide, fluorescein, pyridone, and fluorinated benzoic acids), a sorbing tracer (lithium), and fluorescent polystyrene microspheres (i.e., an analog for a colloidal tracer). Of all the tracers injected during the field experiment, only the transport of the nonsorbing bromide and fluorescein tracers can be studied because of the poor quality and unreliability of the data from the other two tracers.

A schematic of the borehole layout in the Phase 1A test is shown in Figure 4-3. More detailed information is provided in *Unsaturated Zone and Saturated Zone Transport Properties* (BSC 2001c, Section 6.8). Only injection into borehole 3 (located in the Tptpv1 layer of the CHn unit) was considered. Borehole 3 is about 20 cm above the Tptpv1–Tac interface. The injection tests into boreholes 1 (located in the Tptpv1 layer, but further removed from the interface), 2, and 4 (located in the Tac layer of the CHn unit) were not analyzed because of the poor quality of the data.
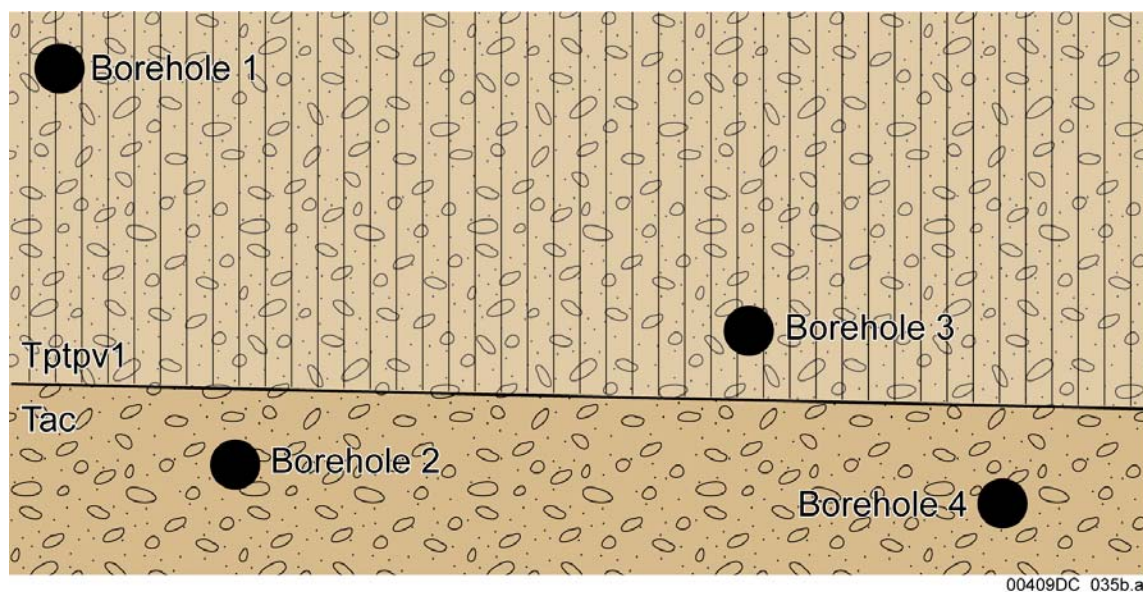
Source: BSC 2003h, Figure 6.13.1-3.

NOTE: The figure is not drawn to scale.

Figure 4-3. Phase 1A Borehole Locations

The field test was completed through excavation by mineback and auger sampling. During mineback, as successive vertical slices were being removed, digital photographs under visible and ultraviolet light were taken to record the distribution of moisture and fluorescein. In addition, rock samples were collected by augering, and the exposed plane was surveyed. The auger samples were analyzed for tracer concentration.

The fluorescein plume in the vicinity of borehole 3 at various locations along the y-axis (originating at the rock face and going into the rock) is shown in Figure 4-4. The plume cross sections show a relatively uniform distribution of fluorescein around the injection borehole, although some borehole shielding effects (tracer blocked or delayed from moving in the direction

of the borehole) can be seen. At all of the mineback faces, the corresponding plume cross sections are more oval than round. Lithologic contacts clearly influence flow and tracer transport. Figure 4-4 shows the distinct geologic layering, denoted by the limited penetration and higher fluorescein concentrations in the less permeable lower layer.
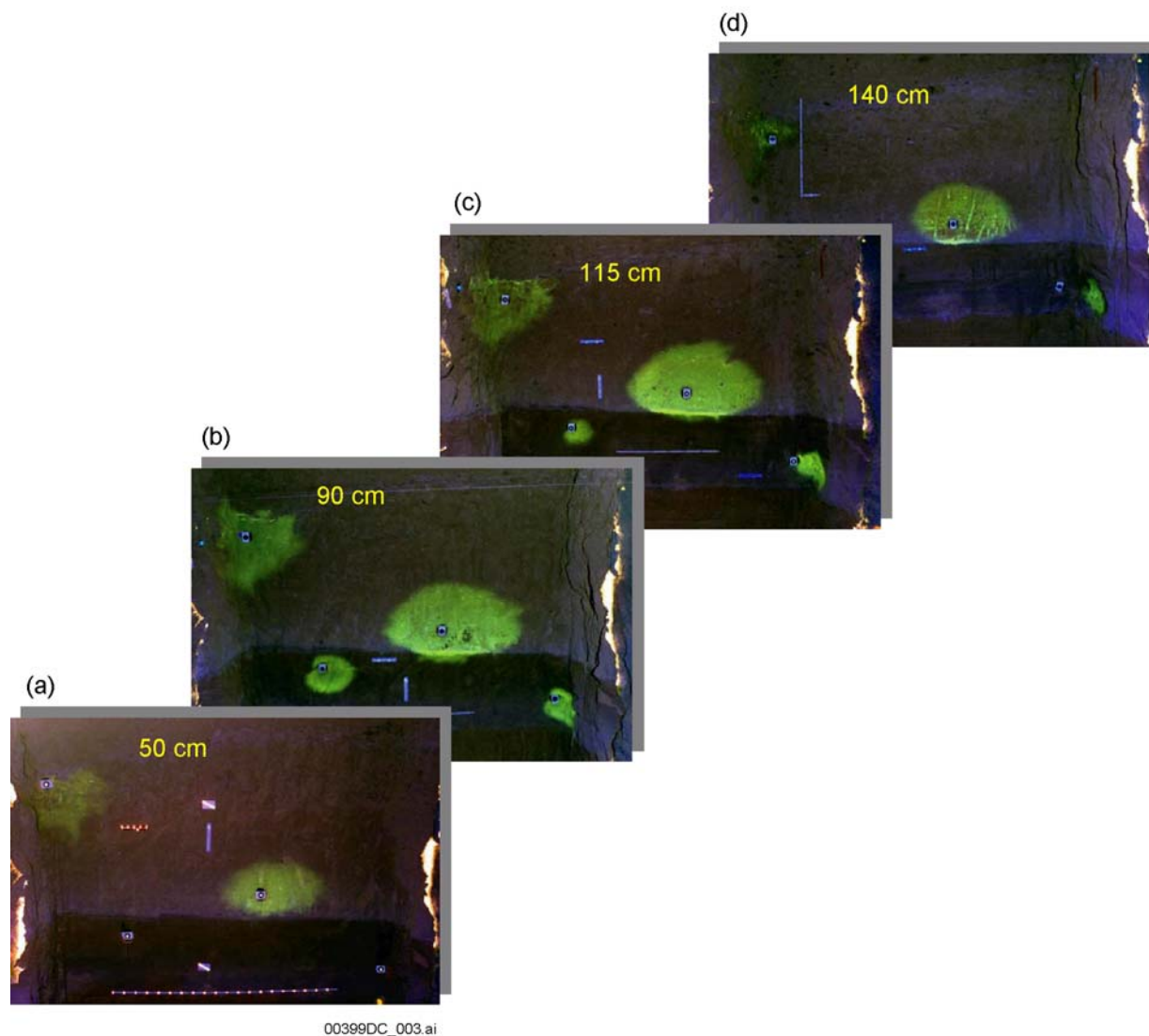
Source: BSC 2003h, Figure 6.13.2-1.

Figure 4-4. Fluorescein Plume at Each of Four Phase 1A Mineback Faces

4.2.1.2   Phase 1B Test

Phase 1B involved the injection of the tracers discussed in the Phase 1A test and collection of pore-water and tracer samples in the lower section of the Topopah Spring Tuff (Tptpv2). This test was designed to acquire data on fracture–matrix interactions in the TSw, providing some of the only such data. The results were used to calibrate fracture properties for the Phase 2 analysis.

In the Phase 1B field test, the tracers were injected into two boreholes (borehole 5 at a rate of 10 mL/hr, and borehole 7 at a rate of 1 mL/hr) in the lower portion of the Topopah Spring basal vitrophyre (Tptpv2 in lithostratigraphic units and tsw39 in the unsaturated zone layers of the hydrogeologic units), which is a relatively low-permeability fractured rock. Samples were obtained in collection boreholes 6 and 8 (Figure 4-5). Detailed information on the design, configuration, and dimensions of the Phase 1B test is provided in *Unsaturated Zone and Saturated Zone Transport Properties* (BSC 2001c, Section 6.8). The tracer solutions were injected at a depth of 1.30 m, measured from the rock face into the injection boreholes. Water samples from boreholes were collected and analyzed regularly during the injection period (Tseng and Bussod 2001).
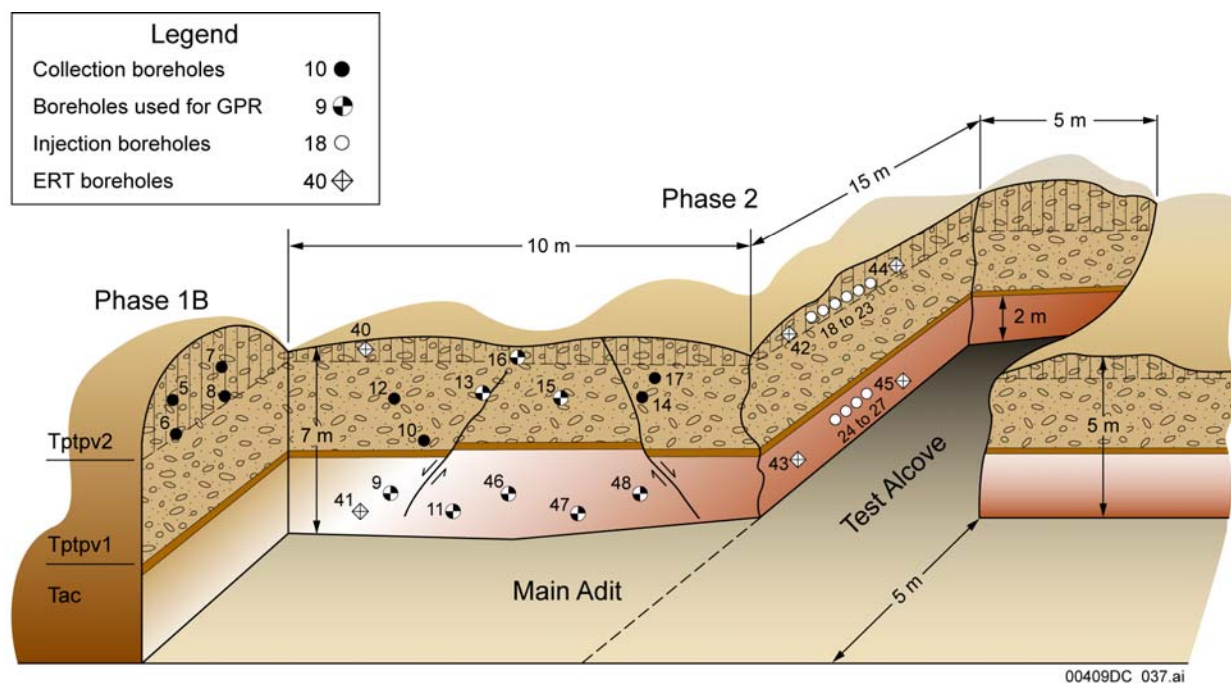
Source: BSC 2003h, Figure 6.13.1-4.

NOTE: GPR = ground penetrating radar; ERT = electrical resistance tomography.

Figure 4-5. Schematic of Phase 1B and Phase 2 Borehole Locations

Breakthrough of all five solute tracers was observed in collection borehole 6, directly below the 10-mL/hr injection borehole 5. No tracer breakthrough was discernible in collection borehole 8 below the 1-mL/hr injection borehole 7. The breakthrough concentrations (the ratios of measured concentration, C to initial concentration, C_0) of bromide and 2,6-difluorobenzoic acid (DFBA) in borehole 6 are shown in Figures 4-6 and 4-7, respectively.

Maximum concentrations are invariably observed at a (horizontal) depth of approximately 1.3 cm into the rock face, which is directly underneath the injection port in borehole 5. However, the value of the maximum concentration and amount of mass recovery vary greatly. Bromide and 2,6-DFBA (both nonsorbing anionic tracers) exhibit reasonable breakthrough patterns and relatively similar maximum relative concentrations compared with other trackers.
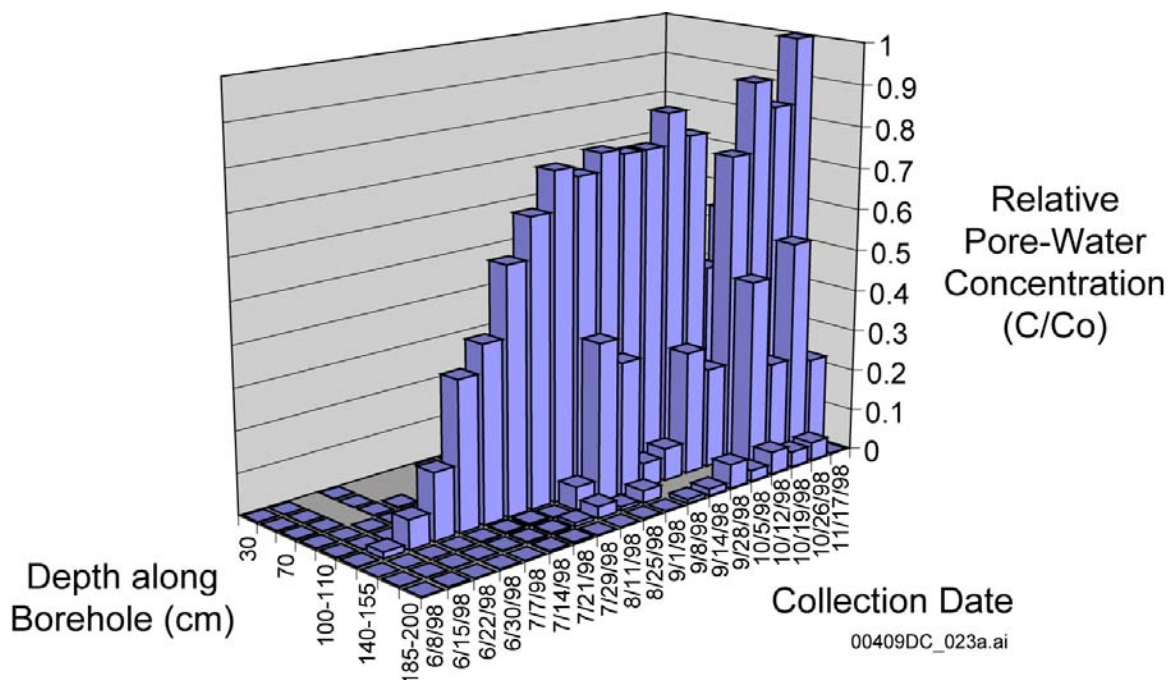
Source: BSC 2003h, Figure 6.13.2-4a.

Figure 4-6. Bromide Concentrations in Borehole 6 for Phase 1B
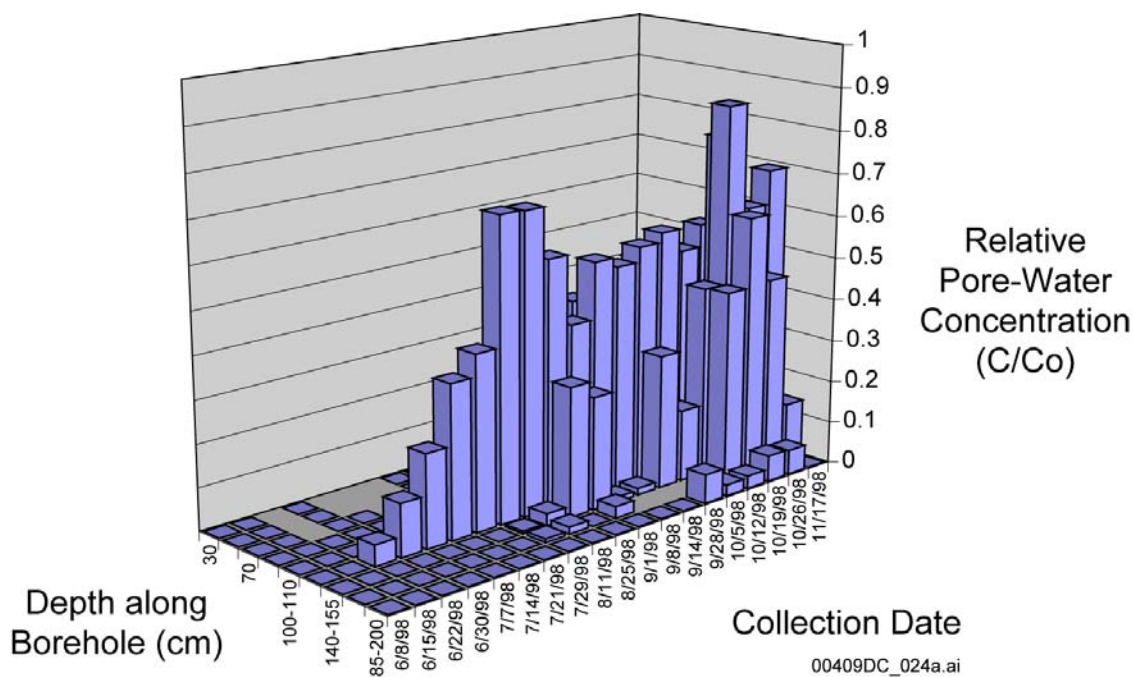
Source: BSC 2003h, Figure 6.13.2-4b.

Figure 4-7. 2,6-DFBA Concentrations in Borehole 6 for Phase 1B

4.2.1.3   Phase 2 Tests

Phase 2 tests were designed to incorporate large volumes of the rock. A detailed description of this test phase can be found in *Unsaturated Zone and Saturated Zone Transport Properties* (BSC 2001c, Section 6.8).

Phase 2 testing involved a 7-m-high, 10-m-wide, and 10-m-deep block representing all of the rock units of Phase 1. The injection points for this phase were distributed in two horizontal, parallel planes arranged to test the properties of the lower Topopah Spring Tuff (Tptpv2) and the hydrologic Calico Hills (Tptpv1 and Tac).

Six upper injection boreholes (boreholes 18 to 23) (of which only three were used) and four lower boreholes (boreholes 24 to 27) were drilled into the block, as shown in Figure 4-5. The upper injection plane consisted of 37 injection points distributed along the axes of the injection boreholes and was located in the fractured Topopah Spring Tuff (Tptpv2). As in Phase 1B, this unit represents the base of the TSw basal vitrophyre and is characterized by subvertical fractured surfaces that form columnar joints. The natural fracture pattern present in this unit serves as the conduit for tracer migration into the CHn. The lower horizontal injection plane was located in the Calico Hills Formation (Tac) and included 40 injection points distributed in the four horizontal and parallel injection boreholes. These boreholes were designed to incorporate the lower part of the block in the event that the top injection system did not involve the entire block during the testing program. Phase 2 also included 12 collection boreholes drilled in a direction perpendicular to that of the injection boreholes (see Figure 4-5, boreholes 9 to 17 and boreholes 46 to 48). These boreholes contained collection pads evenly distributed on inverted membranes to collect samples.

Phase 2 included three subphases: 2A, 2B, and 2C. Phase 2A involved injection (at a rate of 1 mL/hr per injection point) into a single instrumented borehole (borehole 23) in the upper injection plane. This borehole is located entirely within the Tptpv2 unit, which consists of fractured, moderately welded tuffs from the basal vitrophyre. In Phase 2B, four instrumented injection boreholes (boreholes 24 to 27) in the lower injection plane were used, and the injection rate was much higher than in Phase 1A (10 mL/hr per injection point). In this case, the injection plane was restricted to the Calico Hills Formation (Tac). Thus, the Phase 2B test was designed to incorporate the lower section of the test block, while the upper section of the block was incorporated during the Phase 2A and 2C tests. Phase 2C involved injection into three upper boreholes (boreholes 18, 20, and 21) at much higher rates than in Phases 1A and 1B (50 mL/hr per injection point). As in Phase 1A, the injection system was located on a horizontal plane in the Tptpv2 unit.

The tracers used in the Phase 2 tests included all the tracers used in Phase 1. Additionally, three fluorinated benzoic acids, a mixture of sorbing solute species (Ni^{2+}, Co^{2+}, Mn^{2+}, Sm^{3+}, Ce^{3+}, and rhodamine WT), and a nonsorbing anionic tracer (I^-) were used. Pad analyses confirm breakthrough of the nonsorbing tracers in 14 of the 15 collection boreholes. Of the sorbing tracers, breakthrough has been confirmed only in the case of lithium in 10 of the 15 collection boreholes. The spatial distributions of bromide and lithium in sampling borehole 16 at different times during Phase 2C tests are shown in Figures 4-8 and 4-9. The lower lithium concentrations are consistent with the difference in the sorption behavior of the two tracers.
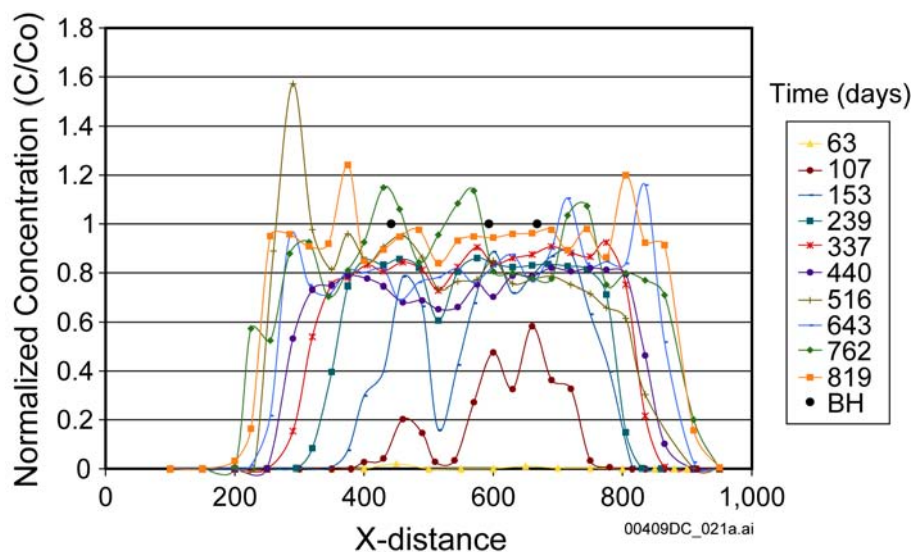
Source: DTN: LA0112WS831372.003.

NOTE: BH = borehole.

Figure 4-8. Spatial Distributions of Bromide in Sampling Borehole 16 at Different Times During Phase 2C Test
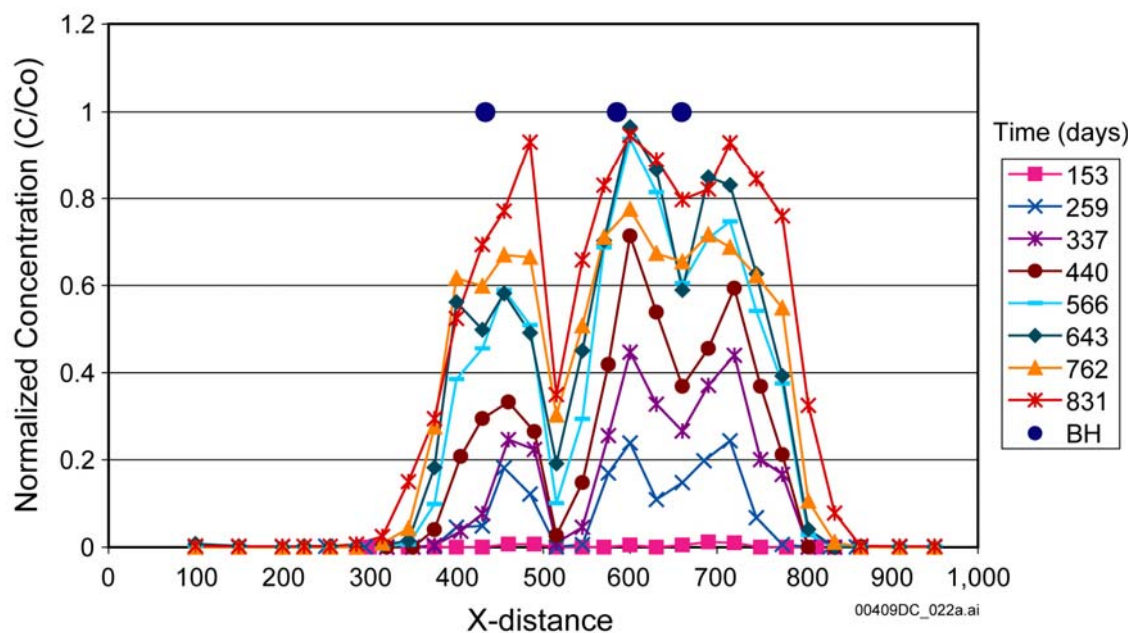
Source: DTN: LA0201WS831372.007.

NOTE: BH = borehole.

Figure 4-9. Spatial Distributions of Lithium in Sampling Borehole 16 at Different Times During Phase 2C Test

4.2.2   The Alcove 8–Niche 3 Test

The drift-to-drift tests at Alcove 8–Niche 3 (in progress) provide information on seepage and transport over spatial scales in the range of 20 m. This is the intermediate scale for relating site-scale processes of seepage and percolation with drift-scale processes of diversion and seepage. Along the long flow paths, the corresponding advective transport is affected by fracture–matrix interaction, which is shown to be an important retardation mechanism that delays the movement of water and tracers through the unsaturated units. A detailed description of the Alcove 8–Niche 3 test can be found in *In Situ Field Testing of Processes* (BSC 2003h, Section 6.12).

Figure 4-10 shows the location of the test site within the ESF main drift and the Enhanced Characterization of the Repository Block (ECRB) Cross-Drift, as well as a three-dimensional representation of the test area, including several slanted (near-vertical) boreholes. Alcove 8 is located within the upper lithophysal zone of the TSw (Tplpul). This unit has some lithophysal cavities that may intersect fractures. The distinctive feature of the test bed in Alcove 8 is a near-vertical fault that cuts across the floor. The fault is open on the ceiling of the alcove, and appears to be closed along the floor. In the test, water and tracers were released in trenches about 5 cm wide and about 5 cm deep that had been etched along this fault. Niche 3 (also referred to as Niche 3107) is approximately 4 m wide, extends to approximately 14 m from the centerline in the ESF main drift, and is about 20 m below the floor of the alcove. The niche is located within Tptpmn, about 20 m below the floor of the alcove; the interface between Tptpul and Tptpmn is about 15 m below the floor of Alcove 8 (BSC 2003h, Section 6.12). The fault in Alcove 8 is visible along the ceiling of Niche 3.

Water was introduced along the fault (about 5 m long) (DTN: GS020508312242.001) under ponded conditions (with 2 cm of water head) until quasi-steady state seepage was observed in Niche 3. Then, a finite volume of water containing two tracers with different molecular diffusion coefficients (bromide and pentafluorobenzoic acid (PFBA)) was introduced into the fault. Once the tracer-laced water had been released into the fault, more tracer-free water was released. Both tracer-laced and tracer-free releases occurred under the same ponded condition. This release of tracer-free water continued until a few months after breakthrough of the two tracers (bromide and PFBA) was observed in the seepage collected in Niche 3.

A water-pressure head of 2 cm was applied at a ponding plot along the fault in Alcove 8. The plot consisted of four trenches of different application rates as a result of heterogeneity along the fault. Figure 4-11 shows the total application rate as a function of time. The considerable temporal variability of the application rate observed during the test was attributed to heterogeneity in (1) the degree of infill and (2) in the properties of the infill materials within the fault just below the ponding plot (Figure 4-10) and to the unsaturated state of the majority of the fault and of the surrounding fractures away from the plot.

After 209 days of water application, two nonsorbing tracers with different molecular diffusion coefficients (bromide and PFBA) and a sorbing tracer (lithium) were introduced into the water at the infiltration plot. Tracer concentrations were measured in three of the trays (at the niche) capturing seeping water from the fault. Figure 4-12 shows the evolution over time of bromide concentration and of the daily seepage rates for a 1.5-month period following arrival of the

wetting front. The bromide concentration increases from a low initial level (about 3 ppm) to the release concentration of 30 ppm about 30 days after the onset of seepage. Given the nonsorbing behavior of bromide, the delayed bromide breakthrough is a good indicator of the importance of matrix diffusion, the absence of which would have resulted in much earlier observations of the 30 ppm concentration.
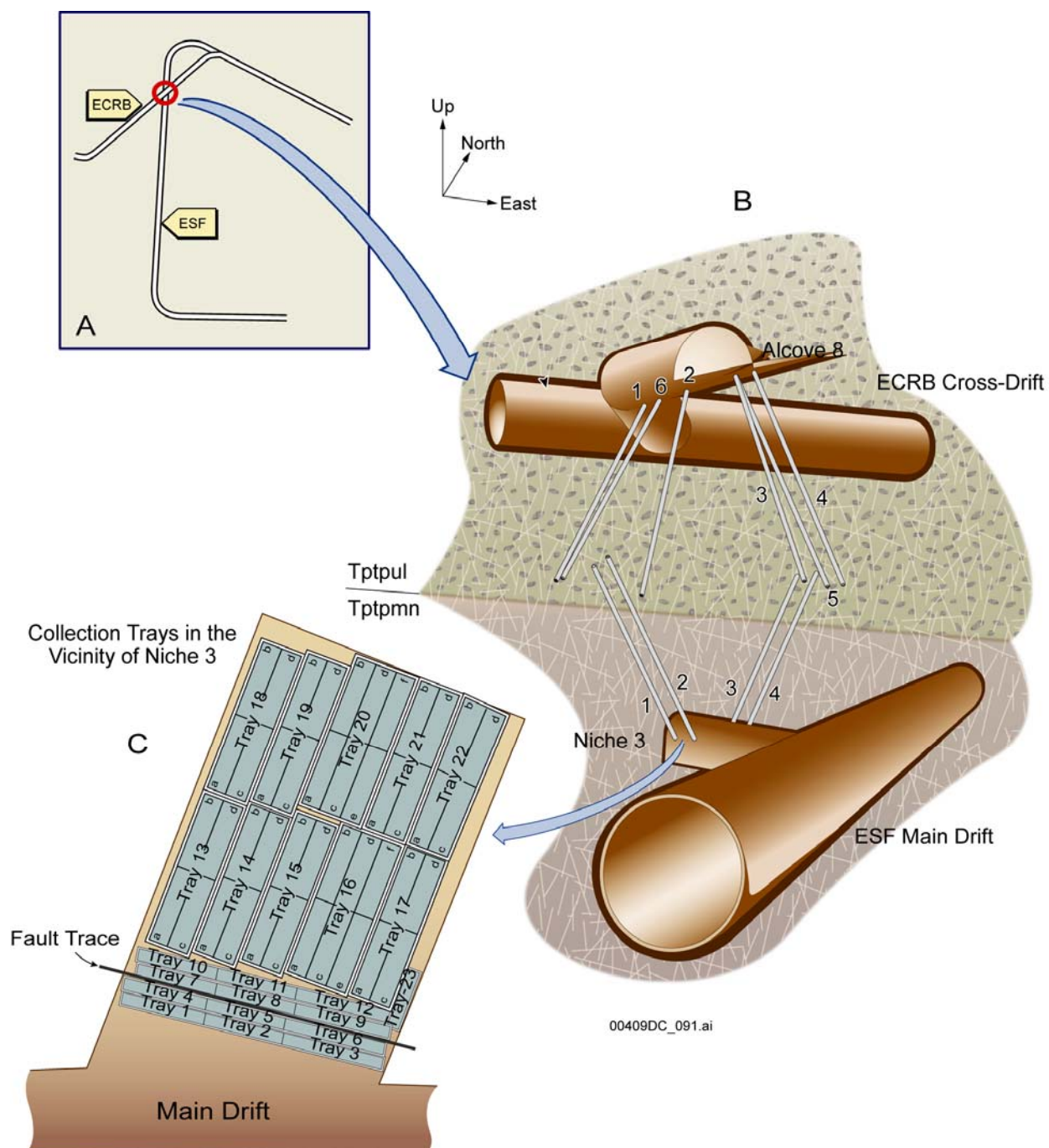
Source: BSC 2003h, Figure 6.12.1-2.

Figure 4-10. Test Bed for the Alcove 8–Niche 3 Tests
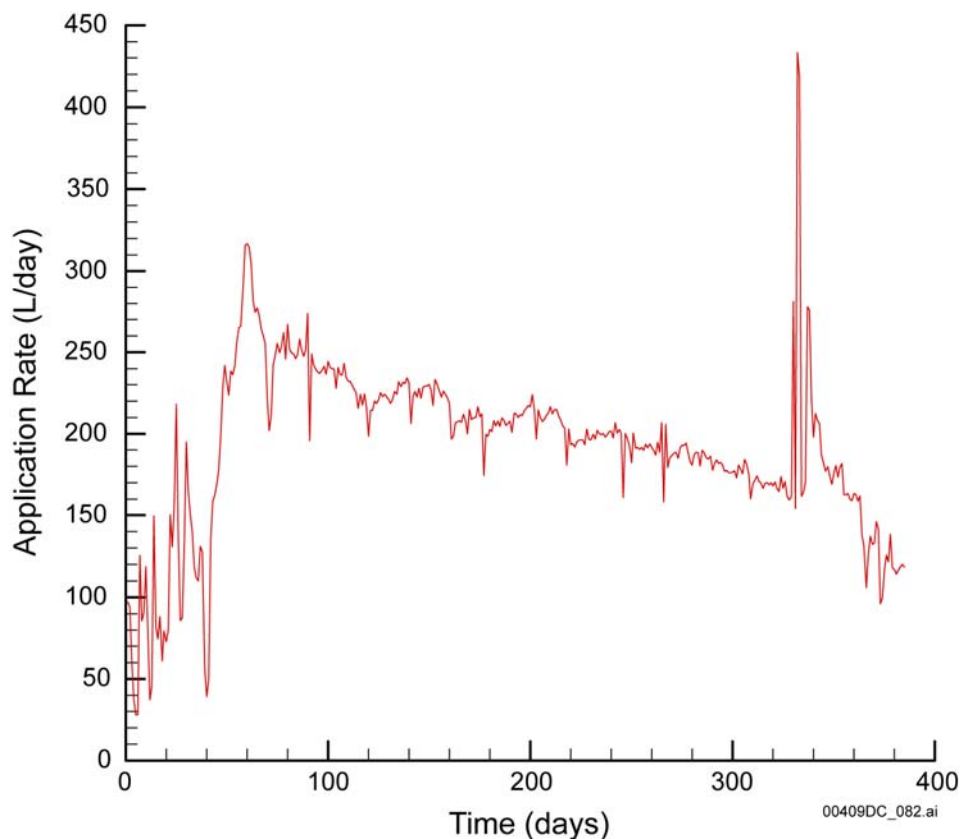
Source: BSC 2003e, Figure 7.4-1.

Figure 4-11. Total Application Rate as a Function of Time
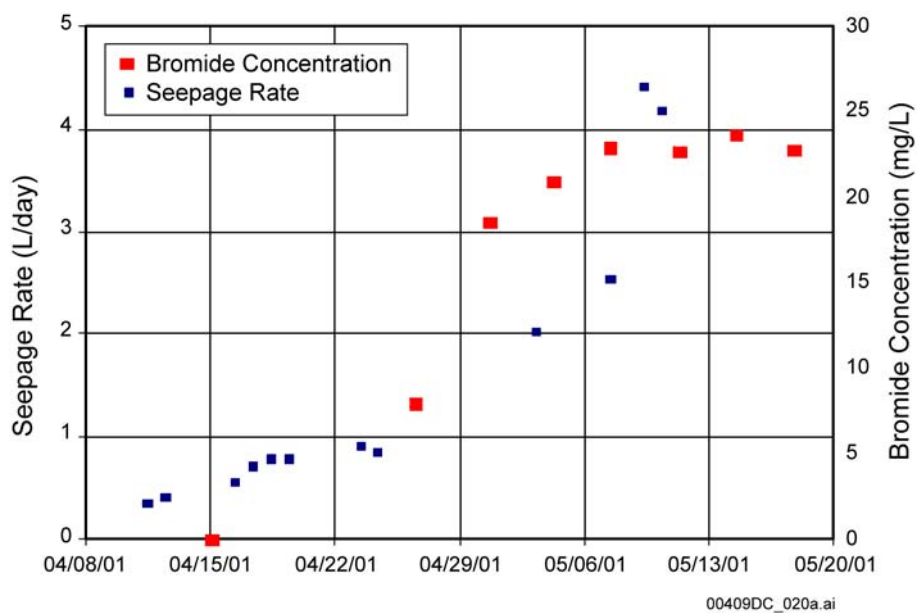
Source: BSC 2003h, Figure 6.12.2-7.

Figure 4-12. Concentration of Bromide Plotted against Seepage Rates Measured for 45 Days after First Observations of Drips in Tray 6

Figure 4-13 shows the tracer concentration in the seepage water at two sampling locations (tray 7 and tray 9+23, sampling trays in field tests, which were picked for discussion because they are the points where lower and upper seepage fluxes were observed). In tray 7, both bromide and PFBA were first detected three weeks after the initial release of the tracers into the fault. The concentration of both tracers gradually increased, though the rise in PFBA concentration clearly preceded that of bromide. This indicates a lower molecular diffusion coefficient for PFBA, and is consistent with the relative sizes of the two species. After peaking, the concentrations decreased and finally reached a relatively constant level. Similar patterns were observed in tray 9+23, but the magnitude and times at which peak concentrations occurred were different, suggesting the involvement of different fractures with different flow pathways, leading to different advective transport. This is further supported by the measured lithium concentrations, which are much higher in tray 9+23 (than that in tray 7) because the shorter pathway and faster flowing fractures intercepted in this case allow less time for matrix diffusion and retardation through sorption. Similar tracer behavior with different diffusion coefficients was observed by Reimus et al. (2003) in tracer experiments in fractured volcanic tuffs at the C-Wells site. This consistency suggests that similar transport processes (advection and matrix diffusion) are at work in the unsaturated and saturated zone barrier systems in the fractured tuffs of low matrix permeability.
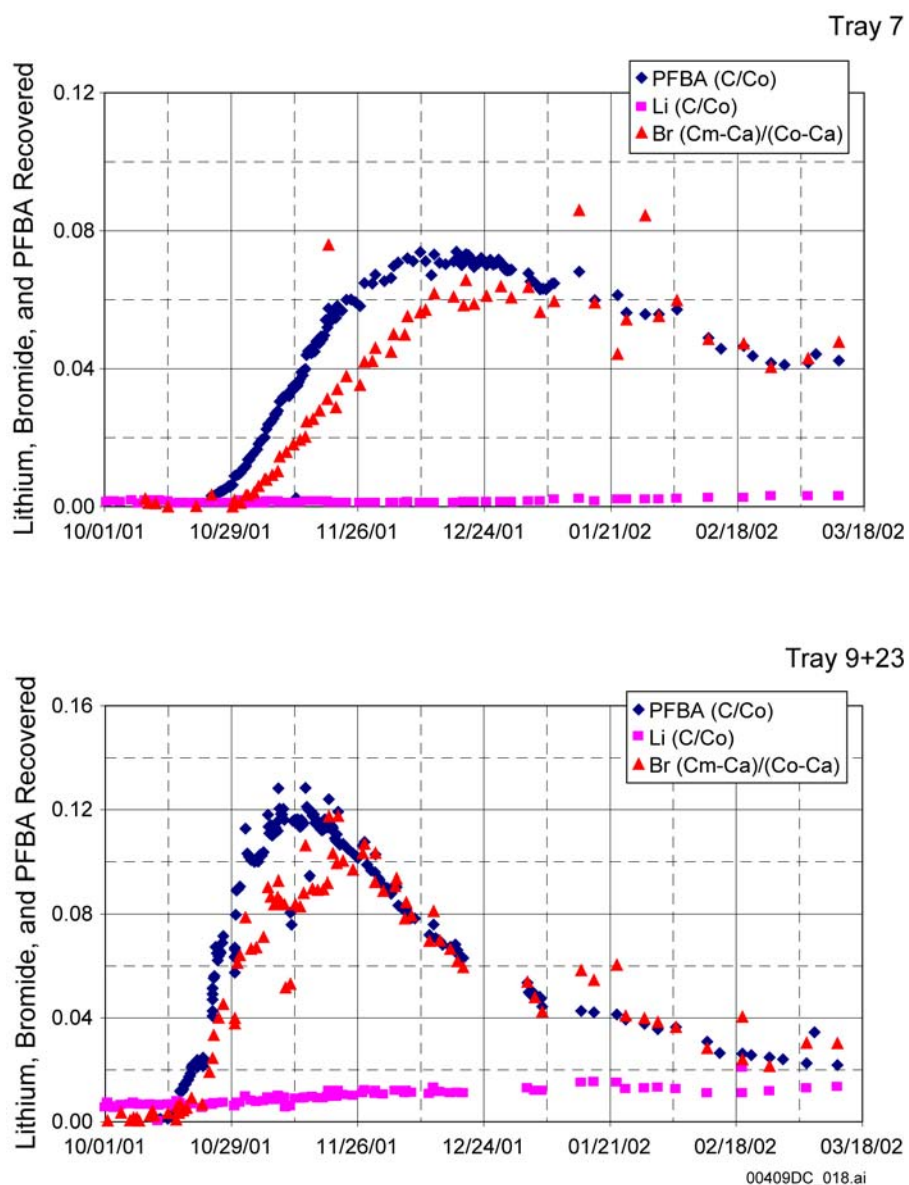
Source: BSC 2003h, Figure 6.12.2-8.

NOTE: Cm is the measured concentration and Ca is the background concentration in the leachate.

Figure 4-13. Concentration of Tracers Measured in Seepage in Niche 3

5. MODEL DEVELOPMENT

This section provides a brief discussion of the sequence of events, processes, and phenomena involved in the transport of radionuclides through the unsaturated zone in Yucca Mountain following the release of radionuclides from the repository. This section introduces the corresponding conceptual and mathematical models, and describes the general simulation approach. Additionally, it describes model development and calibration using a series of field tests on progressively larger spatial and temporal scales. Model calibration demonstrates the ability of the conceptual and mathematical model to adequately capture the underlying transport-related processes in the various tests, establishes confidence in the models, and forms the basis for model validation.

5.1 OBJECTIVES OF THE RADIONUCLIDE TRANSPORT STUDY

The primary objectives of the radionuclide transport study are:

1. To integrate the available data for the development of a comprehensive model of radionuclide transport through the unsaturated zone of Yucca Mountain for a range of current and future climate conditions

2. To identify the controlling transport processes and phenomena, to determine their relative importance, and to evaluate the effectiveness of matrix diffusion and sorption as retardation processes

3. To identify the geologic features that are important to radionuclide transport

4. To estimate the migration of important radionuclide solutes and their decay products from the repository toward the water table

5. To evaluate the effects of various climatic conditions on radionuclide transport

6. To estimate the migration of radioactive colloids from the repository toward the water table, and to determine the sensitivity of colloid transport to the kinetic coefficients of colloid filtration

7. To evaluate through sensitivity analyses the effect of uncertainty in important parameters on the predictions of transport.

These objectives are met through the activities discussed in Sections 5 and 6.

5.2 INTEGRATION OF INFORMATION IN THE DEVELOPMENT OF TRANSPORT MODELS

The development of conceptual models of radionuclide transport through the unsaturated zone involves the synthesis of information from various sources. The corresponding mathematical models are based on inputs stemming from these sources, including studies on hydrology (as affected by the climate), geology and stratigraphy, and radionuclide transport properties and

parameters. This section discusses the interaction of these components and conditions with transport processes.

The processes that control the radionuclide migration through the unsaturated zone are: (1) advection, which is the transport of radionuclides by flowing water; (2) dispersion and diffusion, which lead to a wider distribution of radionuclides over larger portions of the unsaturated zone domain; and (3) sorption of solutes or filtration of colloids, which leads to attachment onto solid grains and removes radionuclides from flowing water. The latter process enhances both diffusion and retardation. All are separately discussed in Section 3.

To understand the integrated transport phenomena in the unsaturated zone system, it is imperative to identify processes, properties, conditions, and their interactions. Conditions that are essential for unsaturated zone transport are:

1. **Precipitation, infiltration, and deep percolation**–Precipitation, infiltration and deep percolation, as these are affected by the climatic conditions, describe a critical source term of transport (i.e., the amount of water that is expected to enter the top boundary of the unsaturated zone). Spatial and temporal variations in the infiltration and percolation rates have a direct impact on water flow and saturation patterns in the unsaturated zone. Under the conditions of fracture-dominated flow, prevalent in the unsaturated zone, the effect on radionuclide advection through the unsaturated zone is immediate, greatly influencing the radionuclide residence time in the unsaturated zone. Additionally, the variations in the saturation patterns in the fractures and the matrix affect diffusive transport (specifically matrix diffusion) and dispersion. Predicting percolation fluxes also requires an understanding of climatic conditions through studies of historical climate and precipitation patterns and their projection into the future. Data from these analyses determine the range of expected precipitation rates during the compliance period. These precipitation rates are then used as the basis for estimating net infiltration, which is the key factor affecting percolation rates and flow patterns and, thus, transport behavior.

2. **Stratigraphy and hydrogeologic properties**–The unsaturated zone system geology, stratigraphy, and hydrogeologic properties define flow pattern of the percolating water in the unsaturated zone. Hydraulic conductivity, wettability, porosity, and fracture characteristics and properties of the various hydrogeologic units, in addition to their fracture characteristics and properties, determine the ability of the unsaturated zone to conduct and store water and are responsible for the existence of fast flow pathways (usually associated with conductive faults and interconnected vertical fractures), perched water bodies (when more permeable units overlie less permeable ones), as well as flow focusing and lateral diversion.

    Information on the system geology and hydraulic properties is obtained by integrating data from: (1) visual observations from outcrops and the ESF; (2) geophysical logging; (3) core data analysis from boreholes at select locations; (4) test data obtained in the course of pneumatic and/or water injection field tests; and (5) inversion of the field data.

Correlating information of the system geology and stratigraphy (including identification of the main hydrogeologic units, their areal extent and thickness, and the presence of faults) with the corresponding rock hydraulic properties and integration into a comprehensive flow model of the unsaturated zone allows the determination of flow fields for the infiltration scenarios discussed in Item 1. For the reasons discussed in Item 1, the flow field and the corresponding water saturation distribution have a direct and significant impact on radionuclide transport.

3. **Source terms**–Radionuclide transport is directly affected by the source term, which describes the combined releases of radionuclides and of water (i.e., the transport agent). Water contacting the waste packages provides the main transport mechanism for radionuclide releases from the repository. Seepage through the ceiling of the waste emplacement drift determines the amount of water that can potentially contact waste. If no seepage occurs, the mobilization and release of radionuclides will be impeded.

By accounting for the range of possible climatic scenarios and through the determination of seepage-relevant parameters, the range of seepage rates (and the corresponding effect on transport) can be estimated.

Seepage is affected by small-scale processes and occurs at a scale smaller than that of mountain-scale precipitation and the corresponding flow fields. Consequently, seepage estimates were obtained from experimental and modeling work performed on the drift scale (information on the subject can be found in *Technical Basis Document No. 3: Water Seeping into Drifts*).

In general, water is diverted away from the waste by vaporization (during the thermal period), diversion around the drift due to the capillary barrier effect, the drip shield, and the waste package. These protective measures and mechanisms would all have to fail at the same location along the waste emplacement drift for water to contact the waste.

Upon release from the package, radionuclide-contaminated water enters the invert at the base of the drift. The extent of radionuclide sorption by the invert material affects release rates to the unsaturated zone. The effect of the invert (which consists of crushed tuff) on sorbing radionuclide species is to reduce the radionuclide source term for unsaturated zone transport. Chemical reactions leading to precipitating species or colloid flocculation can also reduce the radionuclide source term. Information on radionuclide source reduction due to species immobilization is provided by the study of near-field geochemistry. If the released radionuclides do not sorb, or sorb and escape the invert in colloidal form, the water carries them to the large pore space between the crushed tuff blocks of the invert.

4. **Solutes versus colloids**–The form of the released radioactive species (dissolved or as colloids) affects the release mechanism and release rate. If the water contacts the contents of the waste package, then radionuclides are released at the base of the drift. The speciation of the mobilized radionuclides determines the magnitude of matrix diffusion (a function of the molecule/colloid size and electrical properties), sorption

onto (and filtration by) the unsaturated zone rocks, and pore-size exclusion (for colloids only).

Information on the nature of the released radionuclides and their concentrations in the water (the species-related component of the source term) is provided by knowledge of the radioactive substances stored in the waste packages and analysis of phase and speciation changes occurring as a result of chemical reactions and radioactive decay. Additionally, these studies provide information on the expected release concentrations, completing the definition of the radionuclide source term.

5. **Shadow zone**–Because of capillary pressure barrier effects, a shadow zone with reduced saturation and reduced flux is likely to be created underneath the drift. The presence of the shadow zone can lead to significant retardation of radioactive solute and colloid transport (BSC 2003m) by reducing the amount of fracture flow and significantly lowering water saturations relative to the surrounding rock. Because of the low advective flux in the shadow zone, diffusive flux is the only mechanism capable of transporting radionuclides from the invert to the shadow zone and past the boundaries of the shadow zone. The shadow zone has a greater retardation effect on colloid transport (compared to solute transport) because of the much lower diffusion coefficient of colloids.

6. **Transport through the unsaturated zone below the repository**–Once released from the invert, radionuclides are carried by water from the invert's large pores toward the deeper, undisturbed unsaturated zone (fracture advective transport), toward which a small amount of radionuclides is also migrating very slowly through the invert matrix (diffusion and matrix advective transport). The transport of these radionuclides to the water table through the unsaturated zone is significantly affected by the flow field below the repository (through its direct impact on advection), as determined by the interaction of climatic, geologic, source, and near-field conditions discussed in Items 1 through 6.

Transport to the water table is also determined by matrix diffusion and the sorption (for solutes) or filtration (for colloids) behavior of the radioactive species. Matrix diffusion depends on the diffusion coefficients of the various species. This information is available from literature sources or is obtained from laboratory experiments (see Section 4.1). Additional factors affecting matrix diffusion are the fracture frequency and characteristics (obtained from the field and laboratory studies discussed in Item 2 and inversion exercises with the measurements) and the distributions of tortuosity, porosity, and water saturation in the various rocks of the unsaturated zone profile (also available from the studies in Item 2).

Information on the sorption behavior is provided from field and laboratory studies, as discussed in Section 4. Conventionally, an effective linear equilibrium sorption model is assumed with a sorption K_d of the species in question onto the solid phase, including the various unsaturated zone rocks, and natural pseudocolloids, such as clays (in the case of colloid-assisted radionuclide transport). Such field or laboratory studies have been limited to sorption onto the rock matrix. No information is available for the

estimation of sorption onto fracture walls. In the absence of such data, a conservative approach is followed in the models, in which no sorption or filtration is considered in fractures.

Field and laboratory tests are also necessary for the determination of colloid filtration in the unsaturated zone rocks. While limited studies are available, applicability to the unsaturated zone is not well established because the studies were performed under fully water-saturated conditions. Colloid pore-size exclusion (straining, a potentially significant mechanism for larger colloids) can be estimated from pore-size distributions, which can be estimated from the capillary pressure curves of the unsaturated zone rocks under consideration based on field data from Item 2. In light of this uncertainty, the approach followed in the models involves analysis of transport using a very wide range of the corresponding parameters, thus bracketing the possible solutions.

7. **Fracture versus matrix flow and fracture–matrix interaction**–Because of the fracture-dominated flow patterns indicated by the studies in *UZ Flow Models and Submodels* (BSC (2003b, Section 6.6), radionuclides that enter the undisturbed unsaturated zone underneath the repository tend to move rapidly toward the water table through a continuous fracture network. Advection through the matrix would occur and lead to further radionuclide arrivals at the water table but at a far slower rate.

The main mechanisms of retardation are diffusion into the matrix through the fracture walls and through the matrix, and sorption (for solutes) or attachment-filtration (for colloids) onto the matrix, which further enhances retardation by increasing diffusive fracture–matrix fluxes. Radioactive decay is a mechanism to reduce the mass of radionuclides arriving at the water table. Sorption onto natural pseudocolloids, such as clays, can be important in colloid-assisted solute transport, if the natural colloids exist in sufficiently large concentrations. Information on the subject is provided by the study of colloids at the site (BSC 2003d).

Decay species can have significantly different diffusion and sorption behavior. For example, the ^{235}U daughter of ^{239}Pu has a far lower affinity for sorption, leading to faster transport of daughter radionuclides to the water table than that predicted by accounting solely for the parent. Thus, the contribution of daughters significantly impacts the transport of total radionuclides to the water table.

8. **Transport in the saturated zone**–After traveling through the unsaturated zone, radionuclides arrive at the saturated zone. The study of flow and transport through the unsaturated zone provides the water and radionuclide source terms, respectively, for the saturated zone studies. These are also based on data obtained from laboratory and field studies on the saturated zone hydrology and transport behavior, which is documented in *Technical Basis Document No. 11: Saturated Zone Flow and Transport*.

5.3 CONCEPTUAL AND NUMERICAL MODEL

The development of the conceptual and numerical model constitutes an integral component of the study to meet the objectives presented in Section 5.1. The model of radionuclide transport considers a large three-dimensional mountain-scale domain. The fractured rock is conceptualized as a heterogeneous dual-permeability system, in which the distinct hydraulic and transport behavior of fractures and matrix is described by using separate properties and corresponding parameters. This conceptualization allows the description of the complex unsaturated zone flow field (the most important aspect of the transport study), in which fracture flow plays a dominant role.

The grid, conditions, and calibrated hydraulic parameters used in the transport simulations are identical to those used for the analysis of flow in *UZ Flow Models and Submodels* (BSC 2003b, Section 6). These parameters correspond to the permeability barrier model (called the conceptual model of perched water), which uses the calibrated perched-water parameters for fractures and matrix in the northern part of the model domain, and modified property layers (including tsw38, tsw39, ch1z, and ch2z model layers), where the lower basal vitrophyre of the TSw overlies the zeolites of the CHn. A detailed discussion of this perched-water model can be found in *UZ Flow Models and Submodels* (BSC 2003b, Section 6.2). A two-dimensional plan view of the grid at the repository level is shown in Figure 5-1. All three-dimensional transport simulations are based on the steady-state flow fields from *UZ Flow Models and Submodels* (BSC 2003b, Section 6).

The numerical process model used for simulating transport (BSC 2003e, Sections 4 and 6.2) accounts for all major known transport processes. Those processes are: (1) advection; (2) molecular diffusion; (3) hydrodynamic dispersion; (4) kinetic or equilibrium physical and chemical sorption (linear, Langmuir, Freundlich, or combined model); (5) radioactive decay and tracking of resultant daughter radionuclides; (6) colloid filtration (equilibrium, kinetic, or combined); and (7) colloid-assisted solute transport.

Data for the description of the sorption behavior of the investigated radionuclides are taken from the analysis of laboratory experiments (see Section 4.1), while a wide range of possible filtration parameters is used to compensate the limited availability of experimental data. Experimentally determined data (either directly available in the literature or scaled to account for relative size and behavior) are used for the diffusion coefficient, D_0, of solutes (Lide 1993, pp. 5-111 to 5-112), while the Stokes-Einstein equation (Bird et al. 1960, p. 514) is used to estimate the colloidal diffusion coefficients.
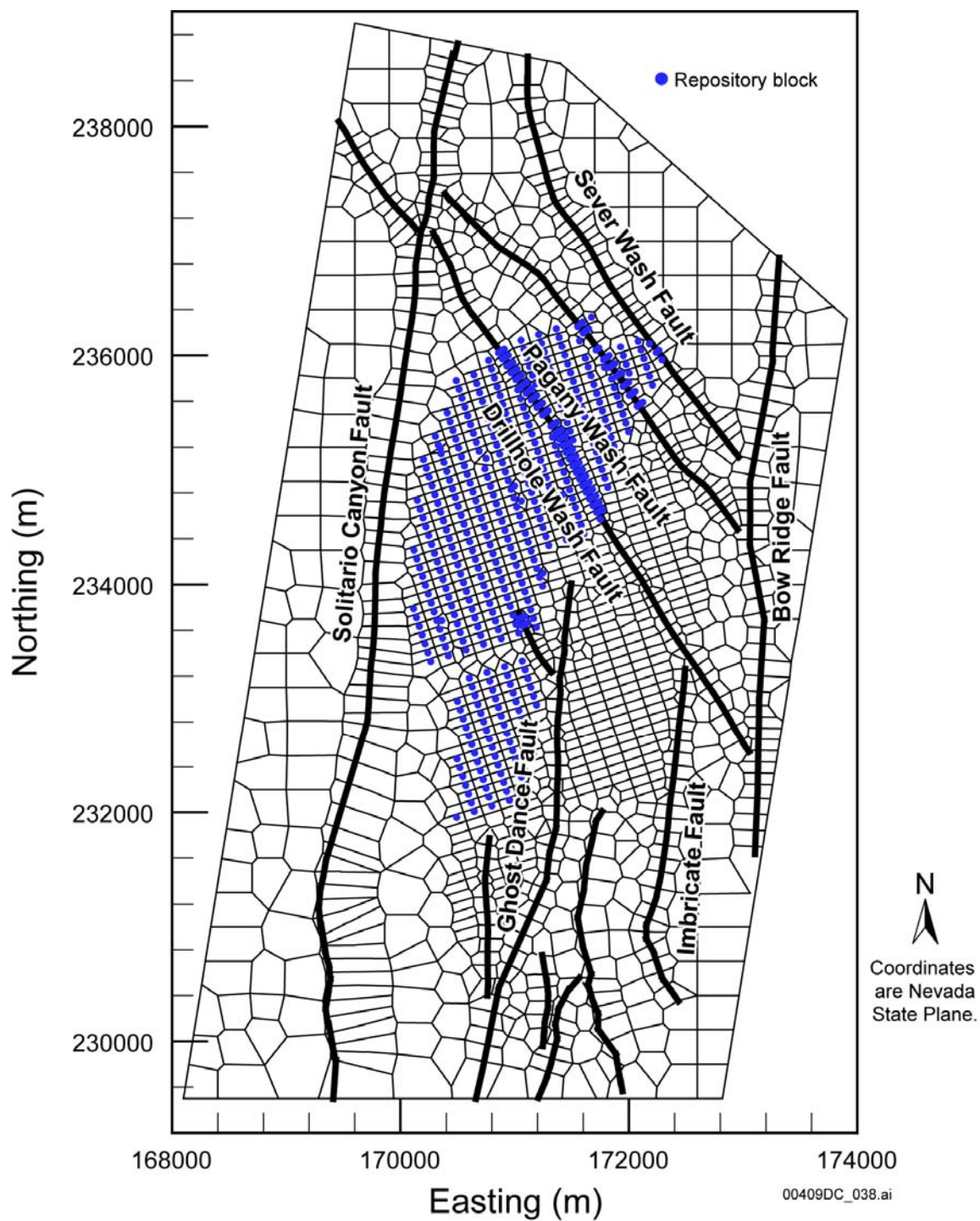
Source: BSC 2003e, Figure 6.7-1.

Figure 5-1. Plan View of the Unsaturated Zone Model Grid at the Repository Level

Radionuclides Considered–The following radioactive solutes were considered in the unsaturated zone transport model:

- ^{99}Tc (a nonsorbing species)
- ^{237}Np, ^{235}U, and ^{233}U (moderately sorbing species)
- ^{241}Am, ^{239}Pu, ^{231}Pa, ^{229}Th, ^{226}Ra, ^{90}Sr, and ^{135}Cs (strongly sorbing species).

Their properties are listed in Tables 5-1 and 5-2. The radionuclides are selected to represent the groups that have different transport magnitudes of sorption, molecular diffusion, and radioactive decay. Due to the lack of such information for fission products of those radionuclides, the fission products are excluded from the transport study. The radionuclides are released at the grid blocks corresponding to the location of the repository (blue dots indicate the location of repository grids in Figure 5-1). Additionally, for the three-dimensional simulations of continuous release, all the important members in the decay chains of ^{241}Am and ^{239}Pu are considered, according to the decay equations (Pigford et al. 1980):

$$^{241}\text{Am} \rightarrow {}^{237}\text{Np} \rightarrow {}^{233}\text{U} \rightarrow {}^{229}\text{Th} \qquad \text{(Eq. 5-1)}$$

$$^{239}\text{Pu} \rightarrow {}^{235}\text{U} \rightarrow {}^{231}\text{Pa} \qquad \text{(Eq. 5-2)}$$

Only the most important members of the radioactive chain are included in these decay equations, which omit decay products with short half-lives because they have a minor effect on the relative abundance of the daughters.

The transport of radioactive colloids was also simulated. Spherical PuO_2 colloids with diameters of 6, 100, 200, and 450 nm were used in this transport model.

Table 5-1. K_d in the Rocks of the Unsaturated Zone

Species	Unit	K_d value (mL/g)	Ranges of K_d value (mL/g)
Uranium	Zeolitic	0.5	(K_d value, probability) (0, 0) (**0.5**, 0.5) (30, 1.0)
	Devitrified	0.2	(K_d value, probability) (0, 0) (**0.2**, 0.5) (4, 1.0)
	Vitric	0.2	(K_d value, probability) (0, 0) (**0.2**, 0.5) (3, 1.0)
Neptunium	Zeolitic	0.5	(K_d value, probability) (0, 0) (**0.5**, 0.5) (6, 1.0)
	Devitrified	0.5	(K_d value, probability) (0, 0) (**0.5**, 0.5) (6, 1.0)
	Vitric	1	(K_d value, probability) (0, 0) (**1.0**, 0.5) (3, 1.0)
Plutonium	Zeolitic	100	(K_d value, probability) (10, 0) (**100**, 0.5) (200, 1.0)
	Devitrified	70	(K_d value, probability) (10, 0) (**70**, 0.5) (200, 1.0)
	Vitric	100	(K_d value, probability) (10, 0) (**100**, 0.5) (200, 1.0)
Americium	Zeolitic	500	Range = 100 to 1000 (**500**)
	Devitrified	1,000	Range = 100 to 2000 (**1,000**)
	Vitric	400	(K_d value, probability) (100, 0) (**400**, 0.5) (1,000, 1.0)
Protactinium	Zeolitic	10,000	Range = 1000 to 20,000 (**10,000**)
	Devitrified	10,000	Range = 1000 to 20,000 (**10,000**)
	Vitric	10,000	Range = 1000 to 20,000 (**10,000**)
Cesium	Zeolitic	5,000	(K_d value, probability) (425, 0) (**5,000**, 0.5) (20,000, 1.0)
	Devitrified	7.5	Range = 1 to 15 (**7.5**)
	Vitric	2	(K_d value, probability) (0, 0) (**2**, 0.5) (100, 1.0)
Strontium	Zeolitic	1,000	Range = 50 to 2000 (**1000**)
	Devitrified	40	Range = 10 to 70 (**40**)
	Vitric	25	Range = 0 to 50 (**25**)
Radium	Zeolitic	2,500	Range = 1000 to 5,000 (**2,500**)
	Devitrified	500	Range = 100 to 1,000 (**500**)
	Vitric	300	Range = 50 to 600 (**300**)
Thorium	Zeolitic	15,000	Range = 1,000 to 30,000 (**15,000**)
	Devitrified	5,000	Range = 1,000 to 10,000 (**5,000**)
	Vitric	5,000	Range = 1,000 to 10,000 (**5,000**)

Source: BSC 2003e, Table 6.5-1.

Table 5-2. Radionuclide Properties in the Transport Simulations

Radionuclide	D_0 (m^2/s)	$T_{1/2}$ (years)
^{99}Tc	4.55×10^{-10}	2.13×10^5
^{237}Np	1.65×10^{-10}	2.14×10^6
^{239}Pu	4.81×10^{-10}	2.41×10^4
^{241}Am	3.69×10^{-10}	4.322×10^2
^{233}U	4.94×10^{-10}	1.59×10^5
^{235}U	4.89×10^{-10}	7.08×10^8
^{231}Pa	4.98×10^{-10}	3.25×10^4
^{229}Th	5.02×10^{-10}	7.90×10^3
^{226}Ra	8.89×10^{-10}	1.599×10^3
^{135}Cs	2.06×10^{-9}	2.30×10^6
^{90}Sr	7.91×10^{-10}	2.90×10^1

Source: BSC 2003e, Table 6.5-2.

5.4   MODEL DEVELOPMENT AND CALIBRATION

The process of calibration determines the main hydraulic parameters of the medium under consideration. The calibrated hydraulic parameters are then used to increase confidence in the transport model using transport parameters available from other independent sources. Corroboration is based on comparison with experimental data for the Busted Butte tracer transport (Sections 5.4.1 to 5.4.3) or other field tests (Alcove 8–Niche 3 test, Section 5.4.4). Calibration is conducted during model development to enhance confidence in the radionuclide transport model.

5.4.1   The Busted Butte Phase 1A Test

The Busted Butte test was used to predict tracer concentration and water saturation following the injection of nonreactive tracers into the Ttptv1 and the subsequent flow and transport in the Tptpv1 and Tac layers. The Busted Butte test series is described in Section 4.2.1, and the Phase 1A test is described in Section 4.2.1.2. The transport of two (nonsorbing tracers Br$^-$ and fluorescein) is analyzed in the transport model report (BSC 2003e). In this analysis, the fluorescein data were used for calibration while the Br$^-$ data were used to increase confidence in the model.

For this three-dimensional numerical study, the underlying geologic model considered a homogeneous and anisotropic unfractured rock matrix with the properties of the Tptpv1 and Tac layers. Because of the injection configuration (as described in Section 4.2.1), only half the domain (i.e., the portion of the domain to the right of the injection point; see Figure 5-2) was simulated, using a grid consisting of 22,463 elements (BSC 2003e). Although the configuration of injection did not lead to a symmetrical system, the effect of such asymmetry was expected to be limited and confined to the earlier part of the field test. TOUGH2 V1.1 MEOS9nT V1.0 (LBNL 1999) was used for the simulations.

Figures 5-2 and 5-3 show the fluorescein distribution (as recorded digitally in the field using an ultraviolet light) and the corresponding numerically predicted distribution (i.e., calibrated) at a distance of $y = 0.90$ m mineback face. The determination of the hydraulic parameters is a significant component of the calibration effort.

A comparison of the two figures indicates good agreement between predictions and observations. The absence of stringers and other features indicative of fracture presence in the field data, coupled with the ellipsoidal size of the plume, supports the assumption of an unfractured (porous) medium. Visual evidence of local heterogeneity in Figure 5-2 notwithstanding, the plume is quite uniform at the scale of observation. Although the simulated horizontal dimension of the plume is somewhat larger than the observed one, the prediction accurately captures several important features of the observed plume: its ellipsoidal shape, the compression of the lower half of the plume that results from its proximity to the less permeable Tac, and the vertical dimension of the fluorescein plume. Due to data deficiencies, calibration cannot be further refined.
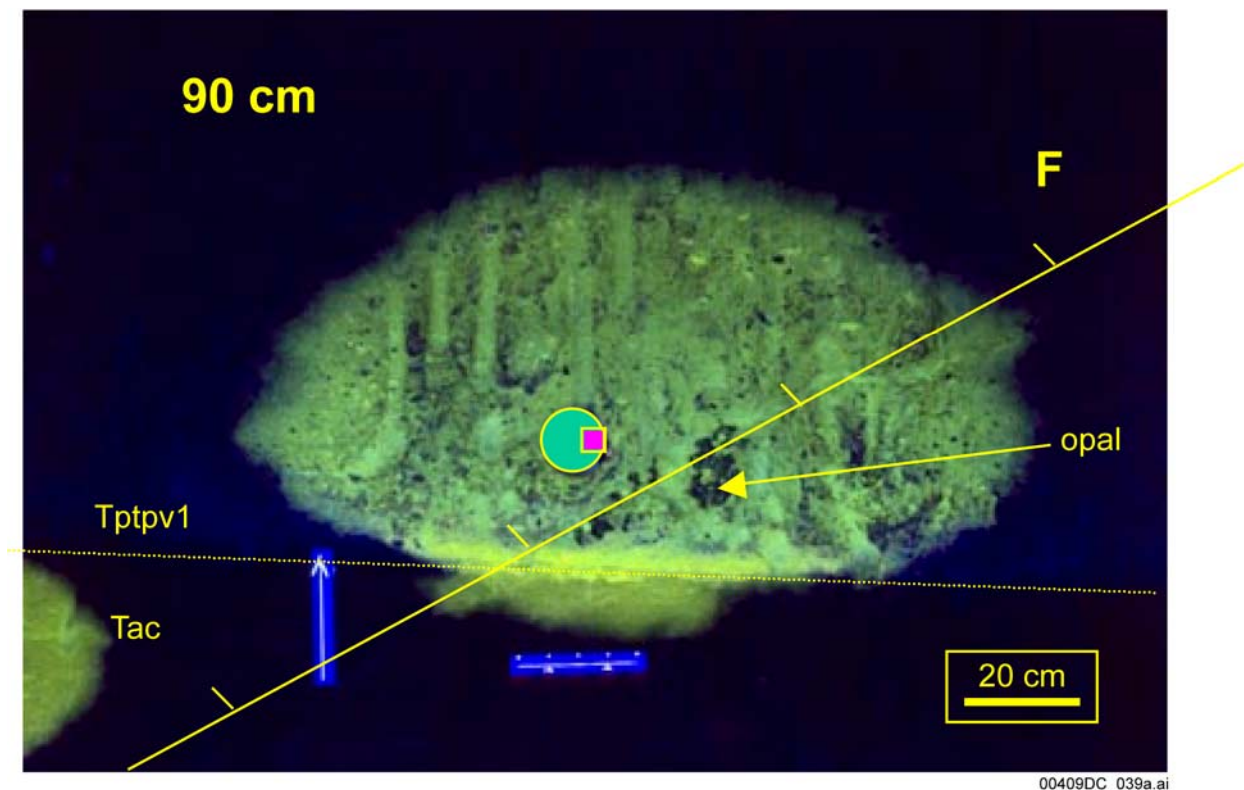
Source: BSC 2003h, Figure 6.13.2-2.

NOTE: The correct scale is the faint feature (20 cm) in the middle of the photograph below the plume.

Figure 5-2. Fluorescein Plume at the Mineback Face (y = 90 cm) at Borehole 3
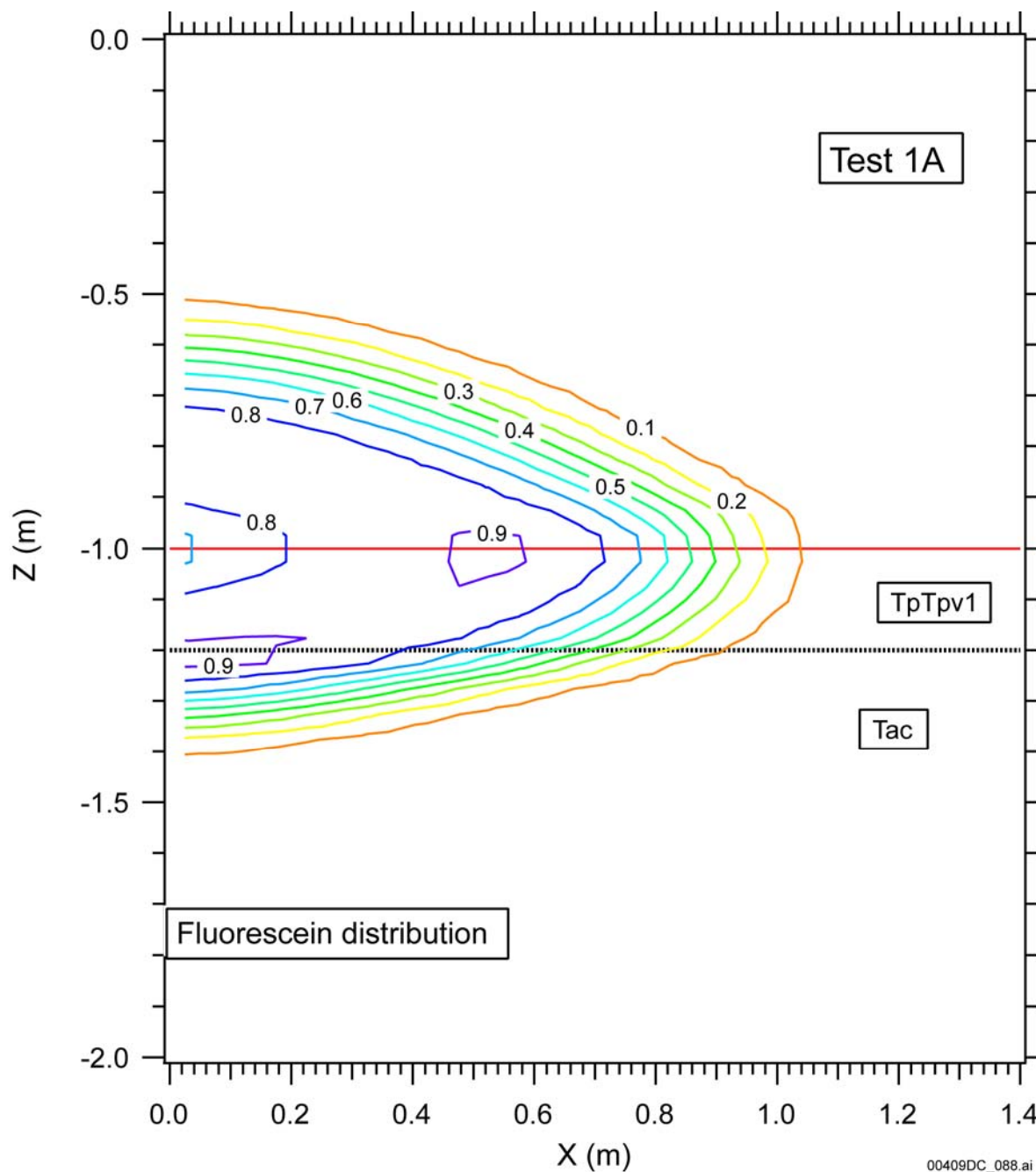
Source: BSC 2003e, Figure 7.3-2.

Figure 5-3. Numerical Prediction (Relative Concentration, C/C_0) of the Fluorescein Plume Using Calibrated Parameters (Busted Butte Test Phase 1A)

Model confidence is increased by using the calibrated properties obtained in the fluorescein simulation (Table 5-3) and the known diffusion coefficient (D_0) of Br⁻ to predict the transport of bromide. Figure 5-4 shows the numerically predicted Br⁻ distribution (relative concentration, C/C_0) at the y = 0.90 m mineback face and the field measurements of the Br⁻ relative concentration, which were obtained from samples taken during the mineback.

Table 5-3. Calibrated Parameters of Flow and Transport from the Analysis of the Busted Butte Phase 1A Field Test

Parameter[a]	Ch1v	Ch2v
ϕ	0.320	0.360
k_x (m^2)	2.14×10^{-13}	8.20×10^{-13}
k_y (m^2)	4.14×10^{-13}	2.82×10^{-13}
k_z (m^2)	6.28×10^{-14}	3.64×10^{-14}
τ	0.22	0.12
α (1/m)[c]	0.471	0.741
n[c]	1.332	1.200
S_r	0.07	0.07
D_0 of Fluorescein (m^2/s)	4×10^{-10}	

Source: BSC 2003e, Table 7.7-3.

The overall predicted and measured Br⁻ distributions agree. The model reasonably reproduces the rather uniform concentrations along the x-axis that crosses the injection point, as well as the magnitude of the observed concentrations. Some discrepancies between observations and predictions appear toward the outer extent of the horizontal axis of the plume, where concentration gradients are steep, and, therefore, differences may be magnified. However, the agreement between observations and numerical predictions is sufficiently good to enhance the confidence of the radionuclide transport model.

Uncertainty in the measurements may also affect the match between prediction and observations. The measured relative concentration of 2.77 (with respect to the injection concentration) in the center of the plume may be real (if, for example, the sample was inadvertently allowed to dry), but it may also be indicative of some error in the measurements.

Source: BSC 2003e, Figure 7.3-3.

NOTE: The solid circles indicate the location of measurements (DTN: LA9910WS831372.008), which appear in the corresponding boxes.

Figure 5-4. Field Measurements and Numerical Prediction (Relative Concentration, C/C_0) of the Bromide Distribution in Busted Butte Test Phase 1A

5.4.2 Busted Butte Phase 1B Test

The Busted Butte Phase 1B test is described in Section 4.2.1.3. Of the five tracers injected during Phase 1B, measurement data for 2,6-DFBA (assumed to be nonsorbing but demonstrating behavior akin to sorption after long times) and Br^- (nonsorbing) were selected from the first 100 days of the Phase 1B test. The 2,6-DFBA data were used for calibration, and the Br^- data set was used to increase model confidence.

The initial (uncalibrated) input parameters of flow and transport for the simulation of the Phase 1B test were also provided by the same sources as in the Phase 1A test. The same model assumptions on model design and the grid used in the simulation of Phase 1A were used here.

A comparison of the measured and numerically predicted breakthrough curves of 2,6-DFBA (based on the calibrated parameters, which include a small K_d value to describe the apparent sorption behavior at long times) in Figure 5-5 shows very good agreement. The shape and breakthrough time of the curves are consistent with the visual observation that the system did not exhibit fracture flow behavior during the Phase 1B test (despite the known presence of a fracture intersecting the two boreholes) and support the validity of the unfractured medium approach used in the simulations.
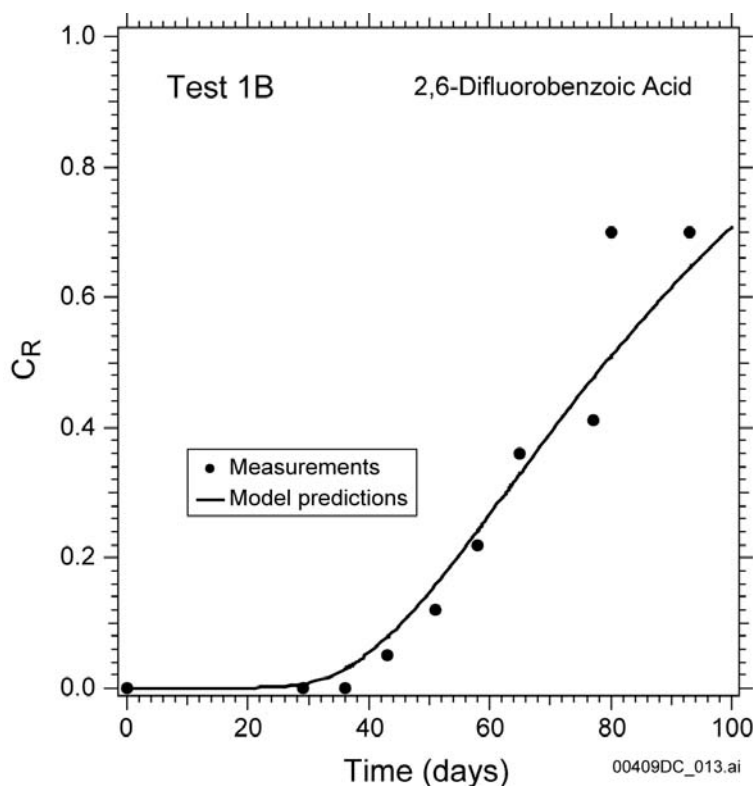
Source: BSC 2003e, Figure 7.3-4.

Figure 5-5.   Observed and Numerically Predicted (Calibrated) Breakthrough Curves of 2,6-DFBA for the Busted Butte Phase 1B Test

The nonzero (although small) distribution coefficient ($K_d = 1.47 \times 10^{-5}$ m^3/kg) for 2,6-DFBA appears to contradict the conventional assumption that 2,6-DFBA is nonsorbing but is actually supported by the long-term sorption behavior of the tracer. In this case, some sorption is plausible because of the nature of 2,6-DFBA (an organic acid) and because of the very low permeability of the rock, which leads to long residence times of the solute. Organic substances are generally considered to be slow-sorbing (Cameron and Klute 1977). Additionally, the long residence time in the rock may allow a slow reaction of 2,6-DFBA with minerals in the rock, a process that would result in a response consistent with an apparent sorption.

The calibrated parameters (based on the 2,6-DFBA transport analysis) were used for the prediction of Br$^-$ transport in Phase 1B of the Busted Butte test (Table 5-4). The known D_0 of Br$^-$ and its K_d value of zero were used to increase confidence in the simulation. A comparison of the measured and numerically predicted breakthrough curves of Br$^-$ in Figure 5-6 shows very good agreement. The level of agreement between observations and numerical predictions enhance the confidence of the radionuclide transport model.

Table 5-4   Calibrated Flow and Transport Parameters from the Analysis of the Busted Butte Phase 1B Field Test

Parameter[a]	tsw39
ϕ	0.270
k_x (m^2)	3.06×10^{-17}
k_y (m^2)	4.06×10^{-17}
k_z (m^2)	1.53×10^{-17}
τ	0.07
K_d of 2,6-DFBA (m^3/kg)	1.47×10^{-5}

Source: BSC 2003e, Table 7.3-5.
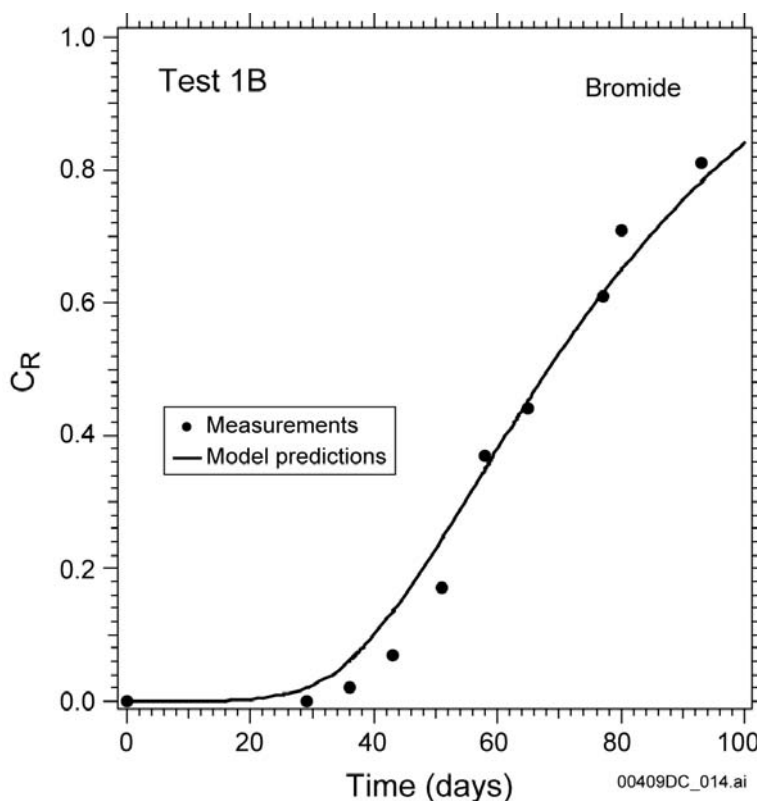
Source: BSC 2003e, Figure 7.3-5.

Figure 5-6. Observed and Numerically Predicted Breakthrough Curves of Bromide in the Busted Butte Phase 1B Test

5.4.3 Busted Butte Phase 2C Test

The Busted Butte Phase 2 tests are described in Section 4.2.1.4. The analysis for this model development and calibration activity is limited to Phase 2C, which appears to have yielded the best quality data. Because of the relatively short spacing between injection boreholes and the long injection period (695 days), the injection can be assumed to be uniform along the three boreholes (see Figure 4-5, boreholes 18, 20, and 21). The implication of this uniformity is that it is possible to model the system using a two-dimensional grid, thus allowing higher spatial resolution.

After reviewing the tracer concentrations recorded at the collection boreholes, the analysis concentrated on data from borehole 16 because it is the closest to the horizontal plane of the three injection wells and, thus, registered the strongest signals (in terms of tracer concentrations). Borehole 16 extends along a horizontal plane (roughly coinciding with the Tptpv2–Tptpv1 interface) about 0.6 m below the plane of the injection boreholes and perpendicular to their main axis.

Based on a review of concentration data for all of the tracers injected, two tracers, Br^- and Li^+, were selected for calibration and model confidence building. The use of Br^- and Li^+ offered two advantages: they registered relatively strong and almost always consistent signals in borehole 16, and they were injected as a solution of LiBr, with equal numbers of Li^+ and Br^- moles in the

system, which provided an additional mass balance constraint. In this analysis, the Li^+ data were used for calibration and the Br^- data for model confidence.

Preliminary simulations indicated that matrix diffusion and Li^+ sorption would be needed to describe the joint transport of Br^- and Li^+. This required that the model domain be a fracture–matrix system, as opposed to a porous medium (without fractures) or one that considered transport only in fractures. A dual-permeability model was employed with a fine-resolution two-dimensional grid ($\Delta x = \Delta y = 0.05$ m).

The initial flow field was obtained by setting an infiltration rate corresponding to 5 mm/yr at the top of the domain and running the flow simulation to steady state. This had to be done at every phase of the model development and calibration process because the changes in the hydraulic parameters during the process affected the flow field.

For the Li^+ calibration process, only the data for times of 337 and 440 days were used. Because of the sorbing behavior of Li^+, the data for times of fewer than 337 days were marked by very low concentrations, significant variability, and corresponding uncertainty. Concentration data for times of greater than 440 days showed rather inconsistent behavior attributed to issues discussed in Section 7.3 of *Drift-Scale Radionuclide Transport* (BSC 2003i). Br^- for 125 and 183 days were used to increase confidence during model development. The data for times less than 125 days were marked by very low concentrations and significant variability. Concentration data for times greater than 183 days indicated a rather uniform distribution along the borehole (as the concentration peak had already been reached).

Figure 5-7 shows the measured and the numerically predicted Li^+ distributions (based on the calibrated parameters shown in Table 5-5) along the collection borehole. The general features of the predicted Li^+ distribution agree with the measured distribution. The locations of the peaks, the peak concentration values (except for the left-most peak), and the general concentration distributions are matched.

Figure 5-8 shows the measured and numerically predicted Br^- distribution along the collection borehole. This distribution was obtained by using the calibrated properties from the analysis of the Li^+ data, the known D_0 and zero sorption for Br^-. The level of agreement between observations and numerical predictions enhances the confidence of the radionuclide transport model. The distribution of Br^- indicates a less diffusive behavior relative to Li^+, because Br^- is nonsorbing. The presence and location of concentration peaks (both observed and predicted) are consistent between the two tracers.
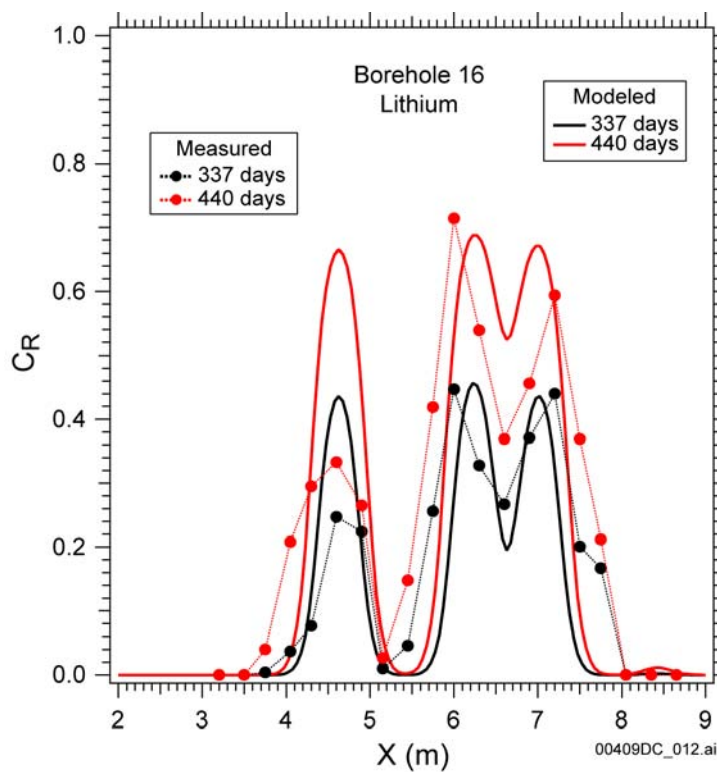
Source: BSC 2003e, Figure 7.3-6.

Figure 5-7. Observed and Numerically Predicted (Calibrated) Breakthrough Curves of Li$^+$ in the Busted Butte Phase 2C Test

Table 5-5. Calibrated Flow and Transport Parameters from the Analysis of the Busted Butte Phase 2C Field Test

Parameter[a]	F-TpTpv1	M-TpTpv1	F-TpTpv2	M-TpTpv2
ϕ	1	0.354	1	0.060
k_x (m^2)	3×10^{-13}	1.3×10^{-13}	1.96×10^{-12}	1.2×10^{-13}
k_z (m^2)	10^{-13}	8×10^{-14}	7.1×10^{-13}	8×10^{-14}
τ	2	0.9	2	0.654
K_d of Li (m^3/kg)	-	5.5×10^{-4}	-	9.3×10^{-4}
K_d of Li (m)[b]	2.5×10^{-6}	-	4.3×10^{-6}	-

Source: BSC 2003e, Table 7.3-8.
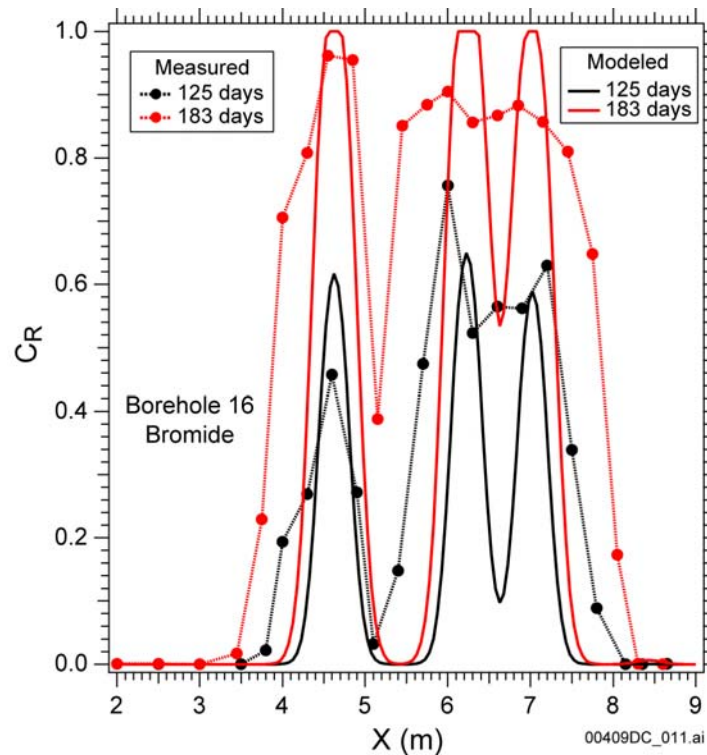
Source: BSC 2003e, Figure 7.3-7.

Figure 5-8.   Observed and Numerically Predicted Breakthrough Curves of Br⁻ in the Busted Butte Phase 2C Test

Inspection of the simulated Br⁻ distribution reveals that the numerical solution accurately predicts the location and magnitude of the concentration peaks but exhibits narrower peaks and indicates a deeper trough between the second and third peaks compared to the measurements. More specifically, the measured concentration of Br⁻ is more uniform along the collection borehole axis than what the numerical simulation predicts, indicating a system that is more diffusive than the advective one described by the simulation.

The discrepancy between the prediction and measured data is attributed to the effects of the collection pad on transport through the host rock. The properties of the collection pad, characterized by high permeability, porosity, irreducible water saturation, and capillary pressure, differ significantly from those of the host rock. Tracer-carrying fracture flow first reaching the collection pad arrives at distinct points (the points where the fractures intercept the borehole) and is quickly redistributed on the initially dry pad. Therefore, the tracer in the pad is more uniform than the one in the overlying rock and the samples indicate a more diffusive system. Under these conditions, it is expected that the most accurate data will be at early times and at locations roughly under the injection boreholes where the effects of the pad are minimized.

5.4.4 Matrix Diffusion Model, Alcove 8–Niche 3 Test

The Alcove 8–Niche 3 tests measure seepage and tracer transport over 20- to 30-m in the vicinity of a near-vertical fault (see Section 4.2.2).

This section discusses selected results of simulations performed to evaluate the relative importance of matrix diffusion on radionuclide transport. For this evaluation, the calibrated flow field (BSC 2003e, Section 7.4.3) from the seepage data of the Alcove 8–Niche 3 test was used in the simulation of tracer transport processes. A three-dimensional numerical grid was constructed for the simulation. The fault was represented as a vertical fracture, and surrounding fractured rock is approximated as a dual-continuum system consisting of overlapped, interacting fracture and matrix continua. The results of the transport simulations are compared with the Alcove 8–Niche 3 tracer tests to increase confidence in the matrix diffusion model.

The role of matrix diffusion was examined by running transport simulations for tracers having different molecular diffusion coefficients (Br^- and PFBA). The effect of changing the fracture-matrix interface area was also considered. It was assumed that changes in the interface area would not significantly alter the flow field during the period of the tracer test. The transport simulations also assumed zero dispersivity. Because tracers were introduced into infiltrating water at about 200 days after infiltration started, the matrix near the fault was assumed to be almost saturated during the tracer test and the matrix imbibition would be insignificant.

Figure 5-9 provides a comparison of simulated breakthrough curves at the niche to the observed data. The simulated breakthrough curve for the original fracture–matrix interface area exhibits a much larger peak concentration value but only slightly earlier arrival times compared to the field data. Through the calibration process, optimum results were obtained when the interface area (originally determined by the numerical grid and subsequently reduced through the active fracture model to describe flow patterns in the matrix–fracture system) was increased by a factor of 45. Such an increase is justified in order to apply the active fracture model (developed for flow, which can only occur when water saturation exceeds the high residual saturations of Yucca Mountain rocks) to transport (in which diffusion only requires continuity of the liquid phase, and will occur even below residual water saturations). With the adjusted interface area, the simulations match the data more closely, although the concentration at a given time for the Br^- tracer is generally overestimated by the model, while the simulated PFBA concentration is slightly underestimated.

Both fracture and fault surfaces are rough; thus the actual interface areas between these surfaces and the matrix are larger than what would be, assuming flat surfaces. The fault zone may include a great number of crushed matrix blocks that have smaller sizes than the fracture spacing in a nonfaulted zone. These crushed matrix blocks can make a significant contribution to the matrix diffusion within the fault, but are not considered in the numerical grid, where the fault is simply treated as a vertical fracture. To compensate for the effects of these mechanisms, the model's fault–matrix interface areas need to be increased. Note that the weighting factor of 45 to increase the interface area is consistent with the range of values that Neretnieks (2002, p. 200) reported in studies on different media.
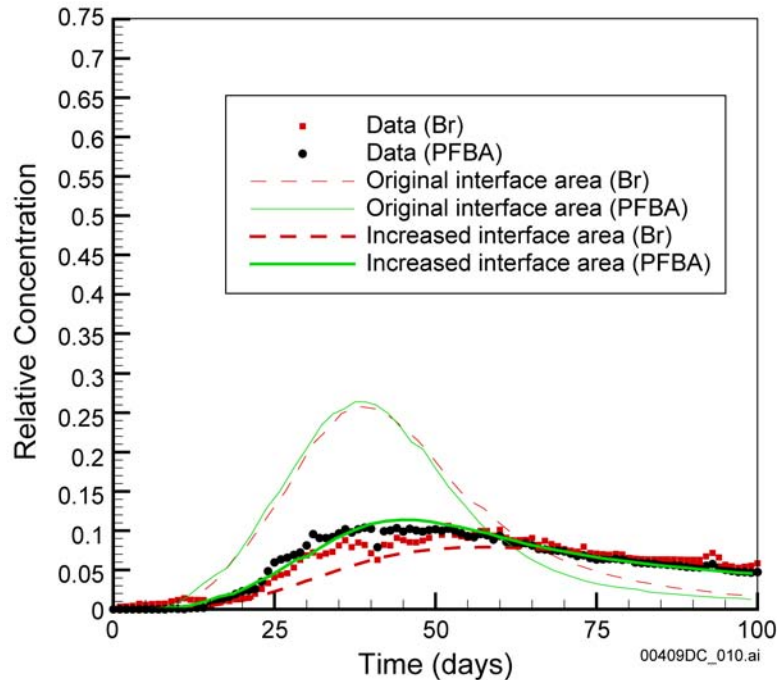
Source: BSC 2003e, Figure 7.3-9.

Figure 5-9.   Comparisons between Simulated Breakthrough Curves at the Niche for Two Fault–Matrix Interface Areas and the Observed Data

One plausible explanation for the improved match is that the matrix blocks within the fault zone are smaller than the fracture spacing, which was used to characterize the block size in the numerical model. The fault zone is in essence a highly fractured, rubblized zone of matrix with small spacings between fractures. The smaller matrix block corresponds to shorter equilibration times for the tracer concentrations at the center and outer surface of the matrix block. The shorter equilibration time reduces the role of matrix diffusion on overall solute transport behavior, and, consequently, differences in behavior of solutes having different molecular-diffusion coefficients.

6. UNSATURATED ZONE TRANSPORT PREDICTIONS AND UNCERTAINTIES

This section presents the results from modeling transport in the unsaturated zone to examine the relative importance of the processes and phenomena that influence transport of both sorbing and non-sorbing radionuclides as solutes, as well as the transport of radionuclides as colloids. The results are based on the arbitrary and unrealistic assumption that a finite mass of the specific radionuclides selected for these analyses is released across the repository footprint into the unsaturated zone. The unsaturated zone flow field considered for these analyses is based on the range of values for present day infiltration. The results presented here focus on evaluation of transport processes and do not represent estimates of the anticipated performance of the unsaturated zone as a barrier or of its contribution to the overall performance of the repository system.

It is important to indicate that studies in this section are not intended to address realistic scenarios of radionuclide transport in the unsaturated zone of Yucca Mountain. (Such studies are the subject of TSPA investigations.) Instead, the focus of the study is to stress the unsaturated zone system under extremely aggressive conditions (see discussion in Section 6.3.8) in an effort to determine the weak points in its overall performance, the main pathways of transport, and their relative importance.

6.1 SOLUTE TRANSPORT

In these studies the transport of three radioactive solutes through the unsaturated zone are considered. The three solutes (^{99}Tc, ^{237}Np, and ^{239}Pu) cover the range of sorption behavior. ^{99}Tc is nonsorbing, ^{237}Np is mildly sorbing, and ^{239}Pu sorbs strongly onto the unsaturated zone rocks (see Table 5-1). In these studies, a mean present-day infiltration and instantaneous radionuclide release is assumed. An instantaneous release scenario corresponds to a single abrupt event during which a finite mass of radionuclides is suddenly released in the liquid phase of the fractures of the rock of the repository horizon. Study of the performance following an instantaneous release describes the ability of the unsaturated zone to store and retard the migration of a limited mass of radioactive substances.

In this case, transport is described by the conventional concept of cumulative breakthrough at the water table. This is quantified by a radionuclide mass fraction, R_M, defined as

$$R_M = \frac{M}{M_0}$$ (Eq. 6-1)

where M_0 is the instantaneously released initial mass of the radionuclide and M is the radionuclide mass that has exited from the domain of interest (i.e., in the unsaturated zone) at the time of observation. The radionuclide mass remaining in the domain undergoes radioactive decay and decreases over time. In the instantaneous release studies, only the mass of the parent radionuclide is considered (i.e., the decay products are not tracked).

6.1.1 Transport Behavior of ^{99}Tc, ^{237}Np, and ^{239}Pu

The breakthrough curves of ^{99}Tc (a nonsorbing radionuclide), ^{237}Np (a mildly sorbing radionuclide), and ^{239}Pu (a strongly sorbing radionuclide) at the water table for the unsaturated zone flow field corresponding to present-day infiltration are shown in Figures 6-1 to 6-3. The simulations compare transport for the bounding cases of upper-bound, mean, and lower-bound infiltration values for present-day infiltration. The mean infiltration value is considered as a base-case scenario. The lower- and upper-bound infiltration values cover the uncertainties associated with infiltration models of possibly lower and higher rates, respectively.

The values of R_M in Figures 6-1 to 6-3 show a very strong dependence on the infiltration regime. In the simulation of ^{99}Tc transport (Figure 6-1), the t_{10} time (defined as the time at which R_M is 0.1) for the infiltration rate of lower-bound case is about 13,900 years, while the t_{10} time for the mean infiltration case is about 83 years. Thus, t_{10} is an indicator of the effects of the most conductive geologic features (i.e., certain fractures) on transport. The t_{50} (defined as the time at which R_M equals 0.5) is not reached within 1 million years for the low infiltration regime but is reached at 6,640 years for the mean infiltration regime. The higher infiltration case (the upper-bound present-day levels) leads to a decrease of t_{10} to about 6 years and of t_{50} to 230 years when compared to those of the mean infiltration case. The term R_M is relative, and these findings are only important if the magnitude of the released mass at the repository becomes significant. Figure 6-1 also shows that the maximum attainable value of R_M increases with infiltration rate. This is expected, because lower infiltration results in lower velocities and longer transport times through the unsaturated zone, and, consequently, more radioactive decay.

The moderate sorption of ^{237}Np results in retardation of its transport through the unsaturated zone system, as the cumulative breakthrough R_M of the ^{237}Np mass fraction at the water table indicates (Figure 6-2). Comparison to the cumulative breakthrough of the nonsorbing ^{99}Tc (Figure 6-1) reveals very different t_{10} and t_{50}. The moderate sorption of ^{237}Np is sufficient to result in a large increase in t_{10} and t_{50} compared to those for the nonsorbing ^{99}Tc. Because of radioactive decay and significant retardation, the maximum attainable R_M varies over a larger range and does not necessarily reach a plateau within the simulation period. As was the case for ^{99}Tc, the increased infiltration rate for the upper-bound conditions leads to faster transport and shorter transport times from the repository.

The cumulative breakthrough R_M for ^{239}Pu at the water table for present-day infiltration is shown in Figure 6-3. If the contributions of the decay products (i.e., ^{235}U and ^{231}Pa) are neglected, R_M for the upper bound infiltration case first reaches a plateau when R_M equals 0.1 (at a time of 20 years, a clear indication of fracture flow) and then a second plateau at about 100,000 years (denoting matrix flow). This behavior results from the strong sorption of ^{239}Pu.
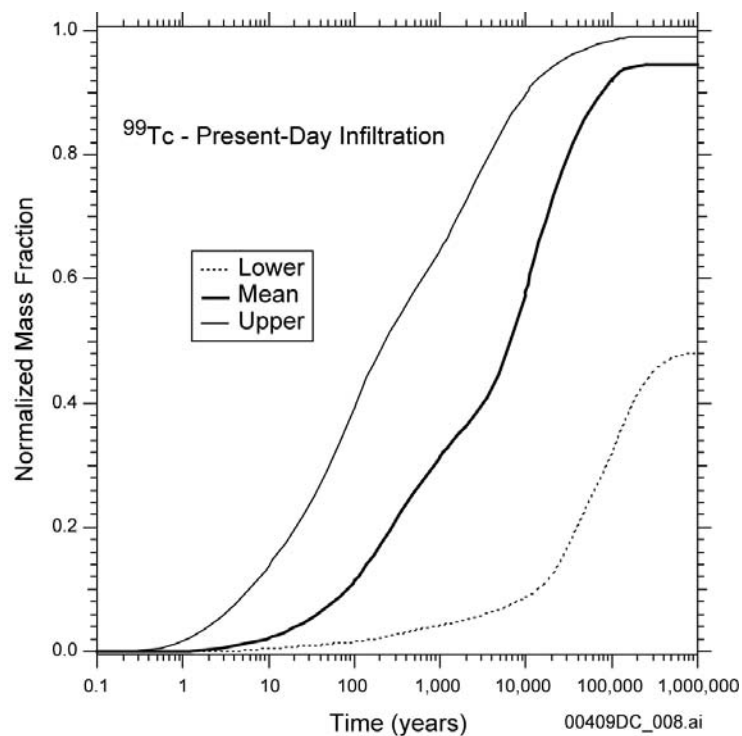
Source: BSC 2003e, Figure 6.8-1.

Figure 6-1.   Cumulative Breakthrough of the ^{99}Tc Mass Fraction R_M at the Water Table for Different Present-Day Climate Scenarios
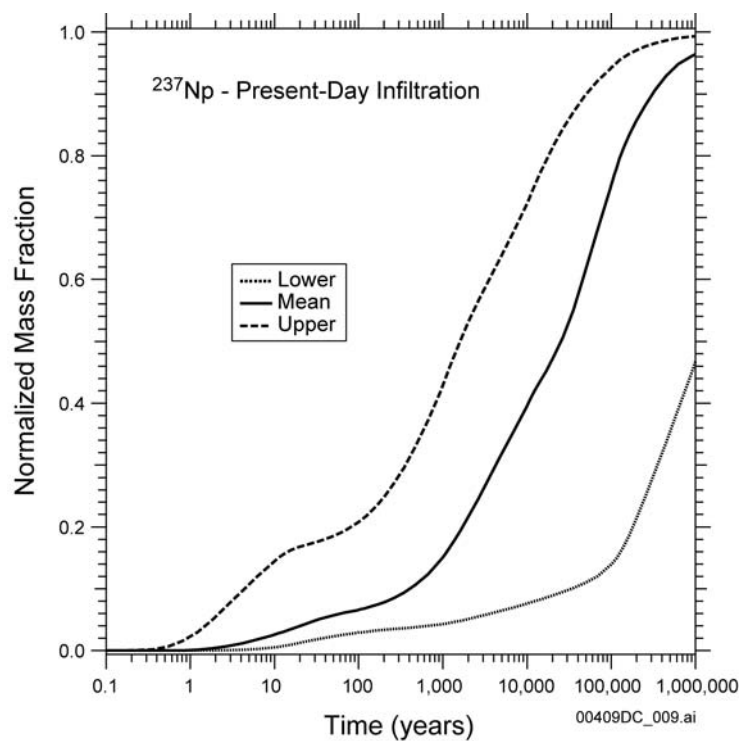
Source: BSC 2003e, Figure 6.9-1.

Figure 6-2.   Cumulative Breakthrough of the ^{237}Np Mass Fraction R_M at the Water Table for Different Present-Day Climate Conditions

Source: BSC 2003e, Figure 6.10-1.

Figure 6-3. Cumulative Breakthrough of the ^{239}Pu Mass Fraction R_M at the Water Table for Different Present-Day Climatic Scenarios

In the upper-bound infiltration case, the two plateaus in R_M are higher than those for present-day infiltration but occur at about the same times (indicating that fracture and matrix transport are important). As in the cases of ^{99}Tc and ^{237}Np, higher amounts of infiltration lead to an earlier arrival of ^{239}Pu at the water table. However, the mass arriving at the water table represents a very small portion of the initial release because ^{239}Pu is strongly sorbed by the rock.

6.1.2 Areal Distribution Patterns of Solute Transport at the Water Table

The simulation of solute transport through the fractures of the unsaturated zone from the repository horizon assuming instantaneous release produced maps of radionuclide distribution at the water table for a range of timescales and infiltration scenarios. In this section, the results of the simulation of ^{99}Tc in terms of its areal distribution pattern at the water table for 10 and 100 years are presented. These results were chosen to show the relationship between transport and site geology and percolation patterns. In the analysis of these results, the reader is cautioned to consider the discussion of overall uncertainties presented in Section 6.3.8.

In the study of radionuclide transport, the relative mass fraction X_R is defined as:

$$X_R = \frac{X}{X_0} = \frac{C}{C_0} = C_R$$

(Eq. 6-2)

where X is the radionuclide mass fraction in the liquid phase, C is the radionuclide mass concentration in the liquid phase, and the subscript 0 denotes the value of the subscripted

parameter in the water released from the repository. The distributions of the ^{99}Tc-X_R in the aqueous phase in the fractures immediately above the water table for times of 10 and 100 years are shown in Figure 6-4 for mean present-day infiltration conditions. These results are compared to maps of surface infiltration (Figure 3-1) and percolation fluxes at the repository level and at the water table (Figure 6-5).

The relatively high X_R values in Figure 6-4 corresponds to the location of faults, namely Drill Hole Wash Fault and Pagany Wash Fault, shown in Figure 6-5. This correspondence indicates that the fractures associated with these faults control the transport of ^{99}Tc from the repository horizon to the water table. These two faults show measurable radionuclide presence at the water table as early as times of 10 years. At the same time, strong signatures of ^{99}Tc also coincide with the locations of the Sundance Fault and Sever Wash Fault. The significance of the fractures associated with the Drill Hole Wash Fault and the Pagany Wash Fault as the dominant conduit of ^{99}Tc to the water table is further supported by the distribution of the relative mass fraction in the fractures at 100 years (Figure 6-4), when a large zone of high ^{99}Tc concentrations extends outward from those fault axes. At this time, in addition to the Sundance Fault, the northern portion of the Ghost Dance Fault appears to contribute significantly to transport.

Figure 6-4 shows an absence of ^{99}Tc breakthrough through the fractures in the southern half of the model domain. This pattern arises from the variable geology at the base of the TSw. Below the TSw in the northern part of the repository, the zeolitic CHz layers predominate, while the vitric CHv layers occur below the southern part. The permeabilities of the fractures and matrix of the vitric layers are similar in magnitude (BSC 2003f, Section 6). Because of this similarity, combined with the large fracture spacing, the CHv behaves like a nonfractured porous medium (BSC 2003f, Section 6) and slows the transport of ^{99}Tc toward the water table relative to transport through the zeolitic layers.

Although the zeolitic layers in the northern part of the repository have fracture spacing and fracture permeability similar to the vitric CHv layers in the south, their matrix permeability is about five orders of magnitude lower than their fracture permeability (BSC 2003f, Section 6). Consequently, matrix flow in the zeolitic layers in the northern part of the repository is slow, and practically all the flow occurs in the fractures, leading to the fast transport observed in the fractures (Figure 6-4).

In summary, the observed transport pattern is consistent with the infiltration and percolation distributions. The correspondence between percolation flux in Figure 6-5 and the transport patterns in Figure 6-4 shows that the water flow pattern dictates the advective transport pattern. The dominance of fracture flow is supported by the relative magnitudes of hydraulic properties in the fractures and in the matrix. The permeability of the fractures in the faults can be as high as hundreds of Darcies (BSC 2001d, Section 6; Bodvarsson et al. 1999, p. 15). The resulting fast advective transport is the reason for the transport pattern observed in Figure 6-4.
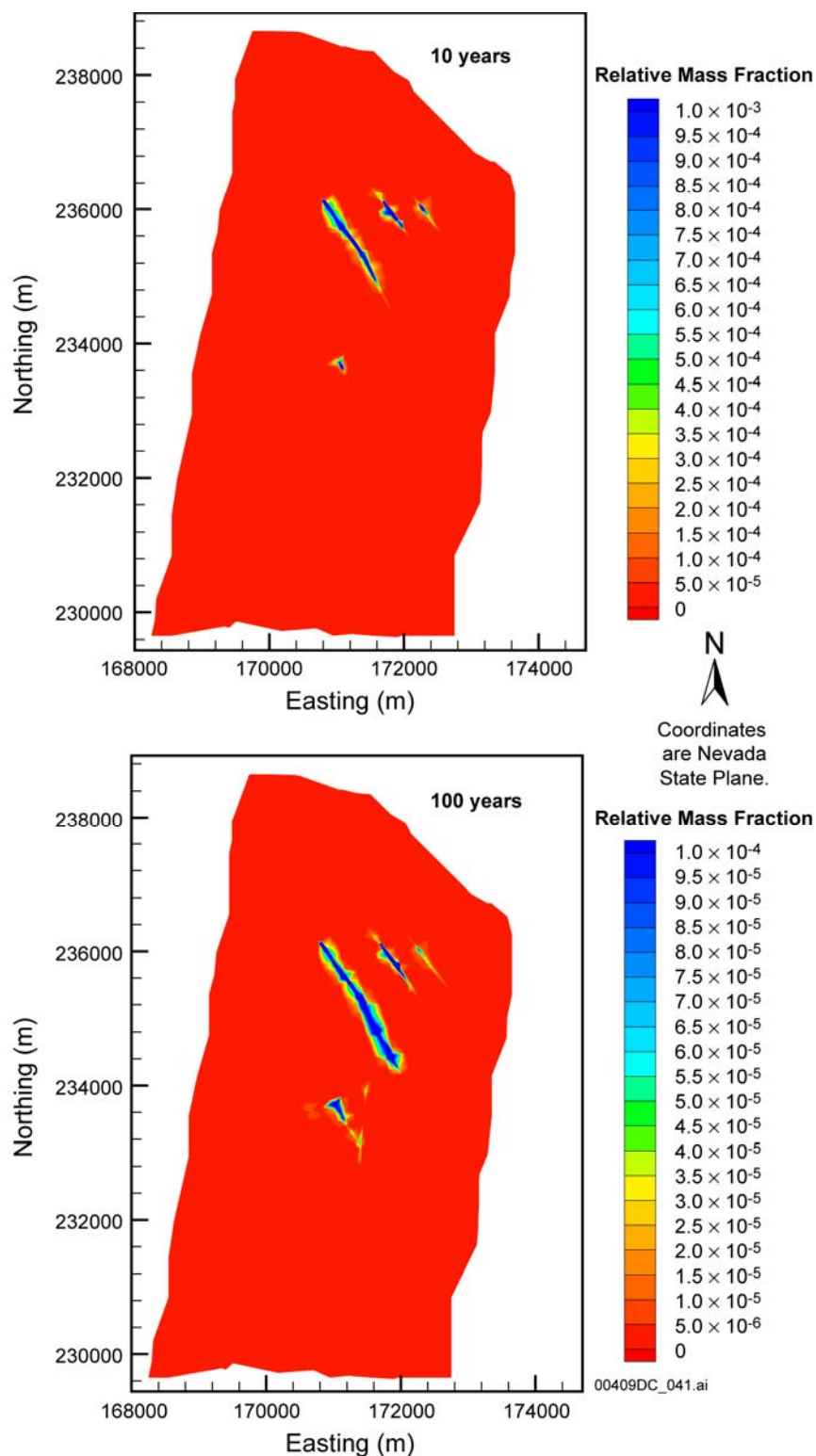
Source: BSC 2003e, Figure 6.8-12 and Figure 6.8-14.

Figure 6-4. Distribution of the Relative Mass Fraction X_R of ^{99}Tc in the Fractures at the Water Table at 10 and 100 Years for Mean Present-Day Infiltration
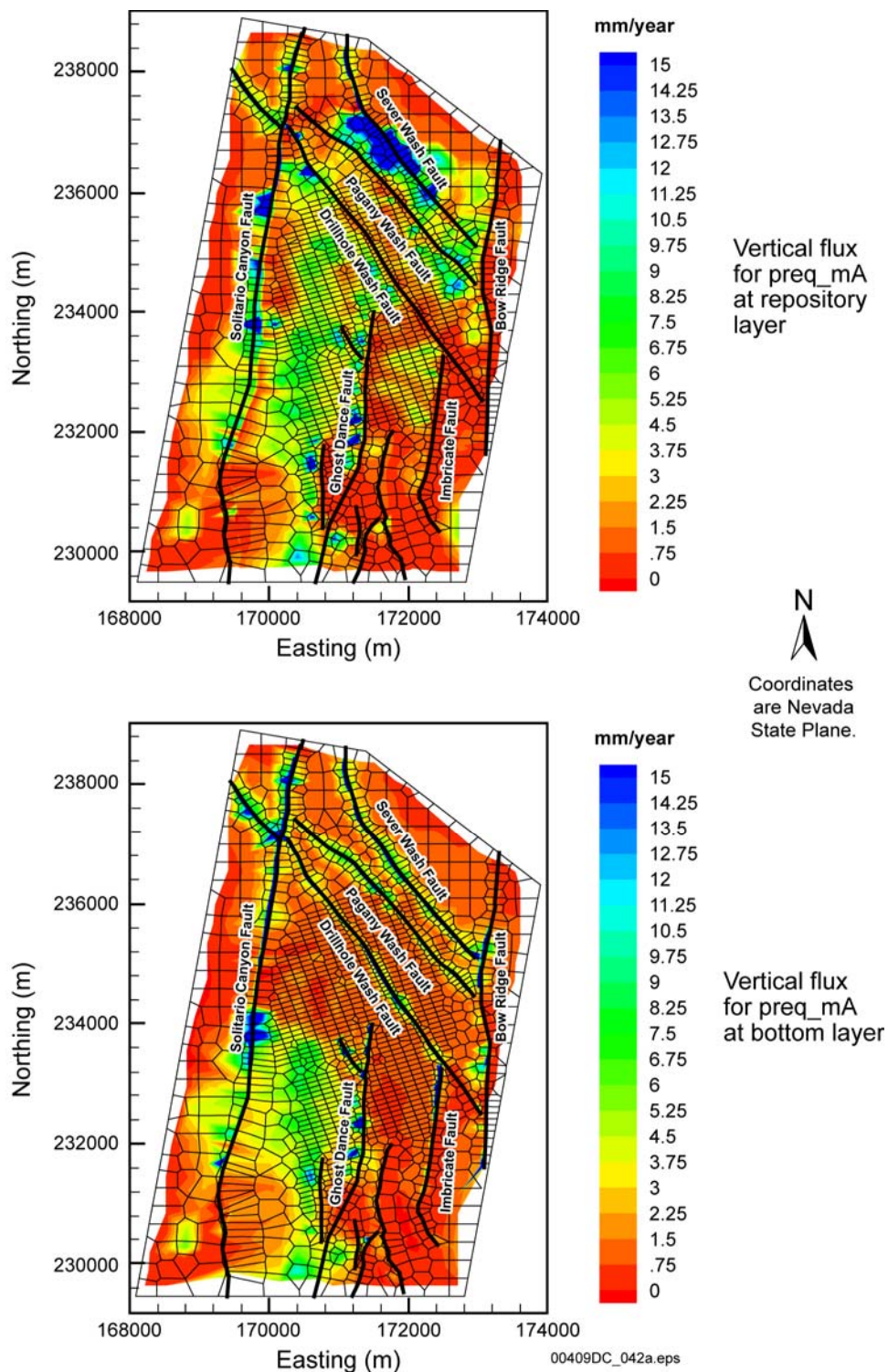
Source: BSC 2003b, Section 6, Figures 6.1-2 and 6.6-1.

Figure 6-5. Percolation Fluxes at the Repository Level and at the Water Table Level

6.2   TRANSPORT OF RADIOACTIVE CLASS I COLLOIDS

This section discusses the transport of Class I colloids (PuO_2) through the unsaturated zone. Breakthrough curves as a function of colloid size and areal distribution patterns at the water table are presented. For these studies, colloids are assumed to undergo irreversible filtration into (i.e., attachment onto) the matrix of the unsaturated zone rocks.

A mean present-day infiltration pattern is assumed for these studies, and the colloids are continuously released into the fractures of the rock of the repository horizon. For this release scenario, the breakthrough concept is based on the normalized or relative release rate R_F, which is defined as the ratio of the radionuclide mass flux at the water table to the initial flux at the repository. Then, t_{10} and t_{50} are defined as the times at which R_F equals 0.1 and 0.5, respectively.

6.2.1   Transport Behavior of Colloids

Figure 6-6 shows the relative release rate R_F of four colloid sizes at the water table for irreversible filtration. The release rate of the colloids at the repository, reflecting their radioactive decay, is included in the figure for reference. Two observations are particularly important. The first is the observation of very fast breakthrough for the three larger colloids (characterized by a consistent, rapid rise of the breakthrough curve for all three), which is consistently rapid for all three colloids. The value of t_{10} for the three larger colloids is only about 5 years. After the fast rise, t_{50} is not reached for any colloid, and the R_F begins declining as radioactive decay reduces source-term concentrations. The second observation is that the smallest colloid (6 nm) exhibits the slowest breakthrough. More importantly, this colloid never reaches the 0.1 relative release rate, because it is small enough to enter the matrix and become attached to the matrix walls. These observed phenomena (the larger colloids as well as the smaller one) result from a combination of the following factors:

- The larger colloids have a greater transport velocity. Because of their size, the larger colloids can only move through the center of pores and fractures where velocities are larger than the average water velocity. In this case, the 450-nm colloid is assumed to move at 1.5 times the average water velocity (i.e., the maximum pore velocity).

- The larger colloids cannot penetrate into the matrix from the fractures because of size exclusion. Thus, the colloid mass in the fractures is not reduced through colloidal diffusion or hydrodynamic dispersion, and, therefore, practically all of it moves exclusively through the fractures. The 6-nm colloid is capable of diffusing into the matrix, shown by the slower breakthrough, the very slow and slight rise of the curve, and the low maximum R_F value in Figure 6-6.
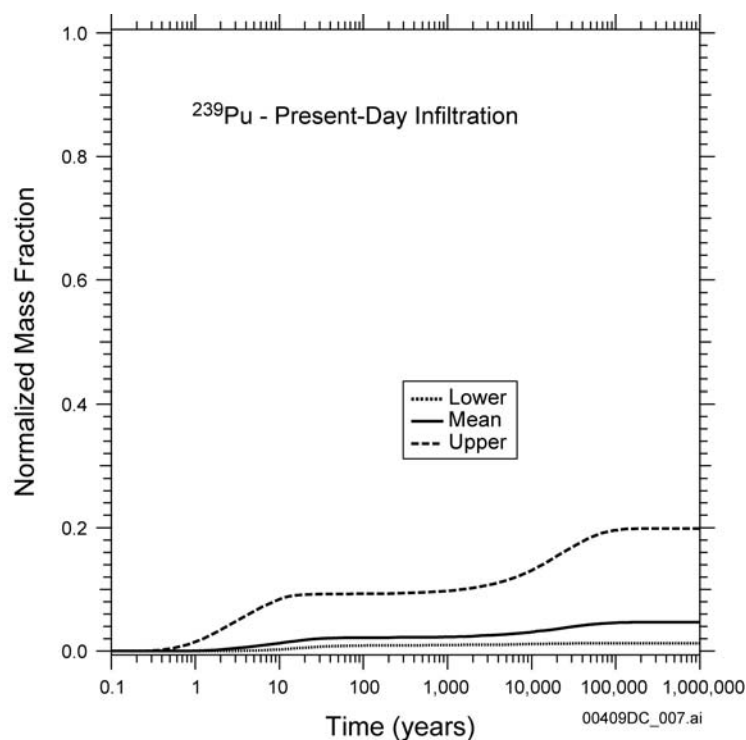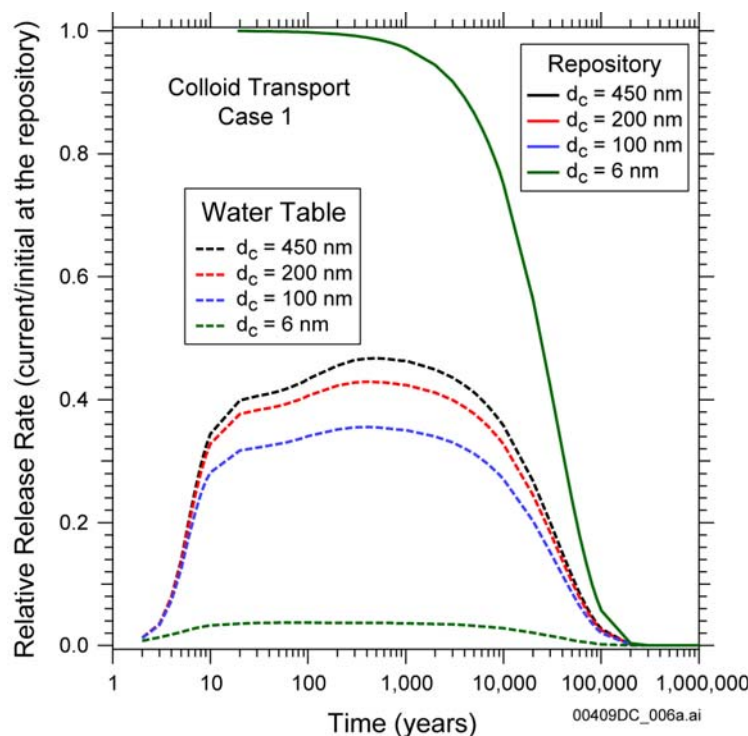
Source: BSC 2003e, Figure 6.18-1.

Figure 6-6.   Cumulative Breakthrough of the Colloid Mass Fraction R_M at the Water Table for Several Colloid Sizes for the Case of No Backward Filtration Following Attachment

After the initial rapid rise, the slope of the R_F curve for the larger colloids decreases and then increases again before it begins to decline at a point that coincides with the beginning of the decline in concentration due to decay. This last upward trend is associated with the beginning colloidal breakthrough via the matrix. The breakthrough of the 6-nm colloid is attributed to the arrival of colloids at the water table through the matrix.

6.2.2   Areal Distribution Patterns of Colloid Transport at the Water Table

Figure 6-7 shows the areal distribution of the 6-nm colloid's fracture relative mass fraction and its matrix relative filtered concentration of the 6-nm colloid at the water table at a time of 1,000 years. The fracture relative mass fraction describes the colloidal transport of radionuclides by water flow through the fractures only. The process of matrix filtration (discussed in Section 2.2.3) concentrates the colloids that flow from the fracture to the matrix. The smaller pores of the matrix exclude a portion of the colloids. Matrix filtration can also occur within the matrix itself, when flow from larger pores to smaller pores results in exclusion of colloids from the smaller pores.

Source: BSC 2003e, Figures IV-22 and IV-24.

Figure 6-7. Distribution of the 6-nm Colloid at the Water Table at 1,000 Years for Fracture Relative Mass Fraction and Matrix Filtered Relative Concentration

The significance of the faults in the distribution of fracture concentration is evident from the correspondence between the distribution in Figure 6-7 and the Drill Hole Wash Fault and the Pagany Wash Fault in Figure 6-5. As in the case of the solute transport patterns in Figure 6-4, the highest concentrations of the 6-nm colloid occur underneath the northern part of the repository. This is where fracture flow and advective transport through the faults dominate. The matrix relative filtered concentration describes the amount of colloids that have been attached to the matrix. Its distribution follows that of the fracture concentration and indicates that filtration and immobilization in the matrix occurs after the 6-nm colloids diffuse into the matrix.

The corresponding distributions of the 450-nm colloid at the same time and location are shown in Figure 6-8. The areal extent of the fracture relative mass fraction shows a significantly broader distribution, indicating that more fractures over a wider area are involved. This was expected because the larger colloid moves faster through the fractures while being subject to less diffusion (i.e., the larger colloids tend to stay in the center of the flow channel and have less contact with the matrix surface). As for the smaller colloid and its solute transport patterns, breakthrough occurs only in the area underneath the northern part of the repository, where fracture flow and advective transport dominate. One interesting observation is that the relative mass fractions for the 450-nm colloid exceed 1, corresponding to concentrations larger than those in the release stream. This is caused by straining (pore-size exclusion). Because of its larger size, the straining is more pronounced for the 450-nm colloid than for the 6-nm colloid and leads to higher concentrations at earlier times behind the interface.

The pattern of the matrix relative filtered concentration differs significantly from that of the fracture relative mass fraction. The matrix-filtered concentrations in the northern part of the repository for the 6-nm colloid are high compared to those for the 450-nm colloid. The 450-nm size experiences a greater degree of matrix filtration because of its larger size. However, significant filtered concentrations appear in the southern part of the repository (the area of the vitric tuff concentration), where the fracture and matrix permeabilities are similar and flow is matrix dominated. In this region, colloids move through the matrix where they are immobilized through filtration.
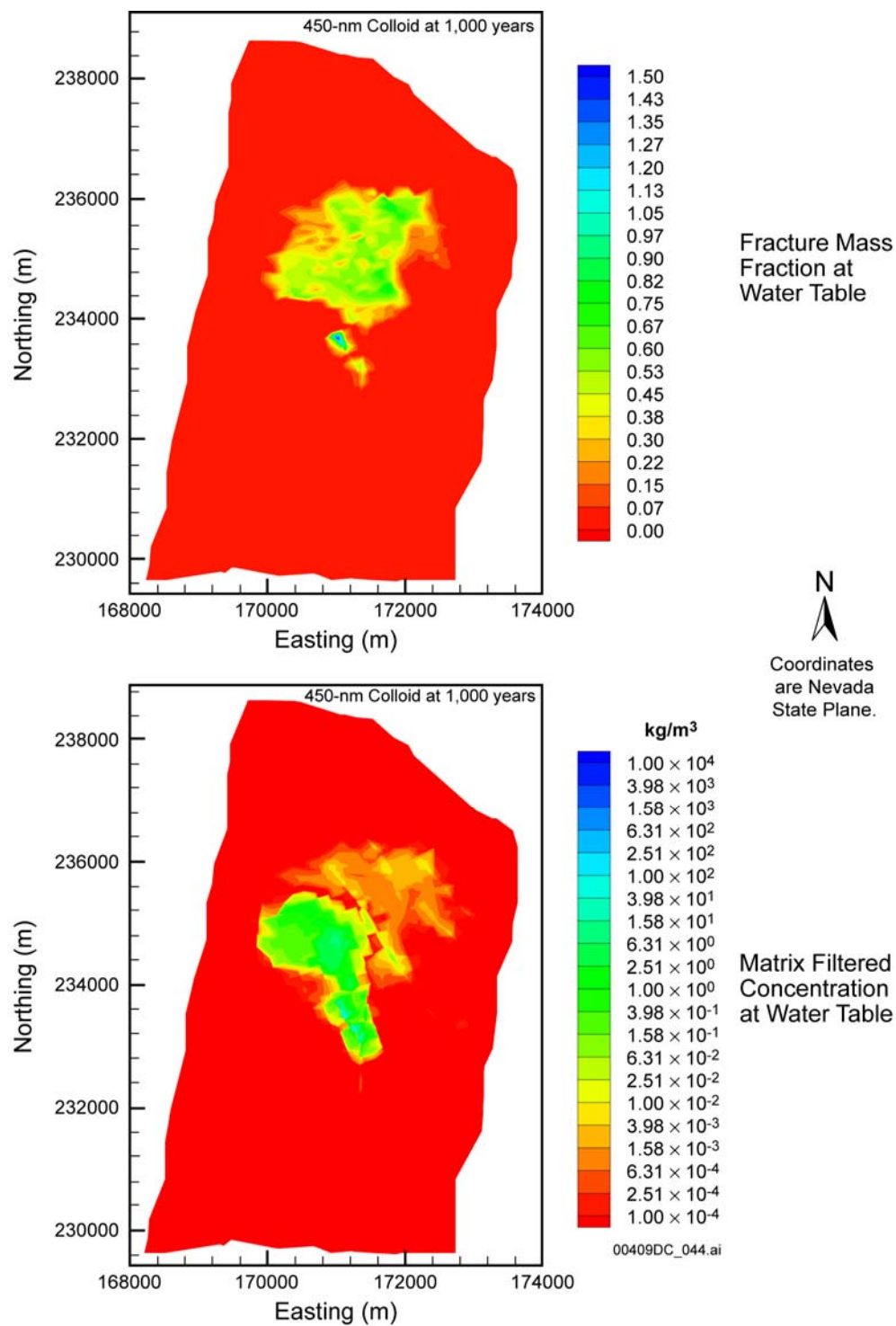
Source: BSC 2003e, Figures IIV-22 and IIV-24.

Figure 6-8.   Distribution of the 450-nm Colloid at the Water Table at 1,000 Years for Fracture Relative Mass Fraction and Matrix Filtered Relative Concentration

6.3   UNCERTAINTIES AND SENSITIVITIES

The uncertainties related to the model of radionuclide transport through the unsaturated zone are summarized below. In general, parameter-related uncertainties are addressed by investigating the sensitivity of transport behavior to these parameters when they are varied to cover the range of possible values.

6.3.1   Uncertainties in Matrix Diffusion of Solutes and Colloids

Uncertainties in matrix diffusion are reflected in the values and spatial distribution of the effective diffusion coefficient, which is a composite quantity involving the molecular diffusion coefficient D_0, the medium tortuosity, the water saturation, and the active area over which diffusion occurs. Given the uncertainties in the estimation of these parameters, the range of variability of the effective diffusion coefficient can be represented by the chosen value of D_0 (a parameter that is relatively easy to determine).

To address this issue, the sensitivity of radionuclide transport through the unsaturated zone for a wide range of D_0 values (spanning nearly three orders of magnitude) is investigated for ^{99}Tc and ^{237}Np (see Figure 6-9). As expected, Figure 6-9 indicates that D_0 has a significant impact on breakthrough predictions, resulting in faster arrival times for lower D_0 values.

Analysis of the colloid transport mechanisms indicates that diffusion is less significant than in solute transport, because the colloid diffusion coefficient is smaller due to its larger size, and size-exclusion effects at the interfaces of different geologic units further limit entry through diffusion into the matrix, especially for larger colloids (BSC 2003e, Section 6.19). However, matrix diffusion effects become increasingly important for a decreasing colloid size (see Figure 6-6). In modeling, ignoring the effect of colloid matrix diffusion results in increased migration of colloids.

Although the estimation of the colloid diffusion coefficient is quite reliable, there are fundamental uncertainties about the validity of the expressions used to estimate the effective diffusion coefficient of colloids under unsaturated conditions (BSC 2003e, Section 6.2.6.1). Even if these expressions are valid, they involve products of water saturation and tortuosity, which lead to significant uncertainty.
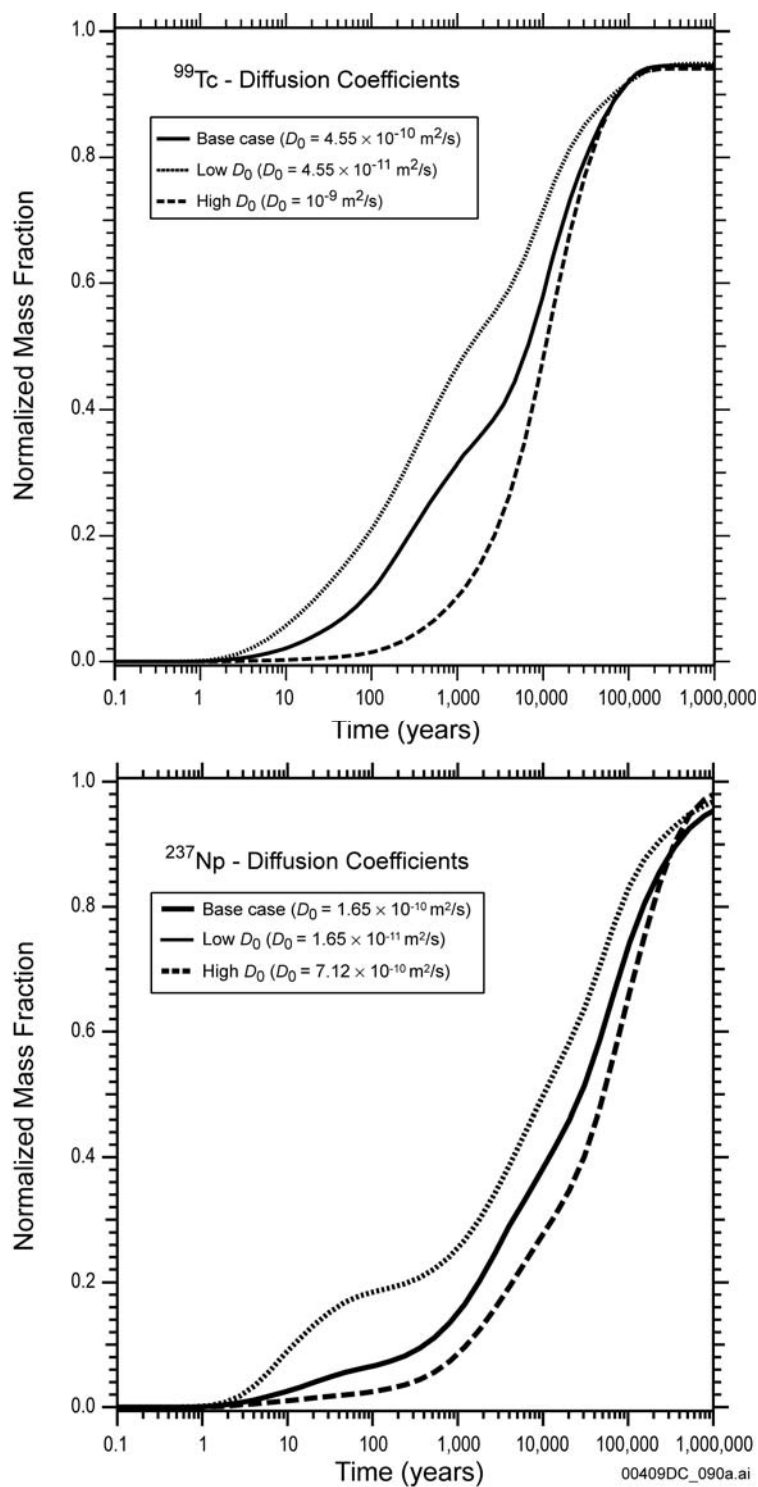
Source: BSC 2003e, Figures 6.8-28 and 6.9-5.

Figure 6-9.   Effect of Varying Diffusion Coefficients on the Cumulative Breakthrough of the ^{99}Tc and ^{237}Np Mass Fraction R_M

6.3.2 Uncertainties in Sorption

Uncertainties in sorption are reflected in the values and spatial distribution of the K_d. To address this issue, the sensitivity of radionuclide transport through the unsaturated zone is studied for K_d values that cover the range between zero (no sorption) to maximum reported values (BSC 2003e, Table 6.5-1).

The breakthrough of ^{237}Np at the water table is shown in Figure 6-10 for a range of K_d values. The results in Figure 6-10 indicate that K_d has a significant impact on breakthrough, with faster arrival times predicted for lower values of K_d. The relative effect of K_d uncertainty on transport appears to be much more pronounced than that for D_0 uncertainty.
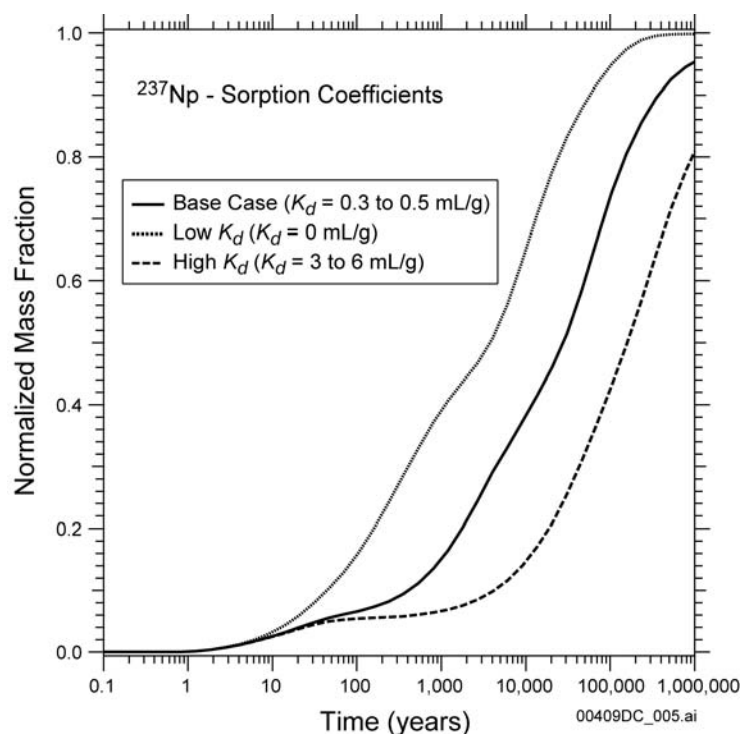
Source: BSC 2003e, Figure 6.9-6.

NOTE: The range in K_d values indicates differences in the various hydrogeologic units.

Figure 6-10. Effect of Varying Sorption Coefficients on ^{237}Np Breakthrough at the Unsaturated Zone

6.3.3 Uncertainties in the Colloid Retardation Kinetics

Basic knowledge of the parameters that control the kinetic filtration of colloids (forward and backward filtration coefficients) in unsaturated matrix and fractures is practically nonexistent. When fast backward filtration is assumed (i.e., the opposite of the irreversible filtration discussed in Section 6.2), the results (shown in Figure 6-11) are similar to that in Figure 6-6 for no backward filtration, where only slightly higher R_F values are observed because the colloids that enter the matrix are not irreversibly attached. The increase in the R_F value of the 6-nm colloid is slightly greater than for the larger colloids, because a larger fraction enters the matrix. The

relative insensitivity to the forward filtration model in the matrix is a result of the dominant role of fractures in the three-dimensional site- scale system, with the matrix appearing to contribute only minimally to colloid transport.
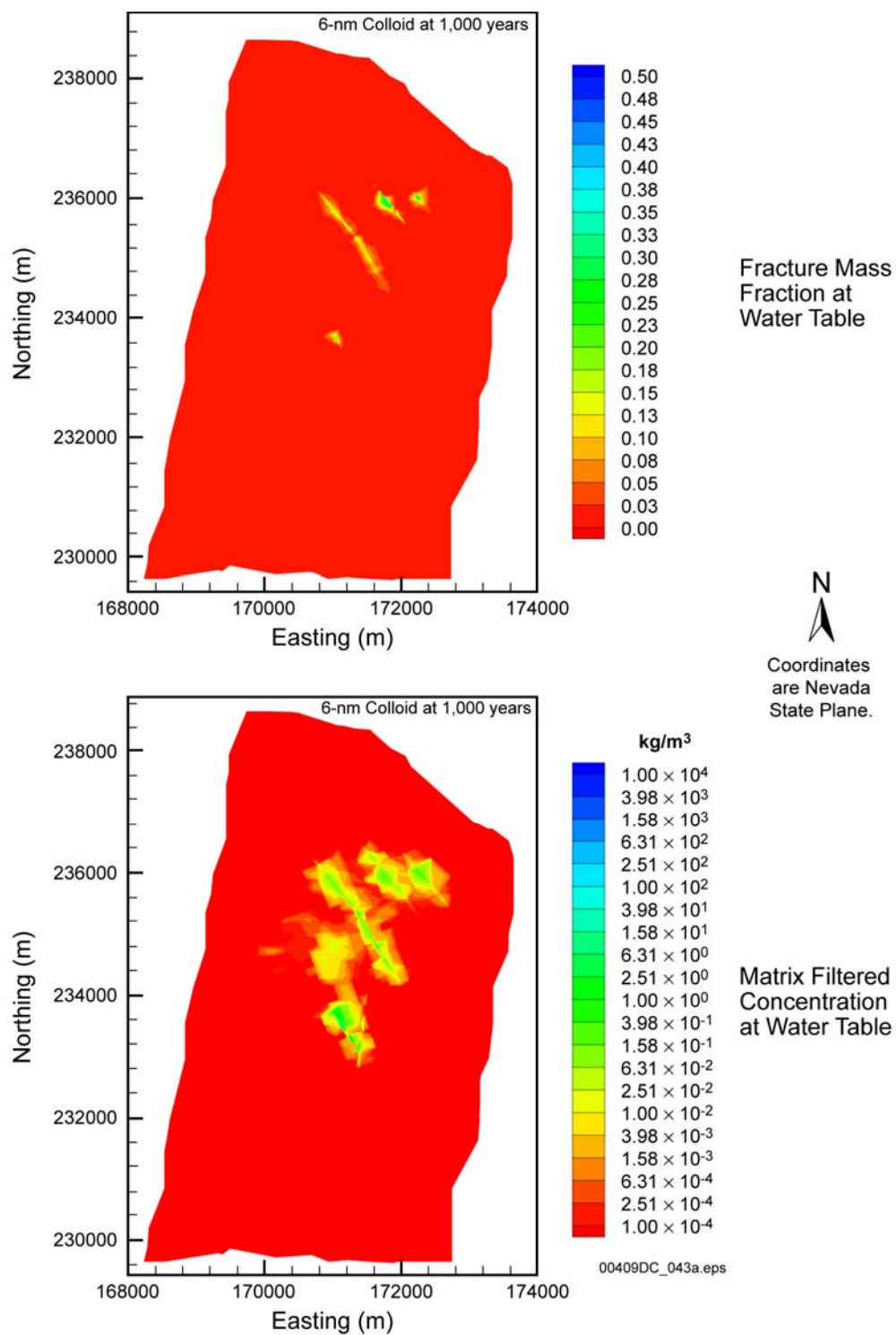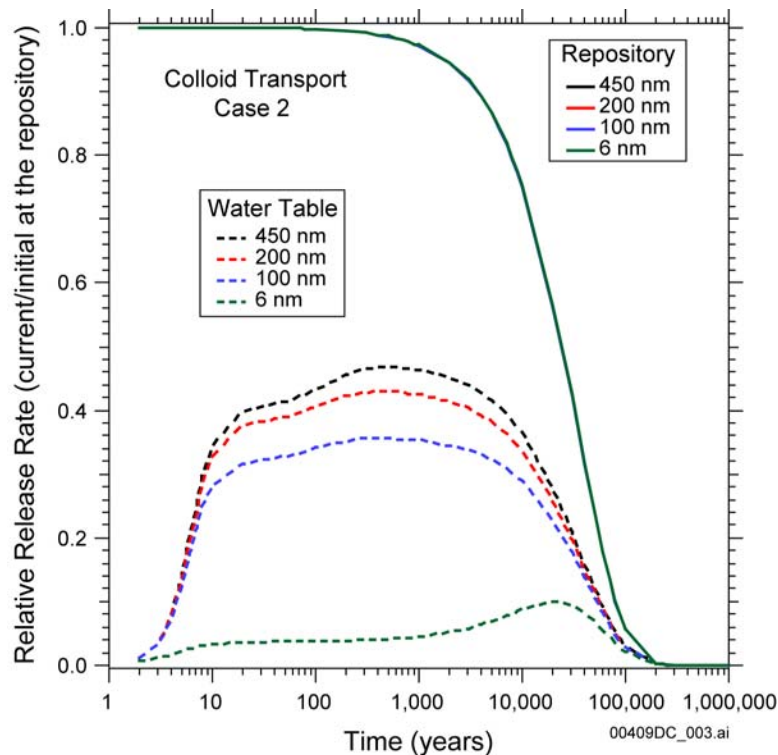

Source: BSC 2003e, Figure 6.18-1.

Figure 6-11. Cumulative Breakthrough of the Colloid Mass Fraction R_M at the Water Table for Several Colloid Sizes for the Case of Fast Backward Filtration Following Attachment

These results indicate that transport is insensitive to the filtration parameters in the matrix, but the significance of this observation may be limited given the difficulty of larger colloids in penetrating the matrix. Because the available kinetic models are developed from theoretical principles (Herzig et al. 1970) and tested under saturated conditions in laboratory experiments involving uniform sand columns (van de Weerd and Leijnse 1997) or small-scale field tests (Harvey and Garabedian 1991), the application of the model to the unsaturated zone conditions at Yucca Mountain adds uncertainties to the colloid transport model results.

6.3.4 Uncertainty in the Mode of Radionuclide Release

The mode of radionuclide release (instantaneous versus continuous) is uncertain. It is entirely possible that such releases will vary spatially as well as temporally in the repository. The effect of the release mode is investigated by repeating the transport simulations of ^{99}Tc, ^{237}Np, and ^{239}Pu (the transport of which was previously studied under instantaneous release in Section 6.1) for a continuous release scenario. For this release scenario, the breakthrough concept is based on the normalized or relative release rate R_F, which is defined as the ratio of the radionuclide mass

flux at the water table to the initial flux at the repository. Then, t_{10} and t_{50} are defined as the times at which R_F equals 0.1 and 0.5, respectively.

The breakthrough curves at the water table for continuously released ^{99}Tc, [237]Np, and [239]Pu for present-day infiltration are shown in Figure 6-12. The radionuclide flux from the repository relative to initial conditions is also shown for reference. Because the water flux is constant for the simulation, the decrease in the relative radionuclide flux from the repository over time is a result of radioactive decay of the source term. For each radionuclide, R_F reaches a maximum value and then subsequently decreases as a result of the decay of the source-term. The intersection of the repository flux curve with the water-table curve occurs after the maximum R_F value and indicates the time when the relative release rate to the water table is equal to the relative flux from the repository.
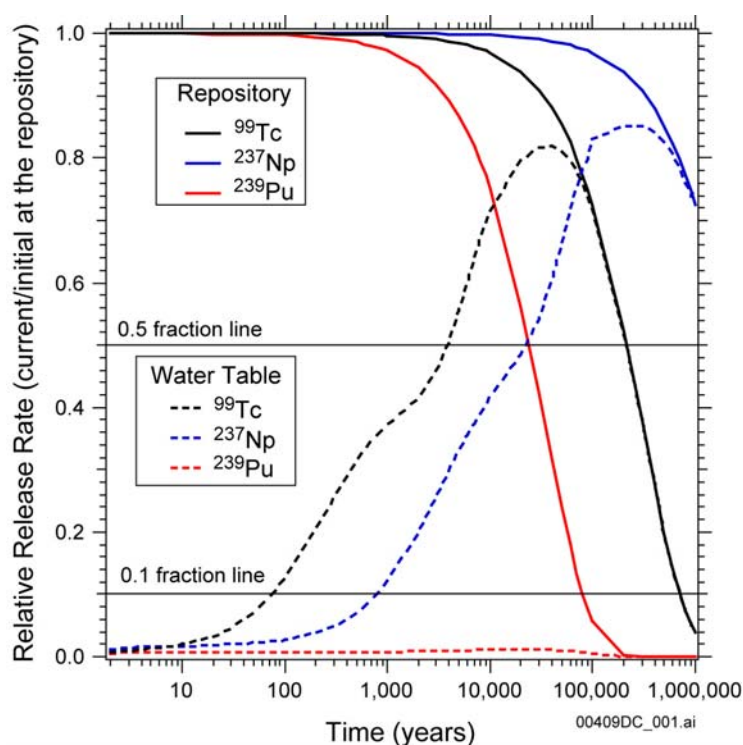
Source: BSC 2003e, Figure 6.15-1.

Figure 6-12. Normalized Relative Release R_F of ^{99}Tc, [237]Np, and [239]Pu at the Water Table for Continuous Release and Mean Present-Day Climate Scenarios

The contributions of radioactive decay products can add another element of uncertainty. The transport of the three-member [239]Pu→[235]U→[231]Pa chain (continuous release) is illustrated in Figure 6-13, in which the relative release rates at the water table are computed as the ratio of the total outflow rates (i.e., sum of individual member fluxes) to the total inflow rates at the repository. The importance of considering all the members of the chain in the computations is illustrated by comparing Figure 6-13 to the curve for the [239]Pu release rate at the water table in Figure 6-12, where only the parent species was accounted for. The release stream becomes depleted in [239]Pu due to decay after about 100,000 years, at which time [235]U is practically the

only species entering the unsaturated zone from the repository. Given the long half-life of ^{239}Pu and the much longer half-life of ^{235}U, the decay-product contributions must be regarded as important and cannot be neglected.
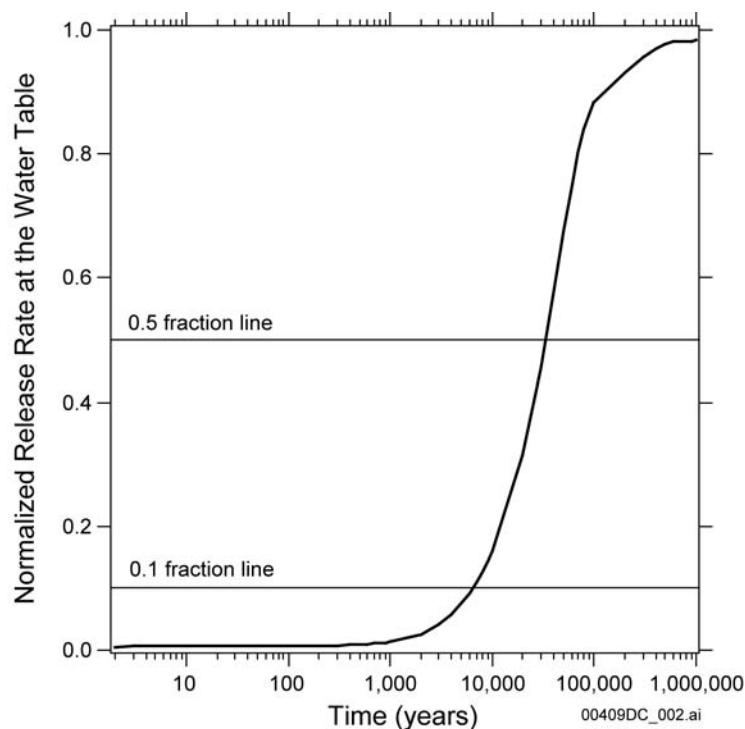
Source: BSC 2003e, Figure 6.16-2.

Figure 6-13.   Normalized Relative Release R_F of the Sum of All Members of the ^{239}Pu Chain at the Water Table for the Continuous Release Mean Present-Day Climate Scenarios

6.3.5   Climatic Uncertainties

Climatic changes affect the amount of infiltration and can have a significant effect on unsaturated zone flow, which can correspondingly affect unsaturated zone transport. Higher infiltration is invariably associated with faster transport and earlier radionuclide arrivals at the water table. This uncertainty is addressed by estimating transport under the entire range of climatic scenarios, thus bounding the possible outcomes (see Figures 6-1 to 6-3).

6.3.6   Uncertainty in the Hydrologic Model and in the Flow and Hydraulic Properties

The radionuclide transport model is intertwined with the underlying hydrogeologic model and, thus, is subject to the same uncertainties regarding flow fields, flow patterns, interaction of geologic and hydraulic regimes, impact and behavior of faults, heterogeneity and spatial distribution of the main hydrogeologic units in the unsaturated zone, heterogeneity in the flow properties and characteristics of the fractured rock units, interconnectivity of fracture networks, and the distribution of water saturations in the fractures and matrices of the unsaturated zone. These directly affect both advective transport (and, consequently, transport times to the water table) and diffusive fluxes.

6.3.7 Uncertainties in Fracture–Matrix Interactions

The interaction between fractures and the rock matrix is described using the active fracture matrix conceptualization (Liu et al. 1998, pp. 2638 to 2641), in which only a portion of fracture networks are active (hydraulically conductive) under unsaturated conditions. The active portion is defined as a function of water saturation S to the power of the active fracture parameter γ (less than or equal to 1 and greater than or equal to 0) (Liu et al. 1998, pp. 2638 to 2641). When γ equals 0 or S equals 1 (corresponding to a saturated condition), all fractures are active, while a γ value of 1 indicates the smallest active fracture portion for a given saturation.

The impact of uncertainties in γ on three-dimensional site-scale flow and transport through the unsaturated zone was investigated in *UZ Flow Models and Submodels* (BSC 2003b, Section 6.8). Sensitivity studies indicated that transport is more sensitive to uncertainty in the value of γ than flow (which exhibits relative insensitivity to γ). Additionally, the effect is more pronounced at earlier times because diffusive fluxes become progressively smaller as the concentrations in the matrix and fractures approach equilibrium. The sensitivity of transport to γ is demonstrated in Figure 6-14, which shows a substantial retardation in the arrival of a conservative radionuclide (with the diffusion coefficient of ^{99}Tc) at the water table when γ is reduced by 50% from its original calibrated value of approximately 0.6. In this case (which involved radionuclide release directly into the repository fractures), t_{10} increased by more than an order of magnitude (from 40 to 650 years), while t_{50} doubled (from 3,500 to 7,000 years).

6.3.8 Overall Uncertainties

While the results presented in this document clarify some issues of radionuclide (solute and colloid) transport in the unsaturated zone, caution should be exercised in their interpretation because of the conceptual approach and assumptions of the simulation, as well as some knowledge uncertainties (especially in the area of colloid behavior).

Data analysis uses relative quantities with respect to the radionuclide concentration in the water released from the repository. Thus, predictions of large relative concentrations may mean little unless and until the radionuclide release becomes possible, significant, and known. Moreover, the analysis assumes that conditions for the creation and stability of solute and colloidal species exist and that the effects of the near-field chemical, physical, mineralogical, and thermal conditions on their creation and stability over time can be ignored. In that sense, the results discussed in this section reflect transport after radioactive species (chemically nonreactive solutes and/or stable colloids) manage to enter the fractures underneath the repository.

As discussed earlier, the three-dimensional site-scale simulations discussed in Section 6.1 do not describe a realistic (expected-case) scenario because they are based on the unrealistic assumption that a finite mass of the specific radionuclides selected for these analyses is released uniformly as solutes or colloids across the repository footprint, including the faults, into the unsaturated zone. This approach allows the capture of the earliest possible arrivals at the water table, and is conservative (at a minimum) in the early part of the simulation period. It presupposes the near-simultaneous rupture of all the waste-containing vessels, the ability of water dripping into the repository to focus exclusively on the ruptured vessels and to flow through them, a spatially and temporally constant contaminant release from each waste package, and the absence of any

immobilization process (e.g., solute precipitation, colloid flocculation) before radionuclides enter the fractures. The geologic model used in the analysis involves continuous fracture-to-fracture flow in certain portions of the unsaturated zone, greatly facilitating transport from the repository to the groundwater. The analyses do not consider processes that affect colloid stability, or sorption of solutes and attachment of colloids to fracture walls. The K_d values used in the sorption analyses were obtained by a process that consistently underestimates the distribution coefficients. Additionally, the approach followed in this study assumes radionuclide releases directly into the fractures, does not consider the retardation effects of the invert on the repository floor, ignores the retardation effects of the shadow zone, disregards solute sorption and colloid attachment onto fracture minerals.
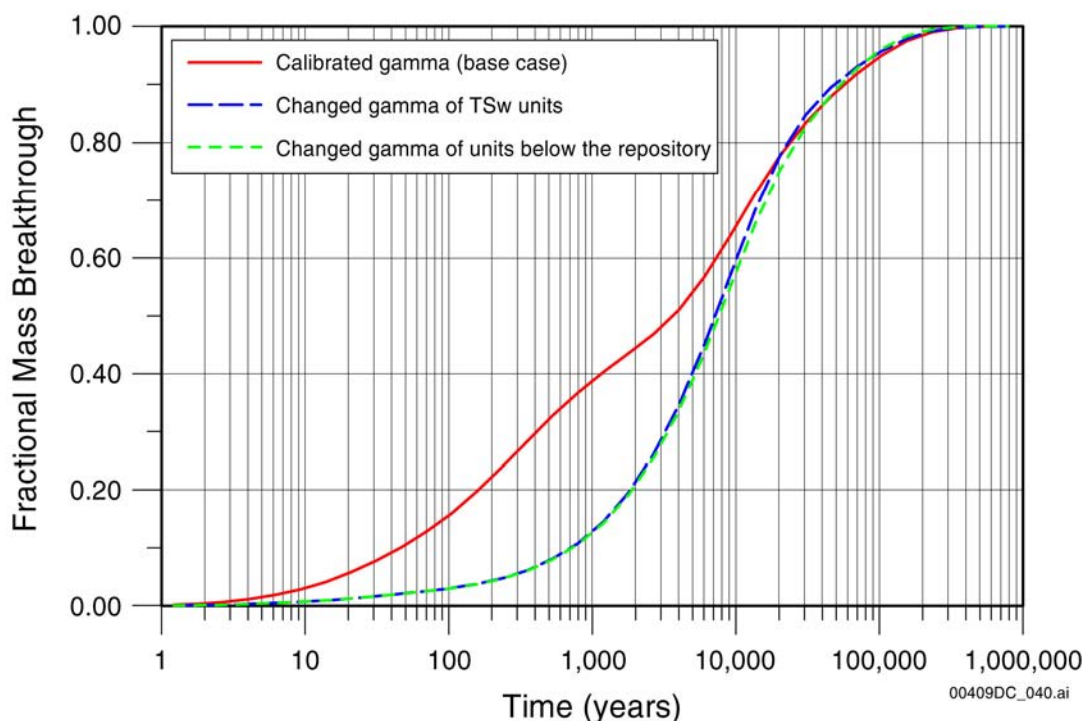
Source: BSC 2003b, Section 6.8, Figure 6.8-3.

NOTE: Red solid line = calibrated rock hydraulic properties; blue dashed line = smaller γ of TSw units; green solid line = smaller γ of all units below the repository.

Figure 6-14. Comparison of a Simulated Breakthrough Curve of Relative Radionuclide Mass at the Groundwater Table Obtained for the Base Case (Using Calibrated Rock Hydraulic Properties), a Case Using a Smaller (Half) Value of γ of the TSw Units, and Another Case Using a Smaller (Half) Value of γ of All Units below the Repository

The results presented here focus on evaluation of transport processes and do not represent estimates of the anticipated performance of the unsaturated zone as a barrier or of its contribution to the overall performance of the repository system. In that respect, these results should be viewed as an attempt to stress the unsaturated zone system under extremely conservative conditions in order to:

- Determine the main pathways of potential radionuclides transport to the water table

- Identify the dominant processes affecting transport and retardation, and the relative importance of the various hydrogeologic units to retardation

- Evaluate the relative importance of processes and phenomena affecting transport

- Determine the relative transport behavior of general types of radioactive species (e.g., solutes versus colloids, nonsorbing versus sorbing).

INTENTIONALLY LEFT BLANK

7. UNSATURATED ZONE TRANSPORT ABSTRACTION FOR THE TOTAL SYSTEM PERFORMANCE ASSESSMENT FOR THE LICENSE APPLICATION

7.1 UNSATURATED ZONE TRANSPORT ABSTRACTION MODELING APPROACH

The unsaturated zone transport abstraction model computes the movement of radionuclides released from the engineered barrier system into the unsaturated fractured geologic media downward to the water table as a dynamically linked module in the TSPA-LA. The abstraction model is based on a particle-tracking method available in FEHM, which is a general software package for geohydrologic flow, transport, and heat transfer problems. The unsaturated zone transport abstraction model operates within the same modeling domain as the three-dimensional mountain-scale unsaturated zone flow and transport process models previously described. The unsaturated zone flow fields are pregenerated using TOUGH2 and saved for use by the transport abstraction model in the TSPA for the license application (TSPA-LA) computations. The use of pregenerated flow fields increases the efficiency of transport simulations. The unsaturated zone transport abstraction model is based on a dual permeability formulation to address the importance of fracture flow and fracture–matrix interactions on radionuclide transport. The influence of spatial variability is included through a three-dimensional model that incorporates the appropriate geometry and geology.

Radionuclides that enter the unsaturated zone from the engineered barrier system are carried by water traveling through the fractured media downward to the water table. Any radionuclide that reaches the water table is removed from the unsaturated zone transport system and enters the saturated zone system for TSPA computations. Advection; dispersion; sorption; fracture–matrix interaction, including matrix diffusion, colloid-facilitated transport, radioactive decay/ingrowth, climate change, and water table rise are represented in the unsaturated zone transport abstraction model.

In the TSPA simulations, the transport calculations are carried out using multiple realizations to capture the uncertainty in the transport parameterization, the unsaturated zone flow fields, and the radionuclide source term.

7.2 PARTICLE-TRACKING METHODOLOGY

In this model, a particle-tracking technique is employed that can be used for transient, multidimensional finite-difference or finite-element codes. The mathematical basis for the particle-tracking technique and issues specific to the use of this technique for simulation of radionuclide transport in the unsaturated zone are further discussed in *Particle Tracking Model and Abstraction of Transport Processes* (BSC 2004). Radionuclide sorption on colloids is modeled using the same linear equilibrium sorption (K_d) model as used for sorption onto the rock matrix (see Section 2.2.2). A large K_d onto colloids leads to greater radionuclide interaction with colloids. This leads to enhanced radionuclide transport, unlike sorption onto the rock matrix. Therefore, the evaluation of K_d on colloids is made such that the K_d is not underestimated. Colloid transport is treated for two colloid types: waste-form colloids in which radionuclides are permanently attached and groundwater colloids, to which radionuclides reversibly sorb. Colloid diffusion is not treated, due to the low diffusivities for most colloids. Radionuclide mass sorbs reversibly to groundwater colloids with a constant equilibrium sorption parameter. Colloids

undergo reversible filtration in the porous medium. For the purposes of computing radionuclide transport, flow through the unsaturated zone is approximated, assuming that the system (rock mass and flow conditions) has not been influenced by repository waste heat effects (see Section 3.6). Climate change is treated in an approximate way by imparting an instantaneous jump from one steady-state flow field to another, with a corresponding rise or fall in the water table representing the bottom of the unsaturated zone model. Shorter-term transients (e.g., wet and dry years, individual storm events) are assumed to be adequately captured with a model that assumes such transients can be averaged to obtain a long-term, effective steady state.

The top boundary of the transport model is the repository where radionuclides are released from the engineered barrier system into the unsaturated zone. The strength of the source release varies with time and depends on the failure rate of the waste packages. The bottom boundary is the water table, where radionuclides exit the unsaturated zone system and enter the saturated zone. The water table changes in response to climate only in the unsaturated zone transport model abstraction. The water table beneath the repository footprint for present-day climate is spatially varying between 730 m and 840 m elevation above mean sea level. For future climates, the water table is raised to a uniform water table elevation of 850 m. The lateral boundaries, defined by the unsaturated zone flow model, are no-flow boundaries. The transport abstraction model is initiated with a radionuclide concentration of zero throughout the domain. Several key uncertainty parameters and flow fields are sampled stochastically during the multiple realizations performed in TSPA. A more detailed discussion of the parameters used is given in *Particle Tracking Model and Abstraction of Transport Processes* (BSC 2004).

7.3   ABSTRACTION MODEL RESULTS—BASE CASE

Figure 7-1 shows the normalized cumulative breakthrough curves at the water table for the 36 species simulated under the present-day mean infiltration condition. The simulation results reveal that irreversible fast colloids (curves labeled If239, If241, If242, and If243), which are not affected by matrix diffusion and retardation, have the shortest breakthrough times and the greatest breakthrough quantities. Within a period of between 10 and 100 years, more than 50% of the irreversible fast colloids traveled through the unsaturated zone. Dissolved species have the longest breakthrough times among the three transport mechanisms (irreversible fast colloids, irreversible slow colloids, and dissolved species), due to matrix diffusion and matrix adsorption. The results show that for nonsorbing species, such as ^{99}Tc and ^{129}I, about 20% of the mass travel through fast flow paths and arrive at the water table in 100 years or less. The remainder of the mass traveled at much lower velocities due to matrix diffusion. Dissolved species with moderate matrix adsorption, such as the isotopes of uranium, travel more slowly through the unsaturated zone than the nonsorbing species ^{99}Tc and ^{129}I. Within the first 100 years under the present-day mean infiltration conditions, only about 5% of the total ^{233}U mass passed through the unsaturated zone. ^{234}U exhibits a relatively fast transport process with higher mass output than the other dissolved uranium radionuclides because it is produced by the decay of a colloid facilitated species (^{238}Pu). Strongly sorbing species such as ^{242}Pu exhibit transport of less than 15% of the input through the unsaturated zone within the 20,000-year period. Finally, ^{234}U and ^{237}Np have normalized cumulative breakthrough values greater than 1 at 20,000 years due to the decay of ^{238}Pu (Pu238, If238, and Ic238) and ^{241}Am (Am241, If241, and Ic241), respectively.
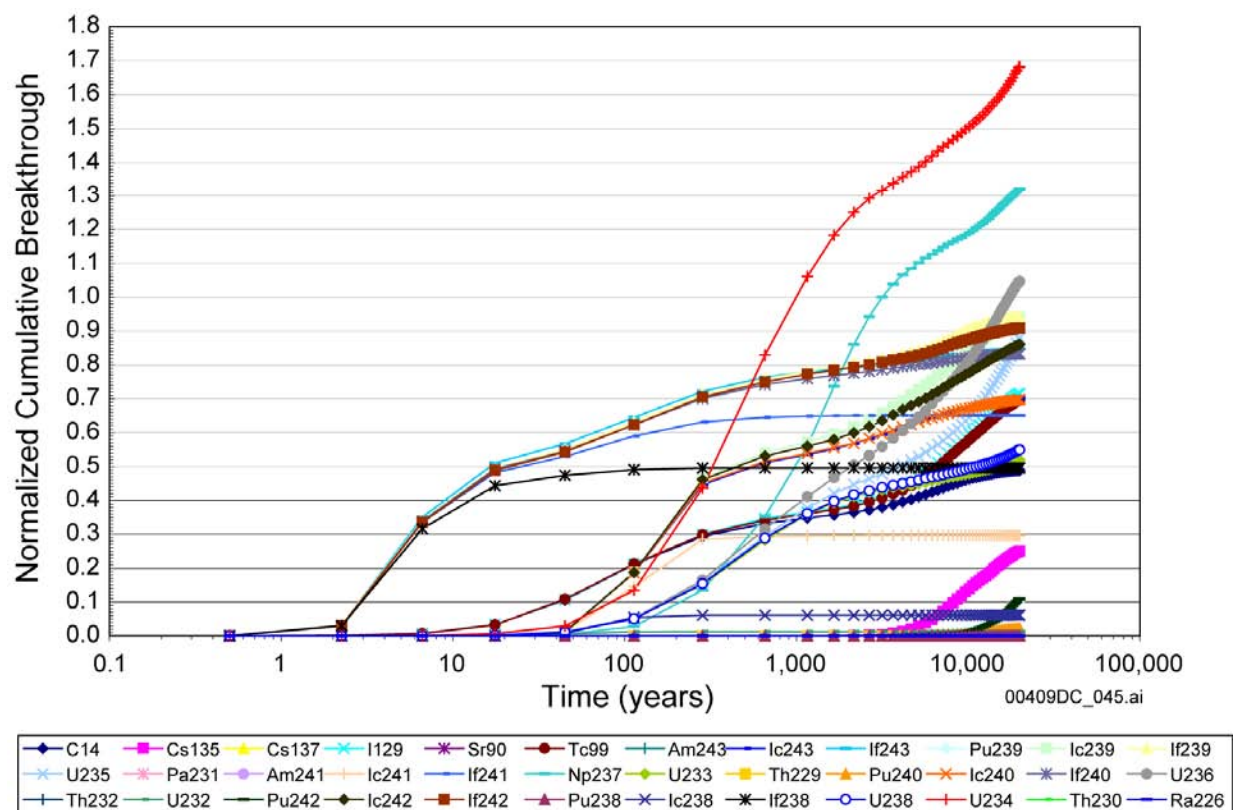
Source: BSC 2004, Figure 6-18.

NOTE: These results are for comparison purposes only. Actual radionuclide mass flux reaching the water table will depend on release rates and locations and will be simulated in the TSPA model. Species with a name starting with "Ic" (e.g., "Ic241") represent irreversible colloids traveling retarded; species with a name starting with "If" (e.g., "If241") represent irreversible colloids traveling unretarded.

Figure 7-1.   Base-Case Model Normalized Breakthrough Curve for 36 Radionuclide Species, Present-Day Mean Infiltration Scenario

The results of simulations based upon current conceptualizations suggest that colloids can play an important role in accelerating the transport of radionuclides in the unsaturated zone, especially the irreversible fast colloids. If the quantity of irreversible fast colloids is low, the impact on dose is not expected to be important. Matrix diffusion and matrix adsorption can play an important role in retarding the movement of dissolved radionuclides and could significantly impact dose predictions. The strength of fracture–matrix interaction due to matrix diffusion and adsorption depends on the matrix diffusion coefficient, matrix adsorption coefficient, fracture spacing, and fracture aperture. In TSPA-LA calculations, those parameters will be sampled based on uncertainty distributions, and the impact on system performance of these uncertainties will be quantified. Another important factor that controls the transport process is infiltration rate. The impact of climate changes on system performance will be investigated using different flow fields developed in *UZ Flow Models and Submodels* (BSC 2003b; DTN: LB0305TSPA18FF.001). These flow fields have different amounts of fracture and matrix flow, and water table elevation changes are also included. Based on the results presented here, under the wetter climate conditions, radionuclide transport velocities will increase during the wetter climates due to increased infiltration and greater fracture flow.

7.4   COMPARISON WITH THE T2R3D PROCESS MODEL

Full simulation of the three-dimensional unsaturated zone transport system has been performed as part of the validation of the abstraction model. The T2R3D process-model simulations use a finite-volume dual-permeability model formulation. In these comparisons, attention is restricted to a nonsorbing radionuclide, ^{99}Tc. For all model runs using either FEHM or T2R3D, breakthrough at the water table is simulated for a release function consisting of a pulse of radionuclide introduced uniformly across the repository. The comparisons between the models are for the cumulative, normalized arrival time distributions at the water table. Figure 7-2 shows the cumulative transport time distributions through the unsaturated zone for the two models and for the three flow fields (lower, mean, and upper) developed to capture uncertainty in the present-day infiltration rates. For the lower infiltration scenario, the early arrival of a small fraction of the released mass and the steepening breakthrough curve after 10,000 years are observed in both models. The plateau at values between 0.4 and 0.5 at long times is due to radioactive decay of ^{99}Tc. For the mean infiltration flow field, the agreement of the process and abstraction models is also excellent at all transport times. For the upper infiltration scenario, FEHM predicts a somewhat earlier arrival for the fastest moving solute, indicating a difference in the way the two models handle diffusion in rapid fracture flow. The benchmarking results indicate that the main features of the unsaturated zone transport process model are captured with the abstraction model.
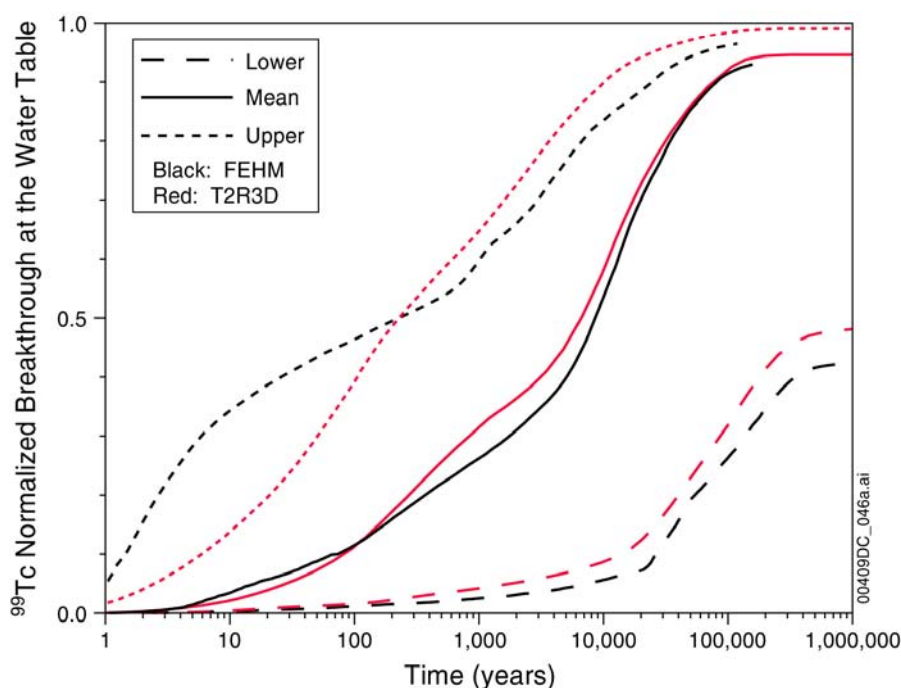
Source: BSC 2004, Figure 7-10.

Figure 7-2.   Comparison of Breakthrough Curves for ^{99}Tc for T2R3D and the Unsaturated Zone Transport Abstraction Model: Simulations for Different Present-Day Infiltration Rate Scenarios (Lower, Mean, and Upper)

For additional abstraction model validation simulations such as comparisons to discrete fracture models and comparisons to the process model on a two-dimensional cross section grid, see *Particle Tracking Model and Abstraction of Transport Processes* (BSC 2004).

INTENTIONALLY LEFT BLANK

8. SUMMARY AND CONCLUSIONS

This technical basis document describes radionuclide transport through the unsaturated zone of Yucca Mountain. It provides a description of the processes and of the underlying conceptual and numerical models, as well as a summary of laboratory and field data supporting the calibration and validation of these models. The numerical studies discussed in this technical basis document are not intended to provide estimates of radionuclide transport to the water table, but aim to (1) determine the main pathways of potential radionuclides transport to the water table; (2) identify the dominant processes affecting transport and retardation and the relative importance of the various hydrogeologic units to retardation; (3) evaluate the relative importance of processes and phenomena affecting transport; and (4) determine the relative transport behavior of general types of radioactive species (e.g., solutes versus colloids, nonsorbing versus sorbing). Additional, uncertainties in the model are discussed.

Numerous geologic, hydrologic, and climatic conditions and factors affect radioactive transport. Processes including advection, matrix diffusion, dispersion, and sorption impact the transport of both solute and colloidal species, while filtration and straining processes pertain specifically to colloid transport through the unsaturated zone. Radioactive-related properties, such as type and decay rates, chain species, and species-specific parameters for sorption and diffusion are also important.

The radionuclide transport model uses flow fields generated by the unsaturated zone flow model. Climatic conditions are key for estimating the net infiltration and deep percolation in the unsaturated zone, and ultimately in estimating groundwater flux. Under a wetter climatic regime, the increased precipitation leads to increased water percolation through the unsaturated zone and the repository, producing faster flow that limits radionuclide retardation by the unsaturated zone. Transport processes in emplacement drifts, as affected by the engineered barrier system, impact the release of radionuclides to the unsaturated zone. Transport through the unsaturated zone provides the source term for the prediction of transport through the saturated zone.

The diffusion of radioactive solutes and colloids into the rock matrix is the only significant retardation mechanism for nonsorbing solutes, such as ^{99}Tc. However, matrix diffusion is far less significant for colloids than for solutes because of the colloids' lower diffusion coefficient, pore-size exclusion limiting entry into the matrix, and enhanced advection through fractures. Mechanical dispersion is not expected to play a significant role in radionuclide transport in the system dominated by fracture flow. In addition, matrix diffusion spreads arrival times to a much greater degree than mechanical dispersion. The effects of lateral dispersion are minimized by the fact that the repository emplacement area is very broad relative to the distance to the water table.

The primary factors on sorption behavior in the unsaturated zone flow system include the nature of the rock's mineral surfaces (i.e., the difference between devitrified, zeolitic, and vitric tuffs), the water chemistry (i.e., the difference between perched and pore water), the specific sorption mechanisms for each radionuclide, the aqueous radionuclide concentrations and their speciation and redox state. Laboratory measurements of sorption have been carried out as a function of time, element concentration, atmospheric composition, particle size, and temperature. The approach for determining adsorption coefficients in the Yucca Mountain studies tends to

underestimate the K_d values, which produces a more conservative prediction of radionuclide mass and arrival times to the water table.

The heat released by radioactive decay affects transport because of the thermal effects on flow. The mountain-scale thermal- TH, THC, and THM process models evaluate thermal effects on unsaturated zone flow. The TH model shows that thermally enhanced flux zones extend 30 m and 100 m for the cases with and without ventilation, respectively, and predicts strong thermal effects in the faults. The THC model simulations indicate that mineral precipitation/dissolution will not significantly affect hydrologic properties and percolation flux through the unsaturated zone. THM-induced changes in large-scale hydrologic properties have no significant impact on the vertical percolation flux through the repository horizon.

Within the shadow zone, heat release will to some degree affect radionuclide transport properties (e.g., the diffusion coefficient and sorption parameters), and the near-field hydrology. The heat release will reduce water saturations beyond the ambient reduction due to flow diversion, and possibly dry out regions in the vicinity of the waste emplacement drifts. The lower water saturations reduce water velocities in the shadow zone and significantly lower diffusive fluxes across the fracture–matrix interfaces. These thermal effects are not considered in the transport model directly because of their uncertainty, and the absence of measured parameters as a function of these changes. However, the issue of temperature effects is indirectly addressed when varying the parameters of a temperature-sensitive process. Thus, potential thermal effects on diffusion or sorption are incorporated in the variation of D_0 and K_d. The sensitivity analysis covering a range of those parameters also incorporates the possible thermal effect.

Transport in the unsaturated zone of Yucca Mountain in the event of radionuclide releases from the repository will occur over spatial scales of thousands of meters and temporal scales of thousands of years. The transport tests that have been conducted involve length scales ranging from a few meters to a maximum of 30 m and time scales that do not exceed 2 years. For obvious reasons, although this would provide an indisputable basis for validation, it is not possible to conduct tests at a scale approaching the one of potential release at the repository. Despite their limited temporal and spatial scale, the field tests have (1) confirmed that the models account for the processes occurring during transport, (2) identified these processes and determined their relative importance, (3) quantified transport and provided estimates of relevant parameters, and (4) convincingly explained the field observations. Thus, these tests have been useful in validating the models at these scales and form the basis for extension to large-scale transport. The Busted Butte test series and the Alcove 8-Niche 3 test data were used for transport model calibration and to increase confidence in the model.

The Busted Butte test series was performed around a hydrogeologic contact between the TSw and the CHn units. A series of injections were carried out with a suite of nonsorbing, sorbing and colloidal tracers, however only selected data sets were usable for transport model calibration and confidence building. The Phase 1 tests were performed within the TSw, over a scale of several meters. The Phase 2 tests covered a larger test volume having a 10-m scale, which included the TSw-CHn contact. The three-dimensional transport model was calibrated with the fluoroscein data while the bromide data was used to increase confidence in Phase 1A. In the Phase 1B tests, bromide, lithium, and 2,6-DFBA provided data on fracture-matrix interactions in the TSw; the non-sorbing 2,6-DFBA and bromide (nonsorbing) data were used for calibration

and confidence building, respectively. In Phase 2C tests, bromide and lithium were used for calibration and confidence building, respectively.

The Alcove 8–Niche 3 tests measured seepage and tracer transport over 20- to 30-m scales in the vicinity of a near-vertical fault. Simulations were performed to evaluate the relative importance of matrix diffusion on radionuclide transport, using the calibrated flow field from the seepage data. Transport simulations for tracers having different molecular diffusion coefficients (bromide and PFBA) were performed. The effect of changing the fracture–matrix interface area was also considered. In order to match the tracer data, the interface area had to be increased by a factor of 45. This is probably related to the fracture geometry within the fault, compared to fracture networks upon which the model is based.

The model of radionuclide transport considers a large three-dimensional mountain-scale domain with steady-state flow fields. The fractured rock is conceptualized as a heterogeneous dual-permeability system, in which the distinct hydraulic and transport behavior of fractures and matrix is described by using separate properties and parameters. This conceptualization allows the description of the complex unsaturated zone flow field (the most important aspect of the transport study), in which fracture flow dominates.

The numerical process model used for estimating transport accounts for advection, molecular diffusion, hydrodynamic dispersion, sorption, radioactive decay and tracking of decay products, colloid filtration, and colloid-assisted solute transport. This approach captures all the known transport processes.

The following general conclusions are drawn from the numerical simulation of radionuclide transport:

- Three-dimensional site-scale simulations indicate that radionuclide transport from the bottom of the repository to the water table is both dominated and controlled by the faults when radionuclide releases occur simultaneously over the entire repository footprint. Faults provide fast pathways for downward migration to the water table but also limit lateral transport across the fault walls into the formation.

- The three-dimensional site-scale simulations for both an instantaneous and a continuous-release regime indicate that radioactive solutes from the repository move faster and reach the water table earlier and over a larger area in the northern part of the repository, compared to the southern part. This is consistent with the geologic model of the unsaturated zone, which is characterized by the presence of highly fractured zeolitic CHn layers in that area. The fractures in these layers are several orders of magnitude more conductive than the corresponding matrices. Thus, flow is fracture-dominated, resulting in the transport pattern observed in the simulation.

- The transport patterns follow the infiltration and percolation distributions. A review of the infiltration pattern at the surface, the percolation flux at the repository level, and the percolation flux at the groundwater level indicates that they correspond to the transport patterns discussed above. Thus, the water flow pattern dictates the advective transport pattern.

- For both an instantaneous and a continuous-release regime, the highly conductive Drill Hole Wash Fault and Pagany Wash Fault are the main pathways of transport in the northern part of the repository. Radionuclides released directly into these faults or reaching them from adjacent areas move rapidly downward to reach the water table at an earlier time. Additionally, the Sundance Fault, Solitario Fault, and Sever Wash Fault are transport-facilitating geologic features, but their effect does not become significant until later times.

- Diffusion from the fractures into the matrix is one of the main retardation processes in radionuclide transport. When radionuclides sorb onto the matrix into which they diffuse, their migration is further retarded. Sorption on the fracture surface increases the concentration gradient into the matrix, further enhancing diffusion into the matrix (BSC 2003e, Section 8.2.1).

- The simulation results presented here do not represent estimates of the anticipated performance of the unsaturated zone as a barrier or of its contribution to the overall performance of the repository system. The simulation results focus on evaluation of transport processes under a set of unrealistic assumptions intended to stress the system. A finite mass of the specific radionuclides selected for these analyses is assumed to be released uniformly (instantaneously or continuously) as solutes or colloids across the repository footprint, including the faults, into the unsaturated zone. The analyses do not consider processes that affect colloid stability, radionuclide solubility, or sorption of solutes and attachment of colloids to fracture walls. Vertical fractures are assumed to be open and continuous and horizontal fractures are assumed to be interconnected and connected to the vertical fractures.

- The importance of faults and perched-water bodies in transport is directly dependent on the underlying geologic and perched-water conceptual models (BSC 2003i, Section 6.20). It is reasonable to expect that changing geologic and perched-water models will lead to substantially different results, given the sensitivity of transport to these geologic features. This fact underscores the importance of representative conceptual models.

- Diversion of percolating water around a waste emplacement drift can reduce the amount of seepage into the drift, which will limit the eventual rate of movement of water into the unsaturated zone below the drift. As a consequence, a shadow zone may form below the drift with reduced saturation and flow rates. If flow is sufficiently reduced, matrix flow may dominate in the shadow zone. Simulation results indicate that where matrix flow dominates, transport times can be orders of magnitude longer than for fracture flow because of the lower flow rate and increased effectiveness of retardation processes.

- Under the approach taken in the three-dimensional site-scale studies, the unsaturated zone of Yucca Mountain appears to be an effective barrier to the transport of the strongly-sorbing radionuclides (^{90}Sr, ^{226}Ra, ^{229}Th, ^{241}Am, ^{221}Pa, and ^{239}Pu) to the water table. The weakly sorbing or nonsorbing species (^{135}Cs, ^{233}U, ^{235}U, ^{237}Np, and ^{99}Tc) arrive at the water table at times that are fractions of their respective half-lives.

- Diffusion into the rock matrix is the only retardation mechanism for nonsorbing solutes. Sorption and matrix diffusion are the main retardation processes in the transport of sorbing radionuclides. Under the conditions of this study, the effectiveness of the unsaturated zone of Yucca Mountain as a natural barrier decreases with a lower sorption affinity of the radioactive solutes and longer half-lives. In evaluating the barrier efficiency, the entire radioactive chain must be considered. Under the conditions of this study, the unsaturated zone of Yucca Mountain appears to be an effective natural barrier to the transport of small colloids. The barrier effectiveness decreases with increasing colloid size.

In summary, the extensive testing and modeling program undertaken to understand and characterize the transport pattern of radionuclides from the repository through the unsaturated zone provides a conservative basis for predicting radionuclide releases into the water table under ambient conditions at Yucca Mountain.

INTENTIONALLY LEFT BLANK

9. REFERENCES

9.1 DOCUMENTS CITED

Bird, R.B.; Stewart, W.E.; and Lightfoot, E.N. 1960. *Transport Phenomena*. New York, New York: John Wiley & Sons. TIC: 208957.

Bodvarsson, G.S.; Boyle, W.; Patterson, R.; and Williams, D. 1999. "Overview of Scientific Investigations at Yucca Mountain—The Potential Repository for High-Level Nuclear Waste." *Journal of Contaminant Hydrology, 38*, (1-3), 3-24. New York, New York: Elsevier. TIC: 244160.

BSC (Bechtel SAIC Company) 2001a. *Unsaturated Zone Flow Patterns and Analysis*. MDL-NBS-HS-000012 REV 00. Las Vegas, Nevada: Bechtel SAIC Company. ACC: MOL.20011029.0315.

BSC 2001b. Software Code: PHREEQC. V2.3. PC. 10068-2.3-00.

BSC 2001c. *Unsaturated Zone and Saturated Zone Transport Properties (U0100)*. ANL-NBS-HS-000019 REV 00 ICN 02. Las Vegas, Nevada: Bechtel SAIC Company. ACC: MOL.20020311.0017.

BSC 2001d. *Radionuclide Transport Models Under Ambient Conditions*. MDL-NBS-HS-000008 REV 00 ICN 01. Las Vegas, Nevada: Bechtel SAIC Company. ACC: MOL.20020409.0011.

BSC 2002. *Geologic Framework Model (GFM2000)*. MDL-NBS-GS-000002 REV 01. Las Vegas, Nevada: Bechtel SAIC Company. ACC: MOL.20020530.0078.

BSC 2003a. *CSNF Waste Form Degradation: Summary Abstraction*. ANL-EBS-MD-000015 REV 01. Las Vegas, Nevada: Bechtel SAIC Company. ACC: DOC.20030708.0004.

BSC 2003b. *UZ Flow Models and Submodels*. MDL-NBS-HS-000006 REV 01. Las Vegas, Nevada: Bechtel SAIC Company. ACC: DOC.20030818.0002.

BSC 2003c. *Development of Numerical Grids for UZ Flow and Transport Modeling*. ANL-NBS-HS-000015 REV 01. Las Vegas, Nevada: Bechtel SAIC Company. ACC: DOC.20030404.0005.

BSC 2003d. *Waste Form and In-Drift Colloids-Associated Radionuclide Concentrations: Abstraction and Summary*. MDL-EBS-PA-000004 REV 00. Las Vegas, Nevada: Bechtel SAIC Company. ACC: DOC.20030626.0006.

BSC 2003e. *Radionuclide Transport Models Under Ambient Conditions*. MDL-NBS-HS-000008 REV 01. Las Vegas, Nevada: Bechtel SAIC Company. ACC: DOC.20031201.0002.

BSC 2003f. *Calibrated Properties Model*. MDL-NBS-HS-000003 REV 01. Las Vegas, Nevada: Bechtel SAIC Company. ACC: DOC.20030219.0001.

BSC 2003g. *Analysis of Hydrologic Properties Data*. MDL-NBS-HS-000014 REV 00. Las Vegas, Nevada: Bechtel SAIC Company. ACC: DOC.20030404.0004.

BSC 2003h. *In Situ Field Testing of Processes*. ANL-NBS-HS-000005 REV 02. Las Vegas, Nevada: Bechtel SAIC Company. ACC: DOC.20031208.0001.

BSC 2003i. *Drift-Scale Radionuclide Transport*. MDL-NBS-HS-000016 REV 00. Las Vegas, Nevada: Bechtel SAIC Company. ACC: DOC.20030902.0009.

BSC 2003j. *SZ Flow and Transport Model Abstraction*. MDL-NBS-HS-000021 REV 00. Las Vegas, Nevada: Bechtel SAIC Company. ACC: DOC.20030818.0007.

BSC 2003k. *Drift-Scale Coupled Processes (DST and THC Seepage) Models*. MDL-NBS-HS-000001 REV 02. Las Vegas, Nevada: Bechtel SAIC Company. ACC: DOC.20030804.0004.

BSC 2003l. *Mountain-Scale Coupled Processes (TH/THC/THM)*. MDL-NBS-HS-000007 REV 01. Las Vegas, Nevada: Bechtel SAIC Company. ACC: DOC.20031216.0003.

BSC 2003m. *Drift-Scale Radionuclide Transport*. MDL-NBS-HS-000016 REV 00. Las Vegas, Nevada: Bechtel SAIC Company. ACC: DOC.20030902.0009.

BSC 2003n. *Abstraction of Drift-Scale Coupled Processes*. MDL-NBS-HS-000018 REV 00. Las Vegas, Nevada: Bechtel SAIC Company. ACC: DOC.20031223.0004.

BSC 2003o. *Mountain-Scale Coupled Processes (TH/THC/THM)*. MDL-NBS-HS-000007 REV 01. Las Vegas, Nevada: Bechtel SAIC Company. ACC: DOC.20031216.0003.

BSC 2003p. *Dissolved Concentration Limits of Radioactive Elements*. ANL-WIS-MD-000010 REV 02. Las Vegas, Nevada: Bechtel SAIC Company. ACC: DOC.20030624.0003.

BSC 2004. *Particle Tracking Model and Abstraction of Transport Processes*. MDL-NBS-HS-000020 REV 00. Las Vegas, Nevada: Bechtel SAIC Company. ACC: DOC.20040120.0001.

Cameron, D.R. and Klute, A. 1977. "Convective-Dispersive Solute Transport with a Combined Equilibrium and Kinetic Adsorption Model." *Water Resources Research, 13*, (1), 183-188. Washington, D.C.: American Geophysical Union. TIC: 246265.

Carey, J.W. and Bish, D.L. 1996. "Equilibrium in the Clinoptilolite-H_2O System." *American Mineralogist*, 81, 952-962. Washington, D.C.: Mineralogical Society of America. TIC: 233145.

Carey, J.W. and Bish, D.L. 1997. "Calorimetric Measurement of the Enthalpy of Hydration of Clinoptilolite." Clays and Clay Minerals, 45, (6), 826-833. Long Island City, New York: Pergamon Press. TIC: 235733.

CRWMS M&O (Civilian Radioactive Waste Management System Management and Operating Contractor) 2000. *Yucca Mountain Site Description.* TDR-CRW-GS-000001 REV 01 ICN 01. Las Vegas, Nevada: CRWMS M&O. ACC: MOL.20001003.0111.

Duffy, C.J. 1993a. *Kinetics of Silica-Phase Transitions*. LA-12564-MS. Los Alamos, New Mexico: Los Alamos National Laboratory. ACC: NNA.19900112.0346.

Duffy, C.J. 1993b. *Preliminary Conceptual Model for Mineral Evolution in Yucca Mountain.* LA-12708-MS. Los Alamos, New Mexico: Los Alamos National Laboratory. ACC: NNA.19900117.0152.

Fabryka-Martin, J.; Wolfsberg, A.V.; Dixon, P.R.; Levy, S.; Musgrave, J.; and Turin, H.J. 1996. *Summary Report of Chlorine-36 Studies: Sampling, Analysis and Simulation of Chlorine-36 in the Exploratory Studies Facility*. Milestone 3783M. Los Alamos, New Mexico: Los Alamos National Laboratory. ACC: MOL.19970103.0047.

Flint, L.E. 1998. *Characterization of Hydrogeologic Units Using Matrix Properties, Yucca Mountain, Nevada.* Water-Resources Investigations Report 97-4243. Denver, Colorado: U.S. Geological Survey. ACC: MOL.19980429.0512.

Flint, L.E. and Flint, A.L. 1995. *Shallow Infiltration Processes at Yucca Mountain, Nevada—Neutron Logging Data 1984-93.* Water-Resources Investigations Report 95-4035. Denver, Colorado: U.S. Geological Survey. ACC: MOL.19960924.0577.

Harvey, R.W. and Garabedian, S.P. 1991. "Use of Colloid Filtration Theory in Modeling Movement of Bacteria Through a Contaminated Sandy Aquifer." *Environmental Science & Technology, 25,* (1), 178-185. Washington, D.C.: American Chemical Society. TIC: 245733.

Herzig, J.P.; Leclerc, D.M.; and Le Goff, P. 1970. "Flow of Suspension Through Porous Media—Application to Deep Filtration." *Industrial & Engineering Chemistry, 62,* (5), 8-35. Washington, D.C.: American Chemical Society. TIC: 223585.

Hevesi, J.A.; Ambos, D.S.; and Flint, A.L. 1994. "A Preliminary Characterization of the Spatial Variability of Precipitation at Yucca Mountain, Nevada." *High Level Radioactive Waste Management, Proceedings of the Fifth Annual International Conference, Las Vegas, Nevada, May 22-26, 1994. 4,* 2520-2529. La Grange Park, Illinois: American Nuclear Society. TIC: 210984.

Ibaraki, M. and Sudicky, E.A. 1995. "Colloid-Facilitated Contaminant Transport in Discretely Fractured Porous Media 1. Numerical Formulation and Sensitivity Analysis." *Water Resources Research, 31*, (12), 2945-2960. Washington, D.C.: American Geophysical Union. TIC: 245719.

Kretzschmar, R.; Barmettler, K.; Grolimund, D.; Yan, Y.; Borkovec, M.; and Sticher, H. 1997. "Experimental Determination of Colloid Deposition Rates and Collision Efficiencies in Natural Porous Media." *Water Resources Research, 33*, (5), 1129-1137. Washington, D.C.: American Geophysical Union. TIC: 246817.

Kretzschmar, R.; Robarge, W.P.; and Amoozegar, A. 1995. "Influence of Natural Organic Matter on Colloid Transport Through Saprolite." *Water Resources Research, 31,* (3), 435-445. Washington, D.C.: American Geophysical Union. TIC: 246819.

LBNL (Lawrence Berkeley National Laboratory) 1999. *Software Code: TOUGH2.* V1.11 MEOS9nTV1.0. MAC, SUN, DEC/Alpha, PC. 10065-1.11MEOS9NTV1.0-00.

Lide, D.R., ed. 1993. *CRC Handbook of Chemistry and Physics*. 74th Edition. Boca Raton, Florida: CRC Press. TIC: 209252.

Liu, H.H.; Doughty, C.; and Bodvarsson, G.S. 1998. "An Active Fracture Model for Unsaturated Flow and Transport in Fractured Rocks." *Water Resources Research, 34*, (10), 2633-2646. Washington, D.C.: American Geophysical Union. TIC: 243012.

McGraw, M.A. and Kaplan, D.I. 1997. *Colloid Suspension Stability and Transport Through Unsaturated Porous Media*. PNNL-11565. Richland, Washington: Pacific Northwest National Laboratory. TIC: 246723.

Montazer, P. and Wilson, W.E. 1984. *Conceptual Hydrologic Model of Flow in the Unsaturated Zone, Yucca Mountain, Nevada.* Water-Resources Investigations Report 84-4345. Lakewood, Colorado: U.S. Geological Survey. ACC: NNA.19890327.0051.

Neretnieks, I. 2002. "A Stochastic Multi-Channel Model for Solute Transport—Analysis of Tracer Tests in Fractured Rock." *Journal of Contaminant Hydrology, 55*, (3-4), 175-211. New York, New York: Elsevier. TIC: 253977.

Pigford, T.H.; Chambré, P.L.; Albert, M.; Foglia, M.; Harada, M.; Iwamoto, F.; Kanki, T.; Leung, D.; Masuda, S.; Muraoka, S.; and Ting, D. 1980. *Migration of Radionuclides through Sorbing Media Analytical Solutions—II*. LBL-11616. Two volumes. Berkeley, California: Lawrence Berkeley National Laboratory. TIC: 211541.

Reimus, P.W.; Haga, M.J.; Adams, A.I.; Callahan, T.J.; Turin, H.J.; and Counce, D.A. 2003. "Testing and Parameterizing a Conceptual Solute Transport Model in Saturated Fractured Tuff Using Sorbing and Nonsorbing Tracers in Cross-Hole Tracer Tests." *Journal of Contaminant Hydrology, 62-63,* 613-636. New York, New York: Elsevier. TIC: 254205.

Robin, M.J.L.; Gillham, R.W.; and Oscarson, D.W. 1987. "Diffusion of Strontium and Chloride in Compacted Clay-Based Materials." *Soil Science Society of America Journal, 51*, (5), 1102-1108. Madison, Wisconsin: Soil Science Society of America. TIC: 246867.

Saltelli, A.; Avogadro, A.; and Bidoglio, G. 1984. "Americium Filtration in Glauconitic Sand Columns." *Nuclear Technology, 67*, (2), 245-254. La Grange Park, Illinois: American Nuclear Society. TIC: 223230.

Simmons, A.M. 2004. *Yucca Mountain Site Description.* TDR-CRW-GS-000001 REV 02. Two volumes. Las Vegas, Nevada: Bechtel SAIC Company. ACC: DOC.20040120.0004.

Triay, I.R.; Cotter, C.R.; Huddleston, M.H.; Leonard, D.E.; Weaver, S.C.; Chipera, S.J.; Bish, D.L.; Meijer, A.; and Canepa, J.A. 1996. *Batch Sorption Results for Neptunium Transport through Yucca Mountain Tuffs*. LA-12961-MS. Los Alamos, New Mexico: Los Alamos National Laboratory. ACC: MOL.19980924.0050.

Tseng, P.H. and Bussod, G.Y. 2001. "Evaluation of the Filter Paper Technique for In Situ Sampling of Solute Transport in Unsaturated Soils and Tuffs." *Water Resources Research, 37,* (7), 1913-1928. Washington, D.C.: American Geophysical Union. TIC: 255448.

USGS (U.S. Geological Survey) 2001. *Future Climate Analysis*. ANL-NBS-GS-000008 REV 00 ICN 01. Denver, Colorado: U.S. Geological Survey. ACC: MOL.20011107.0004.

USGS 2003. *Simulation of Net Infiltration for Modern and Potential Future Climates.* ANL-NBS-HS-000032 REV 00 ICN 02, with errata. Denver, Colorado: U.S. Geological Survey. ACC: MOL.20011119.0334; DOC.20031014.0004; DOC.20031015.0001.

van de Weerd, H. and Leijnse, A. 1997. "Assessment of the Effect of Kinetics on Colloid Facilitated Radionuclide Transport in Porous Media." *Journal of Contaminant Hydrology, 26*, 245-256. Amsterdam, The Netherlands: Elsevier. TIC: 245731.

Wan, J. and Tokunaga, T.K. 1997. "Film Straining on Colloids in Unsaturated Porous Media: Conceptual Model and Experimental Testing." *Environmental Science & Technology, 31*, (8), 2413-2420. Washington, D.C.: American Chemical Society. TIC: 234804.

Wang, J.S.Y.; Trautz, R.C.; Cook, P.J.; Finsterle, S.; James, A.L.; Birkholzer, J.; and Ahlers, C.F. 1998. *Testing and Modeling of Seepage into Drift, Input of Exploratory Study Facility Seepage Test Results to Unsaturated Zone Models.* Milestone SP33PLM4. Berkeley, California: Lawrence Livermore National Laboratory. ACC: MOL.19980508.0004.

9.2   DATA, LISTED BY DATA TRACKING NUMBER

GS000308311221.005. Net Infiltration Modeling Results for 3 Climate Scenarios for FY99. Submittal date: 03/01/2000.

GS020508312242.001. Trench Fault Infiltration in Alcove 8 Using Permeameters from March 5, 2001 to June 1, 2001. Submittal date: 05/22/2002.

LA0112WS831372.003. Busted Butte UZ Transport Test: Phase II Normalized Collection Pad Tracer Concentrations. Submittal date: 12/06/2001.

LA0201WS831372.007. Busted Butte UZ Transport Test: Phase II Normalized Collection Pad Metal Tracer Concentrations. Submittal date: 01/22/2002.

LA9910WS831372.008. Busted Butte UZ Transport Test: Gravimetric Moisture Content And Bromide Concentration In Selected Phase 1A Rock Samples. Submittal date: 11/03/1999.

LB0305TSPA18FF.001. Eighteen 3-D Site Scale UZ Flow Fields Converted from TOUGH2 to T2FEHM Format. Submittal date: 05/09/2003.

INTENTIONALLY LEFT BLANK

APPENDIX A

**DATA FROM THE BUSTED BUTTE TRACER TESTS AND BLOCK TESTS
(RESPONSE TO RT 1.02 AND 3.10 AND GEN 1.01 (COMMENT 27))**

Note Regarding the Status of Supporting Technical Information

This document was prepared using the most current information available at the time of its development. This Technical Basis Document and its appendices providing Key Technical Issue Agreement responses that were prepared using preliminary or draft information reflect the status of the Yucca Mountain Project's scientific and design bases at the time of submittal. In some cases this involved the use of draft Analysis and Model Reports (AMRs) and other draft references whose contents may change with time. Information that evolves through subsequent revisions of the AMRs and other references will be reflected in the License Application (LA) as the approved analyses of record at the time of LA submittal. Consequently, the Project will not routinely update either this Technical Basis Document or its Key Technical Issue Agreement appendices to reflect changes in the supporting references prior to submittal of the LA.

APPENDIX A

DATA FROM THE BUSTED BUTTE TRACER TESTS AND BLOCK TESTS
(RESPONSE TO RT 1.02 AND 3.10 AND GEN 1.01 (COMMENT 27))

This appendix provides a response for Key Technical Issue (KTI) agreements Radionuclide Transport (RT) 1.02 and 3.10 and General Agreement (GEN) 1.01, Comment 27. These agreements relate to providing data from tracer tests at Busted Butte and from Atomic Energy of Canada, Limited (AECL) test blocks from Busted Butte.

A.1   KEY TECHNICAL ISSUE AGREEMENTS

A.1.1   RT 1.02, RT 3.10, and GEN 1.01 (Comment 27)

Agreements RT 1.02 and 3.10 were reached during the U.S. Nuclear Regulatory Commission (NRC)/U.S. Department of Energy (DOE) Technical Exchange and Management Meeting on Radionuclide Transport on December 5 to 7, 2000 (Reamer and Williams 2000), in Berkeley, California. RT Subissue 1, Radionuclide Transport through Porous Rock, and Subissue 3, Radionuclide Transport through Fractured Rock, were discussed at that meeting. NRC concerns underlining these agreements include the desire to justify the inclusion of matrix diffusion and radionuclide sorption in the unsaturated zone transport model and to demonstrate that nonradioactive tracers used in field tests are appropriate homologs for radionuclides (NRC 2002, pp. 3.3.7-16 to 3.3.7-17, 3.3.7-20, and 3.3.7-22).

Agreement GEN 1.01 was reached during the NRC/DOE Technical Exchange and Management Meeting of Range on Thermal Operating Temperatures, held September 18 to 19, 2001 (Reamer and Gil 2001). The NRC provided additional comments at that meeting resulting in GEN 1.01 (Comment 27), which relates to RT 1.02. The section cited below as part of GEN 1.01 (Comment 27) comes from *FY 01 Supplemental Science and Performance Analyses, Volume 1: Scientific Bases and Analyses* (BSC 2001).

Wording of these agreements is as follows:

RT 1.02 and 3.10

> Provide analog radionuclide data from the tracer tests for Calico Hills at Busted Butte and from similar analog and radionuclide data (if available) from test blocks from Busted Butte. DOE will provide data from tracers used at Busted Butte and data from (AECL) test blocks from Busted Butte in an update to the AMR In Situ Field Testing of Processes in FY 2002.

GEN 1.01 (Comment 27)

> There appears to be conflicting evidence with regard to matrix flow and transport at Busted Butte and Pena Blanca.
>
> Although qualitative information is provided, the DOE does not clearly establish how information from anthropogenic and natural analogue sites (Pena Blanca,

Oklo, INEEL) are being used to verify/validate conceptual models, numerical models, and data/model uncertainty with regard to Performance Assessment. Uncertainty introduced by the lack of characterization of the larger repository footprint (southern extension) considered in the lower temperature operating mode is not characterized.

Basis: There appears to be conflicting evidence at Busted Butte and Pena Blanca (Section 11.3.2.7). Matrix flow and transport is reported to dominate tracer tests at Busted Butte. However, geochemical information appears to be limited at Pena Blanca. The differences between the two sites that might explain this difference are not explored, and the way that these results support the analysis of the effects of matrix block discretization on unsaturated zone transport is not discussed.

The effect of the uncertainty resulting from the lack of characterization for the proposed larger repository footprint, particularly the southern extension, is not addressed. Unit thickness and mineralogy in particular may have an effect on transport through the unsaturated zone.

These comments fall under Agreement RT.1.02: Provide analog radionuclide data from the tracer tests for Calico Hills at Busted Butte and from similar analog and radionuclide data (if available) from test blocks from Busted Butte. DOE will provide data from tracers used at Busted Butte and data from (AECL) test blocks from Busted Butte in an update to the AMR In Situ Field Testing of Processes in FY 2002.

DOE Initial Response to GEN 1.01 (Comment 27)

Transport at Busted Butte is dominated by matrix flow because the nonwelded vitric Calico Hills formation is basically a porous medium system, whereas the Pena Blanca site is a welded fractured system. Therefore, it would not be surprising that the two systems have different transport characteristics.

In addition, data collected from natural analogue studies, with the exception of INEEL, have been used so far only for qualitative comparison to the unsaturated zone model results. Limited numerical modeling was performed using the INEEL data. Analog test data from tracer tests at Busted Butte and data from (AECL) test blocks from Busted Butte will be provided in an update to the AMR In Situ Field Testing of Processes before License Application, per KTI agreement RT 1.02.

Flow in the CHn vitric is represented with the same dual-permeability flow and transport models used for other units. Existing project documentation concerning the Busted Butte field tests indicate that flow and transport in this unit is almost entirely in the matrix. This model can be easily calibrated to results that include more fracture transport if results from Busted Butte or other relevant information should indicate that a greater degree of transport occurs in the fractures.

This appendix is the initial DOE response to agreements RT 1.02 and 3.10. The DOE provided an initial response to GEN 1.01 (Comment 27) at the Technical Exchange and Management Meeting of Range on Thermal Operating Temperatures (Reamer and Gil 2001).

A.1.2 Related Key Technical Issue Agreements

KTI agreement RT 1.01 is related to RT 1.02 in that the responses to both agreements are based on data collected from testing the Calico Hills Formation. While RT 1.02 concerns radionuclide transport through unsaturated and saturated porous rock, RT 1.01 mostly deals with unsaturated zone flow and is, therefore, addressed in *Technical Basis Document No. 2: Unsaturated Zone Flow*.

A.2 RELEVANCE TO REPOSITORY PERFORMANCE

The unsaturated and saturated zones are important natural barriers to radionuclide transport at Yucca Mountain. The data in these agreements relate to the unsaturated zone and saturated zone transport models. These models predict the amount and rate of radionuclide arrival at the water table and in the biosphere, and, hence, they predict the performance of these unsaturated zone and saturated zone natural barriers, respectively. Specifically, data from the Busted Butte tracer tests and the associated block tests by AECL are used in the validation of the unsaturated zone transport model.

A.3 RESPONSE

The following NRC concerns related to RT 1.02 and 3.10 and GEN 1.01 (Comment 27) are addressed in this appendix:

1. Provide justification for the inclusion of matrix diffusion (the diffusion of solutes from flowing water in fractures into stagnant or nearly stagnant water in the matrix, which can result in significant transport attenuation) in the unsaturated zone transport model.

2. Provide justification for the inclusion of sorption in the unsaturated zone transport model.

3. Demonstrate that nonradioactive tracers used in field tests are appropriate homologs for sorbing radionuclides.

4. Discuss how conflicting observations from Busted Butte and Peña Blanca are both consistent with and supportive of unsaturated zone flow and transport models.

This appendix presents relevant tracer transport data from field testing at Busted Butte and from laboratory testing of large blocks (ranging in size from approximately $0.3 \times 0.3 \times 0.3$ m to approximately $1 \times 1 \times 1$ m) extracted from Busted Butte to support the discussions related to the four topics above. The first two concerns were originally directed primarily at Alcove 8–Niche 3 testing, but the Busted Butte and AECL large-block test results help address these concerns, so applicable data from these tests are discussed in this appendix. Comprehensive presentations of the transport data from these experiments are provided in *In Situ Field Testing of Processes* (BSC 2003a) for the Busted Butte field testing and by Vandergraaf et al. (2004) for the

large-block testing. The use of the Busted Butte data to perform a corroborative validation of the unsaturated zone radionuclide transport model is discussed in detail in *Radionuclide Transport Models Under Ambient Conditions* (BSC 2003b).

The effects of repository heat loading on flow and transport in the unsaturated zone were not addressed in the Busted Butte field tests and large-block tests; these effects can be addressed only by detailed numerical modeling at scales much larger than these tests or by long-term experiments such as the thermal block testing in the Exploratory Studies Facility (ESF). Although they have been used in a qualitative corroborative manner, data from natural analog sites have not been suitable for quantitative verification and validation of unsaturated zone flow and transport models. This is because these sites have uncertain initial and boundary conditions (i.e., spatially distributed source terms that require dissolution and other processes to initiate transport, unknown variability of infiltration, and flow), and also they do not include conservative (i.e., nonsorbing) species that are needed to quantify flow (BSC 2002). The sorbing nature of the species at natural analog sites also prevents the data from being used to support quantitative analyses of the effects of matrix block discretization on unsaturated zone transport, as matrix transport is significantly retarded by sorption. The Busted Butte and large-block tests were intended to characterize the transport properties of certain units present below the repository, not to determine the thickness and mineralogy of these units at various locations.

Matrix diffusion is inferred from Busted Butte field transport tests on the basis of the following:

- Matrix flow appeared to dominate over fracture flow in the Busted Butte system. Although this result does not provide direct evidence of matrix diffusion, it indicates a sufficient degree of matrix porosity interconnectedness so that a significant amount of matrix diffusion would occur if conditions were conducive to fracture-dominated flow.

- The fact that flow in the Busted Butte system was not dominated by the existing fractures exposed in the test bed indicates that, at least in this system, the matrix must become sufficiently wetted before water will flow very far in fractures. A wetted matrix implies that matrix diffusion will occur when fractures have sufficient water to flow. This implication can be extended to other unsaturated tuff units possessing similar properties if the matrix has a finite, connected porosity and is not hydraulically isolated from fractures by nonporous secondary mineralization.

Sorption was directly observed in Busted Butte field tests and in large block tests by comparing the transport of sorbing tracers with nonsorbing tracers under unsaturated flow conditions. Specifically:

- Lithium ion was weakly retarded in the Busted Butte field tests relative to Br$^-$ and fluorinated benzoates, which are nonsorbing anions.

- Nickel and cobalt, serving as actinide analogs, were highly retarded in the Busted Butte field tests relative to nonsorbing tracers.

- Neptunium was weakly retarded in large block tests relative to nonsorbing tracers (^{3}HHO, fluorescein, and ^{99}Tc as pertechnetate ion).

- Cesium and cobalt were highly retarded in large block tests relative to ^{3}HHO.

Direct evidence of matrix diffusion and sorption within the repository horizon were obtained in a preliminary tracer test from Alcove 8 in the Enhanced Characterization of the Repository Block Cross-Drift to Niche 3 (also referred to as Niche 3107) in the ESF (BSC 2003a). In this test, water flow and solute transport were investigated in a fault zone extending from the Topopah Spring welded tuff unit (Tplpul) in Alcove 8 to the middle nonlithophysal zone (Tptpmn) in Niche 3. Matrix diffusion was indicated by an earlier arrival and higher peak concentration of pentafluorobenzoate relative to Br$^-$ in two collection trays in Niche 3. Sorption was indicated by much attenuated arrivals and concentrations of lithium ion relative to the nonsorbing tracers in these trays (BSC 2003a, Figure 6.12.2-8).

The ability of nonradioactive tracers used in the Busted Butte field transport test to serve as surrogates for radionuclides was addressed by a combination of laboratory batch sorption experiments conducted at Los Alamos National Laboratory (LANL) to compare the sorption behavior of surrogates and radionuclides (Turin et al. 2002) and large block radionuclide transport experiments, including a small number of supporting batch sorption experiments, conducted by AECL at Whiteshell Laboratories in Pinawa, Manitoba (Vandergraaf et al. 2004). The test results are summarized as follows:

- The LANL tests indicated that lithium ion (Li$^+$) and rhodamine WT have similar partition coefficients (K_d values, in milliliters per gram) to neptunium(V) in the vitric tuffs at Busted Butte when using a synthetic Busted Butte pore water. They also indicated that cobalt (injected as Co^{2+}) has similar K_d values to plutonium(V), and nickel (injected as Ni^{2+}) has similar K_d values to americium(III) in tuffs containing significant amounts of clay and iron–manganese oxides. However, in a tuff that contained very little clay and iron–manganese oxides (tptpv1), manganese (injected as Mn^{2+}) had a K_d value that was in better agreement with plutonium(V) than cobalt, and cobalt had a K_d value that was in better agreement with americium(III) than nickel. The sorbing tracers and radionuclides generally do not have the same valence states, chemical speciation, or sorption mechanisms, so the suitability of the tracers as surrogates should not be extrapolated beyond the geochemical and mineralogical conditions at Busted Butte without further analysis. However, as a first approximation, the geochemical and mineralogical conditions at Busted Butte should be quite similar to conditions that exist in the same stratigraphic units beneath the repository horizon.

- Although no direct comparisons were made between surrogates and radionuclides in the AECL large-block tests, these tests confirmed that cobalt is strongly retarded and neptunium is weakly retarded in Busted Butte tuffs under both saturated and unsaturated flow conditions (DTN: LA0108TV12213U.001). Furthermore, supporting batch sorption testing yielded K_d values for cobalt and neptunium that were consistent with the LANL batch experiments. The K_d value deduced for neptunium in one of the block experiments (the only one in which neptunium was recovered) was in good agreement with the batch K_d values for neptunium.

The nonradioactive tracer surrogates identified above that had K_d values similar to those of plutonium, neptunium, or americium for the Busted Butte tuffs and pore waters served as

surrogates for these actinides with respect to retardation behavior in the Busted Butte field transport experiments.

The differences in transport behavior observed at Busted Butte and Peña Blanca should not be considered conflicting given the differences in hydrogeology and transport conditions at the two sites. As the preliminary DOE response to GEN 1.01 (Comment 27) indicates, the Busted Butte system consists of highly porous, nonwelded tuffs with low fracture density and the Peña Blanca system consists of welded tuffs with higher fracture density and lower matrix porosity. Thus, it is not surprising that while matrix flow is dominant at Busted Butte, fracture flow appears to dominate under unsaturated conditions at Peña Blanca. Peña Blanca is probably a better analog for the Topopah Spring welded unit (TSw) in the repository horizon than the nonwelded tuffs at Busted Butte, which are below the repository horizon at Yucca Mountain.

In addition to the hydrogeologic differences between Busted Butte and Peña Blanca, transport conditions at Peña Blanca have included significantly different initial and boundary conditions. There has not been an opportunity at Peña Blanca to directly compare nonsorbing and sorbing solute transport behavior to constrain transport interpretations. It is possible that transport at Peña Blanca may appear to be fracture-dominated primarily because the uranium decay series elements tend to adsorb strongly to fracture surfaces, including both mineral coatings and exposed matrix, which would tend to keep them from being found in the matrix. It is also possible that uranium decay series transport at Peña Blanca appears to be fracture-dominated because of colloid-facilitated transport, which would tend to confine transport to fractures because of the tendency for colloids to be filtered in the matrix.

In summary, both the Busted Butte and Peña Blanca observations are consistent with the unsaturated zone flow and transport models given the hydrogeologic differences between the sites, the greater uncertainty associated with transport interpretations at Peña Blanca, and the fact that the Peña Blanca observations may be biased toward apparent fracture flow.

The information in this report is responsive to agreements RT 1.02, RT 3.10, and GEN 1.01 (Comment 27) made between the DOE and NRC. The report contains the information that DOE considers necessary for NRC review for closure of these agreements.

A.4 BASIS FOR THE RESPONSE

This section is addresses each of the four NRC concerns identified at the beginning of Section A.3.

A.4.1 Justification for the Inclusion of Matrix Diffusion in the Unsaturated Zone Transport Model

The Busted Butte tracer test results provide indirect justification for the inclusion of matrix diffusion in the unsaturated zone transport model. The justification is considered indirect because matrix diffusion was not directly observed at Busted Butte; rather, matrix diffusion is inferred as a viable process that would have occurred under appropriate hydrogeologic conditions. Conditions conducive to matrix diffusion did not exist in the Busted Butte tests because of the nonwelded, unfractured nature of the rock, which resulted in matrix-dominated flow rather than fracture-dominated flow. The matrix-dominated flow gave rise to

single-porosity transport behavior rather than the dual-porosity transport behavior generally associated with matrix diffusion.

However, the fact that there was significant matrix flow at Busted Butte (even at equivalent infiltration rates as high as 1 m/yr, which is more than a factor of 4 greater than the highest rates estimated for Yucca Mountain (Flint et al. 1996), indicates that there was a high degree of matrix porosity interconnectedness, which, in turn, suggests that solute diffusion should readily occur through the matrix under the right circumstances. Solute matrix diffusion coefficients are known to be positively correlated with matrix permeabilities in the saturated volcanic tuffs near Yucca Mountain (BSC 2003c), so it follows that matrix diffusion should occur in unsaturated tuffs with relatively high permeabilities. Matrix diffusion coefficients in saturated tuffs are better correlated with matrix permeability than matrix porosity, presumably because both permeability and diffusion depend on the interconnectedness of the porosity, rather than the porosity itself. Tseng et al. (2003) reported unsaturated matrix permeabilities ranging from 10^{-18} to 10^{-13} m^2 at saturations (expressed as a fraction of full saturation) ranging from 0.25 to 1.0 for the three tuff lithologies present at Busted Butte (DTN: LA0012WS831372.002). Figure A-1 shows how matrix diffusion coefficients are correlated with matrix permeabilities for saturated tuffs from the C-Wells near Yucca Mountain over a permeability range that spans all but the upper end (10^{-14} to 10^{-13} m^2) of the range of unsaturated permeabilities for tuffs at Busted Butte (which were actually either saturated or very close to saturated).

The evidence for matrix-dominated flow at Busted Butte included:

- Fluorescein plumes during Phase 1 of testing (visualized by ultraviolet light illumination), were very broad and did not closely follow fractures or other structural features (BSC 2003a, Figure 6.13.2-2). This result suggests that matrix flow was dominant and that fracture flow was relatively insignificant in the unsaturated tuff system. Although it is also likely that water flow occurred in fractures, the capillary forces in the unsaturated matrix were sufficient to draw the water out of the fractures before it could advance very far beyond the wetting front in the matrix. The result was that water could not physically advance through fractures until the surrounding matrix became sufficiently wetted so that the matrix capillary forces decreased to the point where they were matched by gravitational forces in the fractures.

- In Phase 2 of testing, it took about 120 days for conservative tracers to be detected about 1.3 m beneath injection points in the Topopah Spring Tuff (tptpv2) when they were injected at a rate of about 50 mL/hr at each of 27 injection points. During this time, about 3.9 m^3 of solution were injected. Assuming a cross-sectional area of infiltration of 5 m $\times$ 8 m (40 m^2), the total volume of infiltrated rock was about 40 m $\times$ 1.3 m (52 m^3). Thus, the apparent flow porosity during Phase 2 testing was about 0.075 (or about 3.9/52), which is much greater than the fracture-flow porosity that would be deduced from the number and volume of fractures visible in the Topopah Spring Tuff (which was almost nil). The only way that the flow porosity could exceed the fracture porosity by this much would be if there were a significant amount of matrix flow and water imbibition into the matrix as water advanced through fractures.

- The analyses of tracers in mined-back cores from Busted Butte confirmed the broad distribution of conservative tracers throughout the unsaturated matrix, implying significant water flow through the matrix.

- The large-block tracer tests conducted at AECL also showed evidence of matrix-dominated flow and transport under unsaturated conditions.

00409DC_083.ai
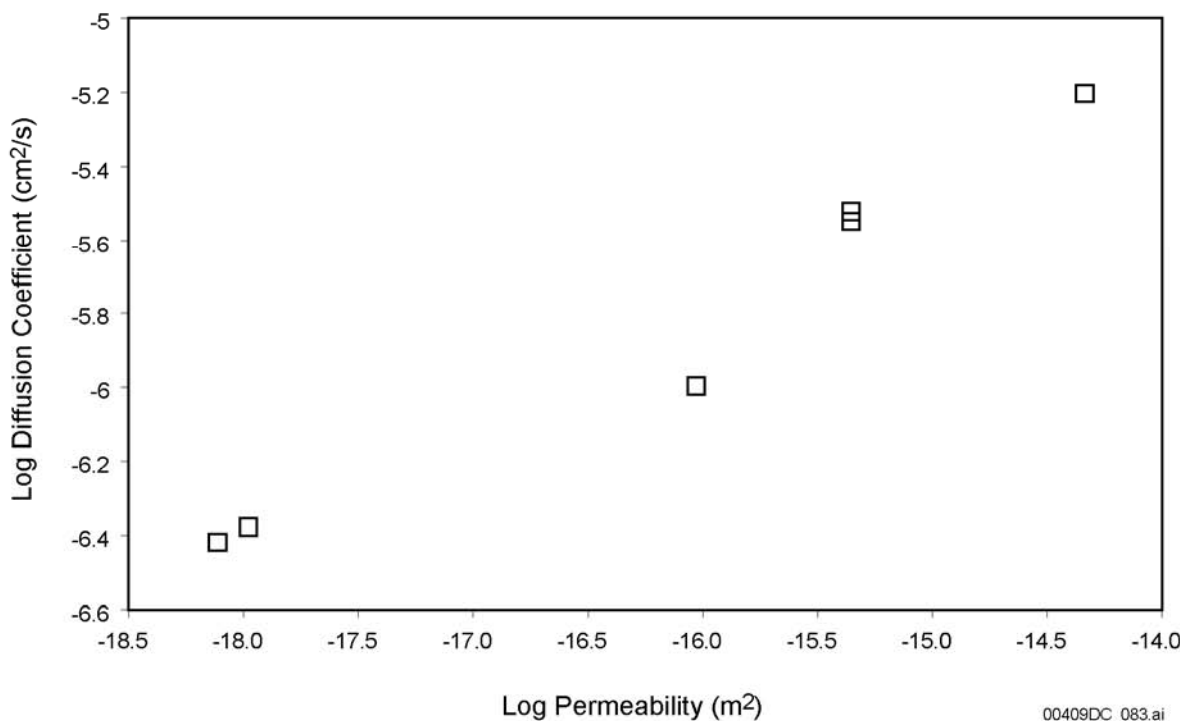
Source: Permeability data: DTN: MO0012PERMCHOL.000. Diffusion coefficients: DTN: LA0303PR831362.001.

NOTE: The permeability range spans all but the upper end of the range of unsaturated permeabilities at Busted Butte.

Figure A-1.   Log Diffusion Coefficients for Br^- as a Function of Log Permeability in Saturated Tuffs from the C-Wells

Attempts were made to obtain direct evidence of matrix diffusion at Busted Butte by pairing conservative tracers with different diffusion coefficients (Br^- and fluorinated benzoates) in injection solutions and looking for differences in their breakthrough curves that were consistent with matrix diffusion. Matrix diffusion would normally be indicated by a lower and later peak concentration and longer tail of the tracer with the larger diffusion coefficient (Br^- in this case). Unfortunately, the tracer test results were inconclusive with regard to direct observation of matrix diffusion because all of the fluorinated benzoate concentrations peaked and then declined even though they were continuously injected (which should have resulted in a monotonic increase in concentration over the course of the tests). In contrast, the Br^- concentrations tended to increase monotonically until they reached a plateau (with some minor exceptions related to injection rate fluctuations). Part of the difference in Br^- and fluorinated benzoate breakthrough curves might be attributable to the fact that Br^- was injected into all the injection boreholes, while the fluorinated benzoates were individually injected into different boreholes.

However, the differences in injection locations cannot explain why the fluorinated benzoate concentrations would peak and then decline. The consistent decline in the concentrations of all fluorinated benzoates as the tests progressed, regardless of their injection location, suggests that a common process occurring throughout the system, possibly microbial activity, caused the fluorinated benzoates to degrade over time. Although there is no direct evidence of such degradation, the fact that the fluorinated benzoates declined in concentration over time made it impossible to compare their responses with Br^- (or I^-) to make inferences about matrix diffusion.

The relative responses of Br^- and pentafluorobenzoate in the Alcove 8–Niche 3 tracer test in the ESF are consistent with matrix diffusion (i.e., a higher and earlier peak concentration of pentafluorobenzoate relative to Br^-) (BSC 2003a, Figure 6.12.2-8). These results appeared to be unaffected by degradation of the pentafluorobenzoate, possibly because the responses occurred more quickly than at Busted Butte and also because the tracers were injected as finite pulses rather than as continuous injections, so a decline in concentration was expected and would have tended to mask any degradation effects. The only mechanism other than matrix diffusion that could have resulted in the relative responses of Br^- and pentafluorobenzoate in the Alcove 8–Niche 3 tracer test is preferential sorption of the Br^-. However, this process seems very unlikely, given that Br^- is a simple anion that should be less likely than fluorinated benzoates to sorb to rock surfaces or any other surfaces that may have been present in the Alcove 8–Niche 3 flow system.

A.4.2 Justification for the Inclusion of Sorption in the Unsaturated Zone Transport Model

Both the Busted Butte field tracer tests and the large-block tests at AECL showed clear evidence of sorption of tracers that were expected to sorb. At Busted Butte, lithium ion was clearly retarded relative to Br^- in all boreholes in which the two tracers were recovered (see Figure A-2). These two tracers were injected simultaneously in all injection boreholes. Furthermore, analyses of mined-back cores at Busted Butte indicated that both nickel and cobalt migrated only very short distances from injection boreholes compared to other tracers that were injected with them (see Figure A-3).

In the large-block tests at AECL, neptunium(V) was clearly retarded relative to nonsorbing tracers under both saturated and unsaturated conditions (Vandergraaf et al. 2004). Also, ^{137}Cs and ^{60}Co moved only very short distances from injection points under both saturated and unsaturated conditions (Vandergraaf et al. 2004).

The only other possible explanation for the retarded transport of these tracers is precipitation as a result of solubility limits being exceeded. However, this explanation can be ruled out for lithium and ^{137}Cs, both of which are extremely soluble (as monovalent cations) in aqueous solutions. Neptunium, nickel, and cobalt have lower solubilities, but the results of batch sorption tests and geochemical calculations (Section A.4.3) indicate that their solubilities should not have been exceeded in the tracer experiments. Thus, it can be concluded that these tracers were retarded by sorption, and it follows that sorption is a viable retardation mechanism that should be included in the unsaturated zone transport model.
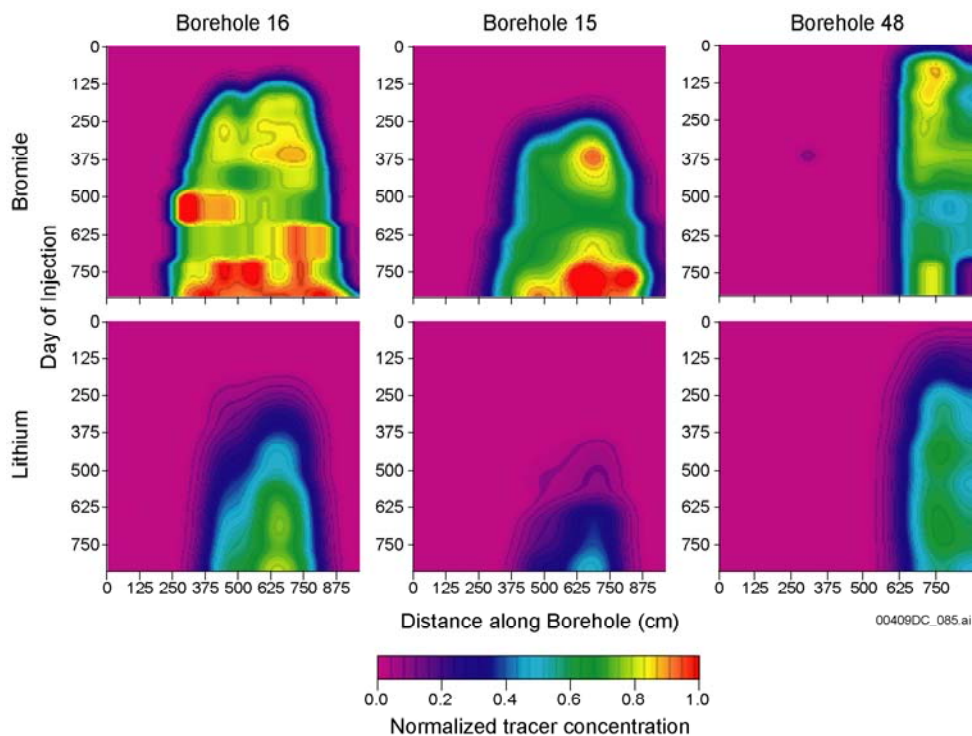
Source: BSC 2003a, Figure 6.13.3-7.

Figure A-2. Responses of Br⁻ (Nonsorbing Tracer) and Lithium (Sorbing Tracer) in Three Observation Boreholes at Busted Butte
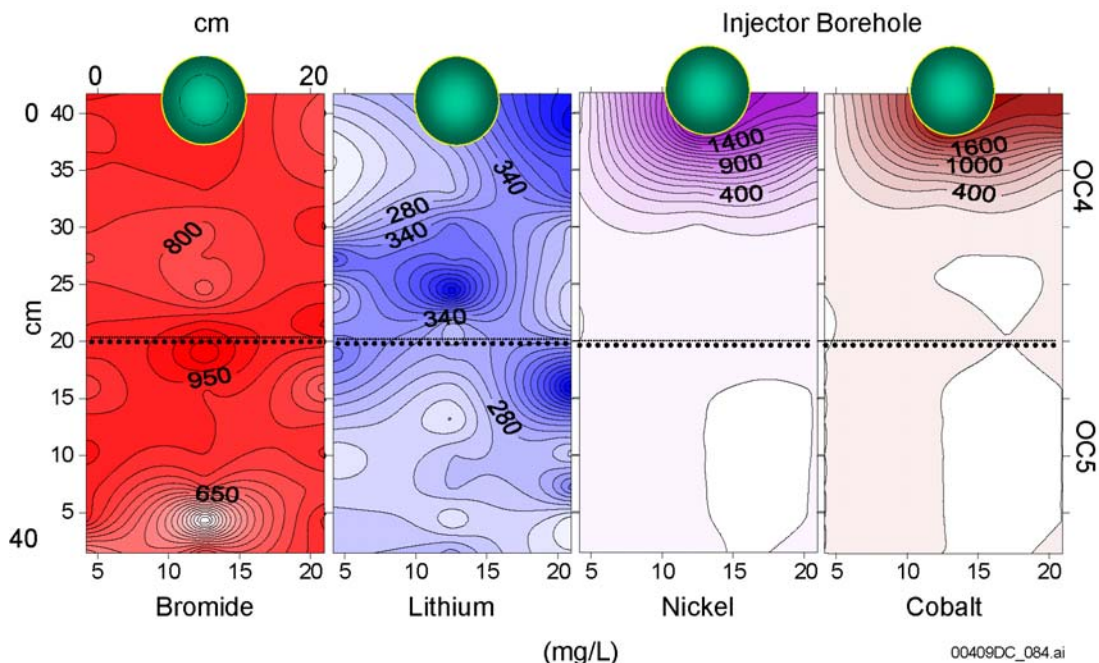
Source: DTNs: LA0211WS831372.001; LA0211WS831372.002.

NOTE: OC4 and OC5 refer to overcores 4 and 5.

Figure A-3. Concentration Profiles of Bromide, Lithium, Nickel, and Cobalt Measured in Overcored Rock Samples from Busted Butte

A.4.3 Nonradioactive Tracers as Appropriate Homologs for Sorbing Radionuclides

The selection of nonradioactive tracers as homologs (or analogs) for sorbing radionuclides was based primarily on the similarity of sorption partition coefficients of the homologs and radionuclides onto Busted Butte tuff. The testing conducted to establish these similarities included batch sorption tests at LANL (Turin et al. 2002) and confirmatory large-block transport tests at AECL (Vandergraaf et al. 2004). The results of these tests are summarized in Section A.3.

Table A-1 lists the K_d values obtained for the surrogates and radionuclides in the LANL batch sorption experiments. For each Busted Butte lithology, there is at least one nonradioactive surrogate with K_d values that are in reasonably good agreement with each radionuclide. Thus, the nonradioactive surrogates should have served as appropriate homologs for the target radionuclides in the Busted Butte tracer tests, at least with respect to retardation behavior. As a first approximation, the geochemical conditions at Busted Butte should be similar to those that exist in the same stratigraphic units beneath the repository horizon. Furthermore, the qualitative agreement between the surrogate retardation factors deduced from laboratory batch sorption tests and from the Busted Butte field tracer tests supports the validity of using laboratory sorption data to predict field-scale transport behavior of sorbing radionuclides in the unsaturated zone.

Table A-1. K_d Values for Radionuclides and Nonradioactive Surrogates in the Three Tuff Lithologies at Busted Butte

Species (surrogate)	K_d Values (mL/g)		
	Tptpv2	Tptpv1	Tac
Neptunium	1.1	0.3	1.4
Lithium (for neptunium)	0.88	0.35	1.3
Rhodamine WT (for neptunium)	1.7	0.39	1.1
Plutonium	960	18	2500
Americium	460	360	460
Cobalt (for plutonium in Tptpv2 and Tac and for americium in Tptpv1)	910	120	1600
Nickel (for americium in Tptpv2 and Tac)	430	48	670
Manganese (for plutonium in Tptpv1)	86	15	98

Source: Turin et al. 2002.

NOTE: K_d values are averaged over the concentration ranges investigated. Ranges of K_d values that account for nonlinearity of sorption isotherms are provided by Turin et al. (2002).

Although Table A-1 indicates that the nonradioactive surrogates used at Busted Butte should serve as reasonable homologs for radionuclides in the Busted Butte rock–water system, (and, by inference, the same stratigraphic units beneath the repository horizon), these tracers should not necessarily be considered suitable as surrogates in all other geochemical and mineralogical systems. For example, the similarity in surrogate and radionuclide sorption behavior should not be extrapolated to reducing (oxygen deficient) environments where plutonium, neptunium, and, to a lesser degree, americium exist in lower oxidation states. Even under oxidizing conditions, the radionuclide–surrogate pairs have significant differences in their solution speciation and, very likely, their sorption mechanisms.

The predominant solution species for each of the surrogates and radionuclides mentioned above in Busted Butte pore water at a pH of 8 and in equilibrium with atmospheric oxygen and CO_2 levels (with the exception of rhodamine WT) are listed in Table A-2 (calculated by the PHREEQC geochemical code STN: 10068-2.3-00). It is apparent that the species associated with each surrogate–radionuclide pair are significantly different, and it would not be surprising if their sorption behavior under different geochemical conditions or in contact with mineral surfaces other than those present in the Busted Butte experiments was significantly different than that reflected in Table A-1. In many cases, the surrogates and radionuclides have significantly different complexation behavior with carbonate and sulfate ions in solution (the primary complexing anions in unsaturated zone pore waters), which could significantly change their sorption behavior at different pH or CO_2 partial pressures than what was experimentally investigated.

Table A-2. Dominant Radionuclide and Surrogate Species in Busted Butte Pore Water at pH 8 in Equilibrium with Atmospheric Oxygen and Carbon Dioxide

Species (Surrogate)	Concentration (mol/kg)	Most Dominant Species (%)	Second Most Dominant Species (%)
Neptunium	1×10^{-6}	NpO_2^+ (79.5)	$NpO_2(OH)$ (10.5)
Lithium (for neptunium)	0.1	Li^+ (~100)	—
Plutonium	1×10^{-7}	$Pu(VI)(CO_3)_2^{2-}$ (59)	$Pu(V)O_2^+$ (38.5)
Americium	1×10^{-8}	$Am(CO_3)^+$ (50)	$Am(OH)^{2+}$ (29)
Cobalt (for plutonium in Tptpv2 and Tac and for americium in Tptpv1)	4.2×10^{-5}	$HCoO_2^-$ (~100)	—
Nickel (for americium in Tptpv2 and Tac)	4.3×10^{-5}	Ni^{2+} (97)	$NiSO_4$ (2.5)
Manganese (for plutonium in Tptpv1)	4.6×10^{-5}	Mn^{2+} (88)	$MnCO_3$ (7)

NOTE: Speciation is based on PHREEQC calculations. Molalities match those used in batch sorption experiments at LANL and in the Busted Butte field experiments (for nonradioactive surrogates). Speciation was not calculated for lithium because lithium is known to be essentially 100% Li^+ (confirmed to be the case for Na^+ and K^+ in the speciation calculations).

In addition to the differences in solution speciation, some of the surrogate–radionuclide pairs are known to have different sorption mechanisms. Li^+ is a cation-exchanging tracer that exchanges with Na^+ and Ca^{2+} on tuff surfaces and rhodamine WT is a large organic molecule that probably interacts by surface complexation of one or more of its functional groups with tuff surfaces. In contrast, the interaction of neptunium(V) with tuff surfaces is thought to be primarily by surface complexation (Triay et al. 1997). Cobalt(II), nickel(II), manganese(II), plutonium(V), and americium(III) all probably adsorb to tuff surfaces primarily by surface complexation reactions, but the different valences of these elements undoubtedly result in significant differences in the nature and stability of the surface species formed. Also, plutonium(V) sorption is known to involve redox reactions (primarily reduction to plutonium(IV)), whereas the metal ion surrogates (Co^{2+}, Ni^{2+}, and Mn^{2+}) all have relatively stable valence states (although Mn^{2+} may oxidize to Mn^{4+} on surfaces).

In summary, the nonradioactive surrogates should have served as appropriate homologs for the target radionuclides in the Busted Butte tracer tests, at least with regard to overall retardation

behavior (based on similarity of K_d values) and without regard to sorption mechanisms. Based on current knowledge, the Busted Butte geochemical system should be quite similar to the geochemical system in the same stratigraphic units beneath the repository horizon. However, care should be taken in extrapolating the similarity in behavior of the surrogates and radionuclides to systems with different geochemistry and mineral surfaces.

A.4.4 Support to Unsaturated Zone Flow and Transport Models Provided by Busted Butte and Peña Blanca Observations

The transport observations at Busted Butte and Peña Blanca (BSC 2002) both offer support to unsaturated zone flow and transport models. The observations at the two sites occurred under significantly different conditions that resulted in different flow and transport regimes. Flow at Busted Butte was predominantly through a nonwelded, unfractured, high-porosity matrix, whereas flow at Peña Blanca was through a fracture network in a lower-porosity, welded matrix. Thus, the observations at the two locations should not be considered conflicting, but rather they should be viewed as data sets that can be used to test and validate the unsaturated zone flow and transport models under different conditions that will exist in different geologic units within Yucca Mountain. The unsaturated zone flow model would predict that fracture flow should be more easily initiated and should extend over greater distances at Peña Blanca than at Busted Butte because of the higher fracture density and greater interconnectedness of fractures at Peña Blanca as well as the much lower capacity for the welded tuff matrix at Peña Blanca to draw water out of fractures by capillary action. Correspondingly, the unsaturated zone flow model would predict that fracture flow would be very difficult to sustain in the high-porosity, high-permeability, unwelded tuff matrix at Busted Butte.

In addition to the hydrogeologic differences between Busted Butte and Peña Blanca, transport conditions at Peña Blanca have included much longer time periods, uncontrolled boundary conditions, a solid source term that requires dissolution or colloid mobilization prior to transport, a more spatially distributed source term, a lack of nonsorbing tracers with which to compare uranium decay-series transport, greater transport distances, and a lower degree of site characterization compared to Busted Butte. It is conceivable that uranium decay series transport at Peña Blanca appears to be fracture dominated because of colloid-facilitated transport, which would tend to confine transport to fractures because of the tendency for colloids to be filtered in the matrix. It is also possible that transport at Peña Blanca may appear to be fracture dominated primarily because the uranium decay series elements tend to adsorb rather strongly to fracture surfaces, including both mineral coatings and exposed matrix. Thus, even if matrix flow is occurring, it may not be apparent because of the sorbing nature of the species being analyzed and the fact that surface area to water volume ratios are much higher in the matrix than in fractures, resulting in much greater retardation in the matrix. Matrix flow versus fracture flow should ideally be assessed using conservative species, which do not exist in the uranium decay series.

Both the Busted Butte and Peña Blanca observations are consistent with the unsaturated zone flow and transport models given the hydrogeologic differences between the sites, the less constrained interpretations possible for the Peña Blanca observations (which result in greater uncertainty), and the fact that the Peña Blanca observations may be biased toward apparent fracture flow.

A.5   REFERENCES

A.5.1   Documents Cited

BSC (Bechtel SAIC Company) 2001. *FY 01 Supplemental Science and Performance Analyses, Volume 1: Scientific Bases and Analyses.* TDR-MGR-MD-000007 REV 00 ICN 01. Las Vegas, Nevada: Bechtel SAIC Company. ACC: MOL.20010801.0404; MOL.20010712.0062; MOL.20010815.0001.

BSC 2002. *Natural Analogue Synthesis Report.* TDR-NBS-GS-000027 REV 0 ICN 02. Las Vegas, Nevada: Bechtel SAIC Company. ACC: MOL.20020520.0288.

BSC 2003a. *In Situ Field Testing of Processes.* ANL-NBS-HS-000005 REV 02. Las Vegas, Nevada: Bechtel SAIC Company. ACC: DOC.20031208.0001.

BSC 2003b. *Radionuclide Transport Models Under Ambient Conditions.* MDL-NBS-HS-000008 REV 01. Las Vegas, Nevada: Bechtel SAIC Company. ACC: DOC.20031201.0002.

BSC 2003c. *Saturated Zone In-Situ Testing.* ANL-NBS-HS-000039 REV 00. Las Vegas, Nevada: Bechtel SAIC Company. ACC: DOC.20040128.0003.

Flint, A.L.; Hevesi, J.A.; and Flint, L.E. 1996. *Conceptual and Numerical Model of Infiltration for the Yucca Mountain Area, Nevada.* Milestone 3GUI623M. Denver, Colorado: U.S. Geological Survey. ACC: MOL.19970409.0087.

NRC (U.S. Nuclear Regulatory Commission) 2002. *Integrated Issue Resolution Status Report.* NUREG-1762. Washington, D.C.: U.S. Nuclear Regulatory Commission, Office of Nuclear Material Safety and Safeguards. TIC: 253064.

Reamer, C.W. and Gil, A.V. 2001. Summary Highlights of NRC/DOE Technical Exchange and Management Meeting of Range on Thermal Operating Temperatures, September 18-19, 2001. Washington, D.C.: U.S. Nuclear Regulatory Commission. ACC: MOL.20020107.0162.

Reamer, C.W. and Williams, D.R. 2000. Summary Highlights of NRC/DOE Technical Exchange and Management Meeting on Radionuclide Transport. Meeting held December 5-7, 2000, Berkeley, California. Washington, D.C.: U.S. Nuclear Regulatory Commission. ACC: MOL.20010117.0063.

Triay, I.R.; Meijer, A.; Conca, J.L.; Kung, K.S.; Rundberg, R.S.; Strietelmeier, B.A.; and Tait, C.D. 1997. *Summary and Synthesis Report on Radionuclide Retardation for the Yucca Mountain Site Characterization Project.* Eckhardt, R.C., ed. LA-13262-MS. Los Alamos, New Mexico: Los Alamos National Laboratory. ACC: MOL.19971210.0177.

Tseng, P.-H.; Soll, W.E.; Gable, C.W.; Turin, H.J.; and Bussod, G.Y. 2003. "Modeling Unsaturated Flow and Transport Processes at the Busted Butte Field Test Site, Nevada." *Journal of Contaminant Hydrology*, *62–63,* 303–318. TIC: 254205.

Turin, H.J.; Groffman, A.R.; Wolfsberg, L.E.; Roach, J.L.; and Strietelmeier, B.A. 2002. "Tracer and Radionuclide Sorption to Vitric Tuffs of Busted Butte, Nevada." *Applied Geochemistry, 17,* (6), 825-836. TIC: 254046.

Vandergraaf, T.T.; Drew, D.J.; Ticknor, K.V.; and Hamon, C.J. 2004. *Busted Butte Final Report on Laboratory Radionuclide Migration Experiments in Non-Welded Tuff Under Unsaturated and Saturated Conditions*. AECL-12180. Revision 1. Pinawa, Manitoba, Canada: AECL Technologies. ACC: MOL.20040318.0481.

A.5.2   Data, Listed by Data Tracking Number

LA0012WS831372.002. Hydrogeologic Properties of Busted Butte Units Derived from USGS Laboratory Measurements. Submittal date: 01/02/2001.

LA0108TV12213U.001. Static Batch Sorption Coefficients and Retardation Coefficients. Submittal date: 08/14/2001.

LA0211WS831372.001. Busted Butte Rock Extractions: Measured and Normalized Metal Tracer Concentrations. Submittal date: 11/19/2002.

LA0211WS831372.002. Busted Butte Rock Extractions: Measured and Normalized Metal Tracer Concentrations. Submittal date: 11/19/2002.

LA0303PR831362.001. Model Interpretations of C-Wells Diffusion Cell Experiments. Submittal date: 04/02/2003.

MO0012PERMCHOL.000. Permeability Data (Using Filtered J-13 Water) from UE-25 C #1, UE-25 C #2, and UE-25 C #3. Submittal date: 12/05/2000.

A.5.3   Software Codes

PHREEQC, V2.3 (STN: 10068-2.3-00).

INTENTIONALLY LEFT BLANK

APPENDIX B

**UNSATURATED ZONE TRANSPORT BELOW THE REPOSITORY
(RESPONSE TO RT 3.01 AND 3.04)**

Note Regarding the Status of Supporting Technical Information

This document was prepared using the most current information available at the time of its development. This Technical Basis Document and its appendices providing Key Technical Issue Agreement responses that were prepared using preliminary or draft information reflect the status of the Yucca Mountain Project's scientific and design bases at the time of submittal. In some cases this involved the use of draft Analysis and Model Reports (AMRs) and other draft references whose contents may change with time. Information that evolves through subsequent revisions of the AMRs and other references will be reflected in the License Application (LA) as the approved analyses of record at the time of LA submittal. Consequently, the Project will not routinely update either this Technical Basis Document or its Key Technical Issue Agreement appendices to reflect changes in the supporting references prior to submittal of the LA.

APPENDIX B

UNSATURATED ZONE TRANSPORT BELOW THE REPOSITORY
(RESPONSE TO RT 3.01 AND 3.04)

This appendix provides a response for Key Technical Issue (KTI) agreements Radionuclide Transport (RT) 3.01 and 3.04. These agreements relate to providing the technical basis for transport through hydrogeologic units, including fault zones, of the unsaturated zone below the repository.

B.1 KEY TECHNICAL ISSUE AGREEMENTS

B.1.1 RT 3.01 and 3.04

Agreements RT 3.01 and 3.04 were reached during the U.S. Nuclear Regulatory Commission (NRC)/U.S. Department of Energy (DOE) Technical Exchange and Management Meeting on Radionuclide Transport held December 5 to 7, 2000 (Reamer and Williams 2001), in Berkeley, California. RT Subissue 3, Radionuclide Transport through Fractured Rock, was discussed at that meeting.

Concerning RT 3.01, the NRC indicated (NRC 2002, pp. 3.3.7 to 3.3.14) that although faults can provide fast pathways for radionuclide transport in the unsaturated zone and the flow and transport characteristics of fault zone pathways can vary widely from those elsewhere in the tuff aquifer, the DOE transport parameters for site recommendation were assigned only by rock type and do not include any specific consideration of faults unless they were treated explicitly as zones of fracture flow. The NRC was concerned that the DOE might not have adequately accounted for the possible effects of these differences in formulating transport parameter distributions in *Unsaturated Zone and Saturated Zone Transport Properties (U0100)* (CRWMS M&O 2000) and in *Uncertainty Distributions for Stochastic Parameters* (BSC 2001). Another related concern was the technical basis for the sorption coefficient (K_d) probability distributions (NRC 2002, pp. 3.3.7-14 to 3.3.7-20).

With regard to RT 3.04, the NRC (2002, pp. 3.3.7-14 to 3.3.7-20) recognized that the DOE used stochastic approaches to identify and constrain data uncertainty in its model abstraction on radionuclide transport in the unsaturated zone for site recommendation and that, to that end, sensitivity analyses and bounding calculations are an important means of providing a risk-informed, performance-based context for DOE data uncertainty and evaluating the need for additional data. The NRC requested that the DOE provide technical support demonstrating appropriate handling of data uncertainty.

Wording of these agreements is as follows:

RT 3.01

> For transport through fault zones below the repository, provide the technical basis for parameters/distributions (consider obtaining additional information, for example, the sampling of wells WT-1 and WT-2), or show the parameters are not important to performance. The DOE will provide a technical basis for the

importance to performance of transport through fault zones below the repository. This information will be provided in an update to the AMR Radionuclide Transport Models Under Ambient Conditions available to the NRC in FY 2002. If such transport is found to be important to performance, DOE will provide the technical basis for the parameters/distributions used in FY 2002. DOE will consider obtaining additional information.

RT 3.04

Provide sensitivity studies for the relative importance of the hydrogeological units beneath the repository for transport of radionuclides important to performance. DOE will provide a sensitivity study to fully evaluate the relative importance of the different units below the repository that could be used to prioritize data collection, testing, and analysis. This study will be documented in an update to the AMR Radionuclide Transport Models Under Ambient Conditions available to the NRC in FY 2002.

B.1.2   Related Key Technical Issue Agreements

None.

B.2   RELEVANCE TO REPOSITORY PERFORMANCE

The unsaturated zone is an important natural barrier affecting the performance of the repository system. The technical basis sought in these agreements is related to the unsaturated zone transport model, which determines the amount and rate of radionuclide arrival at the water table that, in turn, has a direct impact on the performance of this barrier at Yucca Mountain.

B.3   RESPONSE

This response has two parts providing: (1) technical bases for the transport parameters and their distributions for fault zones and the performance of transport through fault zones below the repository (RT 3.01), and (2) sensitivity studies showing the relative importance of the hydrogeologic units beneath the repository for transport of radionuclides (RT 3.04).

Calibration of hydraulic properties has been documented in *Calibrated Properties Model* (BSC 2003a). Flow field simulation results have been documented in *UZ Flow Models and Submodels* (BSC 2003b). Mountain-scale transport simulations, including sensitivity analysis and derivation of K_ds, have been documented in *Radionuclide Transport Models Under Ambient Conditions* (BSC 2003c).

Arguments regarding transport parameters and performance through fault zones below the repository (RT 3.01) include:

- Fault zones were modeled explicitly using the dual-permeability method. Hydraulic properties for the fractures in the fault zone were separately calibrated to account for differences in fracture properties (e.g., fracture spacing, aperture size, and fracture length) as compared to fractures in the rest of hydrogeologic units. However, due to the

limited availability of data for fractures in the fault zone, fractures were simplified into four major rock units. Flow and transport parameters for the matrix of fault zones are identical to those in respective layers in nonfault zones because the matrix material is assumed to be similar in terms of hydraulic properties and sorptive strength (Sections B.4.1.1 and B.4.1.2).

- K_ds were derived from laboratory experiments for three major rock types found in the flow path from the repository to the water table. These coefficients were used for the entire model domain, including the matrix in the fault zones (Section B.4.1.2).

- It was assumed that fractures do not retard transport by sorption, so zero K_d was assigned to all the fractures. This conservative assumption was applied identically to the fault zones and the rest of the model domain (Section B.4.1.2).

- Distributions of radionuclide concentration at the bottom of the repository and at the top of the water table were clearly in agreement with the distributions of infiltration and percolation. These results indicate that faults are dominant conduits for advective radionuclide transport to the water table (Sections B.4.1.3 and B.4.1.4).

- Simulations to evaluate the direct release of radionuclides to the fault were performed. Eliminating radionuclide sources from the vicinity of the faults has a small effect on transport and arrivals at the water table. The interconnected fracture system leads to radionuclide transport to and emergence at the water table through fractures in the fault zone even though radionuclides are not directly released into the faults at the repository (Section B.4.1.5).

- Transport of radionuclides released from the matrix at the repository, instead of releases from fractures, was simulated. Radionuclide transport times are significantly longer when the radionuclides are initially released from repository matrix blocks instead of fractures (Section B.4.1.6).

- Sensitivity analyses of transport parameters (K_ds and diffusion coefficients (D_0s)) were performed for three major radionuclides. D_0 and K_d had a significant impact on breakthrough predictions, resulting in faster arrival times for lower D_0 and K_d values (Section B.4.1.6 and B.4.1.7).

Arguments regarding the importance of the hydrogeologic units beneath the repository for transport (RT 3.04) include:

- Distributions of radionuclides at the base of the Topopah Spring welded unit (TSw) and at the water table have been analyzed to evaluate the impact of geologic conditions (e.g., rock type (zeolitic or vitric), fracture spacing, and permeability) beneath the repository horizon on the pattern of transport. The geologic conditions significantly affect radionuclide transport beneath the repository horizon (Section B.4.2.1).

- Sensitivity analyses to evaluate the effect of the main hydrogeologic units (i.e., TSw, Calico Hills zeolitic unit (CHz), and Calico Hills vitric unit (CHv)) on transport and

retardation of two representative sorbing radionuclides, ^{237}Np and ^{239}Pu, were performed by setting the corresponding K_ds to zero in all the layers of each unit. The sensitivity analyses are sufficient to examine the importance of the main hydrogeologic units beneath the repository for the radionuclide transport. (Sections B.4.2.2 and B.4.2.3.)

- Sensitivity analyses indicate that TSw is by far the most important unit for transport and retardation of sorbing radionuclides. By eliminating sorption in all TSw layers, radionuclides arrive at the water table significantly earlier. The overall effect of no sorption in the CHz and CHv units is insignificant compared to that of the TSw unit (Sections B.4.2.2 and B.4.2.3).

The information in this report is responsive to agreements RT 3.01 and RT 3.04 made between the DOE and NRC. The report contains the information that DOE considers necessary for NRC review for closure of these agreements.

B.4 BASIS FOR THE RESPONSE

B.4.1 Performance of Transport through Fault Zones (RT 3.01)

This section describes the technical bases for conceptual model and parameter determinations for fault zones employed in three-dimensional unsaturated zone flow and transport simulations and the effects of fault zones on flow and transport. This section also provides sensitivity analyses results for different radionuclide release scenarios and transport parameters, including sorption coefficients and diffusion coefficients.

Fault zones in the unsaturated zone model were conceptualized based on the dual-permeability approach, as was also done for the rest of the model domain. The matrix material in fault zones was assumed identical to that found in unfaulted portions of a particular layer of rock characteristic of the rest of the model domain so that the hydrologic properties for the matrix in the fault zones were considered the same as those of corresponding matrix material. Parameter estimation for the fractures relied on the limited data available from borehole measurements and, in consequence, the estimation required approximations and assumptions in the fault zone conceptual model and may result in significant uncertainties in the calibrated properties. However, the approach employed to capture the flow and transport through fault zones in the three-dimensional unsaturated zone flow and transport modeling leads to reasonably conservative estimates of radionuclide travel times to the water table. Even though no separate exercises were performed to validate the calibrated properties for fault zones, the calibrated hydrologic properties for the entire domain are validated by matching observed data, including saturation data, in situ capillary pressure data, and dynamic pneumatic-pressure data. These simplifications and calibration processes will be provided in detail in the following subsections.

B.4.1.1 Estimation of Hydraulic Properties for Faults

Hydraulic properties of faults were estimated by model calibration using the three-dimensional unsaturated zone model grid (BSC 2003a). In the model grid, faults are represented by vertical or inclined 30-m-wide zones based on the dual-permeability concept (BSC 2003d, Section 6.6.1). The faults are separated into four layers: (Tiva Canyon welded unit (TCw), Paintbrush

nonwelded unit (PTn), TSw, and Calico Hills nonwelded unit (CHn)). Hydraulic fracture properties for the fault zones have been calibrated, while matrix properties within fault zones are the same as those of the nonfault zone of the corresponding layer (BSC 2003a, Section 6.3.4). The matrix in the fault zones is assumed to have similar hydraulic properties since it consists of the same geologic material. However, the fractures in the fault zone are expected to have different hydraulic properties, mainly due to different fracture spacing, aperture size, and fracture length.

Fault parameter calibration was accomplished using data from borehole USW UZ-7a, which are the most comprehensive with respect to faults (BSC 2003a, Section 6.3.4). Since saturation, water potential, and pneumatic pressure data are available within the Ghost Dance fault zone from the surface to the upper layers of the TSw, they were inverted to obtain the calibrated fracture properties. The calibrated fracture permeabilities in the fault zone are generally higher than the permeabilities in nonfault zones. A detailed description of the uncertainty is available in *Calibrated Properties Model* (BSC 2003a, Section 6.4).

B.4.1.2 Estimation of Fault Transport Parameters

For transport simulations, properties to be incorporated in addition to hydraulic properties include K_ds, molecular D_0s, and radioactive decay constants. The diffusion coefficients of radionuclides, or analogs, were obtained from the *CRC Handbook of Chemistry and Physics* (Lide 1992), which summarizes the values measured in free water. Therefore, the D_0s and decay constants are unique for radionuclides, independent of rock properties. The K_ds and their probable ranges used in the unsaturated zone transport simulations are obtained from laboratory experiments in which crushed rock samples from the Yucca Mountain site are contacted with groundwater (or simulated groundwater) representative of the site. There are three dominant rock types in the unsaturated zone along potential flow paths from the repository to the saturated zone: devitrified tuff, zeolitic tuff, and vitric tuff. K_ds for the three rock types have been derived from the sorption–desorption experiments performed in conjunction with surface complexation modeling (BSC 2003c, Attachment I). Zeolitic tuff generally is more sorptive than vitric tuff but has a relatively small matrix flow component because of its low matrix permeability. Consequently, all the flow is focused into the fractures, leading to fast transport. Sorption in the zeolitic tuff, thus, may not be able to effectively retard solute transport because fracture–matrix interaction is low.

K_ds have been assigned to the matrix but have been neglected for the fault and nonfault zones. Neglecting sorption in the fractures is based on the assumption that all fractures are open (i.e., they are not even partially filled with a porous medium). Fracture surfaces, often lined with minerals that differ from the bulk of the rock matrix, may be capable of sorbing many of the radionuclides that may be released from the repository (Triay et al. 1997, p. 160). However, characterization of the fracture-lining mineral distributions and sorptive interactions with these minerals has been limited. Also, fracture minerals have a relatively small volume and surface area. For these reasons, an assumption in modeling radionuclide transport is that no sorptive interaction with fracture surfaces occurs and that sorptive interactions are only possible in matrix blocks (BSC 2003c, Section 6.2.3).

B.4.1.3   Effect of Faults on Flow Field

Water entering the unsaturated zone as net infiltration is the major control on overall hydrologic and thermal-hydrologic conditions within the unsaturated zone at Yucca Mountain. Net infiltration is the ultimate source of percolation through the unsaturated zone. Water percolating downward through the unsaturated zone will be the principal means by which radionuclides may be transported from the repository to the water table.

A plan view of the spatial distribution in the mean infiltration map for the present-day mean infiltration scenario, as interpolated onto the TSPA-LA grid, is shown in Figure B-1. Like other climate scenarios, the figure shows higher infiltration rates in the northern part of the model domain and along the mountain ridge east of the Solitario Canyon fault.

The percolation flux is defined as total vertical liquid mass flux through both fractures and matrix and is converted to millimeters per year using a constant water density. Figure B-2 shows an example of percolation fluxes at the repository level for the present-day mean infiltration scenario with the base-case flow fields. Comparisons of the calculated repository percolation fluxes of Figure B-2 with those of the surface infiltration map (Figure B-1) indicate that percolation fluxes at the repository are very different from surface infiltration patterns. Surface infiltration rates and distributions are independent of faults. The differences in percolation flux at the repository level (Figure B-2) is that: (1) flow occurs mainly through faults in the northernmost part of the model domain (with the north coordinate greater than 237,000 m); (2) flow is diverted into or near faults; and (3) a substantial amount of large-scale lateral flow within the PTn impacts the percolation flux distribution in the repository layer.

Table B-1 lists percentages of fracture–matrix flow components and fault flow at the repository horizon and the water table within the model domain (BSC 2003b, Section 6.6.3). Fracture and matrix percentages total 100% while fault flow percentages represent total vertical flux through fault blocks. These statistics are calculated from vertical flow along each grid column using nine base-case scenarios (three climates with upper, mean, and lower infiltration). These statistics indicate that fracture flow is dominant both at the repository horizon and at the water table. At the repository level, fracture flow contributes more than 90% to 95% of the total percolation fluxes. Fracture flow at the water table takes 70% to 80% of the total flow. On the other hand, fault flow percentage increases from about 30% to 40% at the repository to about 60% to 70% at the water table (BSC 2003b, Section 6.6.3). These data indicate that the contribution from the faults to the seepage into the repository is significant and, as the water flows down, the contribution increases and the majority of flow occurs through a few faults at the level of the water table.
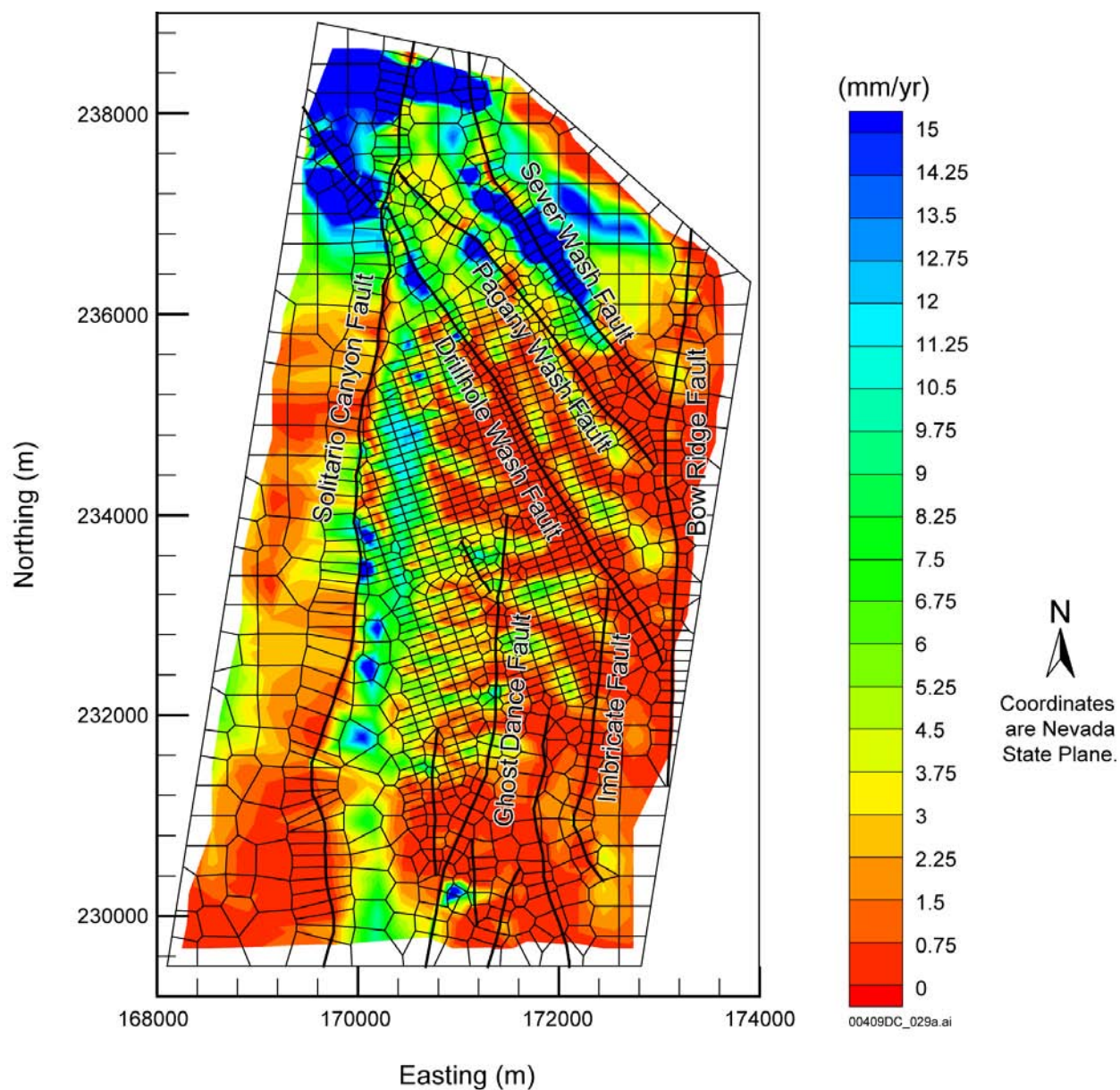
Source: BSC 2003b, Figure 6.1-2.

Figure B-1.   Plan View of Net Infiltration Distributed over the Three-Dimensional Unsaturated Zone TSPA-LA Model Grid for the Present-Day (Base-Case) Mean Infiltration Scenario
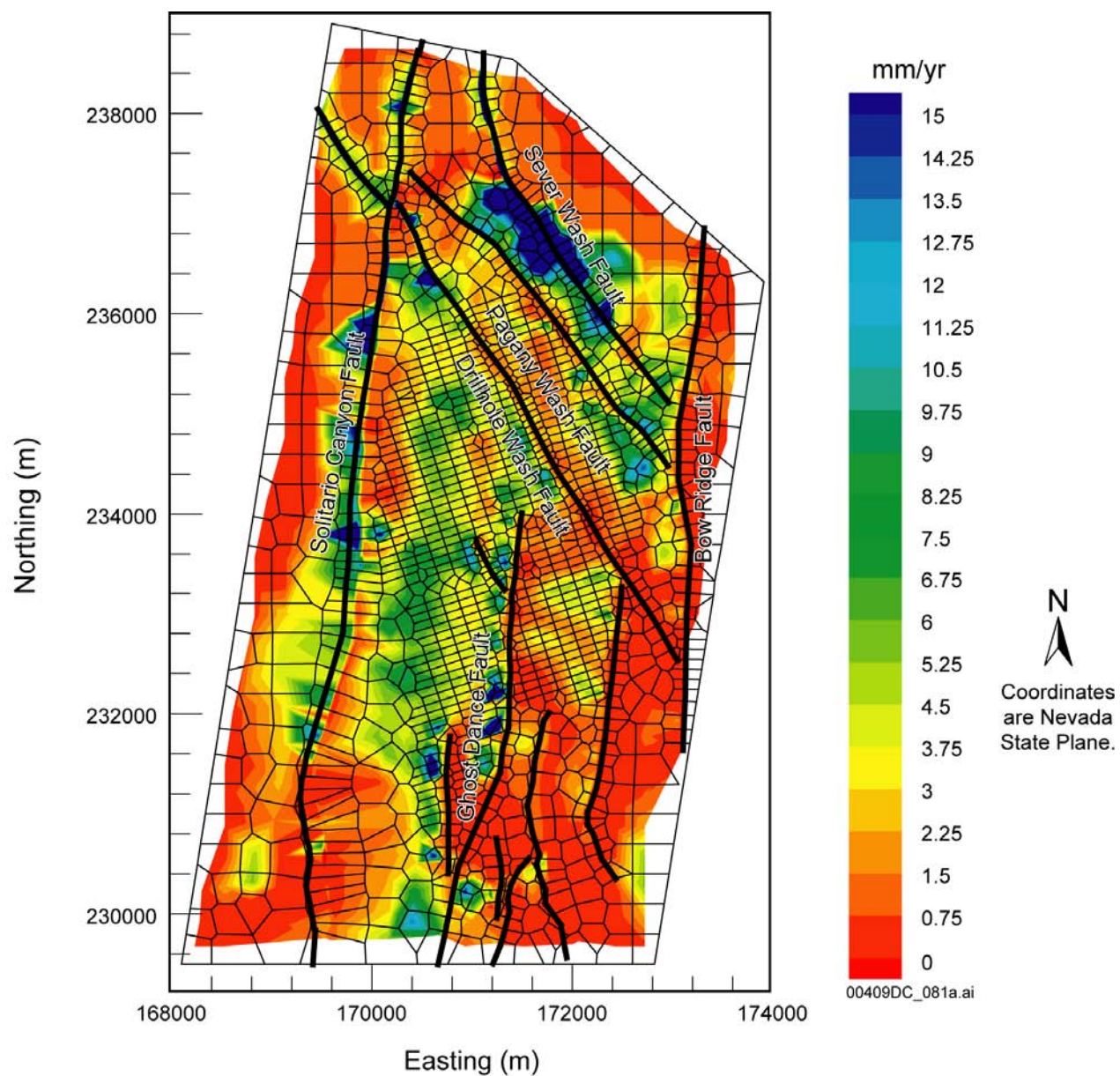
Source: BSC 2003b, Figure 6.6-1.

Figure B-2.   Simulated Percolation Fluxes at the Repository Horizon under the Present-Day Mean Infiltration Scenario

Table B-1. Comparison of Water Flux through Matrix, Fractures, and Faults as a Percentage of the Total Flux at the Repository Horizon and the Water Table for the Nine Base-Case Flow Fields

Climate/Infiltration	Flux at Repository Horizon (%)			Flux at Water Table (%)		
	Fracture	Matrix	Fault	Fracture	Matrix	Fault
Present/Lower	91.35	8.65	58.78	78.05	21.95	71.78
Present/Mean	94.29	5.71	28.62	70.29	29.71	53.73
Present/Upper	94.02	5.98	27.41	77.72	22.28	60.68
Monsoon/Lower	93.46	6.54	31.89	71.37	28.63	66.54
Monsoon/Mean	94.57	5.43	26.83	72.33	27.67	61.06
Monsoon/Upper	94.34	5.66	26.04	78.86	21.14	64.25
Glacial/Lower	92.11	7.89	36.71	70.37	29.63	65.40
Glacial/Mean	94.58	5.42	24.27	70.34	29.66	61.57
Glacial/Upper	94.53	5.47	23.81	76.44	23.56	65.37

Source: BSC 2003b, Table 6.6-3.

B.4.1.4 Radionuclide Transport through Fault Zones

This section summarizes the study of radionuclide transport by means of three-dimensional site-scale simulations representing the unsaturated zone system of Yucca Mountain. The study analyzed the migration of a finite radionuclide mass through the unsaturated zone and investigated the processes and phenomena that affected its arrival at the water table. The three-dimensional site-scale simulations were conducted using T2R3D (LBNL 1999). In the report, only four major elements (^{99}Tc, ^{237}Np, ^{238}U, and ^{239}Pu), out of 11 radionuclides that were considered in the simulations performed for *Radionuclide Transport Models Under Ambient Conditions* (BSC 2003c) were discussed, because those will cover various sorptive affinity, decay rates, and diffusion.

In all three-dimensional studies of site-scale radionuclide transport, liquid radioactive substances were released in the fractures of the elements corresponding to the repository. The initial radionuclide concentration was spatially uniform in the release area, which covered the entire footprint of the repository. The two modes of radionuclide release were instantaneous release and continuous release.

For mean present-day infiltration with the instantaneous release mode, Figures B-3 and B-4 give the relative mass fraction (X_R) distributions of ^{99}Tc in the liquid phase within the fractures and the matrix in the gridblocks directly above the interface between the TSw and the CHn (i.e., at the bottom of the TSw), corresponding to the tsw39 layer, for times of 10 and 100 years. X_R distributions of ^{99}Tc in the fractures and in the matrix immediately above the water table at 10 and 100 years are given in Figures B-5 and B-6. The t_{10} (10% breakthrough time) and t_{50} of ^{99}Tc for the various infiltration regimes are listed in Table B-2.

It becomes apparent that simulated transport is both dominated and controlled by the faults through comparison of transport patterns in Figures B-3 through B-6 with the infiltration pattern at the surface (Figure B-1), the percolation flux at the repository level (Figure B-2), and the percolation flux at the water table level. Infiltration and percolation reflect the transport pattern shown in Figures B-3 through B-6.
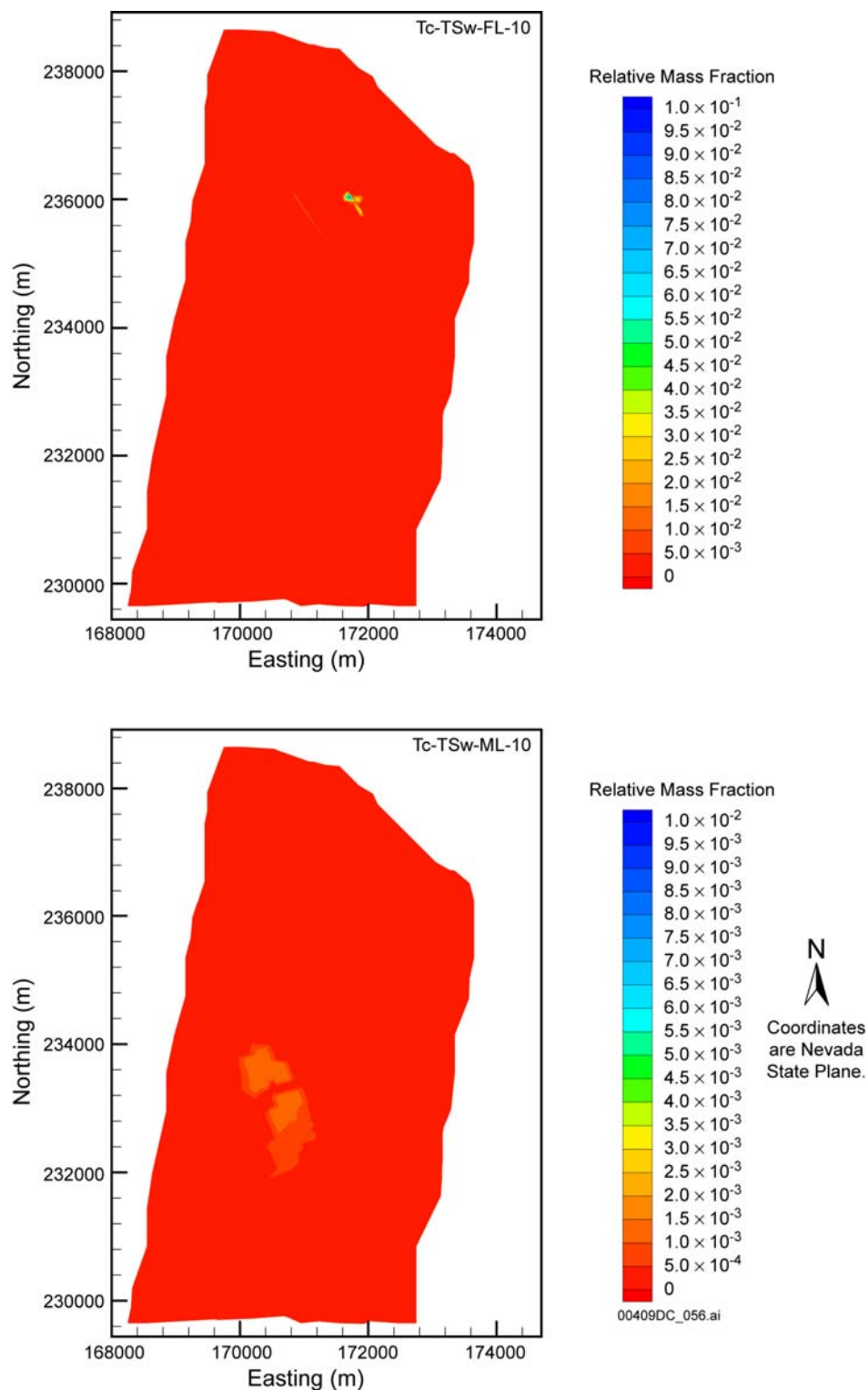
Source: BSC 2003c, Figures 6.8-2 and 6.8-3.

Figure B-3.   Distribution of the Relative Mass Fraction X_R of ^{99}Tc in the Fractures (Top) and the Matrix (Bottom) of the tsw39 Layer at 10 Years for Mean Present-Day Infiltration
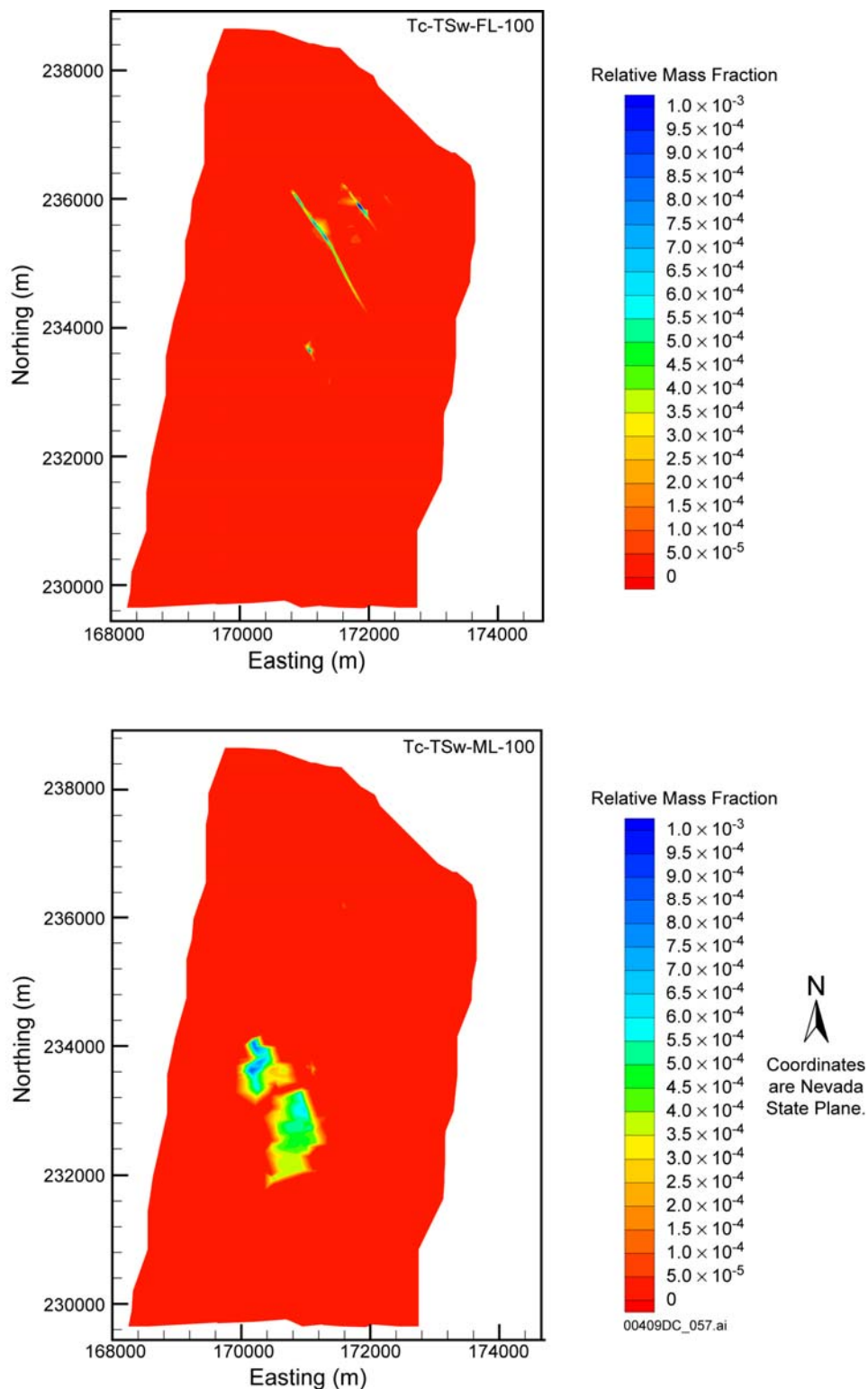
Source: BSC 2003c, Figures 6.8-4 and 6.8-5.

Figure B-4. Distribution of the Relative Mass Fraction X_R of ^{99}Tc in the Fractures (Top) and the Matrix (Bottom) of the tsw39 Layer at 100 Years for Mean Present-Day Infiltration
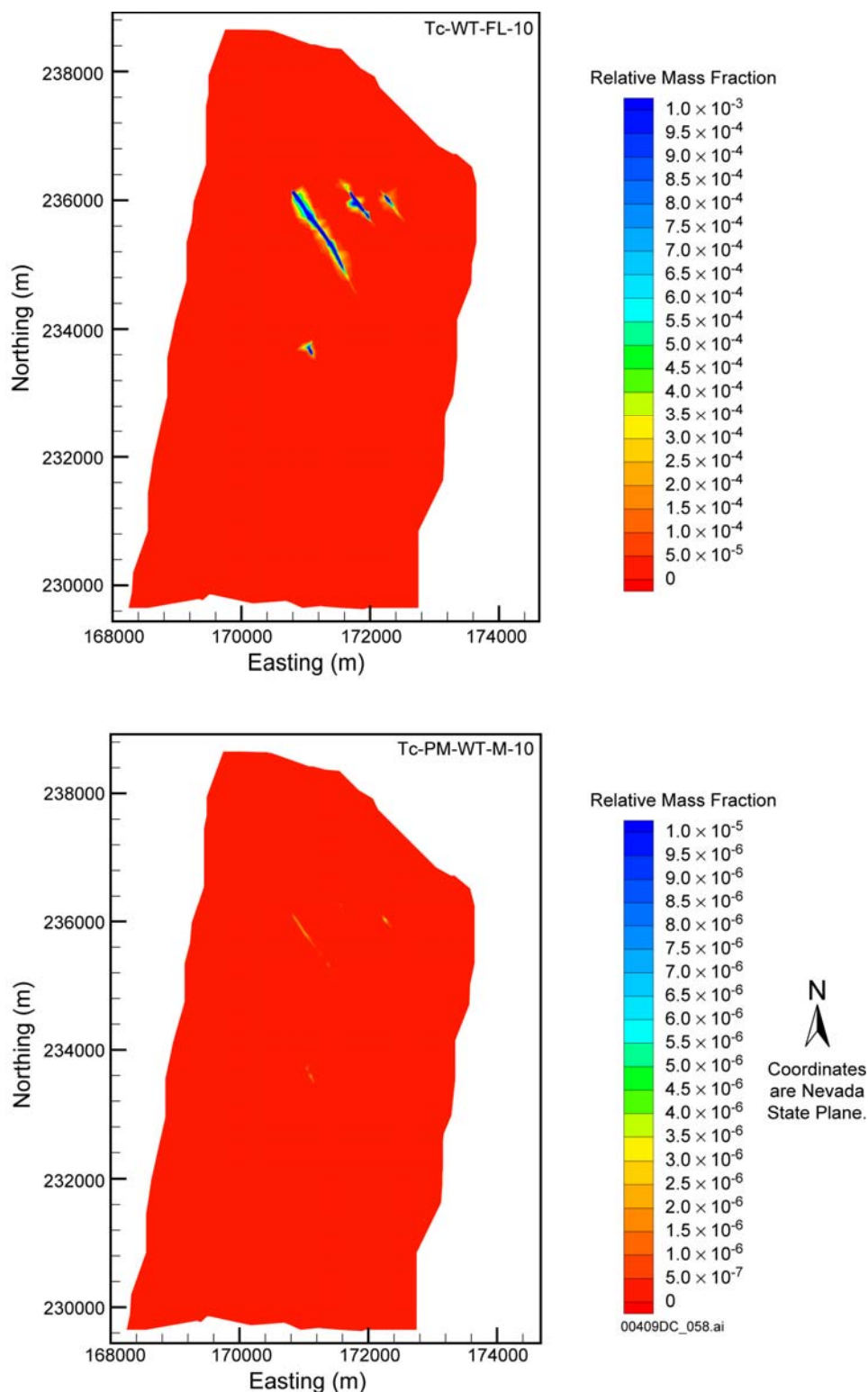
Source: BSC 2003c, Figures 6.8-12 and 6.8-13.

Figure B-5.   Distribution of the Relative Mass Fraction X_R of ^{99}Tc in the Fractures (Top) and the Matrix (Bottom) Immediately above the Water Table at 10 Years for Mean Present-Day Infiltration
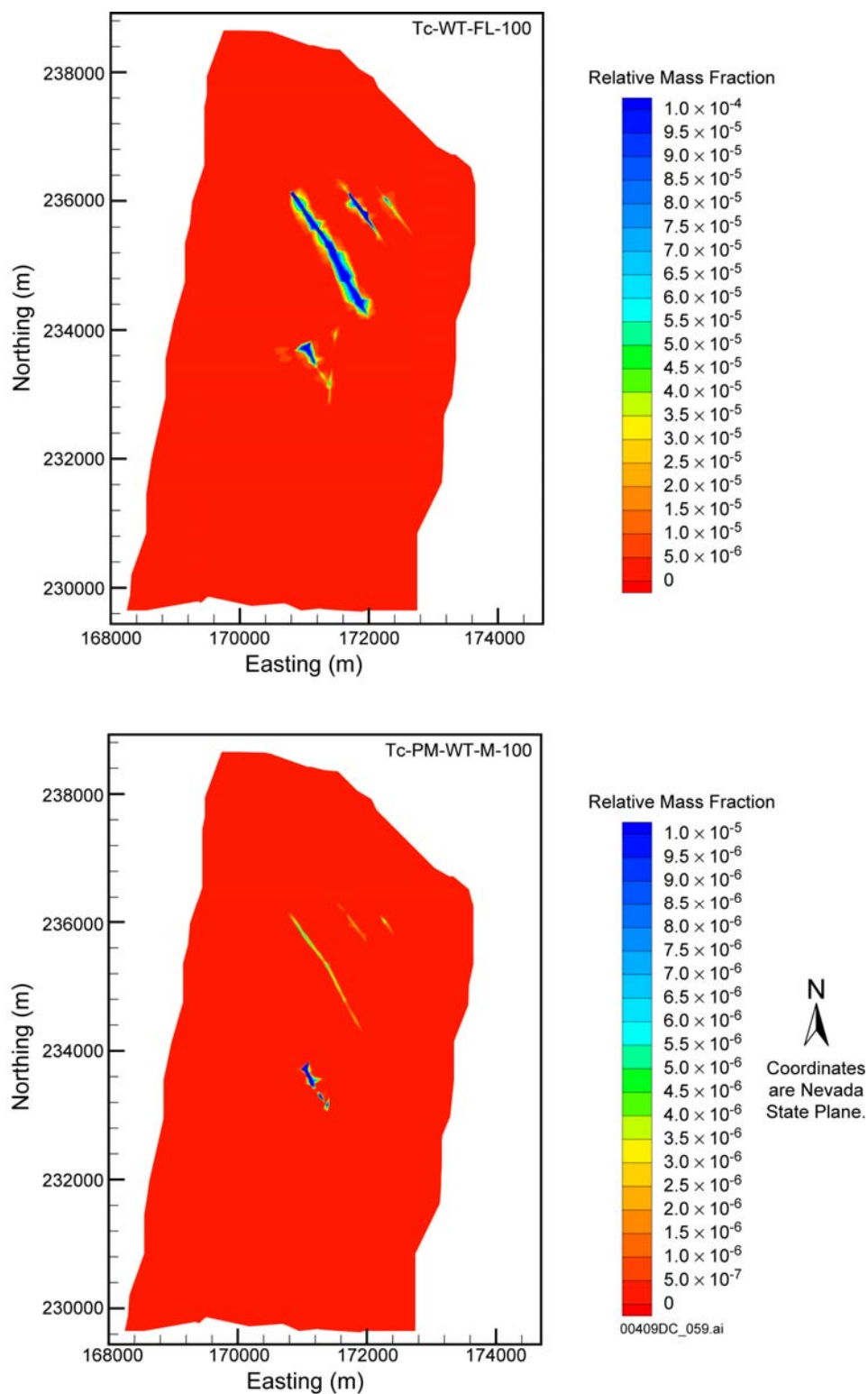
Source: BSC 2003c, Figures 6.8-14 and 6.8-15.

Figure B-6. Distribution of the Relative Mass Fraction X_R of ^{99}Tc in the Fractures (Top) and the Matrix (Bottom) Immediately above the Water Table at 100 Years for Mean Present-Day Infiltration

Table B-2. Radionuclide Transport Times to the Water Table (Instantaneous Release)

Radionuclide	Infiltration Scenario	Present-Day		Monsoon		Glacial-Transition	
		t_{10} (years)	t_{50} (years)	t_{10} (years)	t_{50} (years)	t_{10} (years)	t_{50} (years)
^{237}Np	Lower	33,800	>1,000,000	15	6,160	185	34,400
	Mean	410	25,400	8	2,120	4	1,070
	Upper	4	1,600	2	714	1	336
^{239}Pu	Lower	-	-	86,000	-	-	-
	Mean	-	-	10,400	-	3,710	-
	Upper	1,530	-	4	-	2	-
^{99}Tc	Lower	13,900	>1,000,000	22	1,310	102	8,140
	Mean	83	6,640	9	417	6	164
	Upper	6	230	2	92	1	42

Source: Extracted only for ^{237}Np, ^{239}Pu, and ^{99}Tc from BSC 2003c, Table 6.20-1.

NOTE: t_{10} or t_{50} have not been reached because of radioactive decay; greater than 1 million. Simulations are only up to 1 million years. The t_{10} or t_{50} can be reached after 1 million years.

From the distribution of the fracture X_R at the bottom of the TSw, it is evident that, immediately above the TSw–CHn interface (i.e., in the tsw39 layer), the Pagany Wash and Drill Hole Wash faults in the northern part are the main transport-facilitating features. Radionuclide transport to the tsw39 layer, which is immediately below the repository, is as rapid as 10 years. The Pagany Wash Fault appears to provide the fastest pathway (Figure B-3) during this time. Although ^{99}Tc arrives at the Drill Hole Wash Fault later, it appears to contribute more to transport than the Pagany Wash Fault for times greater than or equal to 100 years. Both faults register a strong signature; their presence is easily identified from the ^{99}Tc distributions (Figure B-4). The predominance of the Drill Hole Wash and the Pagany Wash faults as the main transport-facilitating geologic features at the tsw39 level is pervasive during the entire simulation period.

Review of the fracture X_R distributions at the water table (Figure B-5) indicates that the Drill Hole Wash and Pagany Wash faults continue to be the main transport conduits throughout the geologic profile, from the repository level to the water table. These two faults show measurable radionuclide presence at the water table as early as 10 years and at concentrations that are higher and more widely distributed than those observed at the bottom of the TSw (Figure B-3).

The significance of the Drill Hole Wash Fault as the dominant conduit of ^{99}Tc to the water table is further confirmed in Figure B-6. At 100 years, it shows a high ^{99}Tc concentration that extends outward from the fault axis. In addition to the Sundance Fault, the northern portion of the Ghost Dance Fault and the Solitario Canyon Fault appear to be making significant contributions to transport during the same time frame.

The presence of ^{99}Tc in the matrix at the water table is significantly delayed, and a pattern similar to that is not observed at the bottom of the TSw at early times. Despite significant radionuclide concentrations in the fractures associated with the faults discussed earlier, the matrix shows scant evidence of ^{99}Tc presence (Figures B-5 and B-6). When it occurs, it follows

the fault geometry and orientation and is localized and limited to the immediate vicinity of the faults, indicating an origin consistent with diffusion from the fault fractures with no sign of downward migration through the matrix.

This matrix concentration pattern further attests to the prevalence of fractures as the main transport-facilitating feature. A pervasive feature of the transport pattern at the water table is that the area affected by significant radionuclide concentration is significantly larger in the fracture system than in the matrix. This is the opposite of what is observed at the bottom of the TSw, where the areal distribution of the matrix X_R exceeds the footprint of the fracture X_R. The conclusion is that the fractures are the source of radionuclides appearing in the matrix, and that the large water velocities in the fractures lead to the limited areal extent and penetration of ^{99}Tc into the matrix.

^{237}Np and ^{239}Pu transport through the unsaturated zone of Yucca Mountain following an instantaneous release was also studied. The transport of different radionuclides follows the same general patterns because they are affected by the same mechanisms and controlled by the same geologic features. However, the magnitude of the observed fracture and matrix X_R varies considerably because of the different sorption affinities of these radionuclides related to the unsaturated zone rocks. The difference between ^{99}Tc and the ^{237}Np and ^{239}Pu transport behavior is sorption, which results in universally lower (than ^{99}Tc) concentrations and a more limited areal extent (footprint) of ^{237}Np and ^{239}Pu in the fractures and in the matrix at the same times. A higher sorption affinity leads to lower concentrations (especially in the fractures) and, consequently, more limited areal extent of sorbing radionuclides.

B.4.1.5 Effect of Radionuclide Release Directly into the Fault Fractures

Based on the breakthrough results and the transport patterns discussed in Section B.4.1.4, the early arrival of radionuclides at the Yucca Mountain water table was attributed to advective transport through the fractures associated with the Drill Hole Wash and Pagany Wash faults. The concentration distributions in the fractures at both the bottom of the TSw and at the water table even as early as 10 years and for both types of release (instantaneous and continuous) coincide with the fault outline (Figures B-3 and B-6). Thus, it was important to evaluate the impact of releasing radionuclides directly into the fractures of these faults.

This evaluation was accomplished by performing select radionuclide transport simulations in which the initial radionuclide concentration in repository gridblocks representing the fault (or in gridblocks adjacent to it) had been set to zero. In essence, radionuclide sources were removed from the faults and from the gridblocks on either side. These simulations were limited to mean present-day infiltration and the radioactive solutes ^{99}Tc, ^{237}Np, ^{239}Pu, and ^{235}U, which cover the spectrum of sorption behavior. Both release scenarios (instantaneous and continuous) were investigated.

Contrary to expectations, eliminating potential radionuclide sources from the vicinity of the fault fractures appears to have only a small effect on transport and arrivals at the water table. For instantaneous release (when a finite radionuclide mass is involved), the normalized mass fraction breakthrough curves in Figures B-7 and B-8 show a small increase in t_{10} (in line with

expectations because there is no release into the fast-conducting fault fractures) while t_{50} is practically unchanged.

The contour plots of the ^{99}Tc distribution of X_R in Figures B-9 through B-12 demonstrate the reason for the increase in t_{10} and virtually unchanged t_{50}. The effects of eliminating releases from the immediate vicinity of the faults are obvious at the bottom of the TSw, at which level the radionuclide distribution shows significant retardation compared to that shown in Figures B-3 and B-4. This is particularly evident in the northern part of the repository. Here the outlines of the Drill Hole Wash and Pagany Wash faults (which dominated transport when radionuclides were released throughout the area of the repository) are absent from the contour plots in Figures B-9 and B-10. Remarkably, the X_R distribution at the water table (Figures B-11 and B-12) is very similar to that of direct releases into the faults (Figures B-5 and B-6) and is dominated by transport through the Drill Hole Wash and Pagany Wash faults.

This pattern indicates that avoiding radionuclide release directly into and in the vicinity of faults does retard transport to shallow planes of reference, such as the bottom of the TSw. But given a sufficiently deep unsaturated zone, lateral transport through a vertically and horizontally interconnected fracture network compensates for the lack of direct releases into the faults. Thus, the interconnected fracture system leads to radionuclide transport to and emergence at the water table through fractures associated with faults into which no direct releases at the repository ever occurred. The same pattern is evident in the X_R distribution of all other radionuclides and release scenarios investigated.
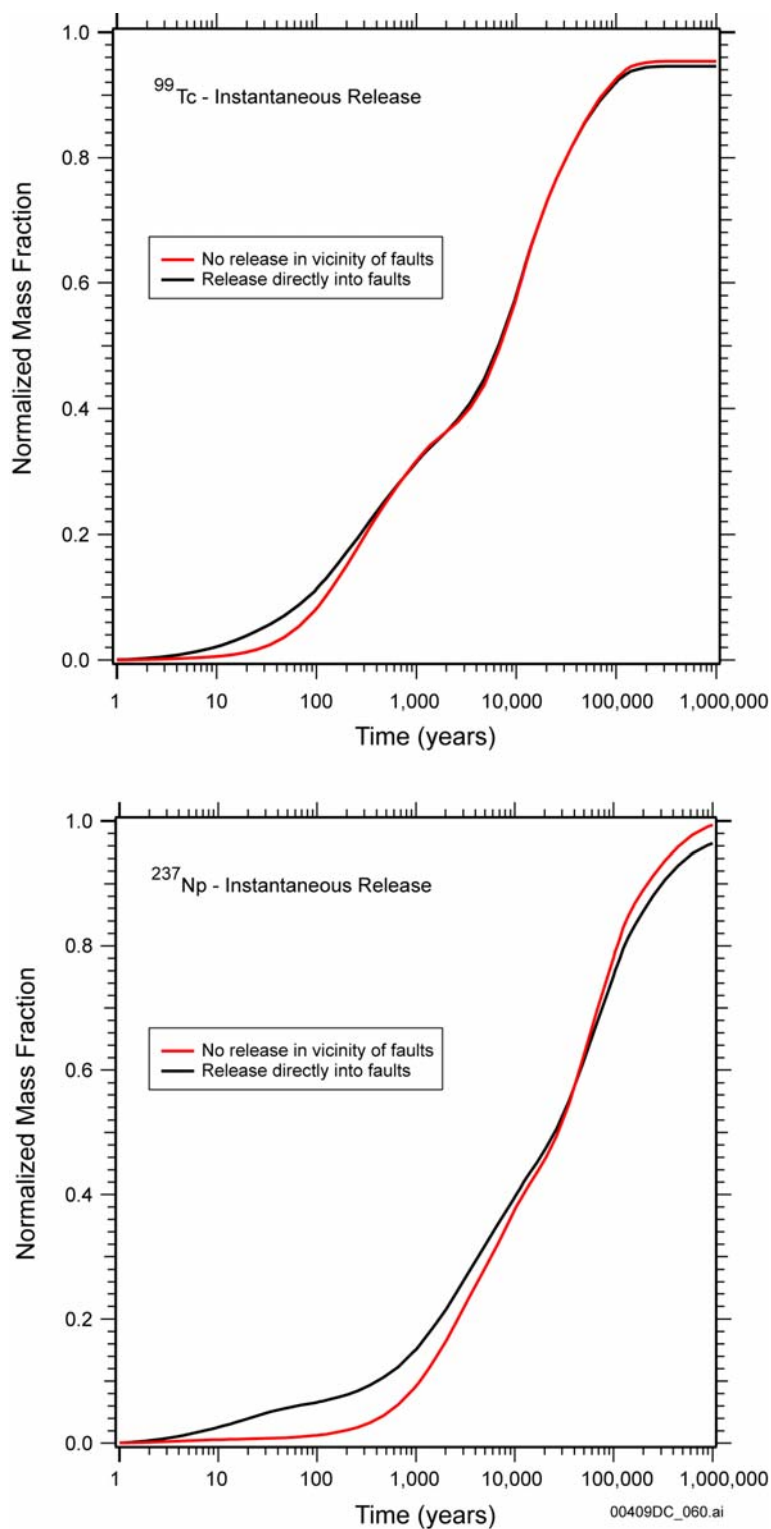
Source: BSC 2003c, Figure 6.20-1.

Figure B-7. Cumulative Breakthrough of the ^{99}Tc and ^{237}Np Mass Fractions R_M at the Water Table (Instantaneous Release, Mean Present-Day Infiltration, No Fault Releases)
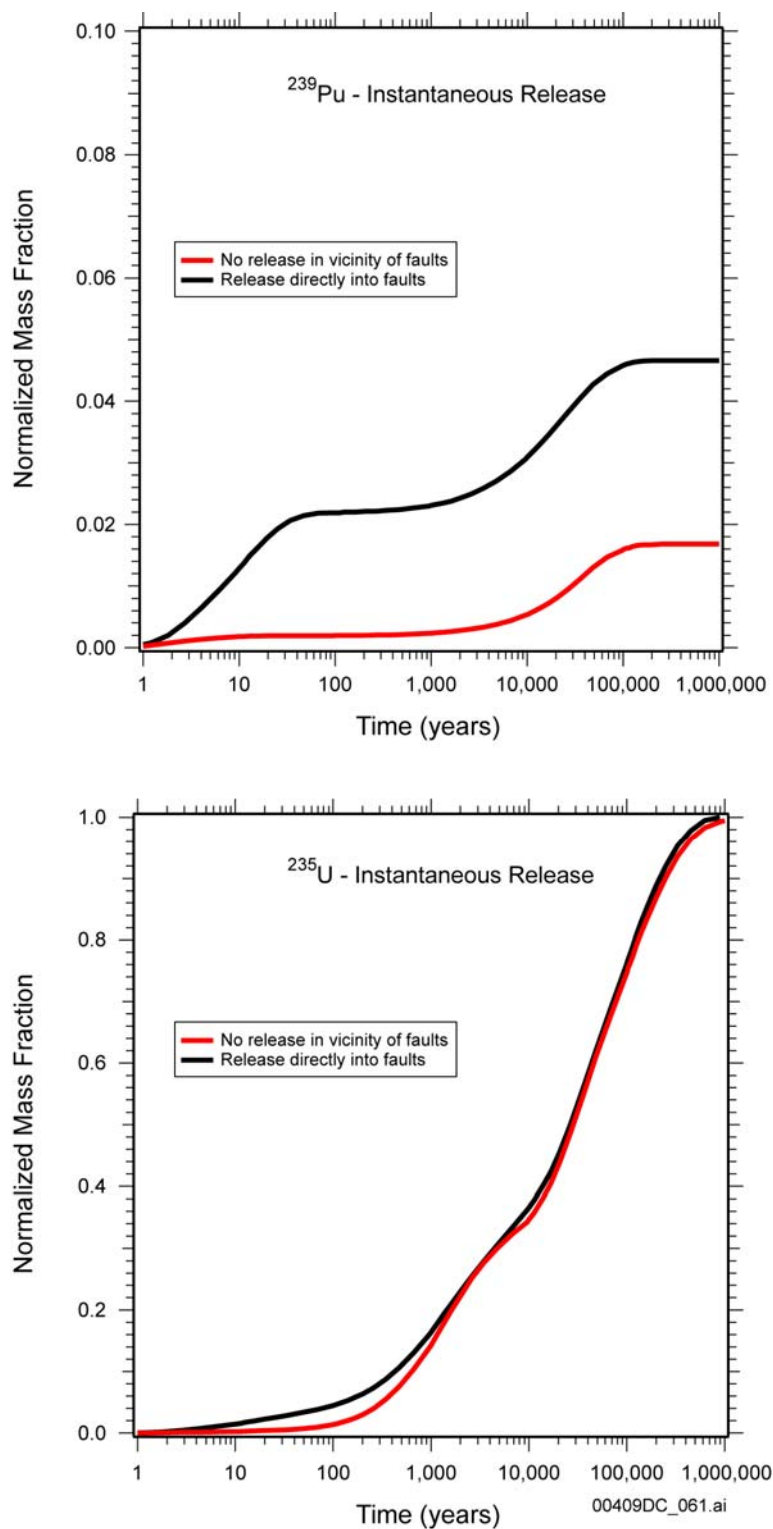
Source: BSC 2003c, Figure 6.20-2.

Figure B-8. Cumulative Breakthrough of the ^{239}Pu and ^{235}U Mass Fractions R_M at the Water Table (Instantaneous Release, Mean Present-Day Infiltration, No Fault Releases)
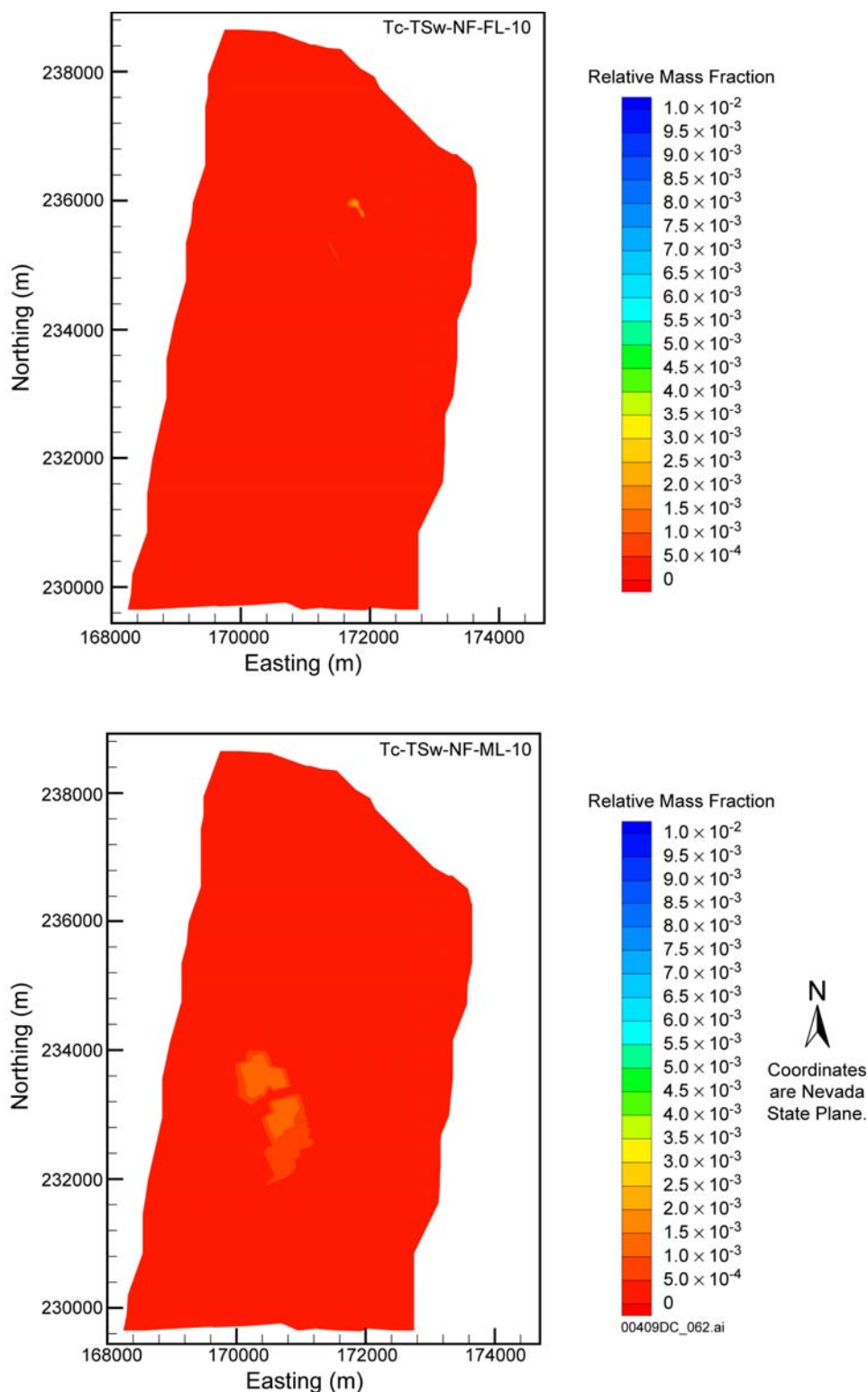
Source: BSC 2003c, Figures VIII.1 and VIII.2.

Figure B-9.   Distribution of the Relative Mass Fraction X_R of ^{99}Tc in the Fractures (top) and in the Matrix (bottom) of the tsw39 Layer at 10 Years (Instantaneous Release, Mean Present-Day Infiltration, No Fault Releases)
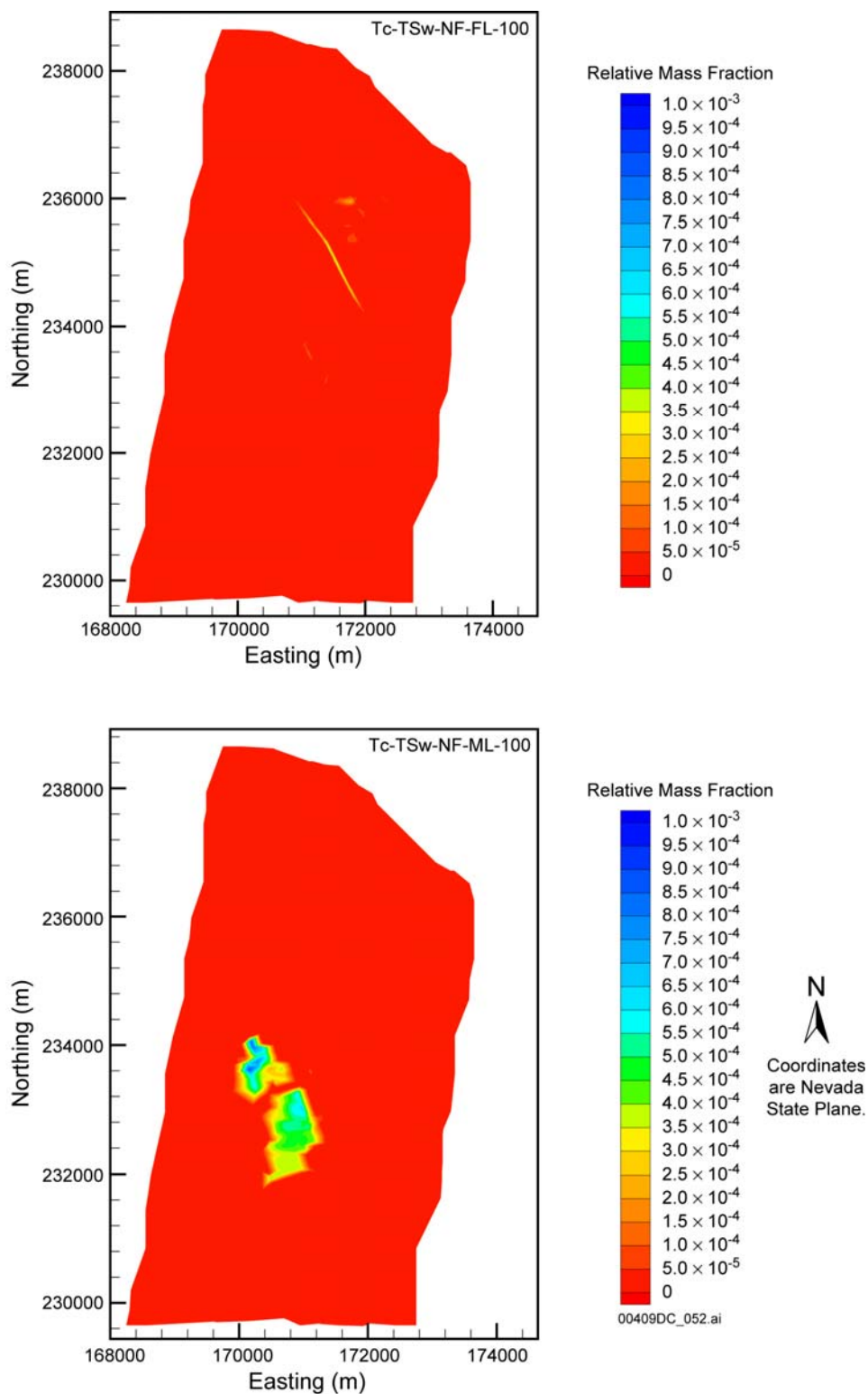
Source: BSC 2003c, Figures VIII.3 and VIII.4.

Figure B-10. Distribution of the Relative Mass Fraction X_R of ^{99}Tc in the Fractures (Top) and in the Matrix (Bottom) of the tsw39 Layer at 100 Years (Instantaneous Release, Mean Present-Day Infiltration, No Fault Releases)
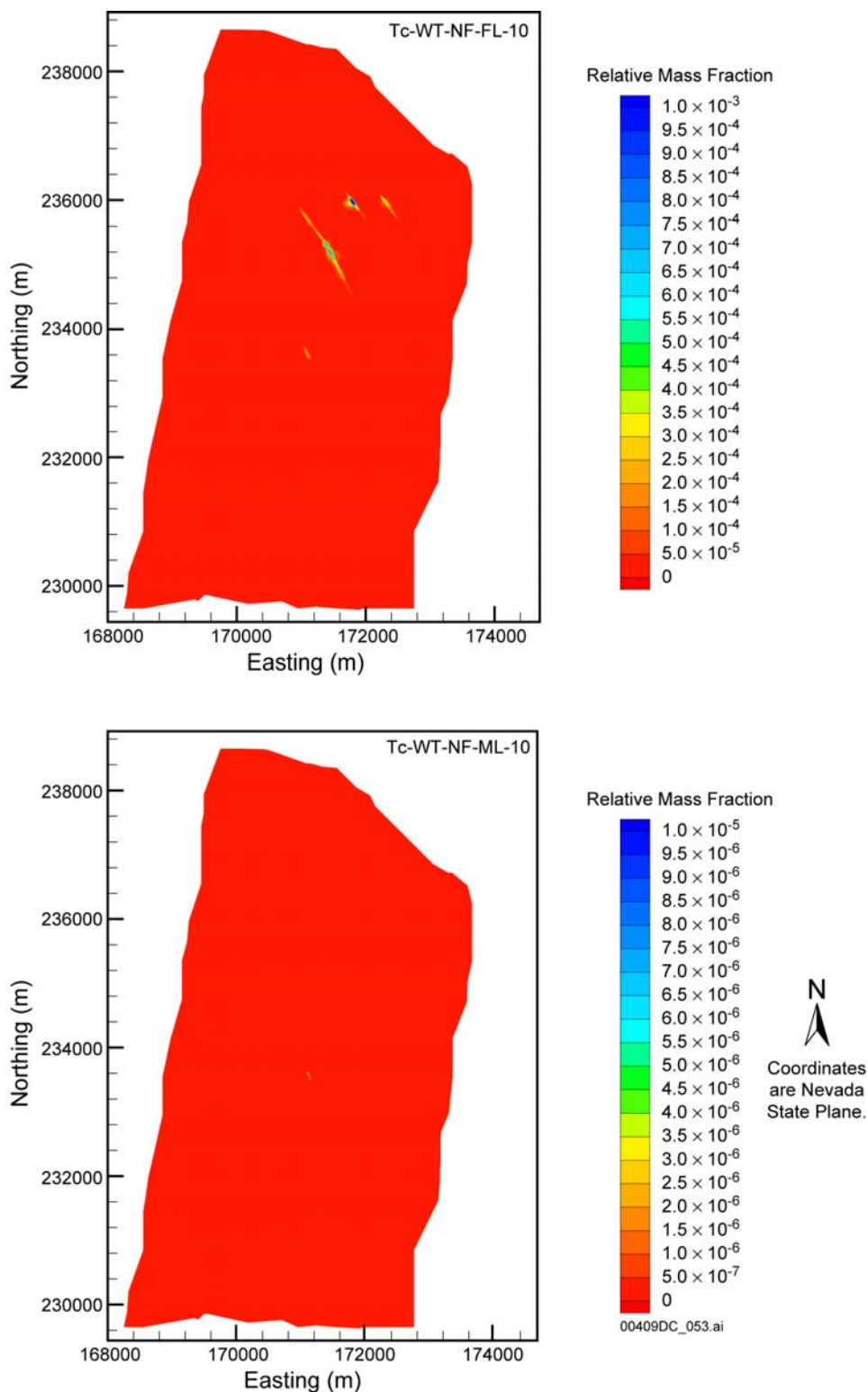
Source: BSC 2003c, Figures VIII.11 and VIII.12.

Figure B-11.   Distribution of the Relative Mass Fraction X_R of ^{99}Tc in the Fractures (Top) and in the Matrix (Bottom) at the Water Table at 10 Years (Instantaneous Release, Mean Present-Day Infiltration, No Fault Releases)
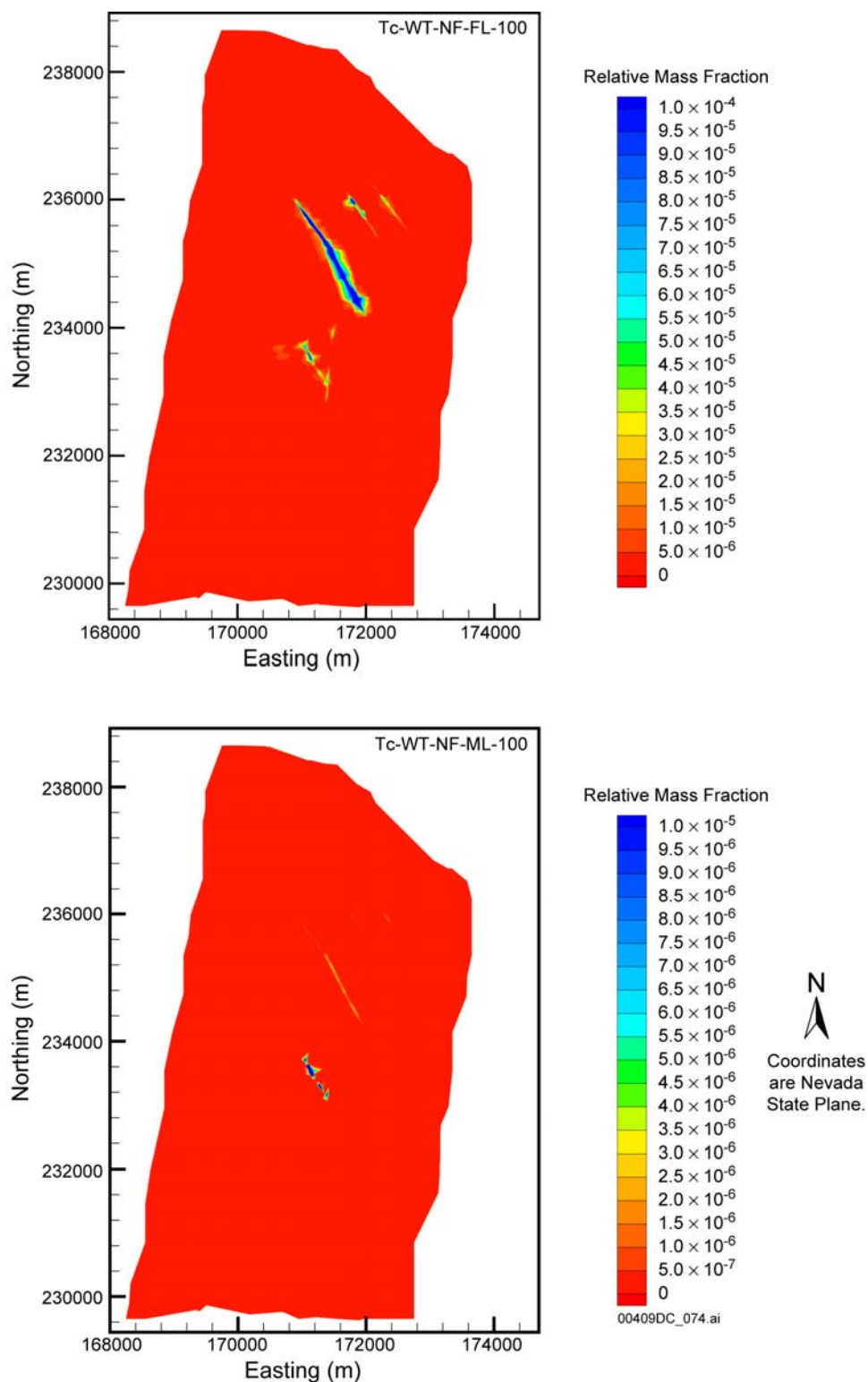
Source: BSC 2003c, Figures VIII.13 and VIII.14.

Figure B-12. Distribution of the Relative Mass Fraction X_R of ^{99}Tc in the Fractures (Top) and in the Matrix (Bottom) at the Water Table at 100 Years (Instantaneous Release, Mean Present-Day Infiltration, No Fault Releases)

B.4.1.6   Effect of Radionuclide Release into the Matrix

The transport simulations presented above are from radionuclides released directly from the repository horizon fractures. However, a sensitivity study was performed with direct releases from the matrix continuum of the repository block under the present-day mean infiltration scenario (BSC 2003b, Section 6.7). Radionuclide transport times to the water table are significantly longer when radionuclides are initially released from repository matrix blocks instead of fractures. For conservative (i.e., nonsorbing ^{99}Tc) transport, transport times are increased by one to two orders of magnitude (Figure B-13, Table B-3). For reactive (i.e., sorbing ^{237}Np) radionuclides, transport times are increased by more than one order of magnitude at 10% mass breakthrough and by approximately two times at 50% breakthrough.
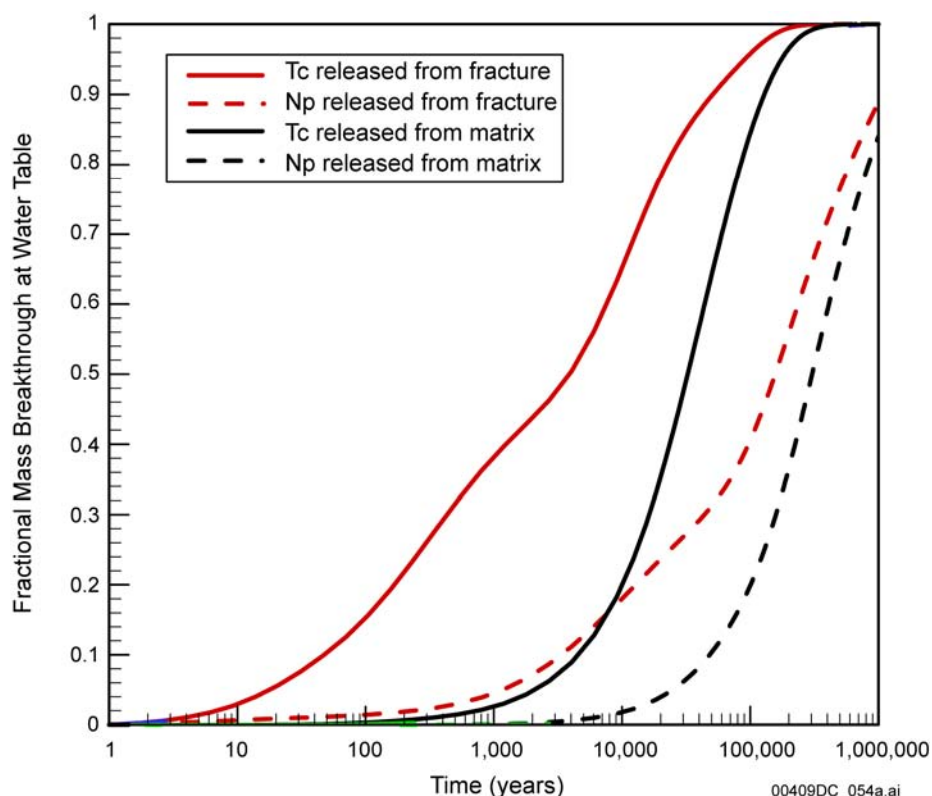
Source: BSC 2003b, Figure 6.7-3.

Figure B-13.   Comparison of Simulated Breakthrough Curves of Cumulative Radionuclide Mass Arriving at the Water Table after Release from Fractures and Matrix Blocks in the Repository, Using the Base-Case Flow Fields under the Present-Day Mean Infiltration Flow Fields for Nonsorbing and Sorbing Radionuclides

Table B-3. Radionuclide (Technetium and Neptunium) Transport Times at 10% and 50% Mass Breakthrough Times for the Base-Case Flow Fields under the Present-Day Mean Infiltration Flow Fields

Designation/ Transport Simulation	Radionuclide Type	t_{10} (years)	t_{50} (years)
preqmA_tc	Nonsorbing	50	3,900
preqmA_tcM[a]	Nonsorbing	4,600	33,000
preqmA_np	Sorbing	3,400	157,000
preqmA_npM[a]	Sorbing	48,000	300,000

Source: BSC 2003b, Table 6.7-4.

NOTE: [a]Radionuclides were released from repository matrix blocks.

B.4.1.7   Sensitivities in Transport Processes

The focus of this response is to determine the processes, the significance of parameter uncertainty, and the effect of differences in geology on radionuclide transport possessing different transport and decay properties.   Three radionuclides will be considered: ^{237}Np (moderately sorbing), ^{239}Pu (strongly sorbing), and ^{99}Tc (nonsorbing).   These analyses demonstrate, through the response of breakthrough curves, the range of radionuclide transport behavior exhibited by the above radionuclides in the TSw, CHv, and CHz hydrogeologic units.

B.4.1.7.1   Sensitivities in ^{99}Tc Retardation Process

The only nondecay mechanism of ^{99}Tc retardation in the transport process through the unsaturated zone is matrix diffusion (including dispersion), because it is nonsorbing and chemical immobilization is not considered. Uncertainties in matrix diffusion are reflected in the values of D_0. Given the uncertainties in the estimation of the parameters, the choice of D_0 in general influences the effective diffusion coefficient.

To address the uncertainty in D_0, the sensitivity of the ^{99}Tc transport through the unsaturated zone for the D_0 values shown in Table B-4, which cover the likely D_0 range, was investigated. The results are shown in Figure B-14. As expected, D_0 has a significant impact on breakthrough predictions, resulting in faster arrival times for lower D_0 values.

Table B-4. Properties of Radionuclides in the Transport Simulations

Radionuclide	D_0 (m^2/s)	$T_{1/2}$ (years)
^{99}Tc	4.55×10^{-10} 4.55×10^{-11} 10^{-9}	2.13×10^5
^{237}Np	1.65×10^{-10} 7.12×10^{-10} 1.65×10^{-11}	2.14×10^6
^{239}Pu	4.81×10^{-10} 4.81×10^{-11} 10^{-9}	2.41×10^4

Source: BSC 2003c, Table 6.5-2.
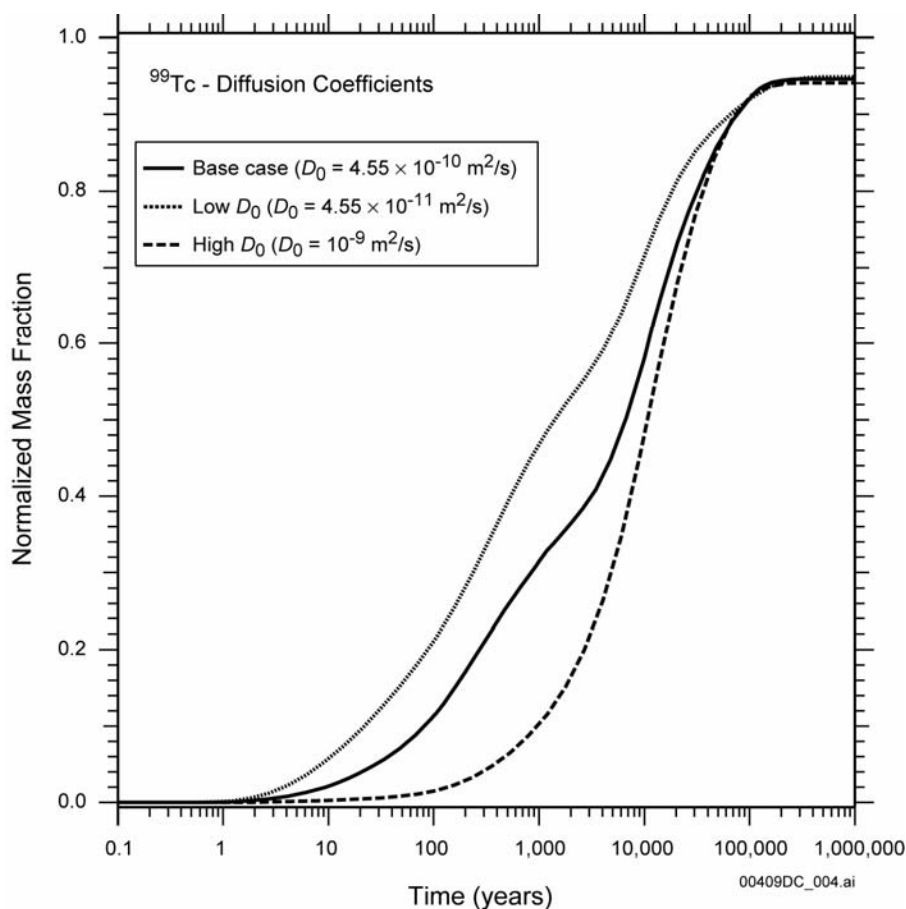
Source: BSC 2003c, Figure 6.8-28.

Figure B-14.   Effect of Uncertainty in D_0 on the Cumulative Breakthrough of the ^{99}Tc Mass Fraction R_M

B.4.1.7.2   Sensitivities in ^{237}Np Transport Predictions

Because ^{237}Np is a sorbing radionuclide, uncertainties in the transport process involve both diffusion and sorption issues. Uncertainties in matrix diffusion are reflected in the values of D_0. To address this issue, the sensitivity of ^{237}Np transport through the unsaturated zone for the

D_0 values shown in Table B-4 was investigated. Sorption coefficients for these runs were kept the same as in the base case (see numbers in bold in Table B-5). The results are shown in Figure B-15. The D_0 values cover the likely range.
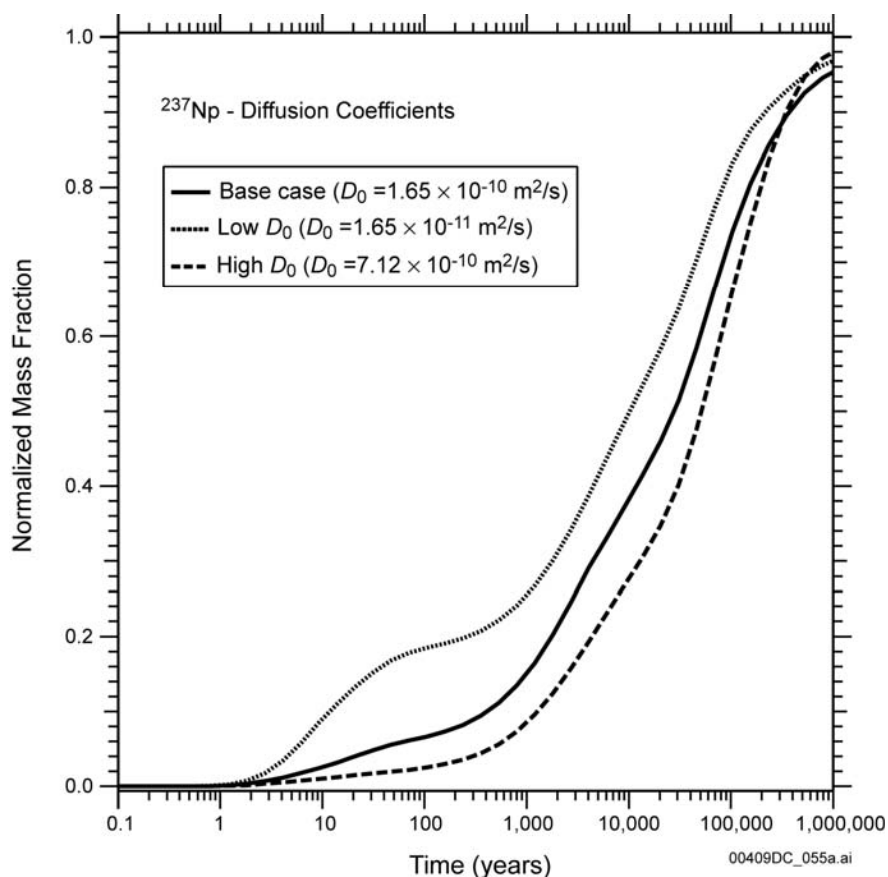
Source: BSC 2003c, Figure 6.9-5.

Figure B-15. Effect of Sensitivity in D_0 on ^{237}Np Breakthrough at the Water Table

As expected, D_0 has a significant impact on breakthrough predictions, resulting in faster arrival times for lower D_0 values. The relative effect of D_0 uncertainty in predicting sorbing ^{237}Np transport is comparatively less pronounced than that of the nonsorbing ^{99}Tc (i.e., the impact of D_0 uncertainty on radionuclide breakthrough predictions appears to be mitigated by sorption). Such uncertainties in sorption are reflected in the values of K_d. To address this issue, the sensitivity of the ^{237}Np transport through the unsaturated zone for the K_d values is shown in Figure B-16. These values cover the range between zero (no sorption, in which case behavior similar to that of ^{99}Tc is expected) to the maximum values shown in Table B-5. As expected, K_d has a significant impact on breakthrough predictions, resulting in faster arrival times for lower K_d values. The relative effect of K_d uncertainty predicting sorbing ^{237}Np transport appears to be much more pronounced than that for the D_0 uncertainty for the range tested here.
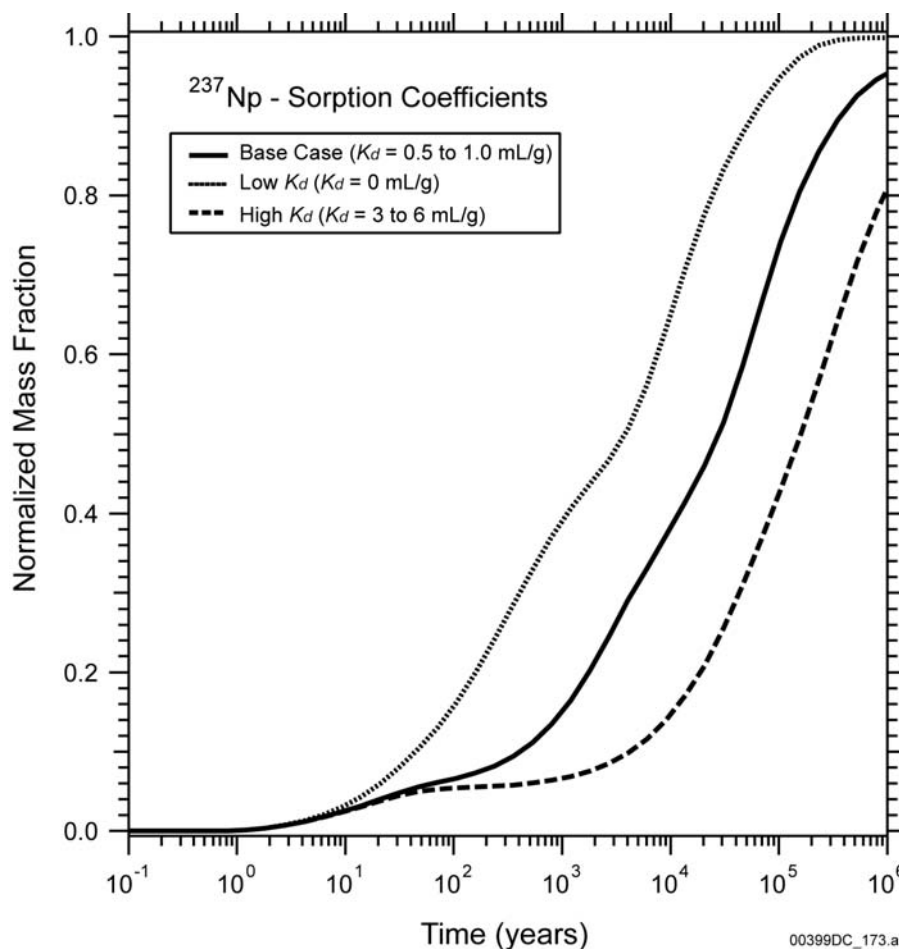
Source: BSC 2003c, Figure 6.9-6.

Figure B-16. Effect of Uncertainty in K_d on ^{237}Np Breakthrough at the Water Table

Table B-5. K_d in the Rocks of the Unsaturated Zone

Species	Unit/Analysis	Coefficients Describing Distribution (mL/g)
Neptunium	Zeolitic	(K_d value, probability) (0, 0) (**0.5**, 0.5) (6, 1.0)
	Devitrified	(K_d value, probability) (0, 0) (**0.5**, 0.5) (6, 1.0)
	Vitric	(K_d value, probability) (0, 0) (**1.0**, 0.5) (3, 1.0)
Plutonium	Zeolitic	(K_d value, probability) (10, 0) (**100**, 0.5) (200, 1.0)
	Devitrified	(K_d value, probability) (10, 0) (**70**, 0.5) (200, 1.0)
	Vitric	(K_d value, probability) (10, 0) (**100**, 0.5) (200, 1.0)

Source: BSC 2003c, Table 6.5-1.

NOTE: The numbers in bold were used in the base-case simulations. Only ^{237}Np and ^{239}Pu excerpted.

B.4.1.7.3   Sensitivity of ^{239}Pu Transport Predictions to Diffusion

Although ^{239}Pu is a sorbing radionuclide subject to the impact of uncertainties in diffusion and sorption, only uncertainty in diffusion is addressed here. The reason for this approach is that

^{239}Pu exhibits sorbing behavior that is so strong that it would be physically unrealistic to reduce K_d to levels that may have an impact on transport prediction. Even an order-of-magnitude reduction in K_d is insufficient to significantly affect ^{239}Pu transport behavior.

Uncertainties in matrix diffusion are reflected in the values of D_0. The sensitivity of the ^{239}Pu transport through the unsaturated zone for the D_0 values shown in Table B-4, which cover the possible D_0 range, was investigated. The results are shown in Figure B-17.

^{239}Pu - Diffusion Coefficients

Base case ($D_0 = 4.81 \times 10^{-10}$ m^2/s)
Low D_0 ($D_0 = 4.81 \times 10^{-11}$ m^2/s)
High D_0 ($D_0 = 10^{-9}$ m^2/s)
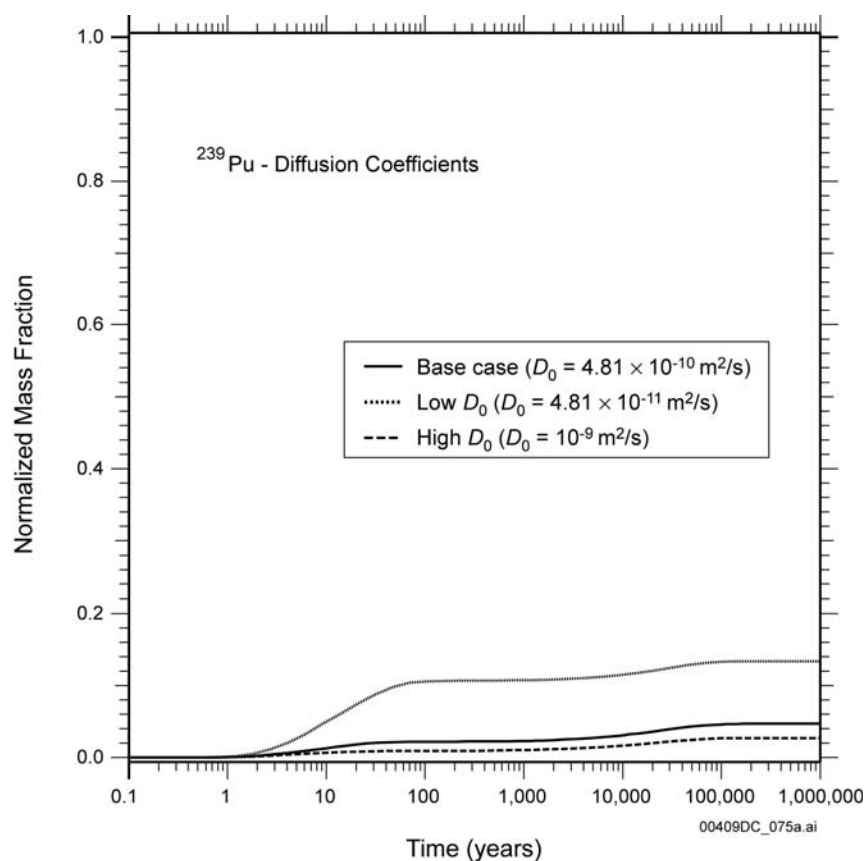
Source: BSC 2003c, Figure 6.10-4.

Figure B-17. Effect of Uncertainty in D_0 on the ^{239}Pu Breakthrough at the Water Table

As expected, D_0 has an impact on breakthrough predictions, resulting in faster arrival times for lower D_0 values. However, the relative effect of D_0 uncertainty in predicting strongly sorbing ^{239}Pu transport is comparatively even less pronounced than that of the mildly sorbing ^{237}Np. That is, the impact of D_0 uncertainty on radionuclide breakthrough predictions appears to be mitigated by sorption.

B.4.1.7.4   Applicability of Uncertainty Studies to Other Radionuclides

The insights obtained from the uncertainty analysis for ^{99}Tc, ^{237}Np, and ^{239}Pu are directly applicable to other radionuclides. By covering the spectrum of sorption behavior and diffusion in the uncertainty study, it is possible to develop rules to broadly predict the effect that would be caused by the uncertainties in the magnitudes of sorption and diffusion. Thus, the effect of

uncertainties in the breakthrough of nonsorbing radionuclides will be analogous to that of ^{99}Tc. Mildly sorbing radionuclides can be described by using the ^{237}Np analog, while strong sorbers will be described by the ^{239}Pu behavior.

B.4.2 Relative Importance of the Main Geologic Units beneath the Repository (RT 3.04)

The importance of the hydrogeologic units beneath the repository for radionuclide transport was evaluated. ^{237}Np and ^{239}Pu were considered for the simulations. These analyses evaluate radionuclide transport behavior in the TSw, CHv, and CHz hydrogeologic units.

B.4.2.1 Effect of Geology beneath the Repository

Analysis of the matrix X_R distributions at the bottom of the TSw and at the water table offers additional insight into transport patterns. At the bottom of the TSw layer, the matrix X_R distributions at early times (bottom images of Figures B-3 and B-4) show the highest concentrations in the southern part of the repository. This is in sharp contrast to the fractures that indicate transport exclusively in the northern part at the same times (top images of Figures B-3 and B-4) and practically no sign of significant ^{99}Tc in the matrix next to the rapidly transporting fractures

The reason for these vastly diverse transport patterns is the significantly different geology at the base of the TSw, which is dominated by vitric CHv layers below the southern part of the repository and zeolitic CHz layers in the northern part. Note that sorptive strength of each hydrogeologic unit in the unsaturated zone model (Table 2-1) was identified based on its rock composition as one of three major rock types (vitric, zeolitic, and devitrified). The permeabilities of the fractures and of the matrix of the vitric layers are similar in magnitude (BSC 2003a, Section 6.3). This permeability parity, coupled with a large fracture spacing, results in a behavior similar to that of a nonfractured porous medium (BSC 2003a, Section 6.6.3). Thus, there is no early evidence of fracture flow in the southern part of the repository.

In contrast, although the zeolitic CHz layers in the northern part of the repository have fracture spacing and permeability similar to the vitric CHv layers in the south, their matrix permeability is about five orders of magnitude lower than their fracture permeability (BSC 2003a, Section 6.3). Consequently, matrix flow in the zeolitic layers in the northern part of the repository is significantly slower than the flow in fractures, with practically all the flow occurring in the fractures, leading to the fast transport observed in the fractures.

The eastward movement of ^{99}Tc in the matrix (bottom images of Figures B-3 and B-4) results from site geology. Once contamination reaches the interface, it moves primarily eastward with the draining water that follows the downward sloping (in this direction), low-permeability TSw– CHn interface. At later times, the matrix X_R footprint shifts northward, as ^{99}Tc diffusing from the fractures advances into the matrix (bottom images of Figures B-3 and B-4).

B.4.2.2 Effect of Sorption in the Main Geologic Units on ^{237}Np Transport

The effect the main hydrogeologic units (i.e., TSw, CHv, and CHz) have on the transport and retardation of ^{237}Np was investigated by separately setting the corresponding K_d to zero in all the

layers of each of these units and then comparing the resulting cumulative breakthrough curve to that for the base case.

The results (for the mean present-day infiltration scenario) are shown in Figure B-18. They indicate that TSw is by far the most important unit in the transport and retardation of ^{237}Np. By eliminating sorption in all the TSw layers, water table arrivals of ^{237}Np occur significantly earlier. The effect of no sorption in the CHz and CHv units are secondary (if not marginal), and become apparent only at later times. The substantial change in transport behavior observed when sorption is not considered in the TSw layers is attributed to the high frequency of fractures in the layers, leading to higher fracture–matrix interfacial area for enhanced diffusion and eventually more sorption onto the matrix. Perched-water bodies found on the bottom of the TSw layer would also increase radionuclide diffusion into the matrix with higher water saturation. Given that no sorption occurs in the fractures, the lack of any appreciable retardation during advection through the CHz and CHv tends to indicate that the diffusion of radionuclides into the matrix is limited by low fracture frequencies. Moreover, advective flow through the matrix of those layers does not contribute significantly to overall radionuclide transport.
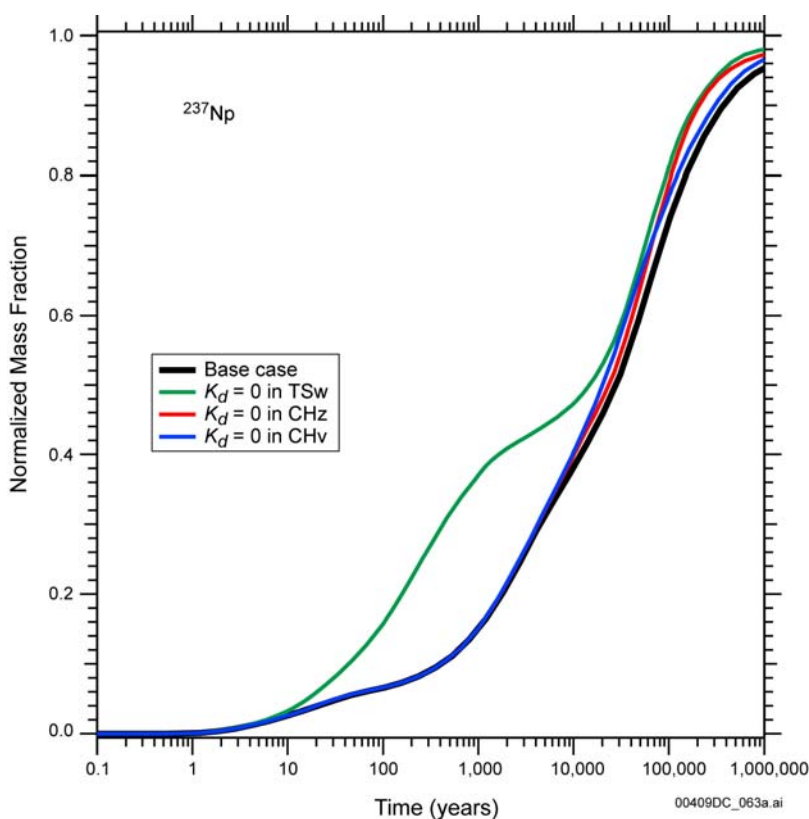
Source: BSC 2003c, Figure 6.9-2.

Figure B-18. Effect of Sorption in TSw, CHz, and CHv on the Cumulative Breakthrough of ^{237}Np at the Water Table

B.4.2.3 Effect of Sorption in the Main Geologic Units on ^{239}Pu Transport

The effect of the main hydrogeologic units (i.e., TSw, CHv, and CHz) on the transport and retardation of ^{239}Pu was also investigated. The cumulative breakthrough curves corresponding to a zero K_d for the TSw, CHv, and CHz units are shown in Figure B-19.

The results (for a mean present-day infiltration scenario) are analogous to, but far more pronounced than, those discussed in the case of ^{237}Np transport. By setting the K_d to zero in all the TSw layers, larger amounts of ^{239}Pu arrive earlier at the water table and a much higher R_M value is attained, indicating that much larger amounts of ^{239}Pu can cross the unsaturated zone. The overall effect of no sorption in the CHz and CHv units is practically insignificant compared to the base case. As in the case of ^{237}Np transport, these results further underscore the importance of the TSw unit on the transport and retardation of ^{239}Pu and illustrate the dominance of fractures in unsaturated zone transport.
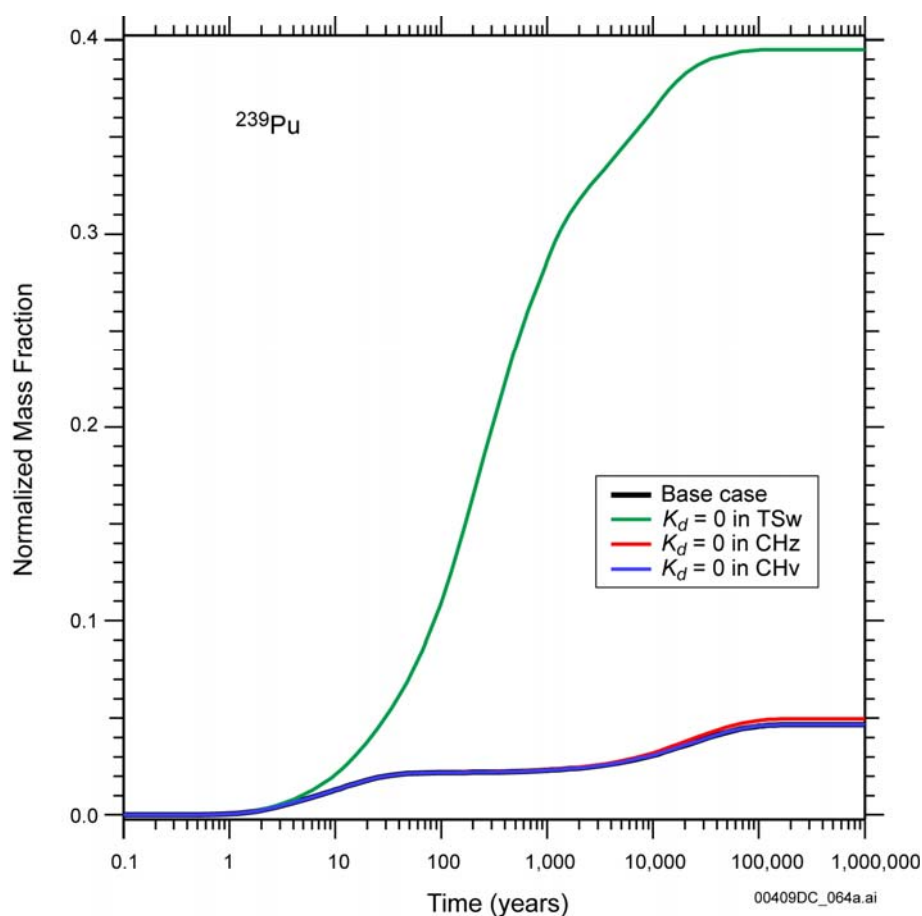
Source: BSC 2003c, Figure 6.10-3.

Figure B-19. Effect of Sorption in TSw, CHz, and CHv on the Cumulative Breakthrough of ^{239}Pu at the Water Table (Mean Present-Day Simulation)

B.5 REFERENCES

BSC (Bechtel SAIC Company) 2001. *Uncertainty Distributions for Stochastic Parameters.* ANL-NBS-MD-000011 REV 00 ICN 01. Las Vegas, Nevada: Bechtel SAIC Company. ACC: MOL.20020506.0917.

BSC 2003a. *Calibrated Properties Model.* MDL-NBS-HS-0003 REV 01. Las Vegas, Nevada: Bechtel SAIC Company. ACC: DOC.20030219.0001.

BSC 2003b. *UZ Flow Models and Submodels.* MDL-NBS-HS-000006 REV 01. Las Vegas, Nevada: Bechtel SAIC Company. ACC: DOC.20030818.0002.

BSC 2003c. *Radionuclide Transport Models Under Ambient Conditions.* MDL-NBS-HS-000008 REV 01. Las Vegas, Nevada: Bechtel SAIC Company. ACC: DOC.20031201.0002

BSC 2003d. *Development of Numerical Grids for UZ Flow and Transport Modeling.* ANL-NBS-HS-000015 REV 01. Las Vegas, Nevada: Bechtel SAIC Company. ACC: DOC.20030404.0005.

CRWMS M&O (Civilian Radioactive Waste Management System Management and Operating Contractor) 2000. *Unsaturated Zone and Saturated Zone Transport Properties (U0100).* ANL-NBS-HS-000019 REV 00. Las Vegas, Nevada: CRWMS M&O. ACC: MOL.20000829.0006.

LBNL (Lawrence Berkeley National Laboratory) 1999. *Software Code: T2R3D.* V1.4. FORTRAN 77, SUN, DEC/ALPHA. 10006-1.4-00.

Lide, D.R., ed. 1992. *CRC Handbook of Chemistry and Physics.* 73rd Edition. Boca Raton, Florida: CRC Press. TIC: 255239.

NRC (U.S. Nuclear Regulatory Commission) 2002. *Integrated Issue Resolution Status Report.* NUREG-1762. Washington, D.C.: U.S. Nuclear Regulatory Commission, Office of Nuclear Material Safety and Safeguards. TIC: 253064.

Reamer, C.W. and Williams, D.R. 2001. Summary Highlights of NRC/DOE Technical Exchange and Management Meeting on Radionuclide Transport. Meeting held December 5 to December 7, 2000, Berkeley, California. Washington, D.C.: U.S. Nuclear Regulatory Commission. ACC: MOL.20010117.0063.

Triay, I.R.; Meijer, A.; Conca, J.L.; Kung, K.S.; Rundberg, R.S.; Strietelmeier, B.A.; and Tait, C.D. 1997. *Summary and Synthesis Report on Radionuclide Retardation for the Yucca Mountain Site Characterization Project.* Eckhardt, R.C., ed. LA-13262-MS. Los Alamos, New Mexico: Los Alamos National Laboratory. ACC: MOL.19971210.0177.

APPENDIX C

**ACTIVE-FRACTURE CONCEPT IN THE
UNSATURATED ZONE TRANSPORT MODEL
(RESPONSE TO TSPAI 3.28 AND 3.29)**

Note Regarding the Status of Supporting Technical Information

This document was prepared using the most current information available at the time of its development. This Technical Basis Document and its appendices providing Key Technical Issue Agreement responses that were prepared using preliminary or draft information reflect the status of the Yucca Mountain Project's scientific and design bases at the time of submittal. In some cases this involved the use of draft Analysis and Model Reports (AMRs) and other draft references whose contents may change with time. Information that evolves through subsequent revisions of the AMRs and other references will be reflected in the License Application (LA) as the approved analyses of record at the time of LA submittal. Consequently, the Project will not routinely update either this Technical Basis Document or its Key Technical Issue Agreement appendices to reflect changes in the supporting references prior to submittal of the LA.

APPENDIX C

ACTIVE-FRACTURE CONCEPT IN THE
UNSATURATED ZONE TRANSPORT MODEL
(RESPONSE TO TSPAI 3.28 AND 3.29)

This appendix provides a response for Key Technical Issue (KTI) agreements Total System Performance Assessment and Integration (TSPAI) 3.28 and 3.29. These agreements relate to the use of the active-fracture concept in the unsaturated zone transport model.

C.1 KEY TECHNICAL ISSUE AGREEMENTS

C.1.1 TSPAI 3.28 and TSPAI 3.29

Agreements TSPAI 3.28 and 3.29 were reached during the U.S. Nuclear Regulatory Commission (NRC)/U.S. Department of Energy (DOE) Technical Exchange and Management Meeting on Total System Performance Assessment and Integration held August 6 to 10, 2001, in Las Vegas, Nevada. TSPAI Subissue 3, Model Abstraction, within the total system performance assessment (TSPA) methodology, was discussed at that meeting (Reamer 2001). No submittal related to these KTI agreements has been made to the NRC.

Subsequent to the agreements, NRC staff concerns underlying TSPAI 3.28 and 3.29 were recorded in *Integrated Issue Resolution Status Report* (NRC 2002, p. 3.3.7-5 and pp. 3.3.7-17 to 3.3.7-18). These concerns mean that, in addition to the language of the agreements (Reamer 2001), there is a general need for improved transparency of model parameter estimation and numerical implementation of the abstraction transport model, based on information provided in *Particle Tracking Model and Abstraction of Transport Processes* (CRWMS M&O 2000a) and *Unsaturated Zone Flow and Transport Model Process Model Report* (CRWMS M&O 2000b). These reports specifically require clarification of the methods of estimating fracture porosity, fracture–matrix connection area, fracture aperture values (and whether they have been adjusted to account for the active-fracture concept), and fracture spacing. The method of implementing the active-fracture concept in the abstraction transport model also requires clarification, including whether or not the fraction of active fractures is factored into the calculation of fluid velocity in the transport model.

The wording of the agreements is as follows:

TSPAI 3.28

> DOE needs to provide independent lines of evidence to provide additional confidence in the use of the active-fracture continuum concept in the transport model (UZ3.5.1). DOE will provide independent lines of evidence to provide additional confidence in the use of the active fracture continuum concept in the transport model. This will be documented in Radionuclide Transport Models under Ambient Conditions AMR (MDL-NBS-HS-000008) and Unsaturated Zone Flow Models and Submodels AMR (MDL-NBS-HS-000006) expected to be available to NRC in FY 2003.

TSPAI 3.29

Provide verification that the integration of the active fracture model with matrix diffusion in the transport model is properly implemented in the TSPA abstraction (UZ3.TT.3). DOE will provide verification that the integration of the active fracture model with matrix diffusion in the transport model is properly implemented in the TSPA abstraction. This verification will be documented in the Particle Tracking Model and Abstraction of Transport Processes (ANL-NBS-HS-000026) expected to be available to NRC in FY 2003.

C.1.2 Related Key Technical Issue Agreements

None.

C.2 RELEVANCE TO REPOSITORY PERFORMANCE

The unsaturated zone is an important natural barrier for the performance of the repository system at Yucca Mountain. The active-fracture concept is an important element of the unsaturated zone transport model, which is used primarily to represent the function of the unsaturated zone barrier below the repository in limiting transport from the drift invert to the saturated zone. The abstraction of the unsaturated zone transport model directly supports TSPA.

C.3 RESPONSE

Both TSPAI 3.28 and 3.29 relate to the use of the active-fracture model for TSPA. This response is guided by both the original language of the agreements (Reamer 2001) and the summary of concerns described in Section C.1.1.

Since agreements TSPAI 3.28 and 3.29 were reached in 2001, and due to subsequent discussions in the *Integrated Issue Resolution Status Report* (NRC 2002), the following model reports have been revised:

- *UZ Flow Models and Submodels* (BSC 2003a)
- *Analysis of Hydrologic Properties Data* (BSC 2003b)
- *Radionuclide Transport Models Under Ambient Conditions* (BSC 2003c)
- *Calibrated Properties Model* (BSC 2003d)
- *Particle Tracking Model and Abstraction of Transport Processes* (BSC 2004).

These revisions provide independent lines of evidence that improve confidence in the active-fracture model, verify the implementation of the active-fracture model with matrix diffusion in the total system performance assessment for the license application (TSPA-LA) abstraction and improve transparency of implementation.

C.3.1 Independent Lines of Evidence for Additional Confidence in Active-Fracture Model (TSPAI 3.28)

In the active-fracture model conceptualization (Liu et al. 1998, pp. 2638 to 2641), only a portion of the fractures in a fracture network are active (i.e., hydraulically conductive) under unsaturated

conditions (Sections 3.2 and 6.3.7 in this technical basis document). The active portion is defined as a function of water saturation, S_e, to the power of the active-fracture parameter γ (where γ is greater than or equal to 0 and less than or equal to 1) (Liu et al. 1998, pp. 2638 to 2641). A γ value of 0 or an S_e value of 1 (corresponding to saturated conditions) indicates all fractures are active, while a γ value of 1 indicates the smallest active-fracture portion for a given saturation. The active-fracture model requires reformulation of the fracture–matrix interface area and the relative permeability and capillary pressure functions of the fracture (BSC 2003a, Section 6.8).

Evidence in support of the active-fracture model comes from the comparison of transport simulations with field data. These cases are summarized below and discussed in detail in Section C.4.1.

Groundwater Age Predictions Compared to ^{14}C Measurements–The sensitivity of groundwater age predictions to the active-fracture model parameter, γ, was evaluated in one-dimensional numerical simulations. A range of γ values of 0.2 to 0.4 provided the best fit to borehole ^{14}C data in the TSw unit (BSC 2003b, pp. 78 to 82). Subsequent testing of a three-dimensional transport model (BSC 2003a, Section 7.5) showed that a γ value equal to the higher value from the range in the one-dimensional study (0.4) provided the best fit to the borehole groundwater age data.

Simulation of Fraction of Active Fractures Compared to Mineral Fracture Coating Data– Fracture coating data provide additional confidence that the active-fracture model appropriately describes water flow in fracture networks (BSC 2003b, Section 7.2.2). The presence of mineral coating on only a portion of the fractures along the Exploratory Studies Facility (ESF) shows that not all fractures transmit water, strongly supporting the concept of the active-fracture model. Furthermore, the estimated number of active fractures predicted from active-fracture model simulations based on the active-fracture model is consistent with measured values. Finally, these predictions used the same range of γ values used to fit the ^{14}C data, providing additional confidence in the active-fracture model.

Consistency Between Active-Fracture Model and Fractal Flow Patterns–Unsaturated flow patterns in a fracture network can be fractal. *Analysis of Hydrologic Properties Data* (BSC 2003b, Section 6.7) shows that the frequency of fractures having mineral coating in the ESF is consistent with a fractal flow pattern in the fracture network. A correspondence between γ and the fractal dimension of the flow system shows that the active-fracture model is theoretically consistent with fractal flow behavior in an unsaturated fracture network.

Final Comments–The active-fracture model describes flow and transport in a fracture network. The testing in Alcove 8–Niche 3 performed to date reflects transport mainly through a fault (see Section 5.4.4 in this technical basis document), which is geometrically distinct from a fracture network. Furthermore, the test conditions resulted in relatively high water saturations. Testing under these conditions cannot provide independent evidence to support the active fracture model. Therefore, because field data are relatively sparse and support the active fracture model only indirectly, TSPA modeling uses a range of active fracture model parameters from three infiltration scenarios, as described in the next section.

C.3.2   Sources and Estimation Methods of Abstraction Transport Model Parameters (TSPAI 3.28 and 3.29)

Input Parameters for Rock Properties for Abstraction Model–The sources for rock properties for the abstraction model are listed in *Particle Tracking Model and Abstraction of Transport Processes* (BSC 2004) (see Table C-1). These include fracture porosity, fracture frequency, active-fracture model parameters, and fracture aperture. The use of these parameters is summarized in Section C.4.2.1.

Table C-1. Input Parameters

Parameter Name	Parameter Source	Parameter Values	Units	Distribution (or single value if fixed)
Fracture porosity	BSC 2003b	Varies from layer to layer	None	Beta distribution. Layers are grouped together based on similar rock properties.
Fracture frequency	BSC 2003b	Varies from layer to layer	1/m	Log-normal distribution
Active-fracture model parameters	BSC 2003a	Varies from layer to layer and with infiltration scenario	None	Fixed value for a specific infiltration
Fracture residual saturation	BSC 2003d	0.01	None	Fixed
Fracture spacing and aperture	BSC 2003b	Varies from layer to layer	m	Layers with similar rock properties are grouped together and the parameters are sampled.
Matrix diffusion coefficient	BSC 2003e	Sampled parameter values	m^2/s	Layers are grouped together based on similar rock properties and parameters are sampled for estimating matrix diffusion coefficient.

NOTE: Citations can be found in *Particle Tracking Model and Abstraction of Transport Processes* (BSC 2004); extracted from *Particle Tracking Model and Abstraction of Transport Processes* (BSC 2004, Section 4, Table 4-2).

Porosity Measurements–Porosity measurements are derived from gas tracer test data and observations of fracture geometry in the ESF, as described in Section C.4.2.2.

Development of Fracture Properties from Field Data–*Analysis of Hydrologic Properties Data* (BSC 2003b, Section 6.1.2) documents the development of fracture properties (i.e., fracture frequency, intensity, fracture interface area, and aperture) from field data. This is summarized in Section C.4.2.3.

Fracture Aperture, Porosity, and Frequency Data in Abstraction Model–Fracture porosity and frequency data (the inverse of fracture spacing) are sampled from a mean and standard deviation for each group of values in order to account for parameter uncertainty (BSC 2004, Section 6.5.7). Fracture apertures in the abstraction model are computed from a relationship between sampled fracture porosity and frequency (BSC 2004, Section 6.5.7). This is summarized in Section C.4.2.4.

Residual Saturation and the Active-Fracture Model γ Parameter Values in the Abstraction Model–For the abstraction model, the active-fracture model γ parameter is tabulated for the lower-bound, mean, and upper-bound infiltration scenarios for the model layers in Tables C-2 to C-4 (BSC 2004, Tables 6-8 to 6-10). The active-fracture model γ parameter is the same for model layers within a given hydrogeologic unit that have the same alteration (e.g. welded, vitric, zeolitic). A constant fracture residual saturation of 0.01 is used for all layers.

Table C-2. Fracture γ Parameter for Lower-Bound Infiltration Scenario

Unsaturated Zone Flow Model Layer[a]	Fracture γ	Unsaturated Zone Flow Model Layer[a]	Fracture γ	Input Description	Type of Uncertainty
tcw11	0.4834	ch1 (zeolitic)	0.2759	This value is read in by FEHM and used in calculating fracture spacing values based on the active-fracture model.	Fixed value for each layer but varies from layer to layer. The value also depends on climate.
tcw12	0.4834	ch2 (zeolitic)	0.2759		
tcw13	0.4834	ch3 (zeolitic)	0.2759		
ptn21	0.1032×10^{-1}	ch4 (zeolitic)	0.2759		
ptn22	0.1032×10^{-1}	ch5 (zeolitic)	0.2759		
ptn23	0.1032×10^{-1}	ch6 (zeolitic)	0.2759		
ptn24	0.1032×10^{-1}	pp4	0.2759		
ptn25	0.1032×10^{-1}	pp3	0.2476		
ptn26	0.1032×10^{-1}	pp2	0.2476		
tsw31	0.3741×10^{-1}	p-p1	0.2776		
tsw32	0.5284	bf3	0.2476		
tsw33	0.5284	bf2	0.2759		
tsw34	0.4764	tr3	0.2476		
tsw35	0.4764	tr2	0.2759		
tsw36	0.4764	pc38[b]	0.00		
tsw37	0.4764	pc39[b]	0.00		
tsw38	0.4764	Pc (zeolitic)[b]	0.00		
tsw39 (zeolitic)	0.2759	pc2f (zeolitic)[b]	0.00		
tsw39 (vitric)	0.2500	pc5 (zeolitic)[b]	0.00		
ch1 (vitric)	0.2500	pc6 (zeolitic)[b]	0.00		
ch2 (vitric)	0.2500	pc4[b]	0.00		
ch3(vitric)	0.2500	tcwff (fault)	0.4000		
ch4 (vitric)	0.2500	ptnff (fault)	0.1138		
ch5 (vitric)	0.2500	tswff (fault)	0.3000		
ch6 (vitric)	0.2500	chnff (fault)	0.3000		

Source: BSC 2004, Table 6-8.

NOTE: [a]See Table 2-1.
[b]Saturated zone model layers.

Table C-3. Fracture γ Parameter for Mean Infiltration Scenario

Unsaturated Zone Flow Model Layer[a]	Fracture γ	Unsaturated Zone Flow Model Layer[a]	Fracture γ	Input Description	Type of Uncertainty
tcw11	0.5866	ch1 (zeolitic)	0.3704	This value is read in by FEHM and used in calculating fracture spacing values based on the active-fracture model.	Fixed value for each layer but varies from layer to layer. The values also depend on climate.
tcw12	0.5866	ch2 (zeolitic)	0.3704		
tcw13	0.5866	ch3 (zeolitic)	0.3704		
ptn21	0.9051×10^{-1}	ch4 (zeolitic)	0.3704		
ptn22	0.9051×10^{-1}	ch5 (zeolitic)	0.3704		
ptn23	0.9051×10^{-1}	ch6 (zeolitic)	0.3704		
ptn24	0.9051×10^{-1}	pp4	0.3704		
ptn25	0.9051×10^{-1}	pp3	0.1989		
ptn26	0.9051×10^{-1}	pp2	0.1989		
tsw31	0.1289	p-p1	0.3704		
tsw32	0.6000	bf3	0.1989		
tsw33	0.6000	bf2	0.3704		
tsw34	0.5686	tr3	0.1989		
tsw35	0.5686	tr2	0.3704		
tsw36	0.5686	pc38[b]	0.00		
tsw37	0.5686	pc39[b]	0.00		
tsw38	0.5686	Pc (zeolitic)[b]	0.00		
tsw39 (zeolitic)	0.3704	pc2f (zeolitic)[b]	0.00		
tsw39 (vitric)	0.2500	pc5 (zeolitic)[b]	0.00		
ch1 (vitric)	0.2500	pc6 (zeolitic)[b]	0.00		
ch2 (vitric)	0.2500	pc4[b]	0.00		
ch3(vitric)	0.2500	tcwff (fault)	0.4000		
ch4 (vitric)	0.2500	ptnff (fault)	0.1138		
ch5 (vitric)	0.2500	tswff (fault)	0.3000		
ch6 (vitric)	0.2500	chnff (fault)	0.3000		

Source: BSC 2004, Table 6-9.

NOTE: [a]See Table 2-1.
[b]Saturated zone model layers.

Table C-4. Fracture γ Parameter for Upper-Bound Infiltration Scenario

Unsaturated Zone Flow Model Layer[a]	Fracture γ	Unsaturated Zone Flow Model Layer[a]	Fracture γ	Input Description	Type of Uncertainty
tcw11	0.5000	ch1 (zeolitic)	0.5000	This value is read in by FEHM and used in calculating fracture spacing values based on the active-fracture model.	Fixed value for each layer but varies from layer to layer. The value also depends on climate.
tcw12	0.5000	ch2 (zeolitic)	0.5000		
tcw13	0.5000	ch3 (zeolitic)	0.5000		
ptn21	0.8319×10^{-1}	ch4 (zeolitic)	0.5000		
ptn22	0.8319×10^{-1}	ch5 (zeolitic)	0.5000		
ptn23	0.8319×10^{-1}	ch6 (zeolitic)	0.5000		
ptn24	0.8319×10^{-1}	pp4	0.5000		
ptn25	0.8319×10^{-1}	pp3	0.5000		
ptn26	0.8319×10^{-1}	pp2	0.5000		
tsw31	0.1000	pp1	0.5000		
tsw32	0.5606	bf3	0.5000		
tsw33	0.5606	bf2	0.5000		
tsw34	0.5700	tr3	0.5000		
tsw35	0.5700	tr2	0.5000		
tsw36	0.5700	pc38[b]	0.0000		
tsw37	0.5700	pc39[b]	0.0000		
tsw38	0.5700	Pc (zeolitic)[b]	0.0000		
tsw39 (zeolitic)	0.5000	pc2f (zeolitic)[b]	0.0000		
tsw39 (vitric)	0.2500	pc5 (zeolitic)[b]	0.0000		
ch1 (vitric)	0.2500	pc6 (zeolitic)[b]	0.0000		
ch2 (vitric)	0.2500	pc4[b]	0.0000		
ch3(vitric)	0.2500	tcwff (fault)	0.4000		
ch4 (vitric)	0.2500	ptnff (fault)	0.1138		
ch5 (vitric)	0.2500	tswff (fault)	0.3000		
ch6 (vitric)	0.2500	chnff (fault)	0.3000		

Source: BSC 2004, Table 6-10.

NOTE: [a]See Table 2-1.
[b]Saturated zone model layers.

C.3.3 Adaptation of the Active-Fracture Model for Abstraction Transport Model Calculations

Particle Tracking Model and Abstraction of Transport Processes (BSC 2004, Section III-5) describes the method for adapting the active-fracture model for abstraction transport model calculations. The active-fracture model is incorporated into the model by effectively reducing the interfacial area and the fracture frequency to account for the fact that not all fractures are flowing. Active-fracture model-based adjustments in terms of γ and S_e are applied to the interface area and fracture spacing. Aperture values are not changed. The detailed discussion is presented in Section C.4.3.

The following addresses the question of whether the fraction of active fractures is factored into the calculation of fluid velocity in the transport model. The fraction of active fractures is

implicitly considered in the calculation of fluid velocity in the transport model because the flow fields are developed and imported directly into the transport abstraction model. Fluid residence time in the fractures is equal to the volume of water in a computational cell divided by the volumetric flow rate of the fluid. In turn, the volume of fluid in a cell is the total volume times the volumetric water content. All these terms are calculated in flow model simulations and imported into the transport model. Therefore, fluid velocities and transport times do not need any further adjustment to account for active fractures because the flow field calculations have already accounted for the active-fracture concept.

C.3.4 Verification of the Active-Fracture Model with Matrix Diffusion Integration in Total System Performance Assessment Abstraction (TSPAI 3.29)

In *Particle Tracking Model and Abstraction of Transport Processes* (BSC 2004, Section 7), the implementation of the active-fracture model in the abstraction model was shown to reproduce the qualitative features of the breakthrough curves documented in the process model reports on which the abstraction is based. Thus, the abstraction model has been compared with the full complexity of the unsaturated zone model and found to be able to represent the system robustly and efficiently for the entire range of parameters and conceptual models required. The following tests were documented in *Particle Tracking Model and Abstraction of Transport Processes* (BSC 2004, Section 7) and are summarized below (see Section C.4.4 for additional details).

Comparison with the Dual-K and MINC Model Formulations on a Two-Dimensional Cross-Sectional Model–*Particle Tracking Model and Abstraction of Transport Processes* (BSC 2004, Section 7.2) describes the comparison of the particle tracking model for abstraction with simulations from *Radionuclide Transport Models Under Ambient Conditions* (BSC 2003c) using the T2R3D code (LBNL 1999) in a two-dimensional cross-sectional model. The particle tracking model tests two alternative conceptual models to describe fracture–matrix interactions: the discrete fracture model and the dual-k formulation. The T2R3D process model uses both the dual-k and multiple interacting continua (MINC) formulations. The conceptual model for the fracture–matrix interactions is shown to impact the predicted behavior, especially for the fastest traveling portion of the solute. Comparisons for the range of diffusion behavior also show that the abstraction model compares adequately with the process models and properly accounts for the role of conceptual model uncertainty in the fracture–matrix interaction model.

Comparison with T2R3D Process Model for Three-Dimensional System–The abstraction transport model results are compared with results from T2R3D, documented in *Radionuclide Transport Models Under Ambient Conditions* (BSC 2003c) and summarized in Section 7.4 in this technical basis document. The agreement between these models shows that all significant features of the unsaturated zone transport system are captured with the abstraction model. The abstraction model is also shown to produce reasonable results for a wide range of diffusion coefficients. The comparison of different fracture–matrix interaction models for the FEHM particle tracking model are also reasonable and provide additional evidence for the correct functioning of the fracture–matrix interaction model. The sensitivity of breakthrough of a conservative tracer to the active-fracture model γ parameter is consistent between the two models, further verifying that the implementation of the active-fracture model with matrix diffusion in the abstraction model replicates the behavior of the process model.

The information in this report is responsive to agreements TSPAI 3.28 and 3.29 made between the DOE and NRC. The report contains the information that DOE considers necessary for NRC review for closure of these agreements.

C.4   BASIS FOR THE RESPONSE

C.4.1   Independent Lines of Evidence

C.4.1.1   Groundwater Age Predictions Compared to [14]C Measurements

The unsaturated zone of Yucca Mountain is a quasi–steady-state flow system, with very small infiltration and percolation rates. The matrix pore-water age corresponds to the mean time required for the groundwater to travel from the ground surface to where it is sampled in the system. The age can be considered constant at each location in this quasi–steady-state flow system, but spatially variable. The migration of water molecules is governed by advection and diffusion, similar to solute transport (Goode 1996). Thus, tracer transport times (ages) can be simulated using a conservative transport model.

The detailed description of the simulation of groundwater ages in the unsaturated zone and comparison with ^{14}C data can be found in *Analysis of Hydrologic Properties Data* (BSC 2003b, Section 7.2.1). [14]C data were collected from perched water, pore water, and gas samples from the Yucca Mountain unsaturated zone (BSC 2002, Section 6.6.4). [14]C data from gas samples are considered to be most representative of in situ conditions and are interpreted to be representative of ages of the in situ pore water (Yang 2002, Section 4.1.2). [14]C data from perched water are not used for active-fracture model testing because perched water comes mainly from matrix flow through the PTn, which is insensitive to the active-fracture model parameters (Wang 2003). [14]C residence ages (BSC 2002, Table 20) were calculated using the data from two boreholes, USW SD-12 and USW UZ-1.

One-dimensional numerical models were developed for the boreholes and the rock properties were taken from calibration with present-day, mean infiltration maps. The value of the active-fracture model parameter γ for model layers within the repository horizon (tsw32 to tsw38, see Table 4-1 for the definition of model layers) is varied for different simulations as a sensitivity test. The top boundary condition corresponds to the present-day infiltration rate for flow and a constant tracer concentration for transport simulations. Simulated water transport times (or ages) for rock matrices are compared with ^{14}C ages. A simulated water transport time at a given depth (or average transport time for water particles from the ground surface) is determined as the time when the matrix concentration reaches 50% of the top boundary concentration.

Figure C-1 shows simulated water ages for different γ values of unsaturated zone model layers tsw32 to tsw38. The considerable sensitivity of simulated results to γ indicates that ^{14}C data are useful for validating the active-fracture model and for constraining the γ values for the TSw unit. For γ values ranging from 0.2 to 0.4, simulated results approximately match the observations. A larger γ value generally corresponds to a longer time for transport into the matrix because of a smaller degree of matrix diffusion, resulting from a smaller fracture–matrix interfacial area available for mass transport between fractures and the matrix.
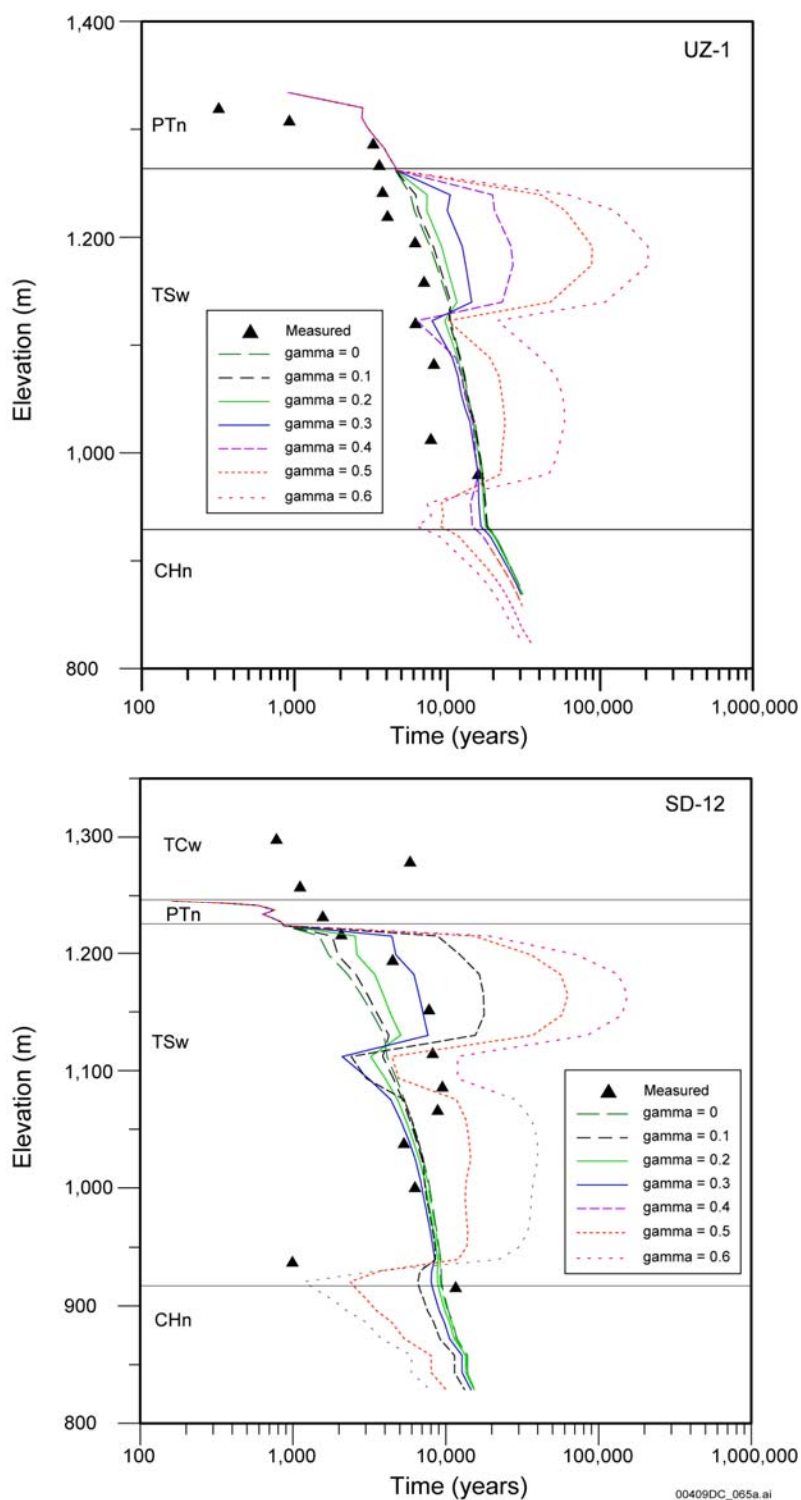
Source: BSC 2003b, Figure 13.

Figure C-1. Comparisons between One-Dimensional Simulated Water Transport Times (Ages) in the Rock Matrix at Boreholes for Several γ Values with Measured ^{14}C Ages at Boreholes USW UZ-1 and USW SD-12

Simulated water ages increase sharply at an elevation of about 1,100 m for the two boreholes (Figure C-1). This is because the upper portion of the TSw unit has relatively small fracture density values and, consequently, a smaller degree of matrix diffusion for a given γ value (Table C-5). For borehole USW UZ-1, the simulated water ages are generally greater than the observations. This may be a result of larger fracture densities (and consequently more matrix diffusion) at the borehole location compared to the layer-averaged fracture properties used in the unsaturated zone model (BSC 2003b, Section 5). The results are fairly insensitive to γ values less than 0.2, and a γ value of 0.2 to 0.4 best captures the magnitude and trends of the measured data in both boreholes.

Estimating groundwater age in the unsaturated zone was also tested with a three-dimensional tracer transport model based on the calibrated groundwater flow field (BSC 2003a, Section 7.5). The three-dimensional transport model simulation was performed using T2R3D V1.4 (LBNL 1999). The three-dimensional flow field obtained with the base-case water-flow simulation (present-day, mean infiltration) is incorporated to simulate the matrix pore-water age in the entire model domain. A pulse tracer source is introduced on the ground surface through fractures, and the tracer concentration in rock matrix in the entire domain was observed. The simulated matrix pore-water age, at a specific location, is then identified as the time required for the tracer pulse (appearing as concentration peaks in the unsaturated zone) to travel to that location and is determined from the concentration breakthrough curve.

The simulated matrix pore-water ages for boreholes USW UZ-1 and USW SD-12 were plotted and compared to the measured age data (^{14}C) used for the one-dimensional study (Figures C-2 and C-3). These figures show that the simulated matrix pore-water ages in the upper portion of the TSw unit are larger than the measured ^{14}C ages for a γ value of 0.6. This is caused mainly by the underestimated advective and diffusive solute flux between fractures and matrix along these subunits. The smaller the flux or the slower the diffusion from fractures to matrix, the older the ages for matrix pore water, which occurs for larger γ values.

Figure C-2 (USW UZ-1) shows that the simulated matrix pore-water ages for the upper TSw units with a γ value of 0.4 match the measured ^{14}C ages well. Simulated ages for lower TSw units are a little bit younger than the measurements but are also within the range of measured ^{14}C age of TSw units. Figure C-3 (USW SD-12) shows that the match between the simulated groundwater ages using a γ value of 0.4 and the measurements is reasonably close (the simulated ages for TSw unit are within the range of the measured ^{14}C age of TSw units).

Table C-5. Fracture Properties for Unsaturated Zone Model Layers

Unsaturated Zone Model Layer	Permeability (m²)				Frequency (m⁻¹)			van Genuchten parameter			Porosity	Std	Afm
	k_G	log(k_G)	$\sigma_{log(kG)}$	N	f	σ_f	N	α (Pa⁻¹)	log(α)	m			
tcw11	3.0×10^{-11}	-10.52	-	2	0.92	0.94	76	5.0×10^{-3}	-2.30	0.633	2.4×10^{-2}	-	1.56
tcw12	5.3×10^{-12}	-11.28	0.78	80	1.91	2.09	1241	2.2×10^{-3}	-2.66	0.633	1.7×10^{-2}	-	13.39
tcw13	4.5×10^{-12}	-11.35	1.15	3	2.79	1.43	60	1.9×10^{-3}	-2.73	0.633	1.3×10^{-2}	-	3.77
ptn21	3.2×10^{-12}	-11.49	0.88	12	0.67	0.92	76	2.7×10^{-3}	-2.57	0.633	9.2×10^{-3}	-	1
ptn22	3.0×10^{-13}	-12.52	0.20	4	0.46	-	-	1.4×10^{-3}	-2.86	0.633	1.0×10^{-2}	-	1.41
ptn23	3.0×10^{-13}	-12.52	0.20	4	0.57	-	63	1.2×10^{-3}	-2.91	0.633	2.1×10^{-3}	-	1.75
ptn24	3.0×10^{-12}	-11.52	-	1	0.46	0.45	18	3.0×10^{-3}	-2.53	0.633	1.0×10^{-2}	-	0.34
ptn25	1.7×10^{-13}	-12.78	0.10	7	0.52	0.6	72	1.1×10^{-3}	-2.96	0.633	5.5×10^{-3}	-	1.09
ptn26	2.2×10^{-13}	-12.66	-	1	0.97	0.84	114	9.6×10^{-4}	-3.02	0.633	3.1×10^{-3}	-	3.56
tsw31	8.1×10^{-13}	-12.09	-	-	2.17	2.37	140	1.1×10^{-3}	-2.96	0.633	5.0×10^{-3}	-	3.86
tsw32	7.1×10^{-13}	-12.15	0.66	31	1.12	1.09	842	1.4×10^{-3}	-2.86	0.633	8.3×10^{-3}	-	3.21
tsw33	7.8×10^{-13}	-12.11	0.61	27	0.81	1.03	1329	1.6×10^{-3}	-2.80	0.633	5.8×10^{-3}	-	4.44
tsw34	3.3×10^{-13}	-12.48	0.47	180	4.32	3.42	10646	6.7×10^{-4}	-3.18	0.633	8.5×10^{-3}	2.50×10^{-3}	13.54
alternate tsw34	1.5×10^{-13}	-12.81	0.75	180									
tsw35	9.1×10^{-13}	-12.04	0.54	31	3.16	-	595	1.0×10^{-3}	-2.99	0.633	9.6×10^{-3}	-	9.68
tsw3[67]	1.3×10^{-12}	-11.87	0.28	19	4.02	-	526	1.1×10^{-3}	-2.96	0.633	1.3×10^{-2}	-	12.31
tsw38	8.1×10^{-13}	-12.09	-	-	4.36	-	37	8.9×10^{-4}	-3.05	0.633	1.1×10^{-2}	-	13.34
tsw39	8.1×10^{-13}	-12.09	-	-	0.96	-	46	1.5×10^{-3}	-2.82	0.633	4.3×10^{-3}	-	2.95
ch1Ze	2.5×10^{-14}	-13.60	-	-	0.04	-	3	1.4×10^{-3}	-2.86	0.633	1.6×10^{-4}	-	0.11
ch1Vl	2.2×10^{-13}	-12.66	-	-	0.10	-	11	2.1×10^{-3}	-2.69	0.633	6.1×10^{-4}	-	0.3
ch[23456]Vl	2.2×10^{-13}	-12.66	-	-	0.14	-	25	1.9×10^{-3}	-2.73	0.633	7.7×10^{-4}	-	0.43
ch[2345]Ze	2.5×10^{-14}	-13.60	-	1	0.14	-	25	8.9×10^{-4}	-3.05	0.633	3.7×10^{-4}	-	0.43
ch6	2.5×10^{-14}	-13.60	-	-	0.04	-	-	1.4×10^{-3}	-2.86	0.633	1.6×10^{-4}	-	0.11
pp4	2.5×10^{-14}	-13.60	-	-	0.14	-	-	8.9×10^{-4}	-3.05	0.633	3.7×10^{-4}	-	0.43
pp3	2.2×10^{-13}	-12.66	-	-	0.20	-	-	1.6×10^{-3}	-2.78	0.633	9.7×10^{-4}	-	0.61
pp2	2.2×10^{-13}	-12.66	-	-	0.20	-	-	1.6×10^{-3}	-2.78	0.633	9.7×10^{-4}	-	0.61
pp1	2.5×10^{-14}	-13.60	-	-	0.14	-	-	8.9×10^{-4}	-3.05	0.633	3.7×10^{-4}	-	0.43
bf3	2.2×10^{-13}	-12.66	-	-	0.20	-	-	1.6×10^{-3}	-2.78	0.633	9.7×10^{-4}	-	0.61
bf2	2.5×10^{-14}	-13.60	-	-	0.14	-	-	8.9×10^{-4}	-3.05	0.633	3.7×10^{-4}	-	0.43
tr3	2.2×10^{-13}	-12.66	-	-	0.20	-	-	1.6×10^{-3}	-2.78	0.633	9.7×10^{-4}	-	0.61
tr2	2.5×10^{-14}	-13.60	-	-	0.14	-	-	8.9×10^{-4}	-3.05	0.633	3.7×10^{-4}	-	0.43

Source: BSC 2003b, Table 7.

NOTE: k is permeability (geometric mean).
σ is standard deviation.
N is number of samples.
f is fracture frequency.
α and m are fitting parameters for the van Genuchten water potential relationship.
Std refers to standard deviation for fracture porosity.
Afm refers to fracture–matrix interface area (m²/m³).
"-" means that no data are available.

The larger γ (0.6 for the TSw units) used in the base-case unsaturated zone flow model gives slightly earlier breakthrough times for solute transport from the repository to the water table and, therefore, provides more conservative results. This is because a larger γ factor corresponds to a larger fracture pore velocity and a smaller effective fracture–matrix interface area (or a smaller degree of fracture–matrix interaction) (BSC 2003a, Section 6.8).
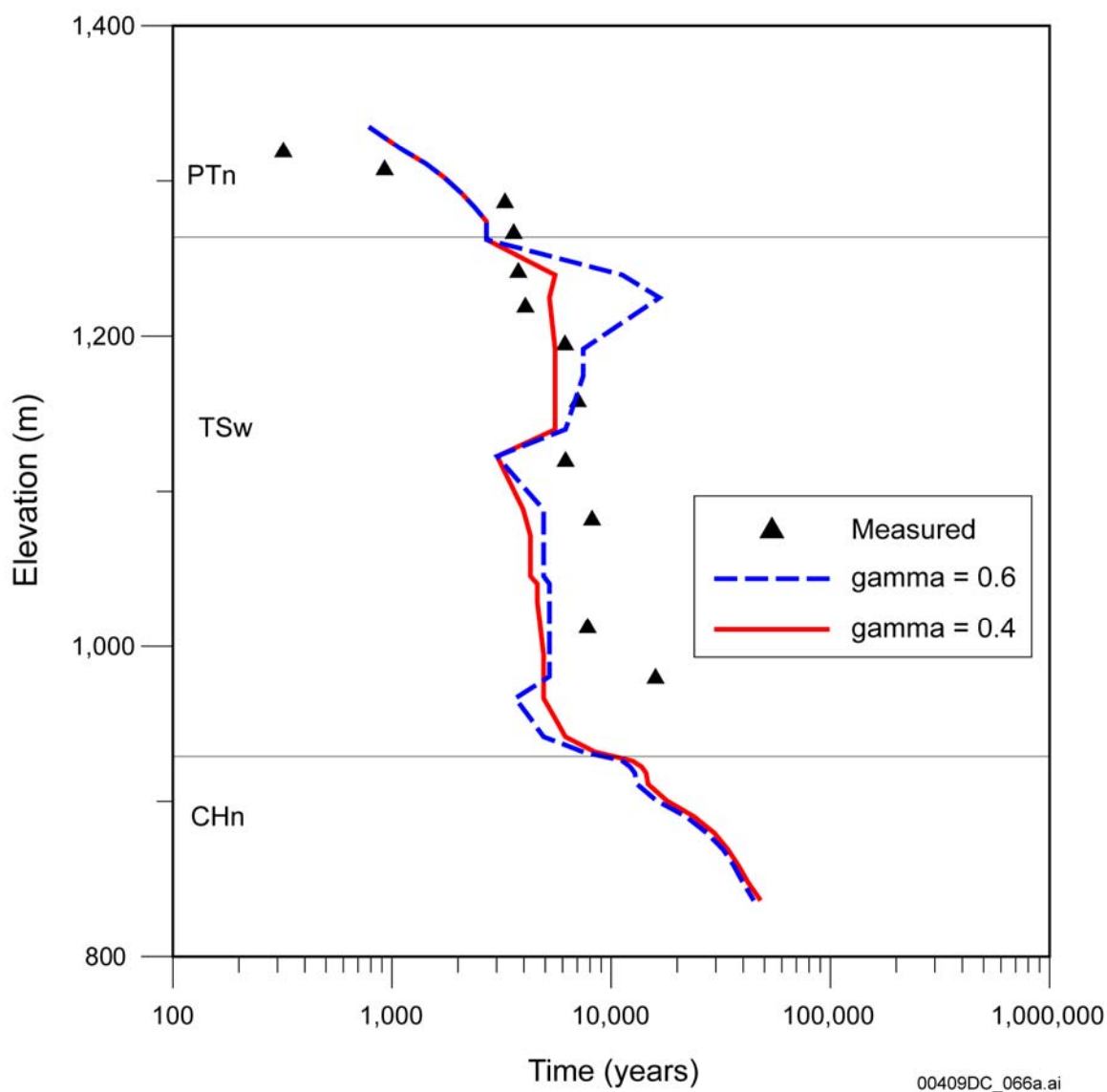
Source: BSC 2003a, Figure 7.5-1.

Figure C-2. Simulated Groundwater Age for Borehole UZ-1 Compared to the Measured ^{14}C Age
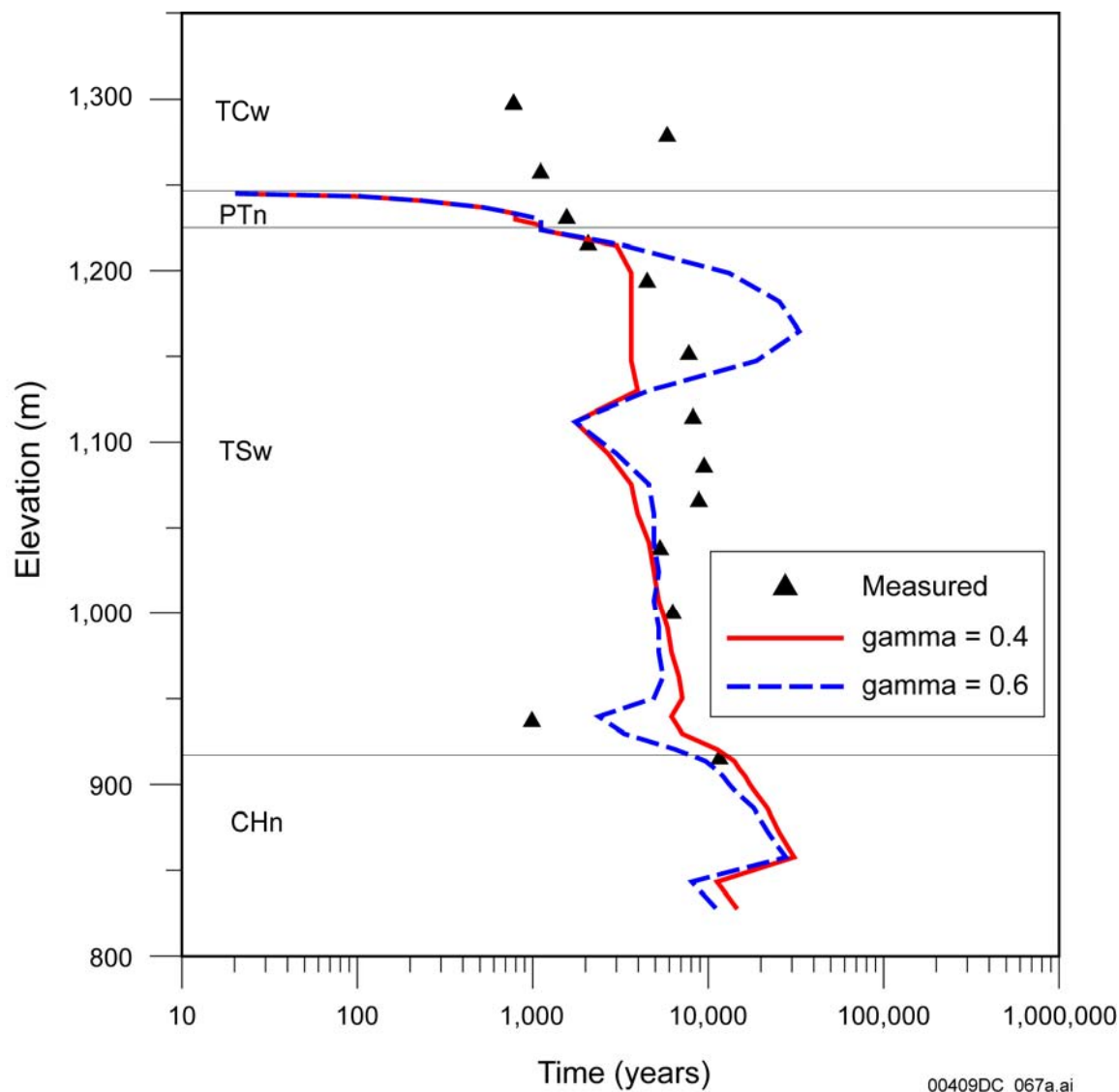
Source: BSC 2003a, Figure 7.5-2.

Figure C-3. Simulated Groundwater Age for Borehole USW SD-12 Compared to the Measured ^{14}C Age

C.4.1.2 Simulation of Fraction of Active Fractures Compared to Mineral Fracture Coating Data

Fracture coating is generally a signature of water flow paths. Therefore, the coating data are useful for testing the active-fracture model that describes water flow in fractures. Details of this effort can be found in *Analysis of Hydrologic Properties Data* (BSC 2003b, Section 7.2.2).

The observed spatial distribution of fractures with coatings in the ESF is used to estimate the portion of active fractures in the unsaturated zone. For a given survey interval along the ESF, a frequency of coated fractures can be estimated for a geologic unit, based on the total number of coated fractures. The ratio of coated-fracture frequency to total fracture frequency provides an

estimate of the portion of active fractures for the given geologic unit (Wang 2003). The estimated average portion of active fractures for the TSw is 7.2%.

The abundance of mineral coating (coating volume divided by total rock volume), divided by the corresponding fracture porosity, gives another estimate of the portion of the active fractures in the unsaturated zone under ambient conditions. Abundance data for all intervals in welded tuffs have an arithmetic mean of 0.084% (BSC 2002, Section 6.10.1.1), while a typical fracture porosity is 1% (Table C-5). Therefore, an estimate of the average portion of active fractures for welded units is 8.4%, close to the estimate determined from the frequency of coated fractures. While fracture coatings may not precisely represent active flow paths in the unsaturated zone and some flow paths may not have coatings (Liu et al. 1998), these values at least give a rough estimate of lower limits for the portion of active fractures in the unsaturated zone (about 10%).

Mineral growth rate data imply that the unsaturated zone fracture network has maintained a large degree of hydrologic stability over time and that fracture flow paths in the deep unsaturated zone are buffered from climate-induced variations in precipitation and infiltration (BSC 2002, Section 6.10.3.9). If the active-fracture model actually represents water flow processes in the unsaturated zone, modeling results based on the active-fracture model should be consistent with this important observation.

To check the consistency of the active-fracture model against the coating data, a one-dimensional model for borehole USW SD-12 is used. The model is the same as that used for the one-dimensional ^{14}C simulations and described in *Analysis of Hydrologic Properties Data* (BSC 2003b, Section 7.2.1) and in Section C.4.1.1. USW SD-12 is chosen because it is located near the middle of the ESF. Two infiltration rates, present-day mean infiltration rate and glacial maximum infiltration rate, are used for simulations. The latter infiltration rate is about five times as large as the former rate and represents the maximum infiltration rate in past climates. Uniform γ distributions within model layers tsw32 to tsw38 are employed.

Figure C-4 shows the simulated average portion of active fractures, f_a, for the relevant model layers (tsw32 to tsw38) as a function of infiltration rate and γ. The average portion is calculated from $f_a = S_e^\gamma$ using the average effective saturation S_e for model layers tsw32 to tsw38. The calculated f_a values range about 10% for γ values close to 0.4, which are similar to those used for matching the ^{14}C data. For the same range of γ values, the calculated f_a values do not change significantly for the two infiltration rates (Figure C-4), which is consistent with the observation of flow-path stability over time.
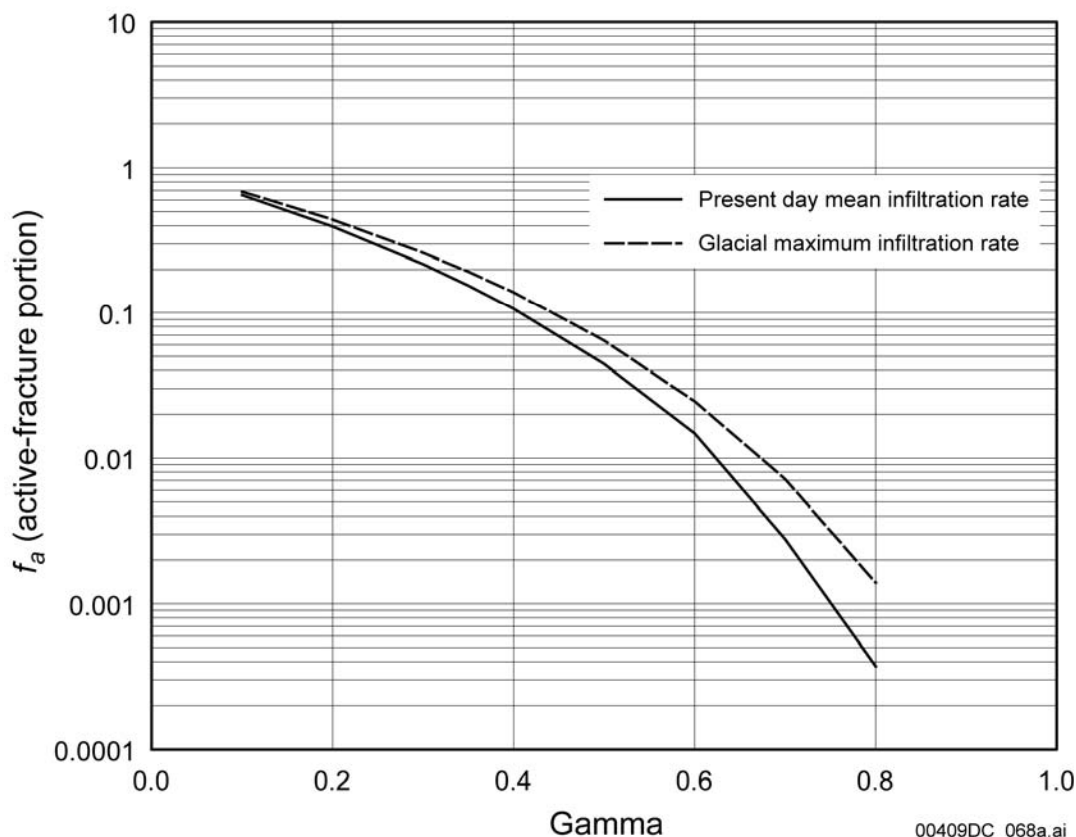
Source: BSC 2003b, Figure 14.

Figure C-4. Simulated Average Portion of Active Fracture for the Relevant Model Layers (tsw32 to tsw38) as a Function of Infiltration Rate and γ

In summary, the simulation results based on the active-fracture model are consistent with both ^{14}C data and fracture coating data for a similar range of γ values.

C.4.1.3 Consistency between Active-Fracture Model and Fractal Flow Patterns

Unsaturated flow patterns in a fracture network are expected to be (at least approximately) fractal. This is supported by fracture coating data from the unsaturated zone of Yucca Mountain and an analysis from *Analysis of Hydrologic Properties Data* (BSC 2003b, Section 6.7) showing that the distribution of coated fractures in the ESF are consistent with a fractal model. Detailed line survey data for coated fractures from the Tptpmn (tsw34) unit (which has the largest number of survey intervals) are analyzed using the box counting method to describe the spatial pattern of fractures that transmit water.

In *Analysis of Hydrologic Properties Data* (BSC 2003b, Section 6.7), a correspondence between γ and the fractal dimension of the flow system is also derived and shows that the active-fracture model can simulate fractal flow behavior in an unsaturated fracture network. This correspondence improves confidence in the active-fracture model because it demonstrates that it is theoretically consistent with an independently derived fractal conceptualization of unsaturated flow that is supported by field data. This section presents the analysis of the fracture coating

data and derivation of the correspondence between γ and the fractal dimension of the flow system from *Analysis of Hydrologic Properties Data* (BSC 2003b, Section 6.7).

The locations of the coated fractures along the survey line form a set of points in a one-dimensional space. For a given box size (length of a segment) l, there are $30/l$ small boxes (or segments) for a given survey interval that is 30 m long. N in this section denotes total numbers of boxes that cover at least one location of the coated fractures (along the survey line) for all the survey intervals. Figure C-5 shows that the observed N values as a function of l can be fitted by a power function with a power of −0.5 that corresponds to a fractal dimension of 0.5 for the set of points. This indicates that coated fractures may result from a fractal flow pattern in the corresponding fracture network.
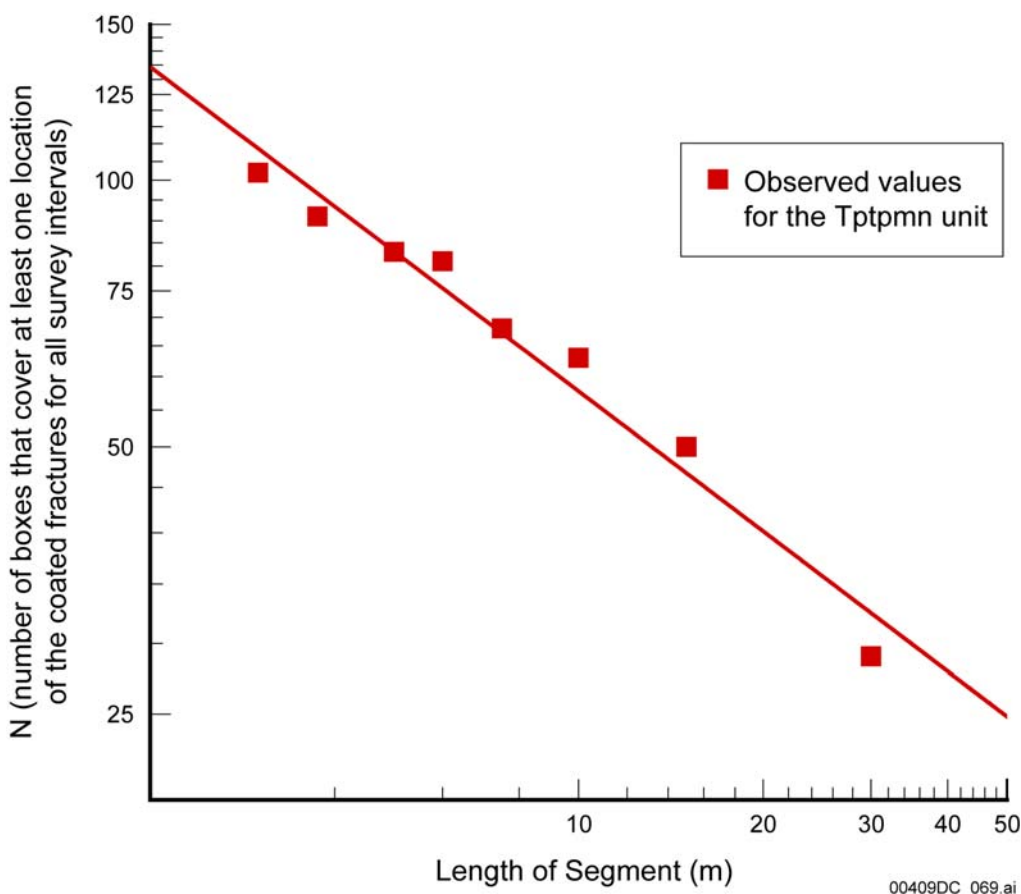
Source: BSC 2003b, Figure 7.

NOTE: The data points correspond to observed values for the Tptpmn unit.

Figure C-5.   Relation between *N* and Length of Segment

A fractal pattern is characterized by the fractal dimension, d_f, that is generally noninteger and less than the corresponding Euclidean dimension of a space, D. The most straightforward method of determining d_f is based on box counting. In this case, the fractal dimension is determined from the following equation by counting the number (N) of boxes (e.g., square and

cubic for two-dimensional and three-dimensional problems, respectively), needed to cover a spatial pattern, as a function of the box size (l) (Feder 1988, pp. 14 to 15):

$$N(l) = \left(\frac{L}{l}\right)^{d_f} \qquad \text{(Eq. C-1)}$$

where L refers to the size of the whole spatial domain under consideration (BSC 2003b, Equation 61). Figure C-6 shows a box-counting procedure for a spatial pattern with a d_f value of 1.6 in a two-dimensional domain with size L (Yamamoto et al. 1993, Figure 3).

If a spatial pattern is uniformly distributed in space, the fractal dimension will be identical to the corresponding Euclidean dimension. In this case, the box number, N^*, and the box size l have the following relation (BSC 2003b, Equation 62):

$$N^*(l) = \left(\frac{L}{l}\right)^{D} \qquad \text{(Eq. C-2)}$$

Consider Figure C-6 to be a gridblock containing a fracture network and the corresponding flow pattern in the fracture network to be fractal. In this case, only a portion of the medium within a gridblock contributes to water flow (Figure C-6). This is conceptually consistent with the active-fracture model (Liu et al. 1998). In Figure C-6, a box is shaded if it covers one or more fractures (or fracture segments) that conduct water. For simplicity, fractures are assumed to be randomly distributed in space, and, thus, the dimension for water saturation distribution is the corresponding Euclidean dimension when all the connected fractures actively conduct water. Combining Equations C-1 and C-2 gives (BSC 2003b, Equation 63):

$$[N(l)]^{1/d_f} = [N^*(l)]^{1/D} \qquad \text{(Eq. C-3)}$$

The average water saturation (S) for the whole gridblock (Figure C-6) is determined as (BSC 2003b, Equation 64):

$$S = \frac{V}{l^D \phi N^*(l)} \qquad \text{(Eq. C-4)}$$

where V is the total water volume (excluding residual water) in fractures within the gridblock (Figure C-6), and ϕ is fracture porosity. Similarly, the average water saturation, S_b, for shaded boxes with a size of l is given as (BSC 2003b, Equation 65):

$$S_b = \frac{V}{l^D \phi N(l)} \qquad \text{(Eq. C-5)}$$

I = L

I = L/2

I = L/4

I = L/8

00409DC_070.ai
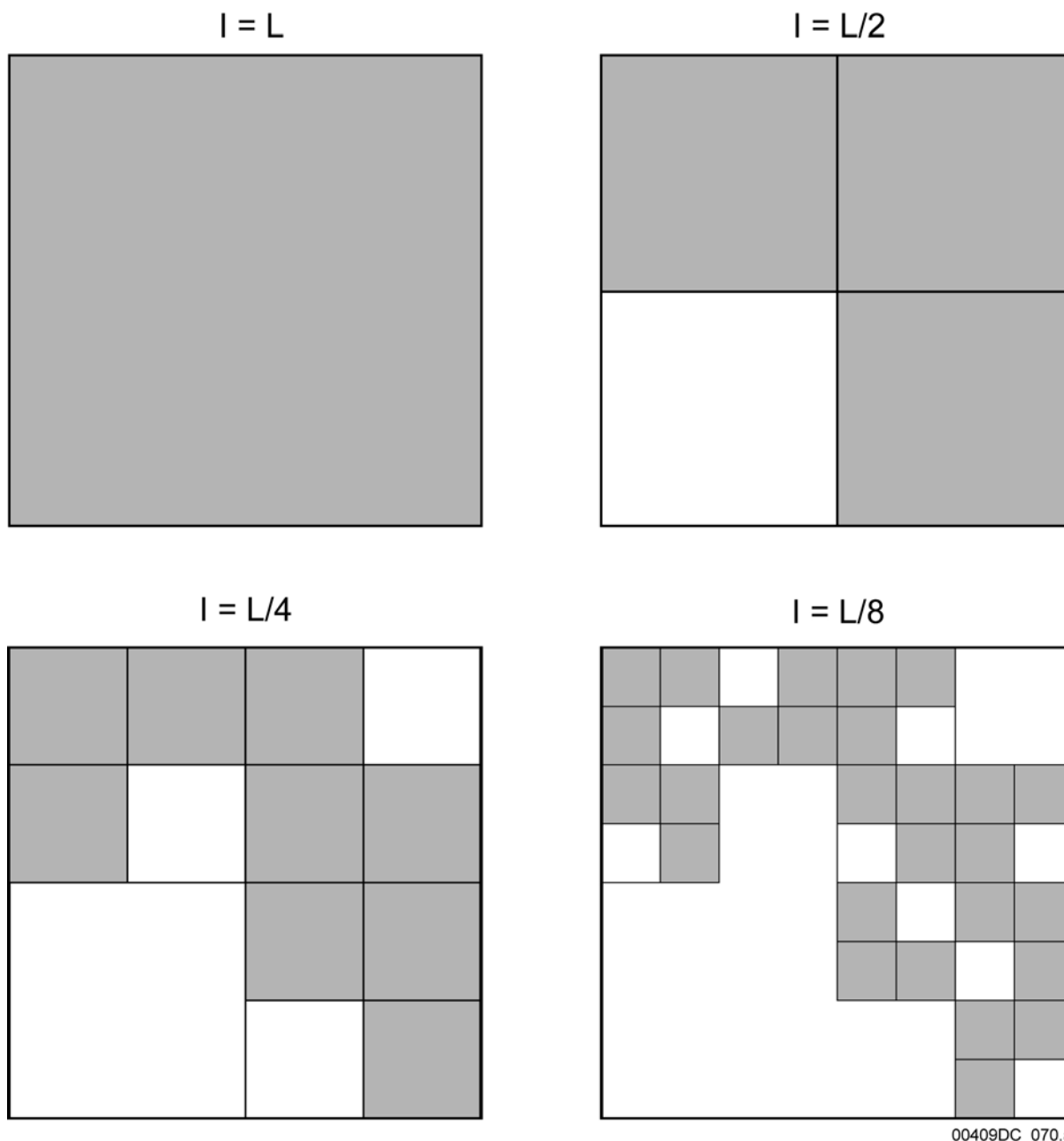
Source: BSC 2003b, Figure 8.

NOTE: Shaded areas contain saturation and active flow.

Figure C-6. Demonstration of Box Counting Procedure for Several Box Sizes

From Figure C-6 (BSC 2003b, Equation 66):

$$\frac{V}{l_1^{\ D}\phi} = 1 \tag{Eq. C-6}$$

Based on Equations C-3 through C-6, the average saturation for shaded boxes with a size of l_1, S_{b1}, can be expressed by (BSC 2003b, Equation 67):

$$S_{b1} = S^{\frac{d_f}{D}} \tag{Eq. C-7}$$

Because a self-affine fractal is similar at different scales, the procedure for deriving Equation C-7 from a gridblock with size L can be applied to shaded boxes with a smaller size l_1. In this case, for a given box size smaller than l_1, the number of shaded boxes will be an averaged number for those within the relatively large shaded boxes with a size of l_1. Again, a box size $l_2 < l_1$ gives a saturation relation (BSC 2003b, Equation 68):

$$S_{b2} = (S_{b1})^{\frac{d_f}{D}} = S^{\left(\frac{d_f}{D}\right)^2} \tag{Eq. C-8}$$

The procedure to obtain Equation C-8 can be continued until it reaches an iteration level n^* at which all the shaded boxes with a size of l_n cover active fractures only. The resultant average saturation for these shaded boxes is (BSC 2003b, Equation 69):

$$S_{bn} = (S)^{\left(\frac{d_f}{D}\right)^{n^*}} \tag{Eq. C-9}$$

By active fracture definition, S_{bn} should be equivalent to the effective saturation of active fractures. Equation C-9 is similar to $f_a = S_e^{\gamma}$, obtained from a key hypothesis of the active-fracture model that the fraction of active fractures in an unsaturated fracture network is a power function of the average effective saturation of the network. Comparing these two equations yields (BSC 2003b, Equation 70):

$$\gamma = 1 - \left(\frac{d_f}{D}\right)^{n^*} \tag{Eq. C-10}$$

Equation C-10 provides the first theoretical relation between the parameter γ and the fractal dimension for a fractal flow system, while γ was initially developed as an empirical parameter (Liu et al. 1998). Therefore, the active-fracture model essentially captures fractional flow behavior at the subgridblock scale (d_f less than D), whereas traditional continuum approaches assume a uniform flow pattern (or effective-saturation distribution) at that scale (corresponding to a d_f value of D or a γ value of 0). In other words, the active-fracture model can be used for simulating fractal flow behavior in an unsaturated fracture network that cannot be handled by the traditional continuum approach.

Equation C-10 implies that in the fractal flow model γ is not a constant, but a function of saturation, because both iteration level n^* and d_f may be dependent on water saturation for a given fracture network. However, a constant γ is a reasonable treatment at least for a limited range of water saturations (or flow conditions), which is the case for the Yucca Mountain unsaturated zone where fracture saturation is typically less than 10% under ambient conditions. It is not clear how γ depends on the other hydraulic parameters for a large range of water saturations. Experimental evidence seems to indicate that γ is a weak function of saturation (at least for porous media), which is discussed below. The fractal flow concept and Equation C-10) can be applied to porous media also, as long as their fingering flow patterns are fractals. Therefore, results from porous media can be used to conceptually evaluate the relation between γ and water saturation for unsaturated fracture networks.

Based on experimental laboratory observations collected by applying water at the top of the corresponding porous media, Wang et al. (1998, pp. 2188 to 2189) reported a relation between flow conditions and a parameter, F, defined as the ratio of horizontal cross-sectional area occupied by fingers to the total cross-sectional area. F corresponds to f_a, defined as the portion of active fractures in a fracture network (Liu et al. 1998). Wang et al. (1998, pp. 2188 to 2189) related F to the ratio of average water flux through the whole cross-sectional area, q, to saturated hydraulic conductivity of the porous medium, K_s, by

$$F \approx \left(\frac{q}{K_s}\right)^{1/2} \qquad \text{(Eq. C-11)}$$

for q/K_s values between 0.4 and 1.0 (BSC 2003b, Equation 71). By definition, the average water flux within fingers, q_F, can be related to q by (BSC 2003b, Equation 72):

$$q_F = \frac{q}{F} \qquad \text{(Eq. C-12)}$$

and the average water saturation of fingers, S_F, can be related to the average water saturation for the whole cross-sectional area, S_e, by (BSC 2003b, Equation 73):

$$S_F = \frac{S_e}{F} \qquad \text{(Eq. C-13)}$$

It is expected that flow within a gravitational finger is gravity-dominated. In this case (BSC 2003b, Equation 74):

$$\frac{q_F}{K_s} = k_r = S_F^{\beta^*} \qquad \text{(Eq. C-14)}$$

Equation C-14 uses the Brooks–Corey (Brooks and Corey 1964) model for describing relative permeability (k_r)–saturation relationship. $\beta*$ is a constant. Combining Equations C-11 to C-14 yields (BSC 2003b, Equation 75):

$$F = (S_e)^{\frac{\beta*}{1+\beta*}} \qquad \text{(Eq. C-15)}$$

Comparing the above equation with Equation 1 of Liu et al. (1998) gives (BSC 2003b, Equation 76):

$$\gamma = \frac{\beta*}{1+\beta*} \qquad \text{(Eq. C-16)}$$

Therefore, γ is a constant under certain conditions in porous media. Consequently, it is expected that γ should be a weak function of saturation for unsaturated fracture networks if fingering flow patterns in a porous medium are considered to be an analog of flow patterns in the networks.

Note that Equation C-16 cannot be directly used for estimating γ values for fracture networks (in the active-fracture model) because detailed flow mechanisms are different for unsaturated fractured rock and porous media. It also needs to be emphasized that Equation C-16 is valid for porous media under a condition of q/K_s equal to 0.4 to 1.0 (Wang et al. 1998, pp. 2188 to 2189). The relationship between γ and other hydraulic properties has not been established for a fracture network.

C.4.2 Methods of Model Parameter Estimation and Numerical Implementation

C.4.2.1 Input Parameters for Rock Properties for the Abstraction Model

Rock properties (i.e., rock density, fracture porosity, spacing, aperture, active-fracture model parameter γ, and fracture residual saturation) are used as inputs to the FEHM unsaturated zone transport model (BSC 2004, Section 4). The validity and uncertainty of those parameters are documented in the corresponding reports *Analysis of Hydrologic Properties Data* (BSC 2003b), *Calibrated Properties Model* (BSC 2003d), and *UZ Flow Models and Submodels* (BSC 2003a). In *Particle Tracking Model and Abstraction of Transport Processes* (BSC 2004), the mean values of those parameters are used to demonstrate the abstraction of the unsaturated zone transport model. TSPA evaluates uncertainty in fracture porosity and spacing.

C.4.2.2 Porosity Measurements

The estimation of fracture porosity is described in *Analysis of Hydrologic Properties Data* (BSC 2003b, Section 6.1.3).

C.4.2.2.1 General Strategy

Fracture porosity is herein defined as the effective porosity of fractures in which fluid flow and solute transport take place. In this study, a combination of porosity data derived from gas tracer

tests in the ESF and porosity estimates based on the geometry of fracture networks are used to develop representative fracture porosities for the unsaturated zone model layers.

Gas tracer tests were performed in the ESF to obtain estimates of the effective fracture porosity for the Topopah Spring middle nonlithophysal welded tuff, corresponding to the tsw34 model layer. Since gas tracer transport times through the fractured rocks are directly related to the storage of the corresponding fracture networks, analyses of tracer breakthrough data can provide reliable estimates of fracture porosity for the model layer tsw34.

Gas tracer test data are available only for model layer tsw34. Fracture porosity in the other model layers is estimated from equations relating the geometry of fracturing observed in the ESF which are normalized by the values derived from the gas tracer tests for tsw34 according to *Analysis of Hydrologic Properties Data* (BSC 2003b, Equation 12):

$$\phi_{\text{model layer x}} = \phi_{tsw34}\frac{\phi_{\text{2-D, model layer x}}}{\phi_{\text{2-D, tsw34}}} \quad \text{or} \quad \phi_{\text{model layer x}} = \phi_{tsw34}\frac{\phi_{\text{1-D, model layer x}}}{\phi_{\text{1-D, tsw34}}} - \quad \text{(Eq. C-17)}$$

where ϕ_{tsw34} is fracture porosity for tsw34, estimated from the gas tracer data, and $\phi_{\text{1-D}}$ and $\phi_{\text{2-D}}$ are the one-dimensional and two-dimensional porosities determined from one-dimensional borehole and two-dimensional mapping data, respectively. A so-called two-dimensional porosity for a model layer can be estimated using the aperture and the total fracture length per unit area (fracture intensity). The fracture intensity is based on tracer lengths given by the detailed line survey in the ESF and the area enclosing the traces (see Equation C-27, Section C.4.2.3). The equation used to calculate the two-dimensional porosity (BSC 2003b, Equation 10) is:

$$\phi_{2-D} = bI \quad \text{(Eq. C-18)}$$

where b is the fracture aperture, and I is the fracture intensity (m/m^2). When no intensity data are available (in cases where the unit does not intersect any portion of the ESF or Enhanced Characterization of the Repository Block (ECRB) Cross-Drift) (BSC 2001, Section 6.1), the one-dimensional porosity can be estimated by treating all fractures as continuous. The one-dimensional porosity is then calculated by (BSC 2003b, Equation 11):

$$\phi_{1-D} = b\overline{f} \quad \text{(Eq. C-19)}$$

where $\overline{f}$ is the mean fracture frequency.

A large degree of uncertainty exists in the estimates based on Equations C-18 and C-19 for the following reasons. First, the estimated apertures are hydraulic apertures and may be very different from the average geometric apertures, since they are estimated based on air-permeability data. Second, Equations C-18 and C-19 only consider two-dimensional or one-dimensional geometric features, while actual fracture networks are three-dimensional. However, the use of Equation C-17 reduces this uncertainty by normalizing these relationships by the more reliable gas-tracer estimates in tsw34.

The developed fracture porosity values for the unsaturated zone model layers are given in Table C-5. All of these values are on the order of 1%. An alternative approach would have been to use 1% for all units. Use of this scaling scheme for estimating fracture porosities is an approximation for determining the spatial variability of porosity among the model layers.

The overall strategy is essentially a combination of the two general approaches available for estimating fracture porosities in the literature. The first approach is based on field tracer transport data. Researchers outside the Yucca Mountain Project have also used similar approaches, which are summarized in *Analysis of Hydrologic Properties Data* (BSC 2003b, Section 6.1.3.4). This includes the Apache Leap Research Site (Neuman et al. 2001, p. 320) where an estimated mean fracture porosity of 0.014 was obtained from gas pressure data and fracture porosity estimates of 0.001 to 0.07 from gas tracer tests in the northern Ghost Dance Fault in the Yucca Mountain unsaturated zone (LeCain et al. 2000, Table 18).

The second general approach is based on the geometry of a fracture network. This approach considers all the fractures under consideration as connected and requires that fracture apertures can be exactly determined. Although a large degree of uncertainty exists in fracture porosity values estimated from this approach (for several reasons), this approach has often been used when field tracer test data are not available. For example, in their review of numerical approaches for modeling multiphase flow in fractured petroleum reservoirs, Kazemi and Gilman (1993, pp. 270 to 271; pp. 312 to 313) discuss the determination of fracture porosity based on fracture geometry data.

Deriving porosity from the gas-tracer tests for model layer tsw34, and using this result to normalize the geometrically calculated porosity for the other layers, provides consistency with measured data and improves the fracture porosity estimates.

C.4.2.2.2 Fracture Porosity from Gas Tracer Testing Data

The estimated fracture porosities were developed based on several simplifications (Figure C-7). Flow and transport are two-dimensional; dispersion, gas compressibility, and matrix diffusion are ignored; and the testing medium is homogeneous. The estimations were made using:

$$\phi_f{}^* = \frac{Qt_{0.5}}{\pi r_L{}^2 L}$$

(Eq. C-20)

where $\phi_f{}^*$ is the estimated fracture porosity, Q is the volumetric withdrawal rate ($Q_{withdrawal}$ in Figure C-7), $t_{0.5}$ is the mean transport time of tracer, r_L is the distance between the tracer injection and withdrawal zones, and L is the length of injection zone (BSC 2003b, Equation 13). This equation assumes that flow is two-dimensional and confined to a domain of width equal to the length of the injection zone.
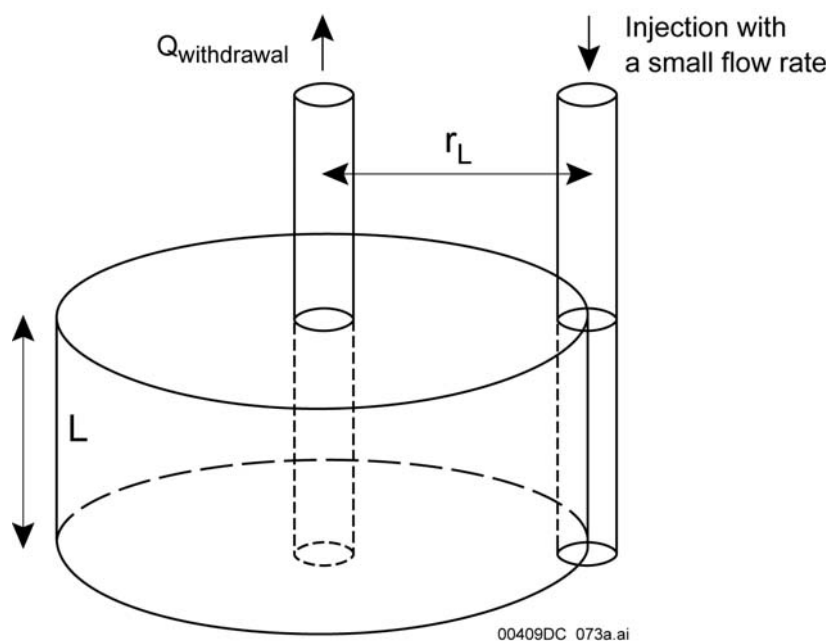
Source: BSC 2003b, Figure 3.

Figure C-7. A Conceptual Model for Estimating Fracture Porosity Using Gas Tracer Testing Data

The average fracture porosity, estimated from Equation C-20 using gas tracer data collected from the Drift Scale Test block and Niche 3, is 1.02×10^{-2}.

C.4.2.2.3 Effects of Several Factors on Fracture-Porosity Estimation Based on Gas Tracer Testing Data

The estimation of fracture porosity based on Equation C-20 does not consider the effects of several factors: gas compressibility, heterogeneity, anisotropy, cavities, dispersion, and matrix diffusion. Potential effects of these factors on estimating fracture porosity are in *Analysis of Hydrologic Properties Data* (BSC 2003b, Section 6.1.3.3).

The determination of fracture porosity depends on the tracer transport times. Diffusion of the tracer into the matrix delays the breakthrough and causes overestimation of fracture porosity. Effects of matrix diffusion on the fracture porosity estimation can be quantified by an analytical solution described in *Analysis of Hydrologic Properties Data* (BSC 2003b, Section 6.1.3, Equation 23).

$$\frac{\phi_f}{\phi_f *} = 1 - \frac{t_{0.5}}{\phi_f *} D_m \left[\frac{A_{fm} \phi_m S_{mg}}{2\beta} \right]^2 V \qquad \text{(Eq. C-21)}$$

where ϕ_f is fracture porosity (considering matrix diffusion), A_{fm} is the fracture–matrix interface area per unit volume of bulk rock, ϕ_m is the matrix porosity, S_{mg} is the gas saturation in the matrix, and β is a constant (0.48) defined by a *erfc(β)* value of 0.5 and determined from Domenico and Schwartz (1990, p. 637). The ϕ_f and ϕ_f* are identical if matrix diffusion is negligible (using a D_m value of 0), as shown in Equation C-21. This equation can be used to

correct the porosity estimates from Equation C-20 to consider the effects of matrix diffusion. Substituting the determined parameter values listed in *Analysis of Hydrologic Properties Data* (BSC 2003b, Section 6.1.3.3) into the right hand of Equation C-21 yields (BSC 2003b, Equation 26):

$$\frac{\phi_f}{\phi_f{}^*} = 0.83 \qquad \text{(Eq. C-22)}$$

This factor is used to consider the effects of matrix diffusion (on average) by multiplying the porosity estimates by a factor of 0.83. The resultant average fracture porosity for tsw34 is 0.0085, and the corresponding standard deviation is 2.5×10^{-3}. The average porosity and standard deviation were obtained from multiple measurements, described in *Analysis of Hydrologic Properties Data* (BSC 2003b, Section 6.1.3.2). This porosity value is used in Equation C-17 for determining fracture porosities in other unsaturated zone model layers. The final fracture-porosity estimates are given in Table C-5.

Fracture-porosity values obtained using different methodologies, based on different types of data and from different sites (described in *Analysis of Hydrologic Properties Data* (BSC 2003b, Section 6.1.3.4)), are consistent with the current estimates (given in Table C-5). These estimates are on the order of 1%, indicating their reasonableness.

C.4.2.3 Development of Fracture Properties from Field Data

The development of fracture properties from field data is described in *Analysis of Hydrologic Properties Data* (BSC 2003b, Section 6.1.2). Fracture frequency and interface area are determined from qualified fracture-property data developed from field data. These include detailed line survey fracture data (collected from the ESF north and south ramps, main drift, and ECRB Cross-Drift, providing spatially varying frequency, length, and fracture dips and strikes) and fracture-frequency data from boreholes.

For calculating fracture frequencies using the detailed line survey in the ESF and ECRB Cross-Drift, the mean fracture frequency is given by the inverse of the mean spacing. The mean spacing is calculated by (BSC 2003b, Equation 1):

$$s = \frac{1}{nf - 1} \sum_{2}^{nf} \left(D_i - D_{i-1} \right) \qquad \text{(Eq. C-23)}$$

where D_i is the distance or station along the ESF where fracture i intersects the detailed line survey and nf is the number of fractures. This is the apparent spacing. It is not the normal distance between the center of fractures and is, therefore, a rough estimate of the true spacing. These values were not corrected for any possible bias in orientation in the detailed line survey. The mean fracture frequency is given by the inverse of the mean apparent spacing (BSC 2003b, Equation 2):

$$f = \frac{1}{s} \qquad \text{(Eq. C-24)}$$

For calculating fracture frequency from borehole data, the data are processed to normalize for core recovery, corrected for bias in orientation, and scaled to represent larger length fracture. To correct for orientation bias for data from vertical boreholes, dip distributions are used as follows (modified from Lin et al. (1993, p. 24, Equation 3-1) (BSC 2003b, Equation 3):

$$f_{cb} = \frac{\sum_i f_{i,0-19°dip}}{\cos(10°)} + \frac{\sum_i f_{i,20-39°dip}}{\cos(30°)} + \frac{\sum_i f_{i,40-59°dip}}{\cos(50°)} + \frac{\sum_i f_{i,60-90°dip}}{\cos(75°)}$$ (Eq. C-25)

where f_{cb} is the fracture frequency corrected for orientation bias and f_i is the fracture frequency corresponding to the range of dip distribution.

Finally, the values of f_{cb} are corrected to represent larger length fractures on the scale of those characterized in the ESF. The detailed line survey fracture data do not include fractures having lengths less than 1 m, while the borehole surveys may include these smaller fractures. A simple correction ratio is used based on comparisons of ESF data with corresponding vertical boreholes for that model layer (BSC 2003b, Equation 4):

$$\overline{f} = f_{corrected} = f_{cb}R$$
$$R = \left(\frac{f_{ESF}}{f_{borehole}}\right)_{average}$$ (Eq. C-26)

Two correction factors R were calculated, one for welded units using data for the Topopah Spring middle nonlithophysal hydrogeologic unit (tsw34) and one for nonwelded units using data for the Pah Canyon Tuff in the Paintbrush hydrogeologic unit (ptn25). These units were selected because both ESF and borehole data are available; these were considered to be representative of the other units.

The fracture intensity is calculated by dividing the trace length of the fracture by the area surveyed. The area surveyed was 6 m (3 m above and below the traceline) times the length along the tunnel considered for that interval. The average fracture intensity I (m/m^2) is given by (BSC 2003b, Equation 5):

$$I = \frac{\sum_{i=1}^{nf} t_i}{\text{area}} = \frac{\sum_{i=1}^{nf} t_i}{(6\,\text{m})(\text{interval length in meters})}$$ (Eq. C-27)

where t_i is trace length in meters for fracture i.

The fracture interface area is calculated by dividing the fracture area by the volume of the interval surveyed. The volume for the interval is estimated by multiplying the interval length surveyed by the square of the geometric mean of surveyed fracture-trace length. The average fracture-interface area per volume A_{fm} (m^2/m^3) is given by (BSC 2003b, Equation 6):

$$A_{fm} = \frac{\sum_{i=1}^{nf} \pi r_i^2}{\text{volume}} = \frac{\sum_{i=1}^{nf} \pi r_i^2}{(\text{interval length})(\text{geometric mean of trace lengths})^2} \quad \text{(Eq. C-28)}$$

where r is the radius of fracture i, or one-half the trace length of fracture i.

Fracture apertures are calculated by the cubic law with the fractures fully connected. The fracture aperture b is then given by Bear et al. (1993, p. 15) (BSC 2003b, Equation 7):

$$b = \left(\frac{12k}{\bar{f}}\right)^{1/3} \quad \text{(Eq. C-29)}$$

where k is the fracture permeability. The fracture aperture determined in this way is an effective hydraulic aperture, not a physical aperture. The k here refers to bulk fracture permeability rather than permeability in a fracture as defined by Bear et al. (1993, p. 15).

The developed fracture properties are given in Table C-5.

C.4.2.4   Fracture–Aperture, Porosity, and Frequency Data in the Abstraction Model

The use of fracture-porosity and spacing data and the estimation of apertures for the abstraction model are described in *Particle Tracking Model and Abstraction of Transport Processes* (BSC 2004, Section 6.5.7). The fracture-porosity and fracture-spacing data are sampled to address the uncertainty of fracture properties on radionuclide transport in TSPA calculations. The data sets list fracture spacing data in terms of fracture frequency, defined as the inverse of fracture spacing. Thus, the fracture frequency is first sampled, and the inverse of the sampled data is taken to derive sampled fracture-spacing data.

Table C-6 lists the uncalibrated fracture-porosity and frequency data based on field information. These are the uncalibrated properties developed in *Calibrated Properties Model* (BSC 2003d). However, fracture-porosity and frequency data are not subject to calibration adjustment in *Calibrated Properties Model* (BSC 2003d); therefore, these properties are carried forward into the calibrated property set without modification.

Among the listed geologic rock layers, only those below the repository that could affect the transport of radionuclides downward toward the water table are sampled. Rock layers below the repository are grouped together based on similarity in fracture-porosity and frequency characteristics. For groups with multiple units having different parameter values, an arithmetic average value is used for the group. There is only one standard deviation for fracture-porosity, so the other groups are assigned a fracture-porosity standard deviation such that the ratio of the standard deviation to the mean is constant for all the groups. Model layer tsw4 has its own

standard deviation for fracture frequency, which is used. For the other groups, the standard deviation is set equal to 0.831 times the mean. This is based on the relationship between fracture frequency and the standard deviation of fracture frequency found for model units above the repository (see Figure C-8). In this way, the mean and standard deviation for each parameter in each group was computed.
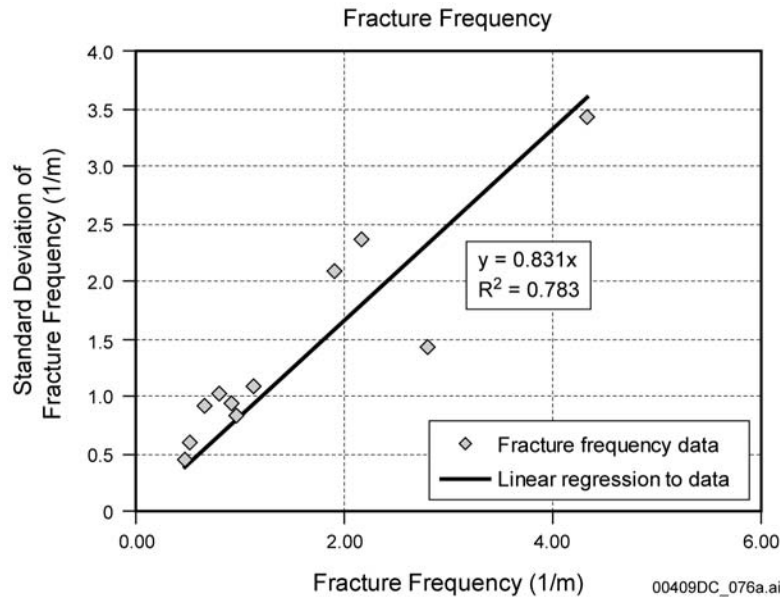
Source: BSC 2004, Figure 6-13.

Figure C-8. Relationship between Fracture Frequency and Standard Deviation

As porosity must lie within the finite range of 0 to 1, a beta distribution with these bounds is suitable for studying the influence of porosity uncertainty on radionuclide transport Table C-7 lists the distribution data for fracture porosity.

Table C-6. Fracture-Porosity and Frequency Data

Unsaturated Zone Flow Model Layer[a]	ϕf	Std.	f (1/m)	f	Input Description	Type of Uncertainty
tcw11	2.4×10^{-2}	–	0.92	0.94	ϕ_f is the fracture porosity and f is fracture frequency. Data are uncalibrated. However, the fracture-porosity and fracture-frequency data are not subject to adjustment in calibration; therefore, those properties are carried forward into the calibrated property set without modification.	As porosity must fall in the range of 0 and 1, a beta distribution is suitable to describe the uncertainty of the porosity values.
tcw12	1.7×10^{-2}	–	1.91	2.09		
tcw13	1.3×10^{-2}	–	2.79	1.43		
ptn21	9.2×10^{-3}	–	0.67	0.92		
ptn22	1.0×10^{-2}	–	0.46	–		
ptn23	2.1×10^{-3}	–	0.57	–		
ptn24	1.0×10^{-2}	–	0.46	0.45		
ptn25	5.5×10^{-3}	–	0.52	0.6		
ptn26	3.1×10^{-3}	–	0.97	0.84		
tsw31	5.0×10^{-3}	–	2.17	2.37		
tsw32	8.3×10^{-3}	–	1.12	1.09		
tsw33	5.8×10^{-3}	–	0.81	1.03		
tsw34	8.5×10^{-3}	2.50×10^{-3}	4.32	3.42		
tsw35	9.6×10^{-3}	–	3.16	–		
tsw36	1.3×10^{-2}	–	4.02	–		
tsw37	1.3×10^{-2}	–	4.02	–		
tsw38/pc38	1.1×10^{-2}	–	4.36	–		
tsw39/pcf39/tsw (zeolitic)/tsw (vitric)	4.3×10^{-3}	–	0.96	–		
ch1 (vitric)	6.1×10^{-4}	–	0.10	–		
ch2 (vitric)	7.7×10^{-4}	–	0.14	–		
ch3(vitric)	7.7×10^{-4}	–	0.14	–		
ch4 (vitric)	7.7×10^{-4}	–	0.14	–		
ch5 (vitric)	7.7×10^{-4}	–	0.14	–		
ch6 (vitric)	7.7×10^{-4}	–	0.14	–		
ch1z/pc1z (zeolitic)	1.6×10^{-4}	–	0.04	–		
ch2z/pc2z (zeolitic)	3.7×10^{-4}	–	0.14	–		
ch3 (zeolitic)	3.7×10^{-4}	–	0.14	–		
ch4 (zeolitic)	3.7×10^{-4}	–	0.14	–		
ch5z/pc5z (zeolitic)	3.7×10^{-4}	–	0.14	–		
ch6z/pc6z (zeolitic)	1.6×10^{-4}	–	0.04	–		
pp4/pc4p	3.7×10^{-4}	–	0.14	–		
pp3	9.7×10^{-4}	–	0.20	–		
pp2	9.7×10^{-4}	–	0.20	–		
pp1	3.7×10^{-4}	–	0.14	–		
bf3	9.7×10^{-4}	–	0.20	–		
bf2	3.7×10^{-4}	–	0.14	–		
tr3	9.7×10^{-4}	–	0.20	–		
tr2	3.7×10^{-4}	–	0.14	–		
tcw fault	2.9×10^{-2}	–	1.90	–		
ptn fault	1.1×10^{-2}	–	0.54	–		
tsw fault	2.5×10^{-2}	–	1.70	–		
chn fault	1.0×10^{-3}	–	0.13	–		

Source: BSC 2004, Table 6-11.

NOTE: [a]See Table 2-1.

Table C-7. Fracture-Porosity and Frequency Distribution Data

Group	Units	Porosity Beta Distribution min = 0; max = 1		Fracture Frequency (m⁻¹)		Fracture Frequency (m⁻¹) Lognormal Distribution		Aperture (m) 2b derived from Eq. C-32: $2b = \dfrac{\phi_f}{f}$
		Mean	Std	Mean	Std	Mean For ln (f)	Std For ln (f)	
1	Chn	1.0×10^{-3}	3.09×10^{-4}	1.26×10^{-1}	1.05×10^{-1}	-2.42	7.24×10^{-1}	7.94×10^{-3}
2	Tsw	2.5×10^{-2}	7.25×10^{-3}	1.75	1.45	2.11×10^{-1}	7.24×10^{-1}	1.43×10^{-2}
3	ch[2,3,4,5] (zeolitic)	3.7×10^{-4}	1.09×10^{-4}	1.40×10^{-1}	1.16×10^{-1}	-2.31	7.24×10^{-1}	2.64×10^{-3}
	Pc[2,5]z							
	Pp4z							
	pp1z							
	bf2z							
	tr2z							
4	pp3d	9.7×10^{-4}	2.85×10^{-4}	2.00×10^{-1}	1.66×10^{-1}	-1.96	7.24×10^{-1}	4.85×10^{-3}
	pp2d							
	bf3d							
	tr3d							
5	ch1z/pc1z ch6z/pc6z	1.6×10^{-4}	4.71×10^{-5}	4.00×10^{-2}	3.32×10^{-2}	-3.57	7.24×10^{-1}	4.00×10^{-3}
6	Ch[1,2,3,4,5,6] (vitric)	6.9×10^{-4}	2.03×10^{-4}	1.20×10^{-1}	9.96×10^{-2}	-2.47	7.24×10^{-1}	5.75×10^{-3}
7	tsw39/pc39 /tswv/tswz	4.3×10^{-3}	1.26×10^{-3}	9.60×10^{-1}	7.97×10^{-1}	-3.87×10^{-1}	7.24×10^{-1}	4.48×10^{-3}
8	tsw [34,35]	1.05×10^{-2}	3.10×10^{-3}	3.97	3.29	1.03	7.24×10^{-1}	2.64×10^{-3}
	tsw [36,37]							
	tsw38/pc38							
9	tsw33	5.8×10^{-3}	1.71×10^{-3}	8.10×10^{-1}	1.03	-6.92×10^{-1}	9.81×10^{-1}	7.16×10^{-3}

Source: BSC 2004, Table 6-13.

A lognormal distribution is applied to characterize the distribution of fracture frequency. A lognormal distribution is justified because: (1) many hydrogeologic parameters, including porosity and permeability, can be characterized by lognormal distributions, and (2) fracture frequencies can theoretically range from 0 to very large values. In a lognormal distribution, the upper range of fracture frequencies is practically limited by several standard deviations. The mean and standard deviation for ln(f) are given in terms of the mean and standard deviation for f by the following relationships from Hogg and Craig (1978, pp. 180 and 432) (BSC 2004, Equations 6-24 and 6-25):

$$\mu_{\ln(f)} = \ln\left(\mu_f\right) - \frac{1}{2}\ln\left(1 + \frac{\sigma_f^2}{\mu_f^2}\right) \qquad \text{(Eq. C-30)}$$

$$\sigma_{\ln(f)} = \sqrt{\ln\left(1 + \frac{\sigma_f^2}{\mu_f^2}\right)} \qquad \text{(Eq. C-31)}$$

For further information on this derivation, see *Drift-Scale Radionuclide Transport* (BSC 2003e, Attachments I and XI, equations I-1, I-2, and XI-4 through XI-7.) Values for $\mu_{\ln(f)}$ and $\sigma_{\ln(f)}$ are given in Table C-7.

In TSPA-LA calculations, fracture porosity and fracture frequency are sampled independently. The basis for this approximation is that there is only a very weak correlation between fracture porosity and frequency (BSC 2004, Figure 6-14). Therefore, correlating these two parameters is not warranted.

The sampled fracture-porosity and frequency data are used in deriving the fracture spacing and aperture based on the following relationship (BSC 2004, Equation 6-26):

$$\phi_f = (2b)f \qquad \text{(Eq. C-32)}$$

where $2b$ is the fracture aperture (m), f is the fracture frequency (m^{-1}), and ϕ_f is the fracture porosity. Fracture frequency is the inverse of the fracture spacing.

C.4.2.5 Residual Saturation and the Active-Fracture Model γ Parameter Values for the Abstraction Model

Fracture residual saturation and fracture γ parameter values are used by FEHM to calculate the fracture spacing based on the active-fracture model (Liu et al. 1998). In TSPA-LA, a constant fracture residual saturation of 0.01 is used for all layers (BSC 2004, Section 6.5.6). Values for fracture parameter γ and their sources are tabulated for the lower-bound, mean, and upper-bound infiltration scenarios for the model layers in Tables C-2 to C-4 (BSC 2004, Tables 6-8 to 6-10).

C.4.3 Adaptation of the Active-Fracture Model for Abstraction Transport Model Calculations

The fracture−matrix interaction submodel of the transport model is described in *Particle Tracking Model and Abstraction of Transport Processes* (BSC 2004, Section 6.4.3) and derived in *Particle Tracking Model and Abstraction of Transport Processes* (BSC 2004, Section III-1). The governing equations required for the fracture–matrix interaction submodel is a solute transport system in a domain consisting of parallel flow in a fracture and adjacent matrix, with fracture–matrix solute interaction via molecular diffusion in the rock matrix. For simplicity, longitudinal dispersion is not considered in either medium, advection is considered only in the z-direction, and diffusion is considered only normal to the flow direction. The rationales for these simplifications are as follows. With regard to longitudinal dispersion, this submodel is intended only to capture the impact of diffusion because dispersion is captured separately in the particle tracking algorithm. Likewise, the advection from fracture to matrix (or the reverse) is separately implemented in the particle tracking algorithm. Therefore, the remaining processes to be included as part of the transfer functions are advection and diffusion in the z-direction only.

The transport equation for the fracture is derived from first principles to demonstrate the means by which terms in the dimensionless groups must be altered to include the effects of the active-fracture model. Taking a control volume in the fracture of width b (half of the full aperture), depth d, and length Δz, the following terms of the transient solute mass balance (units of each of these terms are solute mass per time) are (BSC 2004, Equation III-1):

$$bd\Delta z\theta_f R_f \frac{(C - C_{prev})}{\Delta t} \qquad \text{(Eq. C-33)}$$

where C_{prev} represents the concentration at the previous time step, θ_f is the volumetric water content in the fracture, and R_f is the fracture retardation factor. For advection (BSC 2004, Equation III-2):

$$bd\overline{V}_z(C_{z+\Delta z} - C_z) \qquad \text{(Eq. C-34)}$$

where $\overline{V}_z$ is the Darcy velocity in the fracture, equal to volumetric flow rate divided by the total cross-sectional area in the fracture. For diffusion into matrix (BSC 2004, Equation III-3):

$$d\Delta z\theta_m D_m \left.\frac{\partial C_m}{\partial x}\right|_{x=b} \qquad \text{(Eq. C-35)}$$

where D_m is the effective diffusion coefficient in the matrix and θ_m is the matrix volumetric water content. These terms form the overall solute mass balance equation (BSC 2004, Equation III-4):

$$bd\Delta z\theta_f R_f \frac{(C - C_{prev})}{\Delta t} = -bd\overline{V}_z(C_{z+\Delta z} - C_z) + d\Delta z\theta_m D_m \left.\frac{\partial C_m}{\partial x}\right|_{x=b} \qquad \text{(Eq. C-36)}$$

Dividing by $bd\Delta z\theta_f$, making use of the relation for the fracture-interstitial pore-water velocity $V_f = \overline{V}_z/\theta_f$, and taking the limit as Δz and Δt go to 0, yields (BSC 2004, Equation III-7):

$$R_f \frac{\partial C_f}{\partial t} = -V_f \frac{\partial C_f}{\partial z} + \frac{\theta_m D_m}{\theta_f b} \left.\frac{\partial C_m}{\partial x}\right|_{x=b} \qquad \text{(Eq. C-37)}$$

The subscript f on the concentration denotes the fracture.

Given the assumptions listed at the beginning of this derivation, the differential equation governing transport in the matrix is (BSC 2004, Equation III-8):

$$R_m \frac{\partial C_m}{\partial t} = D_m \frac{\partial^2 C_m}{\partial x^2} - V_m \frac{\partial C_m}{\partial z} \qquad \text{(Eq. C-38)}$$

where V_m is the interstitial pore-water velocity in the matrix, and D_m is the matrix retardation factor.

In the active-fracture model of Liu et al. (1998), the fraction of the connected fractures in a network that flow, f_a, is expressed as (BSC 2003b, Equation 52):

$$f_a = S_e{}^\gamma \qquad \text{(Eq. C-39)}$$

where γ is a positive constant depending on properties of the corresponding fracture network, and the effective water saturation in connected fractures is given by (BSC 2003b, Equation 53)

$$S_e = \frac{S_f - S_r}{1 - S_r} \qquad \text{(Eq. C-40)}$$

where S_f is the water saturation of all connected fractures and S_r is the residual fracture saturation.

The active-fracture model requires that adjustments be applied to the interface area and the mean spacing between flowing fractures. These adjusted parameters can then be used in the transport model calculations. Examining the individual terms of the mass balance for the fracture, the accumulation term (Equation C-33) is unchanged by the active-fracture model, because it is based on the storage volume in the fracture, as well as sorption parameters. Storage volumes in the dual-k flow fields are fully defined by the fracture volume fractions and the fluid saturations in the fracture continuum. Fluid saturations are model output from the flow simulations, and no further correction for transport is required for the accumulation term. Likewise, the Darcy velocity in the advection term (Equation C-34) is fully defined by the flux through the fracture continuum, so no active-fracture model corrections are required for advection either.

The diffusion term (Equation C-35) consists of a flux $\theta_m D_m \left. \dfrac{\partial C_m}{\partial x} \right|_{x=b}$ times an interfacial area. This interfacial area term, according to the active fracture model, should be reduced to account for the fact that not all fractures are flowing. Liu et al. (1998, Equation 12) give the following reduction factor for correcting the advective flux term (nomenclature from Liu et al. (1998) is used in this equation) (BSC 2004, Equation III-34):

$$R = \left(\frac{A_{fm,a}}{A_{fm}} \right)\left(\frac{n_{f,a}}{n_f} \right)\left(\frac{d}{d_a} \right) \qquad \text{(Eq. C-41)}$$

Although Liu et al. (1998) refer to R as the fracture–matrix interface area reduction factor, it is clear from their derivation that the term represents the ratio of the fluxes for the uncorrected and corrected cases, correcting for both the interface area and the transport length scale associated with the distance between the flowing fractures (the third term on the right-hand side of this equation). Therefore, in the FEHM simulations, active-fracture model-based adjustments should be applied to both the interface area and the spacing B. The term d/d_a is the adjustment to the fracture spacing, where d is the fracture spacing, and d_a is the fracture spacing in the active-fracture continuum, and is described by the following relation (Liu et al. 1998, Equation 17) (BSC 2004, Equation III-35):

$$\frac{d}{d_a} = S_e{}^{\gamma} \qquad \text{(Eq. C-42)}$$

Thus, the geometric spacing B in the FEHM transport simulations is multiplied by $S_e{}^{\gamma}$ to obtain the spacing between flowing fractures.

The interface-area portion of the adjustment consists of the first two terms on the right hand side of Equation C-41, the first to account for the reduction in wetted area within an individual fracture, and the second to account for the reduction in area associated with a smaller number of wetted fractures. This term can be related to the active-fracture model parameters using Equations 13 and 14 of Liu et al. (1998) (BSC 2004, Equation III-36):

$$\left(\frac{A_{fm,a}}{A_{fm}}\right)\left(\frac{n_{f,a}}{n_f}\right) = S_e{}^{1-\gamma} S_e{}^{\gamma} = S_e \qquad \text{(Eq. C-43)}$$

To implement this area reduction term in FEHM, the geometrically defined aperture, b, is divided by S_e. The adjustment to b is for convenience and actually arises from the need to adjust the interface area in the fracture-transport equation.

Fracture-hydraulic properties in the process model and the constitutive relationships are defined for active fractures as a function of the effective water saturation of active fractures. This is related to the effective water saturation in connected fractures, S_e, by (BSC 2003b, Equation 54):

$$S_{ae} = \frac{S_e}{f_a} = S_e{}^{1-\gamma} \qquad \text{(Eq. C-44)}$$

Because $S_{ae} \leq 1$, γ should be in a range between 0 and 1. The effective water saturation of active fractures is related to the actual water saturation in active fractures, S_a, by (BSC 2003b, Equation 55):

$$S_{ae} = \frac{S_a - S_r}{1 - S_r} \qquad \text{(Eq. C-45)}$$

However, the volumetric water content used in Equations C-35 through C-37 is not modified for the active-fracture model formulation because it is equal to the product of S_e (for all the connected fractures) and fracture porosity.

C.4.4 Verification of the Active-Fracture Model with Matrix Diffusion in the Abstraction Model

Particle Tracking Model and Abstraction of Transport Processes (BSC 2004, Section 6.4.3) describes the fracture–matrix interaction submodel. For transport in a dual-permeability system at the field scale, the flow model consists of one matrix grid cell for each fracture cell. However, important processes associated with flow and transport occur at scales smaller than those considered in the mountain-scale unsaturated zone model, particularly in the immediate region of

the matrix adjacent to each flowing fracture. Therefore, the incorporation of fracture–matrix interactions into the model is, in essence, an upscaling problem. The goal of this development is to utilize a suitable idealized system that captures, at the small scale, important transport processes and allows this small-scale behavior to be simply upscaled for inclusion in the large-scale model. As demonstrated below (taken from *Particle Tracking Model and Abstraction of Transport Processes* (BSC 2004, Section 6.4.3)), this upscaling method will allow testing of alternate conceptual models for the fracture–matrix interaction model for transport.

To accomplish the upscaling within the particle tracking transport model, the transfer function approach is used, constructing an idealized transport model at the small scale that allows the transfer functions to be tabulated. In a dual-permeability system, transport behavior is vastly different depending on whether solute starts in the fracture or in the matrix. Therefore, the transfer function method is adapted in the unsaturated zone transport model to accommodate dual-permeability behavior.

The approach consists of using transfer functions to determine both the residence time in a cell and whether the particle enters the next cell in the fractures or the matrix. In this way, the combined fracture and matrix system will be treated as a unified medium in which there is a distribution of transport times depending on whether the particle enters the cells in the fracture versus the matrix. The transfer functions themselves (described below and in Attachment III of *Particle Tracking Model and Abstraction of Transport Processes* (BSC 2004)) are computed based on an idealized fracture–matrix transport model with parallel flow in the fractures and matrix. The steps of the algorithm are as follows (the algorithm starts with a known particle location, either in the fracture or matrix continuum):

1. Determine probabilistically whether the particle should move to the other medium due to advective flux to that medium.

2. Determine probabilistically whether the particle will leave this cell via the current medium or the other medium.

3. Use the conditional transfer function to determine probabilistically the residence time of the particle.

4. Determine probabilistically which cell the particle moves to next (whether it starts in the fracture or matrix continuum in the next cell has been determined previously in step 2) using the relative total flux to adjacent nodes.

This approach handles the combined fracture and matrix continua as a single porous medium through which mass travels and apportions the particles to each continuum according to the diffusive and advective fluxes defined by the flow field and the transport parameters. In the most general case, the dual-permeability flow model at the mountain scale prescribes a net flow through the fracture continuum, a net flow through the matrix continuum, and a fracture-to-matrix (or matrix-to-fracture) fluid flux. To implement this algorithm and allow the transfer function to be computed readily, step 1 takes the fracture–matrix advective flux term and applies it immediately when the particle enters the cell. Then, after potentially shifting the particle from one medium to the other via advection (with no increase to the transport time) the

subsequent transfer functions are based on parallel flow in the two continua with no flux between the continua.

This approach, which amounts to a form of upwinding of the fracture–matrix fluid flux term, simplifies the transfer function process by eliminating the need for an additional variable, the fracture–matrix advective flux, in the construction of the transfer function curves. Instead, a probability p_{fm} of the particle transferring to the other medium (step 1) is assigned as

- $p_{fm} = 0$ if the fracture–matrix flux term f_{fm} is into the medium in which the particle already resides
- $p_{fm} = f_{fm}/(f_{fm} + f_{in})$, where f_{in} is the total flux into the continuum in which the particle currently resides.

Step 2 accounts for the fact that there is a finite probability that, due to matrix diffusion, the particle will leave the cell through the other medium regardless of where it originates. In the transfer function approach, solute mass is introduced in the model system (the two-dimensional discrete fracture model) in either the fracture fluid or the matrix fluid. For the general case of water flow through both the fracture and matrix, mass leaves the discrete fracture model via either medium. Therefore, conditional transfer functions must be generated to obtain the probabilities in step 2. That is, for mass injected with the fracture fluid entering the discrete fracture submodel, there is a breakthrough curve for mass leaving the model via the fracture fluid, and a similar breakthrough curve for mass leaving via the matrix fluid.

Similarly, there are two breakthrough curves for mass injected with the matrix fluid. The plateau values attained for a given transfer function curve represents the probability of leaving via a particular medium in step 2. In other words, the probability of a particle leaving via a given continuum equals the steady-state solute mass flux (the plateau of the transfer function curve) divided by the total mass flux through the discrete fracture model. This step provides a way to assign probabilities for moving particles between the media via diffusion in a system in which water flows through both continua.

Once step 2 is completed using the steady-state solute mass flux derived from the conditional transfer functions, the transfer function to apply to obtain the residence time for step 3 becomes known. This part of the method is identical to that described previously, which involves generating a random number between 0 and 1 and determining the particle residence time from the transfer function.

Finally, step 4 routes the particle to the appropriate connecting cell in the finite volume domain, as described earlier. If the particle is determined to enter an adjoining cell via the fracture continuum, then the internodal fluxes associated with the fractures are used to define the probabilities of traveling to each connected fracture cell. Similarly, for transport to an adjoining matrix cell, matrix fluxes are used.

The process employed in this model to obtain the transfer functions for the dual permeability transport submodel consists of a series of numerical simulations on the idealized model system shown in Figure C-9.
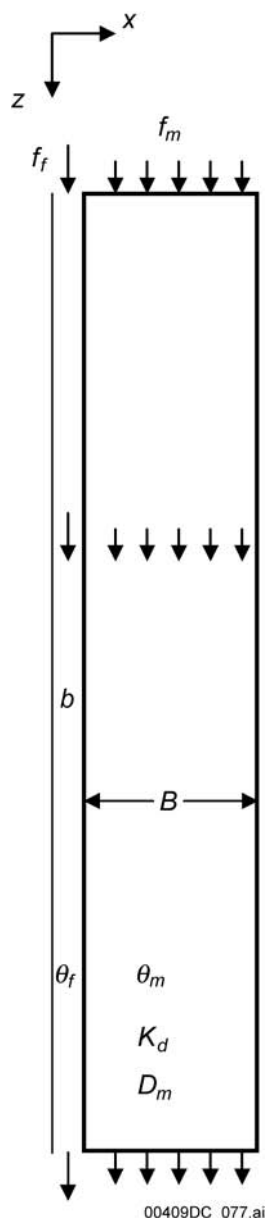
Source: BSC 2004, Figure 6-5.

Figure C-9. Schematic of the Fracture-Transport Submodel

Because each gridblock in the mountain-scale model possesses different hydrologic and transport parameters, a procedure for deriving a nondimensional form of the submodel is required to make the method practical. *Particle Tracking Model and Abstraction of Transport Processes* (BSC 2004, Attachment III) presents the derivation of the nondimensional model and presents the method for generating the transfer function curves. In summary, there are three nondimensional groups that, if specified, fully capture the range of behavior of the submodel (BSC 2004, Equations 6-9 to 6-11):

$$p_1 = \frac{D_m \tau_f R_f}{B^2 R_m} \qquad \text{(Eq. C-46)}$$

$$p_2 = \frac{D_m \tau_f \theta_m}{bB\theta_f} \qquad \text{(Eq. C-47)}$$

$$p_3 = \frac{\tau_f R_f}{\tau_m R_m} \qquad \text{(Eq. C-48)}$$

In these equations, D_m is the effective diffusion coefficient; τ_f and τ_m are the fluid transport times in the fracture and matrix, respectively; R_f and R_m are the retardation factors in the fracture and matrix, respectively; B is the half-spacing between flowing fractures; b is the fracture half-aperture; and θ_f and θ_m are the volumetric water contents of the fracture and matrix, respectively. For a given parameter vector (p_1, p_2, p_3), there is a unique set of conditional transfer function curves of the form $\hat{C}$ versus $\hat{t}$, where $\hat{C}$ is the normalized breakthrough curve for the nondimensional time $\hat{t}$ given by (BSC 2004, Equation 6-12):

$$\hat{t} = \frac{t}{R_f \tau_f} \qquad \text{(Eq. C-49)}$$

The set of conditional transfer function curves consists of a total of four normalized curves for each (p_1, p_2, p_3): mass input in fracture, output in fracture; mass input in fracture, output in matrix; mass input in matrix, output in fracture; and mass input in matrix, output in matrix. This capability for sampling conditional transfer functions associated with the fracture–matrix interaction dual permeability submodel of the unsaturated zone transport abstraction model has been implemented and documented in FEHM V2.21 (LANL 2003).

The final issue associated with implementing the transfer function approach is the means by which the idealized model of Figure C-9 is simulated. Two alternative conceptual models are implemented in this abstraction model to simulate different types of fracture–matrix interaction conceptualizations. In the first alternative conceptual model, called the discrete fracture model formulation, a two-dimensional numerical grid is used with fine discretization in the matrix close to the fracture. This allows sharp gradients in concentration close to the fracture to be captured. The second alternative conceptual model, called the dual-k formulation, uses a numerical grid with one finite volume cell that is paired with each fracture grid cell. This type of discretization is identical to that used in the dual-k transport formulation of the T2R3D process model.

It could be argued that the discrete fracture model formulation more accurately captures the small-scale transport processes. However, the dual-k formulation has the advantage of consistency with the model formulation on which the flow simulations are based. Furthermore, as a practical matter, the three-dimensional process model uses a dual-k formulation for transport, so, for benchmarking purposes, the dual-k approach is more likely to yield comparable results.

In *Particle Tracking Model and Abstraction of Transport Processes* (BSC 2004, Section 7), the implementation of the active-fracture model in the abstraction model was shown to reproduce the qualitative features of the breakthrough curves documented in the reports on which this abstraction is based. Thus, the abstraction model has been compared in the full complexity of the unsaturated zone model and found to be able to represent the system robustly and efficiently for the entire range of parameters and conceptual models required. The following tests were documented in *Particle Tracking Model and Abstraction of Transport Processes* (BSC 2004, Section 7).

C.4.4.1 Comparison of the Particle Tracking Model with Simulations in a Two-Dimensional Cross-Sectional Model

Particle Tracking Model and Abstraction of Transport Processes (BSC 2004, Section 7.2) describes the comparison of the particle tracking model for abstraction with simulations from *Radionuclide Transport Models Under Ambient Conditions* (BSC 2003c) using T2R3D in a two-dimensional cross-sectional model. The particle tracking model tests two alternative conceptual models to describe fracture–matrix interactions: the discrete fracture model and the dual-k formulation. The T2R3D process model uses both the dual-k and MINC formulations. *Radionuclide Transport Models Under Ambient Conditions* (BSC 2003c) showed that these formulations, which constitute alternative conceptual models for transport, can produce significantly different results.

Two alternative conceptual models have been developed on the two-dimensional cross-sectional model using T2R3D. The simulations called dual-k use a finite-volume dual-permeability model formulation in which the fracture–matrix diffusion term is governed by a simple gradient calculated as the difference in concentration between the media divided by a characteristic distance, on the order of the flowing fracture spacing. In addition, in *Radionuclide Transport Models Under Ambient Conditions* (BSC 2003c), the MINC conceptual model employs a series of gridblocks in the matrix.

The unsaturated zone abstraction model implemented in FEHM is capable of simulating either situation. In the conceptualization termed the discrete fracture model fracture–matrix interaction model, sharp concentration gradients are captured through use of a transfer function obtained using a discrete fracture model with fine discretization in the matrix, analogous to a MINC formulation. By contrast, a dual-k model can be used to generate transfer functions, and those results might be expected to resemble those of T2R3D when an analogous dual-k formulation is used.

In all abstraction model cases, the flow field on which the transport model is run is a dual-k flow field because the particle tracking abstraction model was formulated with the dual-k flow assumption. Therefore, the transport runs with the discrete fracture model formulation for the fracture–matrix interaction submodel employ a finely discretized matrix block for transport but a single matrix block for the flow field. This approach should enable sharp gradients likely to be present for solute transport to be captured in the model.

Figure C-10 plots the comparison results of the particle tracking model and the two alternative conceptual models simulated with T2R3D. For the case of no diffusion, there is excellent

agreement between the particle tracking model and the dual-k, no-diffusion model using T2R3D. Slight differences may be attributable to subtle differences in model formulation, numerical errors for one or the other model, or the fact that 1 of the 11 nodes designated as a repository node in the T2R3D runs was omitted from the particle tracking runs because it was found to be located in the PTn. Even with these possible sources for the difference, the agreement provides confidence that particle routing and transit times are properly implemented.
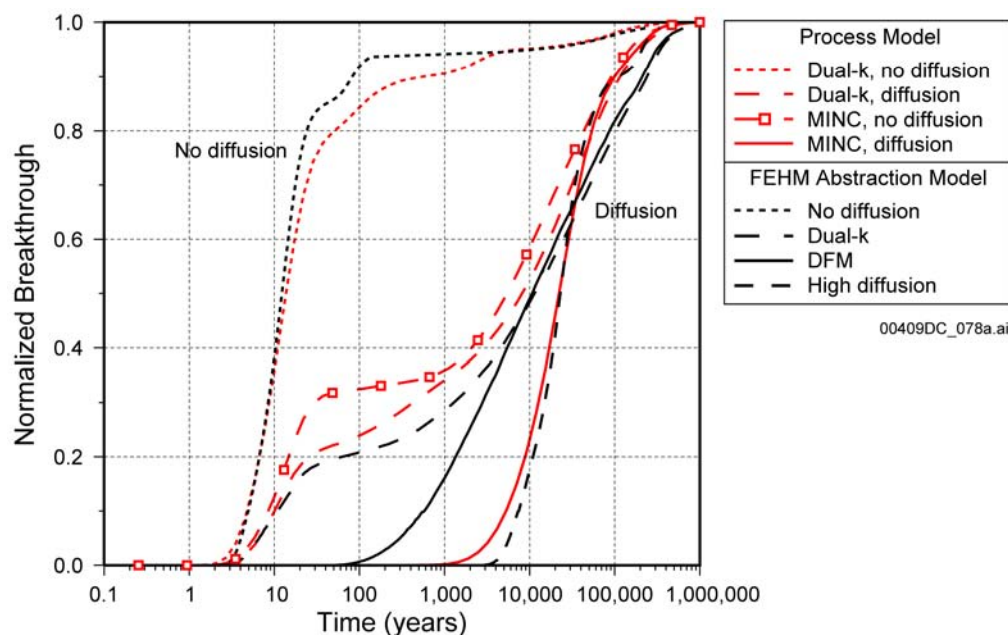
Source: BSC 2004, Figure 7-9.

Figure C-10. Comparison of the Particle Tracking Model with Process Models for a Two-Dimensional, Mountain Scale Model, with and without Diffusion, for Dual-k and Discrete Fracture Model Formulations for the Fracture–Matrix Interaction Model

The mismatch between the MINC, no diffusion and the dual-k simulations (both T2R3D and particle tracking) indicates that there are differences in the flow regime for the MINC model. The reasons for this difference stem from the fact that the numerical discretization of this model is different than that of the dual-k model. Because of differences in the flow regimes of the MINC and dual-k flow models, the particle tracking runs, which input the dual-k flow field rather than the MINC flow field, are not expected to match the MINC results precisely. Nevertheless, the particle tracking and MINC models are expected to predict similar breakthrough curve features when the former are computed with the discrete fracture model conceptual model transfer function curves. By contrast, diffusion in the dual-k transport model is expected to predict much earlier breakthrough of a portion of the solute mass.

The simulations with diffusion in Figure C-10 confirm this result. In this figure, various FEHM particle tracking simulations are benchmarked against simulations using a dual-k or MINC formulation for the two-dimensional cross section. The difference in predicted behavior between the two conceptual models is reflected in the FEHM simulations in a manner similar to that of the process models. Comparing the MINC and FEHM discrete fracture models, first arrivals in both cases occur much later in time than for the dual-k models.

For comparison, a high-diffusion case is also presented to illustrate the upper limit of breakthrough times for this flow field. Regarding the dual-k models, the characteristic feature of early arrival of a significant portion of the mass at times similar to that of pure fracture transport is produced in both the process and abstraction models. The fraction of the mass arriving early is somewhat lower in the FEHM model than in the T2R3D model, but qualitatively, the dual-k transfer function curves yield behavior quite similar to the process model result using T2R3D. Also, both the process model and abstraction model results converge at longer transport times, regardless of the formulation of the fracture–matrix interaction model or the value of diffusion coefficient used. Finally, the high-diffusion FEHM simulation is shown to bracket the behavior of the breakthrough curves in the figure, with results that are very close to that of the MINC model.

All of these indicators show that the abstraction model compares adequately with the process models and properly accounts for the role of conceptual model uncertainty in the fracture–matrix interaction model. The relatively minor differences of the models employing the dual-k fracture–matrix conceptual model are probably attributable to subtle differences in model formulation and mathematical techniques for solving the transport problem.

C.4.4.2   Comparisons with the Full Three-Dimensional Transport Model Being Used in Total System Performance Assessment for License Application

In *Particle Tracking Model and Abstraction of Transport Processes* (BSC 2004, Section 7.3), the full complexity of the unsaturated zone in terms of heterogeneities in fluid flow conditions and properties is considered using comparisons with the full three-dimensional transport model used in TSPA-LA. The radionuclide ^{99}Tc is released at the repository horizon, and the breakthrough at the water table is recorded and compared to results from T2R3D, documented in *Radionuclide Transport Models Under Ambient Conditions* (BSC 2003c).

C.4.4.2.1   Comparisons of FEHM and T2R3D for the Dual-k Conceptual Model

The comparison of FEHM and T2R3D for the dual-k conceptual model is discussed in Section 7.4 and shown in Figure 7-2 of this technical basis document. The cumulative transport time distributions through the unsaturated zone for ^{99}Tc for the two models' three flow fields (lower, mean, and upper) show excellent agreement, considering the vast range of infiltration conditions covered in these comparisons. This agreement demonstrates that all significant features of the unsaturated zone transport system are captured with the abstraction model.

C.4.4.2.2   Influence of Diffusion Coefficient and Fracture–Matrix Interaction Alternate Conceptual Model

Figure C-11 shows the behavior of the FEHM model over the complete range of diffusion coefficients, from no diffusion to a case in which diffusion is set so high that it effectively yields a composite medium behavior. The envelope of behavior as a function of diffusion is quite large, whereas the behavior of T2R3D is reproduced when the same parameters and conceptual model for fracture–matrix interactions is selected. This result illustrates that the abstraction model yields reasonable results over a wide range of diffusion coefficients, one of the key parameter uncertainties in the TSPA model.

Also shown in Figure C-11 is the predicted behavior using the discrete fracture model formulation for the fracture–matrix interaction model. No process model results are available for comparison due to the computational limitations of simulating the full three-dimensional model using a MINC formulation. The results are reasonable, given the model behavior shown in Figure C-10 for the smaller two-dimensional cross-sectional model. The main differences for these alternative conceptual models are at the earliest arrival times, where the dual-k model predicts much faster arrivals at the water table. For later transport times the two curves track each other closely, showing that the results are insensitive to the conceptual model. Finally, all breakthrough curves with diffusion, including the high-diffusion case, converge at large transport times. This result is also reasonable, providing additional evidence for the correct functioning of the fracture–matrix interaction model.
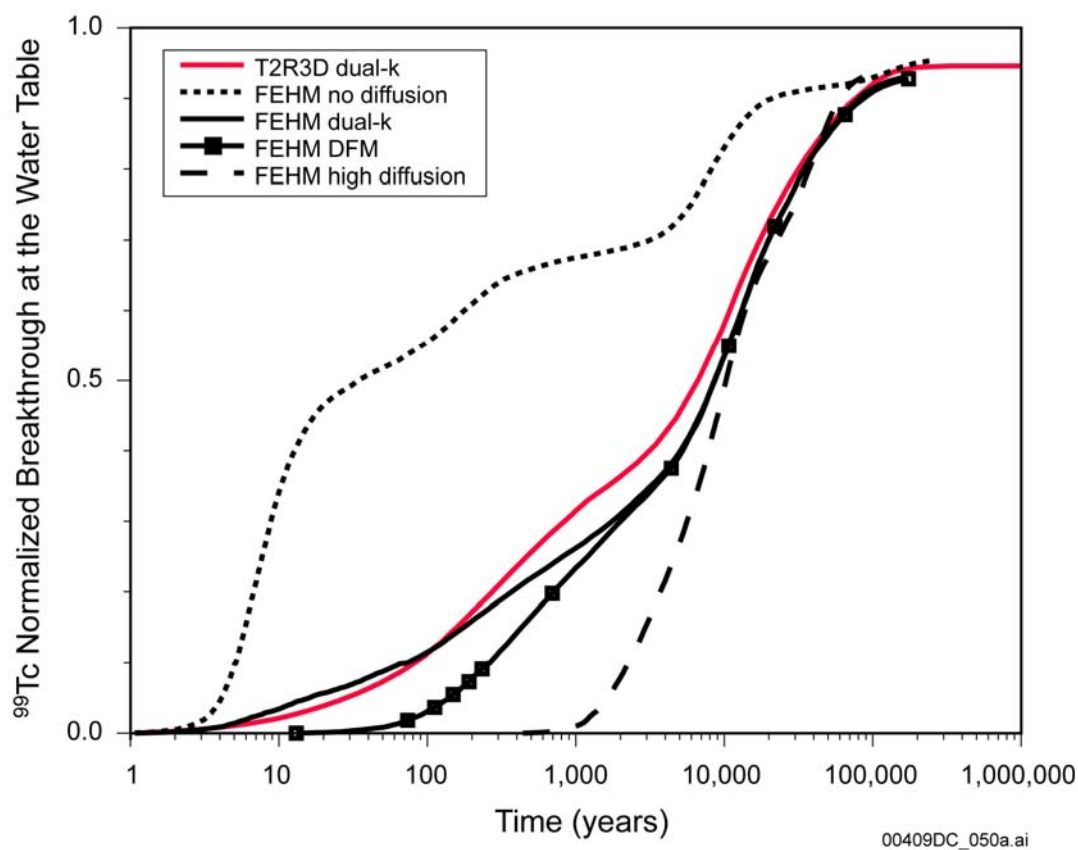
Source: BSC 2004, Figure 7-11.

Figure C-11. Comparison of Breakthrough Curves for ^{99}Tc for T2R3D and the Unsaturated Zone Transport Abstraction Model: Mean Infiltration Scenario, Diffusion in FEHM Ranging from No Diffusion to High Values

C.4.4.2.3   Tests of the Active-Fracture Model Implementation

Simulations for a range of active-fracture model γ parameters show that the active-fracture model formulation in FEHM yields results similar to that of the process model. Process flow model results (BSC 2003a, Section 6.8.1) have demonstrated that the active-fracture model parameters have very little influence on the flow field. Therefore, active-fracture model

parameter changes to the transport model can be applied using flow model results obtained from the base-case flow simulation.

Figure C-12 illustrates the impact of lowering the γ parameter in the same fashion as was done in *UZ Flow Models and Submodels* (BSC 2003a, Section 6.8.2, Figure 6.8-3) and in Figure C-13. Lowering the γ parameter in the TSw in the same manner as in *UZ Flow Models and Submodels* (BSC 2003a) yields a trend toward longer arrival times for the earliest arriving solute for both models. The curves converge at longer transport times. The fact that the lowering of γ in additional units below the repository has no further effect indicates that the principal sensitivity is for the alternate fracture model parameters in the TSw. For the purposes of the abstraction model validation, this qualitative comparison to the results shown in Figure C-13 (also shown and discussed in Section 6.3.7) provides strong evidence that the implementation in FEHM with respect to the alternate fracture model replicates the behavior of the process model.
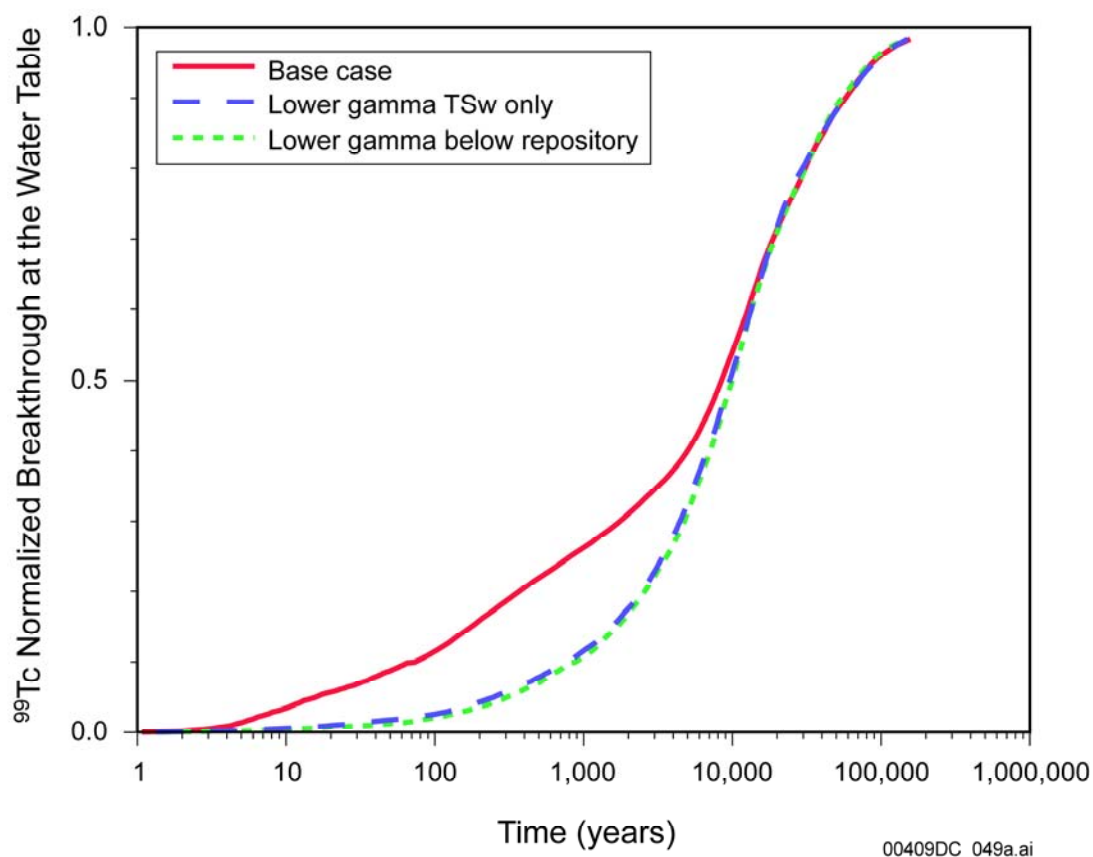
Source: BSC 2004, Figure 7-13.

NOTE: The colors, line types, and legend descriptors were chosen to facilitate a direct visual comparison to the simulation results presented in *UZ Flow Models and Submodels* (BSC 2003a, Figure 6.8-3) (see Figure C-13).

Figure C-12. Breakthrough Curves for Conservative Solute Using the Unsaturated Zone Transport Abstraction Model to Investigate the Role of Alternate Fracture Model Parameter γ: Dual-k Alternate Conceptual Model, Simulation for Different Values of γ in Rock Units beneath the Repository
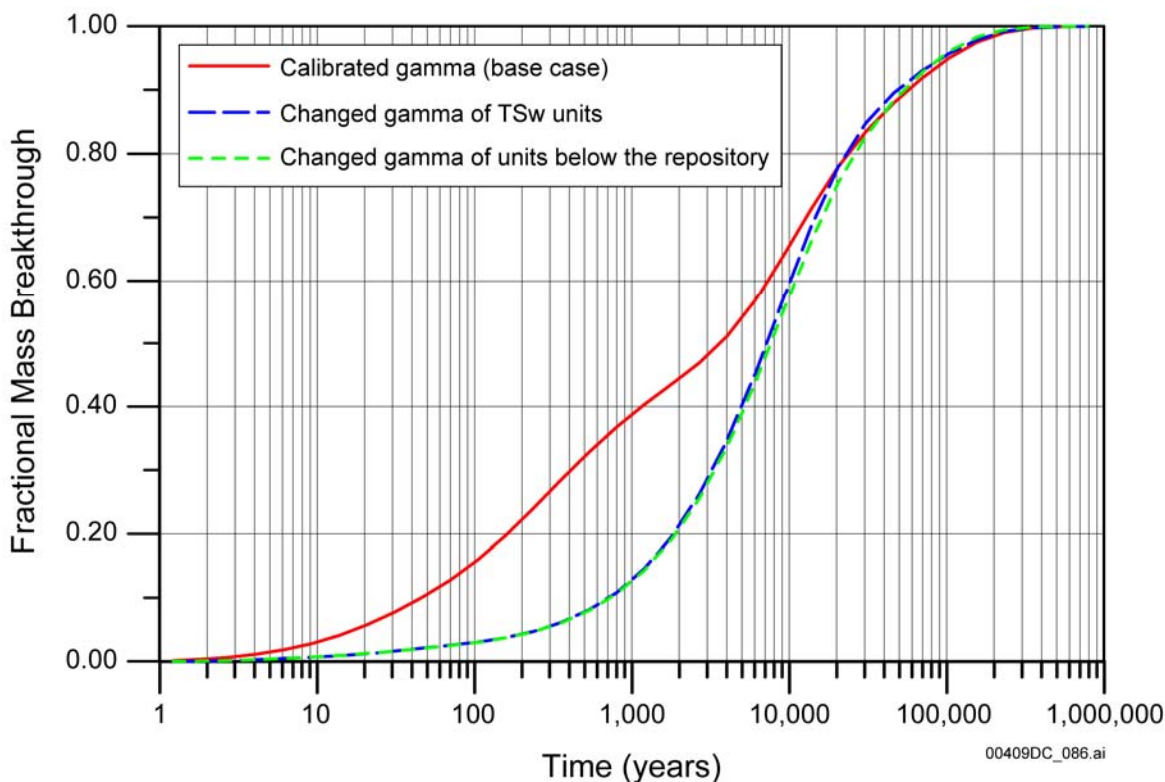
Source: BSC 2003a, Section 6.8, Figure 6.8-3.

Figure C-13. Comparison of a Simulated Breakthrough Curve of Relative Radionuclide Mass at the Groundwater Table Obtained for the Base Case (using Calibrated Rock Hydraulic Properties), a Case Using a Smaller (Half) γ of the TSw units, and Another Case Using a Smaller (Half) Value of γ of All Units below the Repository

C.5   REFERENCES

Bear, J.; Tsang, C.F.; and de Marsily, G., eds. 1993. *Flow and Contaminant Transport in Fractured Rock*. San Diego, California: Academic Press. TIC: 235461.

Brooks, R.H. and Corey, A.T. 1964. *Hydraulic Properties of Porous Media*. Hydrology Paper No. 3. Fort Collins, Colorado: Colorado State University. TIC: 217453.

BSC (Bechtel SAIC Company) 2001. *Analysis of Hydrologic Properties Data*. ANL-NBS-HS-000002 REV 00 ICN 01. Las Vegas, Nevada: Bechtel SAIC Company. ACC: MOL.20020429.0296.

BSC 2002. *Analysis of Geochemical Data for the Unsaturated Zone*. ANL-NBS-HS-000017 REV 00 ICN 02. Las Vegas, Nevada: Bechtel SAIC Company. ACC: MOL.20020314.0051.

BSC 2003a. *UZ Flow Models and Submodels*. MDL-NBS-HS-000006 REV 01. Las Vegas, Nevada: Bechtel SAIC Company. ACC: DOC.20030818.0002.

BSC 2003b. *Analysis of Hydrologic Properties Data*. MDL-NBS-HS-000014 REV 00. Las Vegas, Nevada: Bechtel SAIC Company. ACC: DOC.20030404.0004.

BSC 2003c. *Radionuclide Transport Models Under Ambient Conditions*. MDL-NBS-HS-000008 REV 01. Las Vegas, Nevada: Bechtel SAIC Company. ACC: DOC.20031201.0002.

BSC 2003d. *Calibrated Properties Model*. MDL-NBS-HS-000003 REV 01. Las Vegas, Nevada: Bechtel SAIC Company. ACC: DOC.20030219.0001.

BSC 2003e. *Drift-Scale Radionuclide Transport*. MDL-NBS-HS-000016 REV 00. Las Vegas, Nevada: Bechtel SAIC Company. ACC: DOC.20030902.0009.

BSC 2004. *Particle Tracking Model and Abstraction of Transport Processes*. MDL-NBS-HS-000020 REV 00. Las Vegas, Nevada: Bechtel SAIC Company. ACC: DOC.20040120.0001.

CRWMS M&O (Civilian Radioactive Waste Management System Management and Operating Contractor) 2000a. *Particle Tracking Model and Abstraction of Transport Processes*. ANL-NBS-HS-000026 REV 00. Las Vegas, Nevada: CRWMS M&O. ACC: MOL.20000502.0237.

CRWMS M&O 2000b. *Unsaturated Zone Flow and Transport Model Process Model Report*. TDR–NBS–HS–000002. REV 00, ICN02. Las Vegas, Nevada: CRWMS M&O. ACC: MOL.20000831.0280.

Domenico, P.A. and Schwartz, F.W. 1990. *Physical and Chemical Hydrogeology*. New York, New York: John Wiley & Sons. TIC: 234782.

Feder, J. 1988. *Fractals*. New York, New York: Plenum Press. TIC: 253584.

Goode, D.J. 1996. "Direct Simulation of Groundwater Age." *Water Resources Research, 32*, (2), 289-296. Washington, D.C.: American Geophysical Union. TIC: 252291.

Hogg, R.V. and Craig, A.T. 1978. *Introduction to Mathematical Statistics*. 4th Edition. New York, New York: Macmillan. TIC: 254311.

Kazemi, H. and Gilman, J.R. 1993. "Multiphase Flow in Fractured Petroleum Reservoirs." Chapter 6 of *Flow and Contaminant Transport in Fractured Rock*. Bear, J.; Tsang, C-F.; and de Marsily, G., eds. San Diego, California: Academic Press. TIC: 235461.

LANL (Los Alamos National Laboratory) 2003. *Software Code: FEHM*. V2.21. SUN, SunOS 5.8; PC, Windows 2000 and Linux 7.1. 10086-2.21-00.

LBNL (Lawrence Berkeley National Laboratory) 1999. *Software Code: T2R3D*. V1.4. FORTRAN 77, SUN, DEC/ALPHA. 10006-1.4-00.

LeCain, G.D.; Anna, L.O.; and Fahy, M.F. 2000. *Results from Geothermal Logging, Air and Core-Water Chemistry Sampling, Air-Injection Testing, and Tracer Testing in the Northern Ghost Dance Fault, Yucca Mountain, Nevada, November 1996 to August 1998.* Water-Resources Investigations Report 99-4210. Denver, Colorado: U.S. Geological Survey. TIC: 247708.

Lin, M.; Hardy, M.P.; and Bauer, S.J. 1993. *Fracture Analysis and Rock Quality Designation Estimation for the Yucca Mountain Site Characterization Project.* SAND92-0449. Albuquerque, New Mexico: Sandia National Laboratories. ACC: NNA.19921204.0012.

Liu, H.H.; Doughty, C.; and Bodvarsson, G.S. 1998. "An Active Fracture Model for Unsaturated Flow and Transport in Fractured Rocks." *Water Resources Research, 34*, (10), 2633-2646. Washington, D.C.: American Geophysical Union. TIC: 243012.

Neuman, S.P.; Illman, W.A.; Vesselinov, V.V.; Thompson, D.L.; Chen, G.; and Guzman, A. 2001. "Lessons from Field Studies at the Apache Leap Research Site in Arizona." Chapter 10 of *Conceptual Models of Flow and Transport in the Fractured Vadose Zone.* Washington, D.C.: National Academy Press. TIC: 252777.

NRC (U.S. Nuclear Regulatory Commission) 2002. *Integrated Issue Resolution Status Report.* NUREG-1762. Washington, D.C.: U.S. Nuclear Regulatory Commission, Office of Nuclear Material Safety and Safeguards. TIC: 253064.

Reamer, C.W. 2001. U.S. Nuclear Regulatory Commission/U.S. Department of Energy Technical Exchange and Management Meeting on Total System Performance Assessment and Integration (August 6 -10, 2001). Letter from C.W. Reamer (NRC) to S. Brocoum (DOE/YMSCO), August 23, 2001, with enclosure. ACC: MOL.20011029.0281.

Wang, J.S. 2003. "Scientific Notebooks Referenced in Model Report U0090, Analysis of Hydrologic Properties Data, MDL-NBS-HS-000014 REV00" Memorandum from J.S. Wang (BSC) to File, February 10, 2003, with attachments. ACC: MOL.20030306.0535.

Wang, Z.; Feyen, J.; and Elrick D.E. 1998. "Prediction of Fingering in Porous Media." *Water Resources Research, 34*, (9), 2183–2190. Washington, D.C.: American Geophysical Union. TIC: 250733.

Yamamoto, H.; Kojima, K.; and Tosaka, H. 1993. "Fractal Clustering of Rock Fractures and Its Modeling Using Cascade Process." *Scale Effects in Rock Masses, (Proceedings of the Second International Workshop on Scale Effects in Rock Masses, Lisbon, Portugal, June 25, 1993).* da Cunha, P., ed. 81–86. Rotterdam, The Netherlands: A.A. Balkema. TIC: 253608.

Yang, I.C. 2002. "Percolation Flux and Transport Velocity in the Unsaturated Zone, Yucca Mountain, Nevada." *Applied Geochemistry, 17*, (6), 807–817. New York, New York: Elsevier. TIC: 253605.

INTENTIONALLY LEFT BLANK

APPENDIX D

**EFFECTS OF CEMENTITIOUS MATERIAL
ON UNSATURATED ZONE FLOW AND TRANSPORT
(RESPONSE TO ENFE 1.04)**

Note Regarding the Status of Supporting Technical Information

This document was prepared using the most current information available at the time of its development. This Technical Basis Document and its appendices providing Key Technical Issue Agreement responses that were prepared using preliminary or draft information reflect the status of the Yucca Mountain Project's scientific and design bases at the time of submittal. In some cases this involved the use of draft Analysis and Model Reports (AMRs) and other draft references whose contents may change with time. Information that evolves through subsequent revisions of the AMRs and other references will be reflected in the License Application (LA) as the approved analyses of record at the time of LA submittal. Consequently, the Project will not routinely update either this Technical Basis Document or its Key Technical Issue Agreement appendices to reflect changes in the supporting references prior to submittal of the LA.

APPENDIX D

**EFFECTS OF CEMENTITIOUS MATERIAL
ON UNSATURATED ZONE FLOW AND TRANSPORT
(RESPONSE TO ENFE 1.04)**

This report provides a response for Key Technical Issue (KTI) agreement Evolution of the Near-Field Environment (ENFE) 1.04. This agreement relates to providing additional information on the technical basis for evaluating the impact of emplaced cementitious materials on the hydrologic properties of the unsaturated zone below the repository horizon and consequent effects on radionuclide transport in this region.

D.1 KEY TECHNICAL ISSUE AGREEMENT

D.1.1 ENFE 1.04

Agreement ENFE 1.04 was reached during the U.S. Nuclear Regulatory Commission (NRC)/U.S. Department of Energy (DOE) Technical Exchange and Management Meeting on Evolution of the Near-Field Environment (Reamer 2001) held January 9 to 12, 2001, in Pleasanton, California. ENFE Subissues 1, 2, 3, and 4 were discussed at that meeting. ENFE 1.04 was discussed under Subissue 1, Effects of Coupled Thermal-Hydrologic-Chemical Processes on Seepage and Flow.

At this meeting, DOE presented material on Subissue 1: Comments on Effects of Cementitious Materials (Hardin 2001), concluding that effects of cementitious materials on performance were expected to be modest and proposing additional modeling to support this conclusion.

The wording of the agreement is as follows:

ENFE 1.04

> Provide additional technical bases for the DOE's treatment of the effects of cementitious materials on hydrologic properties. The DOE will provide additional information on the effects of cementitious materials in an update to the *Unsaturated Zone Flow and Transport* PMR (TDR-NBS-HS-000002), available in FY 02. Information provided will include results of evaluation of the magnitude of potential effects on hydrologic properties and radionuclide transport characteristics of the unsaturated zone.

D.1.2 Related Key Technical Issues

ENFE 2.04 is related to this agreement in that it is concerned with trace elements and fluoride concentrations that may be introduced to the repository emplacement drifts through materials, including cement grout. ENFE 2.04 was addressed in *Technical Basis Document No. 5: In-Drift Chemical Environment*, in which the issues regarding cementitious materials were not considered because cementitious materials have been removed from the emplacement drift design (Ziegler 2003).

D.2   RELEVANCE TO REPOSITORY PERFORMANCE

Cementitious material (shotcrete) is planned for use as part of the ground support for the turnout intersections of the main access drifts and for the intersections of the exhaust drifts with the emplacement drifts. The incorporation of cementitious materials in the repository poses two concerns. The first is that the leaching of cementitious materials, particularly the shotcrete supporting the turnout intersections in the main access drifts and the intersections of the exhaust main drifts with the emplacement drifts, will affect repository performance by modifying the hydrologic properties of the surrounding rock and diverting the flow of water entering the drifts. The second concern is that an alkaline plume resulting from leaching of the cementitious material could enhance radionuclide transport to the accessible environment, either through the complexation of radionuclides or through the presence of pseudocolloids.

The original relevance of this agreement to repository performance is described in features, events, and processes (FEPs) that relate to cementitious materials in the repository. These FEPs are described and screened in a series of analysis and model reports. Revised screening summaries for these FEPs will be added to the next revision of the FEP analysis and model reports.

The original relevance of this agreement to repository performance is described in the following FEP:

- **2.1.06.01.0A, Chemical Effects of Rock Reinforcement and Cementitious Materials in the Engineered Barrier System** (BSC 2004a, Section 6.2.18)–Degradation of ground support material (cement, rock bolts, wire mesh) used for any purpose in the disposal region may affect long-term performance through both chemical and physical processes. Degradation may occur by physical, chemical, and microbial processes.

This FEP is excluded from total system performance assessment for license application because cementitious material (i.e., cement grout in ground support) is no longer part of the emplacement drift design for the engineered barrier system (BSC 2004b, Section 4.3).

The following related FEPS also consider the effects of cementitious materials:

- **2.1.09.01.0A, Chemical Characteristics of Water in Drifts** (BSC 2004a, Section 6.2.45)–When flow in the drifts is reestablished following the peak thermal period, water may have chemical characteristics influenced by the near-field host rock and engineered barrier system. Specifically, the water chemistry (pH and dissolved species in the groundwater) may be affected by interactions with cementitious materials or steel used in the disposal region. These point source contaminated waters may coalesce to form a larger volume of contaminated water. This altered groundwater is referred to as the carrier plume because dissolution and transport will occur in this altered chemical environment as contaminants move through the engineered barrier system and down into the unsaturated zone. (There is no defining limit as to what volume of contaminated water constitutes a plume.)

- **2.2.01.01.0B, Chemical Effects of Excavation/Construction in the Near-Field** (BSC 2004c, Section 6.8.2)–Excavation may result in chemical changes to the incoming groundwater and to the rock in the excavation-disturbed zone.

- **2.1.09.17.0A, Formation of Pseudocolloids (Corrosion Product) in the Engineered Barrier System** (BSC 2004d, Section 6.2.29)–Pseudocolloids are colloidal-sized assemblages (between approximately 1 nm and 1 μm in diameter) of nonradioactive material that has radionuclides bound or sorbed to it. Corrosion product pseudocolloids include iron oxyhydroxides from corrosion and degradation of the metals in the engineered barrier system and silica from degradation of cementitious materials.

These FEPs are excluded from total system performance assessment for license application because all introduced cementitious materials inside the repository are to be removed (at closure) except for ground support. These materials include all concrete structures (including inverts), as well as concrete or shotcrete used to support shafts, which is an exception to the nonremoval of ground support materials (BSC 2004b, Section 4.3). The potential effects of the cementitious material in the ground support are not significant to repository performance.

D.3 RESPONSE

There are two principal concerns relating to the incorporation of cementitious materials in the repository. The first concern is that the leaching of cementitious materials, particularly those supporting the turnouts in the main access and exhaust main drifts to the emplacement drifts, will affect repository performance by modifying the hydrologic properties of the surrounding rock and diverting groundwater flow. The second concern is that an alkaline plume could enhance radionuclide transport to the accessible environment, either through the complexation of radionuclides or through the presence of pseudocolloids. Both concerns become relevant only after the repository environment rehydrates following a period of dryout due to heating caused by radioactive decay of the emplaced waste. The dryout period is the period commencing with the boiling of water contained in the pores of the host rock mass surrounding the emplacement drifts after repository closure and ending when the affected rock mass has rehydrated.

An evaluation of the processes involved led to the following findings:

- Because the removal of all nonsupport cementitious materials from the repository is planned prior to closure, the only remaining cementitious materials would be shotcrete supports in the main access and exhaust ventilation drifts and minor quantities of grout used to secure rock bolt supports. Current plans also provide an option for tailoring the shotcrete and grout formulations to ensure that their subsequent alteration and degradation following repository closure do not adversely impact repository performance from geochemical or hydrologic perspectives.

- Both prior to and subsequent to repository closure, shotcrete and grout would be subject to degradation processes involving recrystallization and carbonation of reactive cement ingredients. Following closure, these processes would be accelerated due to increasing temperature, humidity, and CO_2 partial pressure (pCO_2) within the repository. Calculations indicate that, with optimal shotcrete mixes, hydrothermal recrystallization

rates would lead to substantially complete conversion of the cementitious component to silica-rich calcium silicate hydrates prior to rehydration following the repository dryout period. Upon reaction with pore water, these silica-rich phases would generate a leachate with a pH ranging between 10.1 and 10.7 but with concentrations of Ca^{2+} and dissolved silica equivalent to that of currently observed pore waters. Neutralization of the leachate by ambient CO_2 would not result in significant precipitation of calcite and would not, therefore, cause significant modification of the host-rock matrix and fracture permeability or the hydrologic regime.

- Following repository closure, gaseous CO_2 causing carbonation of the shotcrete and grout is restricted to sources within Yucca Mountain. Most will originate through pore-water evaporation due to heating of the rocks surrounding the emplacement drifts. Simple mass-balance calculations indicate that more than sufficient CO_2 would be available to carbonate all shotcrete and grout remaining in the repository. The extrapolation of a concrete carbonation model to 120°C indicates that the rates of carbonation would be so high that carbonation would instead be limited by the diffusion of CO_2 through the host-rock fractures and matrix. Calculations indicate that substantially complete carbonation would occur wherever the dryout period exceeds 1,000 years. This suggests that the shotcrete contained in the main access and exhaust drifts contiguous to the emplacement panels in the interior of the repository would be completely carbonated. However, shotcrete in the peripheral drifts would not be completely carbonated. The kinetics of carbonation by CO_2 gaseous phase diffusion into the shotcrete following rehydration would be hindered, and it is estimated that up to 5,000 more years would elapse before complete carbonation of the remaining shotcrete. Under these conditions, the carbonation reaction kinetics would be rate controlling rather than gaseous CO_2 diffusion through the repository host rocks.

- Because calculations indicate that shotcrete would be substantially altered to silica-rich calcium silicate hydrate phases, and separate calculations indicate that the shotcrete would be partially if not completely carbonated, this suggests that the competition between the two processes will result in a shotcrete degradation product that would be limited in its potential to generate an alkaline plume following rehydration.

- The rate of cementitious material recrystallization or carbonation at the elevated temperatures, humidity, and pCO_2 likely to be encountered in the repository during the thermal period (i.e., that period following repository closure when temperatures are significantly above those prior to emplacement) is not known with any degree of precision. Carbonation reactions are also thermodynamically less favored at elevated temperatures. Carbonation of silica-rich hydrated calcium silicates would also be slower than for portlandite or hydrated calcium silicate gels in freshly mixed cement. Therefore, carbonation at elevated temperatures could be less than predicted on the basis of extrapolated kinetic rates based on activation energies determined at ambient temperatures (assumed to be 25°C in this appendix).

- It is instructive to consider the unlikely possibility that some materials remain that would cause the generation of alkaline solutions following rehydration. The results show that the neutralization of the alkaline leachate by ambient CO_2 in the repository would be

very fast (i.e., on the order of weeks). At the slow percolation rates of pore waters in the rock matrix, all secondary precipitation of calcite is likely to occur within centimeters of the shotcrete interface. Indeed, a finite probability exists that calcite precipitation will occur primarily in situ and that no migration of an alkaline plume would take place. Thus, the issue of alkaline plumes affecting radionuclide transport would be considered extremely unlikely.

- The important question regarding the impact that the precipitation of calcite would have in sealing the host-rock matrix and fractures beneath shotcrete supports in the main access and exhaust ventilation drifts is difficult to assess. Using very conservative assumptions that all the portlandite in Type II cement of the shotcrete was available for leaching following rehydration and that calcite would precipitate within the pores and fractures immediately below the main turnoff intersection footprints, the matrix and fractures of the host rock would be filled to a depth of approximately 7 cm with calcite and to a depth of approximately 4.4 cm below the intersection of the exhaust main and the emplacement drift. If only a 1-cm thickness of rock were to be filled with calcite before it became completely impermeable and if subsequent precipitation were to take place laterally, the impermeable zone would extend an additional 8.4 m toward the emplacement drift on the main access drift side and an additional 7.1 m from the exhaust drift side. However, the standoff of the shotcreted portion of the turnout is a minimum of 60 m distance from the start of the emplacement drift. Therefore, it is unlikely that calcite precipitation would adversely affect the hydrology of the emplacement drift on the main access drift side. However, the situation would be different on the exhaust drift side, where calcite precipitation and sealing would extend laterally to within 1.5 m of the first waste package. The possibility that such sealing would occur is unlikely, however, because the shotcrete formulation can be modified to prevent the leaching of the components that would cause calcite precipitation. Furthermore, carbonation and recrystallization of the cement fraction prior to rehydration would limit leaching of calcite-forming components.

- If it is assumed that the shotcrete would be so altered that calcite precipitation adjacent to the shotcrete would not significantly modify the local hydrology, then the emplaced shotcrete is separated from the nearest waste package in the emplacement drift by a sufficiently large horizontal distance that diffusive mixing at depth of separate plumes from the leaching of shotcrete and radionuclides released by a failed waste package would not occur. However, diffusive mixing of analogous separate plumes at exhaust drift intersections is possible.

- Although the leachate from shotcrete altered by recrystallization and carbonation would be significantly alkaline, the alkalinity would be rapidly neutralized by ambient CO_2 in the vicinity of the emplaced shotcrete. The neutralized plume would differ little in composition from pore water in the repository and would, therefore, have only a minor impact on radionuclide migration, if the neutralized plume were to intersect and mix with a plume bearing radionuclides.

- Colloid generation and transport through leaching of cementitious material could take place only when the grout is young (i.e., prior to extensive hydrothermal

recrystallization and carbonation). Such processes, therefore, can occur only during the initial period following repository closure prior to dryout, when heating is close to its maximum intensity and when the likelihood of waste package failure is minimal. Furthermore, the relatively high ionic strength of the highly alkaline leachate will destabilize the mobilized calcium silicate hydrate colloidal particles, causing aggregation and adhesion. The maximum residual colloid concentration would be comparable or lower than that in the ambient environment. Thus, despite the fact that some radionuclides sorb strongly to such colloidal particles, the colloid concentration would be sufficiently low so that radionuclide sorption on the residual colloid will be of no consequence.

The information in this report is responsive to agreement ENFE 1.04 made between DOE and NRC. The report contains the information that DOE considers necessary for NRC review for closure of this agreement.

D.4 BASIS FOR THE RESPONSE

D.4.1 Background

Earlier repository designs involved the extensive use of concrete and other cementitious materials in the underground facility (Hardin 1998, p. 6-12). Of particular importance was the application of Type II expansive cement for the grouting of rock bolt supports to stabilize the emplacement drifts in order to ensure retrievability until such time as the NRC approves repository closure, the incorporation of a concrete invert structure to facilitate emplacement of the waste packages, and waste package concrete support structures.

A program was implemented to address issues relating to the presence of cementitious materials in the emplacement drifts and their impact on waste package integrity and radionuclide transport in the event of waste package failure (Younker 1996; Meike 1996; Hardin 1998; CRWMS M&O 1998). At the time, the waste package design consisted of a mild steel sacrificial (corrosion allowance) outer barrier over an inner Alloy 22 (UNS N06022) corrosion-resistant barrier. These studies uncovered several issues that increased both complexity and uncertainty in the repository design. Of particular concern were issues relating to the leaching of cementitious materials with mobilization of fluoride (CRWMS M&O 2000; Hardin 2001) and the potential production of residual $CaCl_2$-$MgCl_2$ brines, both of which could result in enhanced corrosion of the steel outer barrier of the waste package (Hardin 1998, p. 6-12). It was determined that alkaline fluids could substantially increase outer barrier corrosion, leading to peak waste package failures at about 6,200 years (DOE 1998, p. 5-19). In addition to effects on the waste package, the extreme alkalinity of the leachate (moving as an alkaline plume) was a concern for decreasing radionuclide sorption in the unsaturated zone transport pathway because actinide sorption coefficients on tuff decreased to zero at high pH (Younker 1996, pp. 1 to 4; CRWMS M&O 1998; DOE 1998). In contrast, laboratory studies revealed that certain radionuclides (e.g., uranium and neptunium) were very strongly retarded within cementitious materials (Hardin 1998, pp. 6-42 to 6-45). Alkaline leachates may also tend to lower the activity of carbonate in solution, thereby potentially decreasing the concentration of uranyl and neptunyl carbonate complexes in solution (Hardin 1998, p. 6-36).

To address some of these concerns, a drip shield was incorporated in the design to protect the waste package from water infiltrating into the emplacement drifts, and the waste package design was modified to provide for a protective Alloy 22 outer barrier and a Stainless Steel Type 316 inner barrier (e.g., see BSC 2001).

When DOE and NRC met to discuss the status of the ENFE KTIs in January 2001, concerns regarding the introduction of cementitious materials were considered to be largely resolved. At this meeting, DOE presented material on Subissue 1: Comments on Effects of Cementitious Materials (Hardin 2001) and concluded that effects of cementitious materials on performance were expected to be modest but proposed additional modeling to support this conclusion.

Subsequently, however, a decision was made to eliminate all cementitious materials from the emplacement drifts, as reflected in *Engineered Barrier System: Physical and Chemical Environment Model* (BSC 2004e). This decision was based predominantly on the potential effects of cement on the chemistry of seepage waters and how this might affect waste package corrosion. Thus, the only aspect concerning Subissue 1 that remained to be addressed was NRC concerns regarding the presence of cementitious materials elsewhere in the repository and their potential interactions with the host rock (Hardin 2001).

A further reduction in the quantity of cementitious materials to remain in the repository after closure was affected with the requirement of *Ground Control for Non-Emplacement Drifts for LA* (BSC 2004f, Section 3.1.4.4.1) and *Subsurface Facility Description Document* (BSC 2004g, Section 3.1.1.4.13.1). This requirement specifies the removal of all noncommitted materials that could impact the long-term performance of the repository, including all concrete structures except those necessary for ground support. All concrete invert structures in all drifts and turnouts would, therefore, be removed prior to closure. Shaft concrete or shotcrete used to support shafts would also be removed. Therefore, the only significant cementitious materials remaining in the repository would be shotcrete supports and grout for rock bolt placement.

D.4.2 Cementitious Materials in the Current Repository Design

The repository incorporates introduced materials necessary for its effective functioning. Among these materials are cementitious materials, which are planned for ground support and concrete invert structures in all underground openings except the emplacement drifts. Three types of cementitious material will be used: cement grout, shotcrete, and concrete. Of these three materials, only cement grout and shotcrete are committed.

Current plans call for the removal of all cementitious materials not required for ground support. According to *Subsurface Facility Description Document* (BSC 2004g, Section 3.1.1.4.13.1):

> The Subsurface Facility shall decommission, decontaminate as required, demolish, dismantle, and remove materials and equipment that cannot become permanent fixtures of the underground repository after closure in order to conform with repository long-term performance requirements that may be affected if those noncommitted materials are left underground…. Noncommitted materials are those materials excluded from the inventory of repository permanent committed materials as documented in analyses supporting Total System

Performance Assessment-License Application and shall be removed from the Subsurface Facility to prevent hydrological and geochemical conditions adverse to waste isolation.

It is, therefore, expected that almost all of the nearly 300,000 tons of concrete will be removed prior to repository closure. Therefore, for the purposes of the evaluation presented in this appendix, only the impact of shotcrete and grout requires further consideration.

The applications of the committed cementitious materials and quantities to be used are summarized in Table D-1. The information in this table is abstracted from *D&E/ PA/C IED Subsurface Facilities Committed Materials* (BSC 2004h) and *Turnout Drift Operations Configuration* (BSC 2004i), which represent current design concepts. The data contained in the table are illustrative only and may change as the design parameters are refined.

Table D-1. Summary of Committed Ground Support Cementitious Materials in Subsurface Openings of the Repository

Subsurface Opening	Committed Material (metric tons)	
	Cement Grout	Shotcrete
Emplacement Drift Turnouts	324	0
Turnout Intersections	281	23,096
Intersections (Exhaust Air Side)	94	5,679
Access/Exhaust Mains	589	0
North Construction Ramp	110	11,061
Exhaust Main	32	0
Intake/Exhaust Shaft	0	0
Shaft Access	87	0
Exhaust Raise (5 m diameter)	0	0
Exhaust Raise (2 m diameter)	0	32
Exhaust Raise Access	5	0
Main Slash	40	0
Intake Main Extension	8	0
Assembly/Disassembly Chambers	15	0
Ventilation Access	8	0
Intake Shaft Access	53	0
Observation Drift and Test Alcove	23	0
Exploratory Studies Facility Main Drift	72	0
Exploratory Studies Facility North Ramp	124	12,098
Exploratory Studies Facility South Ramp	74	7,448
TOTAL (Percentage of All Cementitious Materials)	1,938 (3.16)	59,413 (96.84)

Source: BSC 2004h; BSC 2004i.

In terms of total mass, shotcrete dominates the committed cementitious materials. According to the compositions in Table D-2, grout and shotcrete contain approximately 63 and 18 wt %, respectively, of the most reactive component, cement.

Table D-2. Components of Cementitious Materials

Component	Grout (kg/m³)	Shotcrete (kg/m³)
Cement, Unspecified	1,228	–
Cement, Type II	–	437
Water	546	186
Coarse Aggregate	–	534
Fine Aggregate	–	1,203
Silica Fume	136	30
Super-Plasticizer	27	–
Polyhead	–	4.5
Shotcrete Accelerator	–	1.5
Steel Fiber	–	39

Source: BSC 2004h.

NOTE: Shotcrete also contains 0.09 kg/m³ of Micro Air.

It should be noted that the cement compositions specified in Table D-2 are less than optimal in terms of their reactivity and tendency to generate alkaline plumes upon leaching (DTN: LL020805523125.002). *Ground Control for Non-Emplacement Drifts for LA* (BSC 2004f, Section 6.5.4.2) suggests that a low pH grout and shotcrete and concrete mix will be developed with lesser amounts of Portland cement and silica fume, or, alternatively, other types of grouts and cements that are not of the Portland type could be used. For the purposes of the evaluation presented in this appendix, it will be conservatively assumed that Type II Portland cement will be used because this is the cement used in shotcrete. The issue of cement formulation is discussed further in Section D.4.4.

The cementitious materials most likely to affect repository performance are those associated with the intersections of emplacement drifts with the main access and exhaust drifts. Two types of intersections are specified: (1) the fresh-air side, where a 61-m-radius rail turnout from the 7.62-m-diameter circular main access drift transitions into the horseshoe-shaped 7-m-high by 8-m-wide turnout drift and (2) the exhaust-air side of the emplacement drift and the exhaust main drift intersection (Figure D-1). At these intersections, a 10-cm-thick layer of shotcrete will be applied over the backs of each drift to just below the springline on each side. In total, (1) approximately 36 m of the combined fresh-air main and horseshoe-shaped 7-m-high by 8-m-wide turnout drifts will be shotcreted, and (2) 15 m of the exhaust main and approximately 5 m of the turnout to the emplacement drift will be shotcreted for each emplacement drift. The quantities of shotcrete in each case are estimated to be 161 and 53 MT, respectively, for each turnout (BSC 2004h). Because the emplacement drift centerlines are 81 m apart, and the drifts subtend an angle of 70° to the main drifts over much of the repository, the emplacement drift centerlines will intersect the main drifts with a spacing of 86 m. If 36 m of shotcrete were applied to the main access drift at each intersection with an emplacement drift, then 42% of main access drift contiguous with the emplacement panels would be shotcreted. Similarly, with approximately 15 m of shotcrete applied at 86 m intervals to the exhaust main drifts, 17% of these drifts would be shotcreted contiguous to the emplacement panels. Each emplacement drift turnout will also contain 0.45 MT of grout for rock bolt placement.
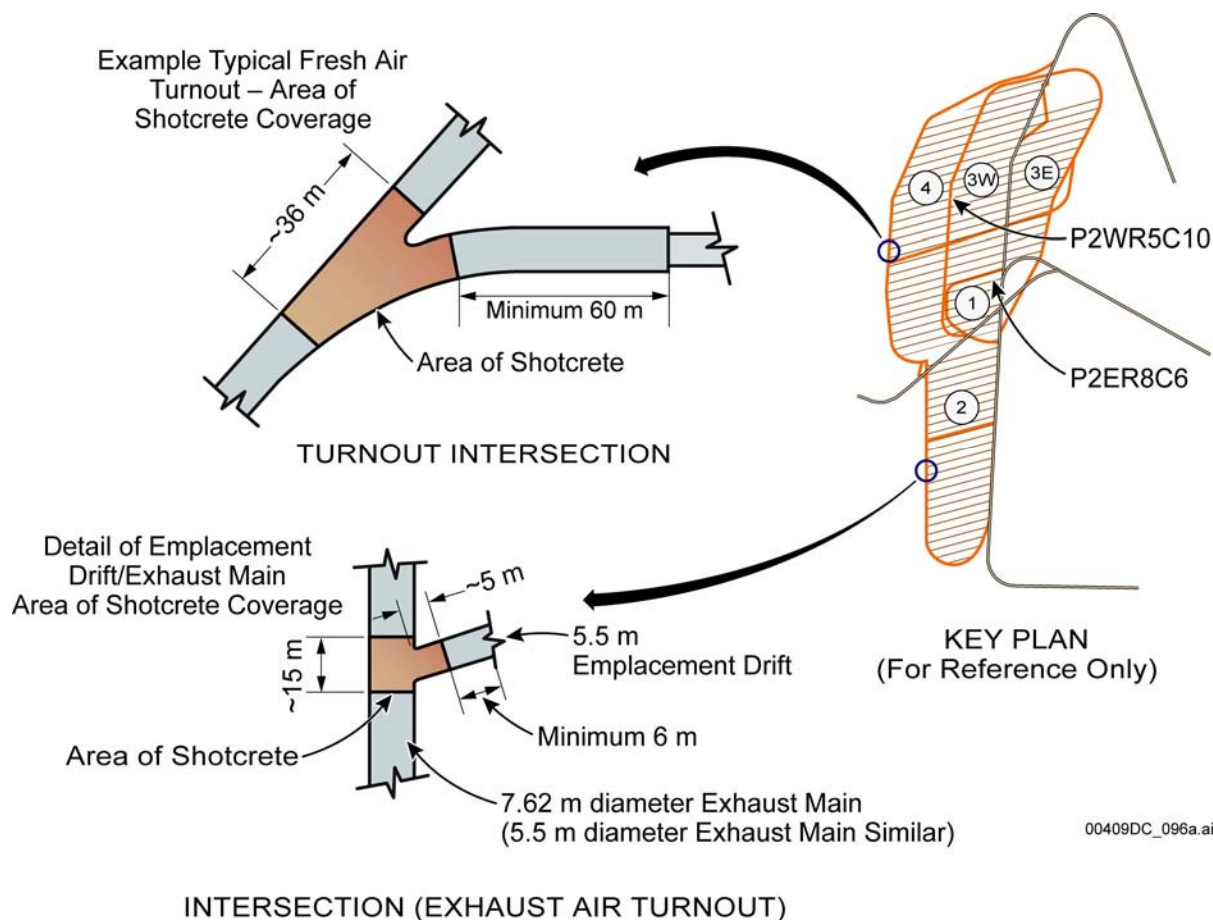
Source: BSC 2003a.

Figure D-1. Schematic of the Current Planned Locations Where Cementitious Material Will Be Used in the Repository Intersections and Turnouts

In the following discussion, scientific and technical bases are presented that assess the impact of the shotcrete support structures and rock-bolt grout on repository performance, particularly in relation to potential modifications to the hydrology and the effect of cementitious leachates on radionuclide migration.

D.4.3 Environment to Which Cementitious Materials Would Be Exposed Following Repository Closure

Upon closure of the repository, the cementitious materials would have aged for a period that could be as long as 100 years, depending on when they were installed during construction, the time required to load the repository, and the duration of the monitoring and performance confirmation period, during which retrievability would have to be maintained. During that time, cementitious materials would be subject to drying and carbonation under thermally driven ventilation, but the maximum temperature excursion to which these materials would be exposed is expected to be modest. The maximum temperatures would occur at the exhaust side of the emplacement drifts and should not exceed 85°C.

After repository closure, ambient temperatures would rise rapidly, and cementitious materials would be exposed to environmental conditions controlled by repository design parameters. The duration and magnitude of the postclosure temperature excursion, the corresponding relative humidity, and the pCO_2 changes to which cementitious materials would be exposed are discussed in the following sections.

Modeled predictions regarding thermal-hydrologic processes within the repository configuration following closure can be found in *Multiscale Thermohydrologic Model* (BSC 2004j, pp. 80 to 82, 95, 116 to 136). Figure D-2 shows that, for a mean infiltration flux case and representative pwr1-2 waste package (BSC 2004j, Table 6.3-10), the peak temperatures adjacent to the main access and exhaust main drifts would range between 130°C and 160°C, although waste packages in a small region adjacent to the northwest margin of Panel 3W could exceed 170°C.

The base-case temperatures of waste packages adjacent to the main access and exhaust main drifts are predicted to fall below the boiling point between 200 and 1,200 years after closure, with the temporal distribution correlating closely with the temperature distribution shown in Figure D-2. This waste package temperature distribution is used as a basis for estimating the maximum temperatures expected in the adjacent main access and exhaust drifts in the repository. The small region of the exhaust main drift adjacent to the northwest margin of Panel 3W in Figure D-2 would be expected to remain above the boiling temperature for the longest time (1,200 years). The evolution of relative humidity would be variable, depending on locality within the repository. At position P2ER8C6 (Figure D-1), adjacent to the main access drift (see BSC 2004j, Figures 6.3-1 and 6.3-7d), the relative humidity would range from a low of 17% after closure for 60 years to approximately 90% after closure for 2,000 years. In location P2WR5C10 (Figure D-1), near the hottest region of the exhaust main drifts, noted above (BSC 2004j, Figures 6.3-1 and 6.3-9d), the relative humidity would fall to about 15% after 40 years and recover to about 90% after 2,000 years, a time when the region occupied by the emplacement drifts would have rehydrated and when leaching of cementitious materials would become operative.

The excursion of pCO_2 during a period of 7,000 years has been modeled in the region surrounding the emplacement drifts (BSC 2004k, Figure 6.4-16). Carbon dioxide would evolve from evaporating pore waters during heating of the rock matrix adjacent to the emplacement drifts and, to a substantially smaller extent, during calcite dissolution as a result of the increasing ambient pCO_2 (BSC 2004l). The initial phase of dryout of the host rocks surrounding the emplacement drifts would cause the generation of a steam atmosphere. The steam would dilute the concentration of CO_2 in the vapor phase in the emplacement drifts, causing it to fall to very low values between closure and eventual rehydration. According to *Drift-Scale Coupled Processes (DST and THC Seepage) Models* (BSC 2004l, Figure 6.5-8), CO_2 partial pressures at the rock in fractures adjacent to the emplacement drift would range from between ambient (1,000 ppmV) and as low as 1 ppmV during that period. The steam, together with the CO_2, would be displaced outward where the steam would condense, causing a differential enrichment of CO_2 in the residual vapor phase and an increase in the pCO_2 in the main access and exhaust main drifts of the repository. Mountain-scale simulations of the repository between 200 and 7,000 years (BSC 2004k) show that the emplacement and main drifts could be exposed to log pCO_2 values of −2.5 (3,200 ppmV) over the first 3,000 years, declining slowly thereafter.

Mean Infiltration Flux Case
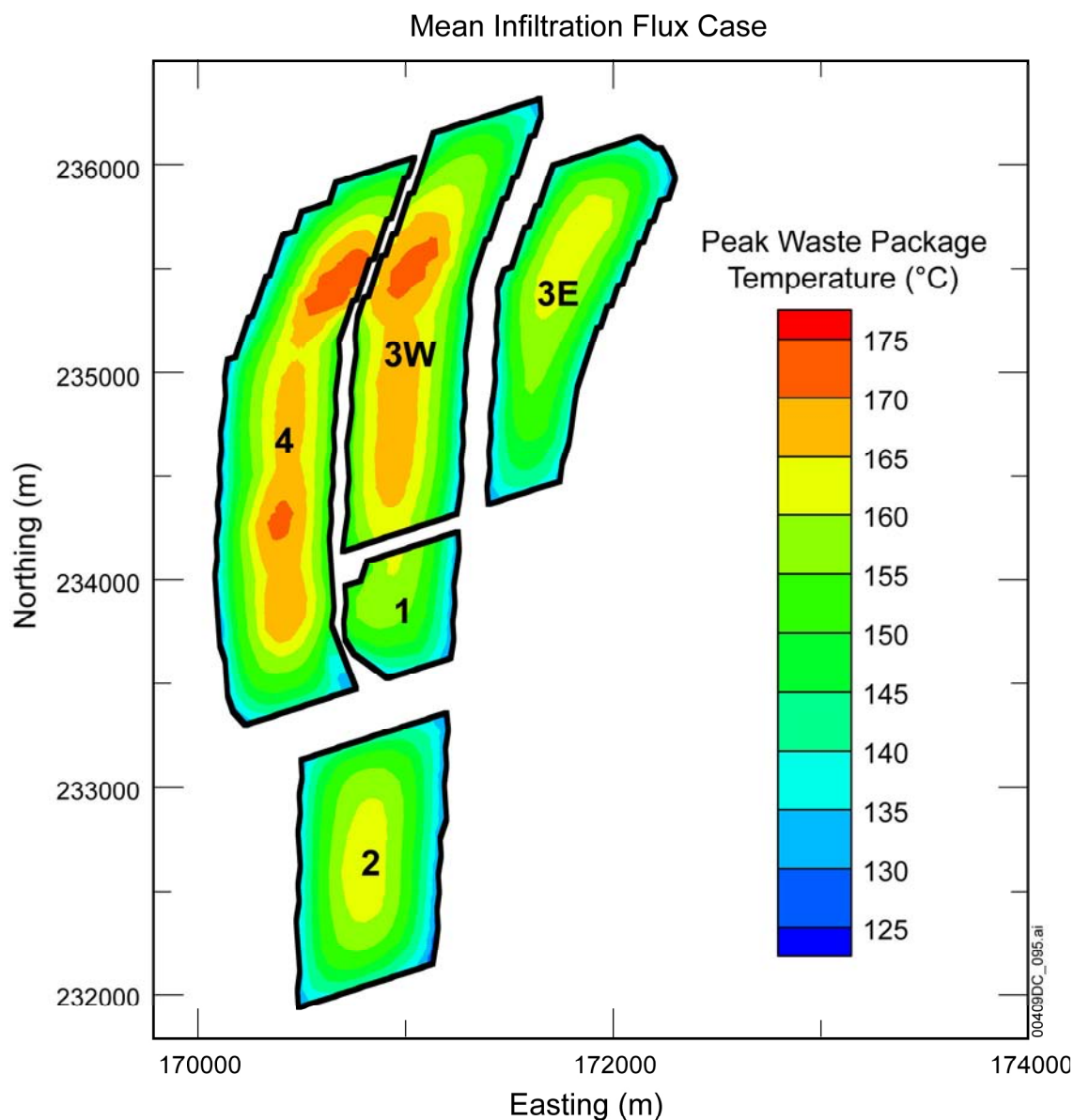
Source: BSC 2004j, Figure 6.3-3.

NOTE: The Pwr1-2 waste package contains waste from a pressurized water reactor and has a higher initial heat generation rate than most other waste packages (BSC 2004j, Table 6.3-10).

Figure D-2. Contour Map of Peak Waste Package Temperature for the Pwr1-2 Waste Package Plotted over the Repository Area for the Mean Infiltration Flux Case

The cited CO_2 partial pressures reflect model results obtained in two dimensions simulating a cross section through Yucca Mountain perpendicular to the axes of the emplacement drifts (BSC 2004k). A zero-flux condition was specified parallel to the emplacement drift axes. This, however, is the direction that CO_2 would migrate if CO_2 were to be sequestered through carbonation of the cementitious materials in main access and exhaust drifts.

The information extracted from *Drift-Scale Coupled Processes (DST and THC Seepage) Models* (BSC 2004l) is not part of any modeling activity that specifically addresses the environment to which cementitious materials in the main access and exhaust main drifts are exposed. The extracted data are, therefore, approximate. Uncertainties in the temperature, relative humidity, CO_2 partial pressure, and hydrology associated with end effects relating to the positioning of waste packages within the emplacement drifts are not addressed. The shedding of pore-water condensate above the emplacement drifts could result in increased concentrations of condensate percolating into and around the main access and exhaust main drifts. Despite these limitations, the data described approximately bound the conditions under which cementitious materials are exposed and provide a basis for estimating their behavior during and following the thermal period.

D.4.4   Fate of the Cementitious Materials

The primary processes that must be addressed to understand the fate of cementitious materials in the repository and their impact on repository performance include the following:

- Dehydration
- Hydrothermal recrystallization
- Carbonation
- Formation and migration of hyperalkaline plumes
- Calcite precipitation and permeability modification in unsaturated zone host rocks
- Colloid generation and transport.

These processes are reviewed in relation to repository performance in the following sections.

The chemistry of cementitious materials is an important aspect of the following reviews. For convenience, a shorthand notation commonly used to describe the composition of cementitious phases will be used in the following sections. The notation for the components described is $C = CaO$; $S = SiO_2$; $H = H_2O$; $A = Al_2O_3$; $F = Fe_2O_3$; $\overline{C} = CO_2$; and $\overline{S} = SO_3$.

Principal constituents of Type II cement used in the formulation of shotcrete are listed below. The chemical composition of Type II Portland cement (Tennis 1999) is 21.1 wt % SiO_2, 4.5 wt % Al_2O_3, 3.4 wt % Fe_2O_3, 63.8 wt % CaO, 2.2 wt % MgO, and 2.7 wt % SO_3. The potential compound composition of Type II Portland cement (Tennis 1999) is 0.54 wt % Na_2O(eq.), 56 wt % C_3S, 19 wt % C_2S, 6 wt % C_3A, and 10 wt % C_4AF.

Portland cement is created by calcining a specified mixture of limestone and clay in a rotary kiln at 1,450°C (Neville 1996). The resulting clinker is then ground to a mean particle size of about 30 μm. The anhydrous cement is composed dominantly of C_2S, C_3S, C_3A, and minor C_4AF, the relative proportions of these phases being a function of the initial feed and the potential application of the cement product. The phases comprising Portland cement are highly reactive with water. Upon mixing with water, therefore, several secondary phases rapidly form that result in creation of a hardened paste. Most prominent of these secondary phases is a colloidal C-S-H gel of indeterminate composition (C:S approximately 1.7:1), which forms from the C_2S and C_3S with concomitant production of secondary CH according to Equations D-1 and D-2 (Nelson 1990):

$$2\,C_3S + 6\,H = C_3S_2H_3 + 3\,CH \qquad\qquad \text{(Eq. D-1)}$$

$$2\,C_2S + 4\,H = C_3S_2H_3 + CH \qquad\qquad \text{(Eq. D-2)}$$

Using these data, the initial concentration of CH in shotcrete cement can be calculated. This information is presented in Section D.4.4.3.

D.4.4.1   Dehydration

Upon closure of the repository, the cementitious materials will have aged for a period that could be as long as 100 years depending on when they were installed during construction, the time required to load the repository, and the duration of the monitoring and performance confirmation period, during which retrievability must be maintained. The Portland cement fraction would initially have contained excess water over that required to hydrate the component phases of the cement. According to Meike (1997), a small portion of this water is expected to be lost due to bleeding during hydration of concrete. Some of this water will have evaporated prior to closure, despite the relatively high ambient relative humidity. The remainder will evaporate during the period up to 1,200 years after the temperature of the shotcrete exceeds the boiling point of water (approximately 96°C), leading to minor enhancement of condensate concentrations above and below the main access and exhaust main drifts. Using the data in Table D-2, it can be shown that young cement in the shotcrete would initially contain 30 wt % of water, but a thermally modified cement would, according to Meike (1997, Table 5), contain only 18 wt % water. Thus, the cement would release 48 wt % of the initial water content before and during the thermal period following closure. This is equivalent to 3.7 wt % of the shotcrete being lost through bleeding or evaporation of water, roughly equivalent to the amount of water released by a corresponding mass of devitrified tuff, which initially contains about 4.2 wt % of water (see Table D-3). However, the quantity of committed cementitious materials is trivial in relation to the total mass of rock that would be desiccated during the thermal period. Therefore, it can be concluded that the excess of water over that required to form the hydrated phases in the cement component of grout or shotcrete would not impact the hydrology of the unsaturated zone within Yucca Mountain.

Table D-3.   Parameters Used to Calculate the Transient Diffusion of CO_2 toward Carbonating Cementitious Material following Repository Closure

Parameter	Units	Value	Source
Diffusion coefficient of CO_2 in air at ambient temperatures[a]	m^2/s	1.39×10^{-5}	Lackner et al. 1999.
Molecular weight $Ca(OH)_2$	g/mol	74.09	Lide 2000, p. 4-50.
Density of portlandite	g/cm^3	2.26	Calculation from Table D-2.
Density of shotcrete	kg/m^3	2,425	Calculation from Table D-2.
Average concentration of portlandite in shotcrete	mol/m^3	1,821	Calculated, this appendix.
Saturated bulk density of tuff	g/cm^3	2,410	BSC 2003b, Section 8.2.4.3.
Fracture tortuosity coefficient, τ	–	0.5	Liu et al. 2003.
Fracture porosity, ϕ	–	0.01	Assumed.
Matrix porosity	–	0.164	Liu et al. 2003.
Saturation	–	0.61	Liu et al. 2003.
Total gas-phase porosity	–	0.174	Assumed.
Water content in rock	kg/m^3	100	Calculated from Liu et al. 2003.
Water content of rock	vol %	4.15	Calculated, this appendix.
HCO_3^- concentration in pore water	mg/L	110	Yang et al. 1996.
CO_2 in pore water	mol/m^3 rock	0.1792	Calculated, this appendix.
CO_2 concentration pores and fractures	mol/m^3	0.5149	Calculated, this appendix.

NOTE: [a]Ambient temperature is assumed to be 25°C for the purposes of this appendix.

Water released through bleeding, rather than evaporation, would initially be highly alkaline, containing dissolved sodium and potassium hydroxides in addition to calcium hydroxide (DTN: LL020805523125.002; Rothstein et al. 2002; Wieland et al. 2004, p. 120). The quantity of alkali present (as Na_2O(eq.)) in Type II Portland cement is about 0.5 wt % (Tennis 1999). If all such alkali were to be released in the initial seeps, it would immediately react with gaseous CO_2 in the host-rock fractures, producing sodium and potassium bicarbonate (DTN: LL030211423125.005). The quantity of alkali metal bicarbonate produced would be about 2.3 kg per metric ton of shotcrete. Sodium bicarbonate is highly soluble and would dissolve in the pore waters following rehydration of the repository.

D.4.4.2   Hydrothermal Recrystallization

After repository closure, the cementitious materials will be subject to recrystallization and carbonation, especially during the dryout period when temperatures, pCO_2$, and humidity are significantly elevated. In this section, the implications of recrystallization of the cementitious component of shotcrete are considered. Carbonation is dealt with separately in Section D.4.4.3. Hydrothermal recrystallization of cementitious materials would have important consequences regarding the leachability of alkaline components with rehydration of the host rocks following the dryout period. The cementitious materials would become progressively less soluble, leaching would be curtailed, the alkalinity of leachate plumes would be less severe and less probable, and modifications to the permeability of the host rocks due to alkaline plume neutralization and calcite precipitation would be attenuated.

The hydrothermal alteration of cementitious materials proceeds in several stages. The original principal constituents (C-S-H gel, portlandite (CH), initially formed C-S-H crystalline silicates and silica fume) alter to a variety of secondary hydrated calcium silicates, the specific phases depending on the duration, temperature, and C/(S+C) mole fraction (Figure D-3) (Nelson 1990; Neville 1996) and overall composition of the cement. (The dashes in C-S-H represent the lack of fixed stoichiometry in this gel phase.) The two most reactive phases are CH and C-S-H gel. Most, if not all, of the available CH could initially transform into calcite because of its high reactivity. The initial formation of CH can be avoided, however, by the addition of sufficient silica fume so that no residual C is available to form CH. Silica fume additions have the added advantage of inhibiting permeability degradation during alteration under hydrothermal conditions at elevated temperatures (Nelson 1990, Chapter 9). Thus, some of the uncertainties associated with CH reactivity are expected to be mitigated with appropriate attention to the cement formulation used.

Figure D-3. Formation Conditions for Various Calcium Silicates
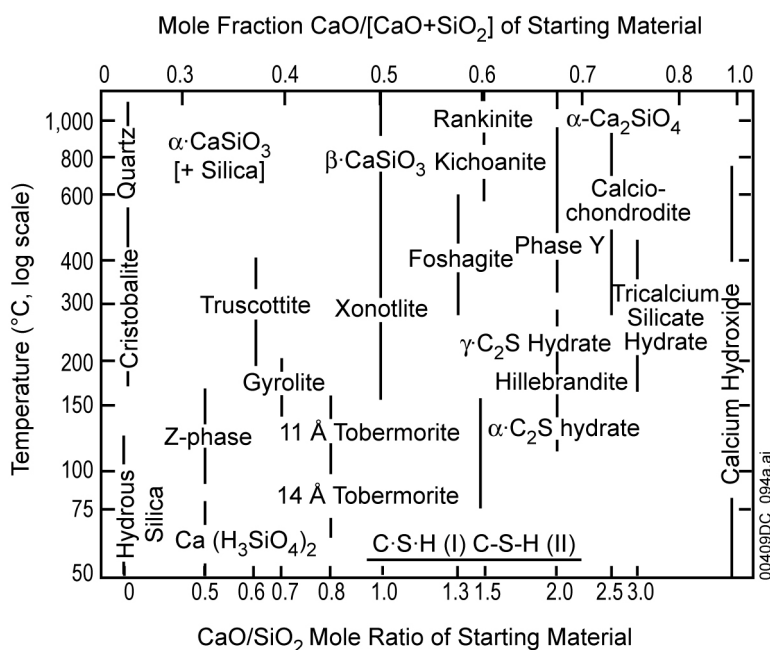
Source: Nelson 1990, Figure 9-2.

The C-S-H gel would carbonate more slowly, and, therefore, it could recrystallize to secondary calcium silicates before extensive carbonation, particularly within the interior of large monolithic concrete structures. Experimental evidence in the published literature indicates that recrystallization of the C-S-H gel is very rapid at elevated temperatures (e.g., see Shaw et al. 2000; Shaw et al. 2002). Shaw et al. (2002) show that C-S-H gel with the composition of gyrolite will recrystallize at 200°C within hours, and, at temperatures of 100°C to 160°C (typical of postclosure repository conditions during the dryout period), recrystallization would take place in a matter of weeks. Therefore, all gel materials are expected to have been transformed to secondary hydrated calcium silicates long before rehydration of the repository. Because of the amorphous nature of silica fume and the high reactivity of portlandite, it can likewise be presumed that all portlandite would react with silica fume additives within a similar time frame, provided that sufficient silica fume would be available to neutralize the portlandite.

Over a longer time period, the recrystallized components of the cement would further react with the minerals contained within the aggregate, causing progressive silication with further phase transitions in the cement and aggregate. Experimental studies have been conducted to evaluate the hydrothermal alteration of cementitious materials representative of those originally selected for emplacement in the repository. Exploratory Studies Facility invert concrete samples (autoclaved at 200°C in 0.003 mol/L $NaHCO_3$ solution for 8 months) indicated the minor formation of such C-S-H phases as scawtite, tobermorite, and xonotlite, together with clays with 2:1 layer smectitic and 1:1 layer serpentinitic structures (Hardin 1998, p. 6-38, Figure 6-38) (see Table D-4 for chemical formulas). A subsequent study showed that Type K cements, with a water-to-cement ratio of 0.35 and autoclaved in a steam atmosphere at 177°C for 8 hours, yielded major secondary phases: hydroxylellestadite and katoite with varying concentrations of portlandite and calcite, together with minor ettringite (DTN: LL020805523125.002). Autoclaving for 16 hours gave essentially identical results, indicating that the brief time period of 8 to 16 hours is sufficient to convert most of the portlandite to C-S-H phases.

Table D-4. $CaO/(CaO + SiO_2)$ Ratios of Cementitious Materials

Phase	Mineral	Chemical Formula	Cement Formula[a]	C/(S+C)
Shotcrete Components (Multiphase Mixtures)	Type II Cement	–	–	0.76
	Type II Cement + Silica Fume	–	–	0.71
	Type II Cement + Silica Fume + Fine Aggregate[a]	–	–	0.23
CaO-SiO$_2$ Binary	Portlandite	$Ca(OH)_2$	CH	1.00
	Hillebrandite	$Ca_6Si_3O_9(OH)_6$	$C_6S_3H_3$	0.67
	Tobermorite	$Ca_5Si_6O_{16}(OH)_2 \cdot 4(H_2O)$	$C_5S_6H_5$	0.45
	Gyrolite	$Ca_{16}Si_{24}O_{60}(OH)_8 \cdot 14H_2O$	$C_{16}S_{24}H_{18}$	0.40
	Cristobalite(alpha)	SiO_2	S	0.00
Other Cement Phases	Ettringite	$Ca6Al_2(SO_4)3(OH)_{12} \cdot 26(H_2O)$	$C_6AS_3H_{32}$	–
	Hydroxylellestadite	$Ca_5(SiO_4,SO_4)3(OH,Cl,F)$	$C_5S_3OH_{0.5}$	0.77
	Katoite	$Ca_3Al_2(SiO_4)1.5(OH)_6$	$C_3A_2S_{1.5}OH_3$	0.50
	Scawtite	$Ca_7Si_6(CO_3)O_{18} \cdot 2(H_2O)$	$C_7S_6H_2$	0.54
	Xonotlite	$Ca_6Si_6O_{17}(OH)_2$	C_6S_6H	0.50

Source: Gaines et al. 1997 (chemical and cement formulas); DTN: LB0408CMATUZFT.002 (C/(S+C) values).

NOTE: [a]Tptpmn and Tptpul (Peterman and Cloke 2002).

The most important issue regarding repository performance concerns the longer-term reaction of the secondary hydrated calcium silicates with the fine aggregate of the shotcrete formulation (see Table D-4). The fine aggregate will be finely pulverized devitrified tuff, a silica-rich volcanic rock (Peterman and Cloke 2002) consisting mainly of cristobalite and alkali feldspars. This silica-rich material will react progressively with the cement component to form more rich silica phases, whose aqueous solubility with respect to Ca^{2+} is drastically lower than cementitious mineral assemblages containing portlandite (see Section D.4.4.4.4).

The silication process can be schematically represented as a series of steps representing two-phase assemblages in a water-saturated binary component system, CaO-SiO$_2$ (+H$_2$O), as represented in Figure D-3. Over the temperature range of the postclosure repository environment with temperatures ranging up to 160°C, the sequence of phase assemblages with progressively increasing silica content would be portlandite-hillebrandite, hillebrandite-tobermorite-14A, tobermorite-14A-gyrolite, and gyrolite-cristobalite(alpha). The chemical formulas and C/(C+S) mole ratios of these phases and that of the CS components of the shotcrete are summarized in Table D-4.

Calculations show that if the Type II cement component of the current shotcrete formulation were to react completely with all silica fume and all of the fine aggregate, there would be insufficient free silica available to generate the most silica-rich gyrolite-cristobalite(alpha) assemblage. Therefore, the most silica-rich phase assemblage that could possibly form with the current shotcrete formulation would be tobermorite-14A-gyrolite, generated according to the following equation:

$$Ca_5Si_6O_{16}(OH)_2 \cdot 4H_2O \quad + \quad 1.5SiO_2 \quad + \quad \frac{5}{8}H_2O$$

$$\text{Tobermorite} \qquad\qquad \text{Cristobalite} \qquad \text{Water}$$

$$= \frac{5}{16}Ca_{16}Si_{24}O_{60}(OH)_8 \cdot 14H_2O$$

$$\text{Gyrolite}$$

(Eq. D-3)
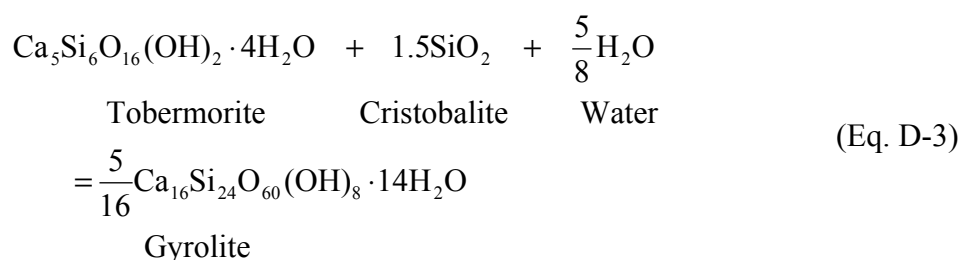
The anticipated kinetics of reactions leading to the formation of this mineral assemblage from the original shotcrete constituents is of critical importance, because this will allow an estimate of the time required for substantially complete shotcrete alteration under repository conditions.

The hydrothermal recrystallization of cement is a complex process that involves many chemical, mineralogical, and microstructural factors, including matrix mineralogy, particle size, porosity; aggregate type, grading, and proportioning (Roy and Langton 1989, p. 1). The recrystallization occurs with concomitant degradation of the physical properties of the cementitious material. Information is available in the literature regarding the formation of gyrolite from tobermorite in some laboratory experiments performed under hydrothermal conditions at elevated temperatures (Kalousek and Nelson 1978; Stevula and Petrovic 1983). At the room temperature, the transformation of tobermorite is very slow and has not been observed in laboratory experiments. For the low temperature scenario, the weathering rate of ancient Roman concrete dating to approximately 2,300 years ago was used as a basis for estimating reaction rates (Roy and Langton 1989).

Certain assumptions were made regarding the mineral mass fraction to derive the kinetic rates of gyrolite formation. This is necessary in the calculation of the kinetic rates, because available data concerning the mass fractions of mineral phases in the literature are qualitative. Specifically, the reactants tobermorite and cristobalite are assigned a unit mass fraction, which remains constant through the investigated time period. The gyrolite product is assumed to be present with a 0.05 mass fraction. This value was arbitrarily chosen to represent low concentrations generally observed in experiments. In addition, ancient Roman concrete is

considered to have been subject to alteration for 2,300 years at an ambient temperature assumed to be 25°C for this appendix. The temperatures of laboratory runs range from 175°C to 300°C. Experiments differed in duration, ranging from 8 hours to 60 days. All were conducted in a steam atmosphere, and, therefore, reactions were catalyzed by the presence of water vapor at elevated pressures. The calculated kinetic rate (1/yr) as a function of temperature is shown in Figure D-4.
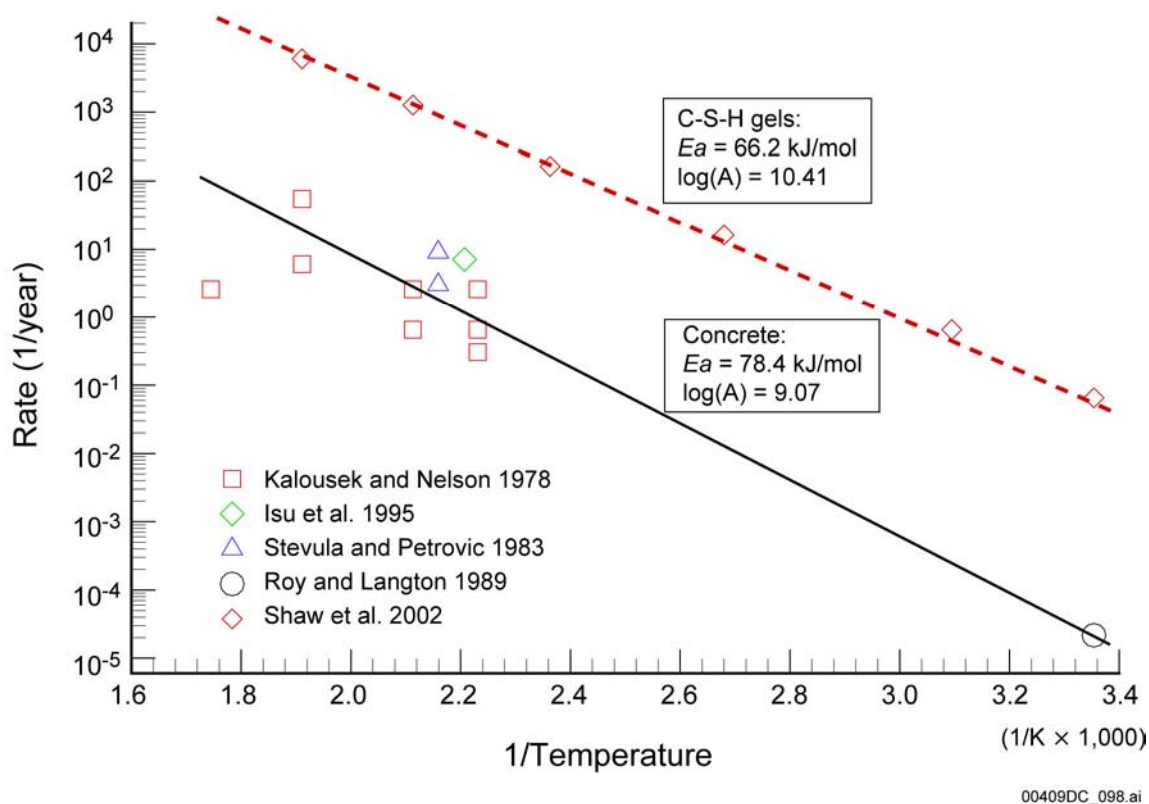
Source: DTN: LB0408CMATUZFT.001.

Figure D-4. Interaction of Cement with Siliceous Aggregate to Form Tobermorite-14A-Gyrolite Assemblages, Based on Laboratory Experiments and Ancient Concrete Weathering

The estimated kinetic rates have large uncertainties because of the use of phase changes to measure reaction rates, and mass quantifications are, therefore, approximations. However, a comparison can be made with the rate of conversion of C-S-H gel of gyrolite composition to gyrolite in a steam atmosphere, as studied by Shaw et al. (2002). The rate of transformation determined by these investigators is also plotted in Figure D-4 for comparison. Their determination is in satisfactory agreement with the estimated rate of formation of gyrolite from tobermorite-14a in the presence of cristobalite. The rate, approximately 2 orders of magnitude higher, and lower activation energy of the gel-gyrolite transformation is consistent with theoretical expectations and provides a measure of confidence in the validity of the rate of formation of gyrolite from tobermorite and cristobalite.

The effect of temperature on reaction rates is quantified using the Arrhenius equation.

$$k = A \cdot \exp(-\frac{Ea}{R\,T}) \qquad\qquad \text{(Eq. D-4)}$$

where k is the rate coefficient (1/yr), A is a constant, Ea is the activation energy, R is the universal gas constant, and T is the temperature (in degrees Kelvin). R has the value of 8.314×10^{-3} kJ/mol·K.

The calculation yields an activation energy of 78.4 kJ/mol and a value for the constant *lnA* of 20.9. The kinetic rates at 100°C, 120°C, and 150°C are 0.0125, 0.0452, and 0.2476 per year, respectively.

This shows that it would take approximately 1,000 years (Ca (1/rate)×10) to produce a tobermorite-14A-gyrolite assemblage through reaction of the cement with the fine aggregate in the shotcrete at 100°C but only about 50 years at 150°C. However, at 150°C, most if not all of the residual capillary pore water would have evaporated, and reaction rates would be retarded. Because capillary water can remain under repository conditions up to about 120°C in the pores of devitrified tuff host rocks, it would be expected that a minimum time for alteration would be somewhat in excess of 200 years. The implication of this estimate is that most of the cementitious component of the shotcrete would be substantially altered to a tobermorite-14A-gyrolite assemblage prior to rehydration. This has significant consequences for carbonation rates, which would be retarded by the presence of more stable silica-rich mineral phases and have lower solubilities with respect to dissolved calcium (Section D.4.4.4.4). Alkaline plume formation subsequent to rehydration would, therefore, be negligible (Section D.4.4.5).

D.4.4.3 Carbonation

The carbonation of cementitious materials in the repository is strongly dependent on the accessibility of gaseous CO_2, and this depends, in part, on the transport of atmospheric CO_2. Prior to repository closure, it can be demonstrated that convective ventilation would be more than sufficient to permit some carbonation of the contained cementitious materials and that carbonation reaction rates would be controlled by gaseous diffusive transport within the open pores of the cementitious material. After closure and backfilling of all access drifts with crushed tuff, advective transport of atmospheric CO_2 would be restricted. Carbonation rates would for the most part be limited by internally driven gas phase thermal convection and diffusion of CO_2 in fractures released from pore waters in the tuffaceous host rocks surrounding the emplacement drifts during the dryout period. Because of the importance of carbonation in affecting the leaching behavior of cementitious materials and because the conditions before and after repository closure would differ significantly, carbonation processes before and after closure are reviewed separately.

Preclosure Conditions–Papadakis (2000) developed a model to calculate carbonation distances in cementitious materials at 25°C. This model has been used in the design of DOE-sponsored laboratory experiments to measure the extent of carbonation of cementitious materials (DTN: LL020711323125.001). The model is used in this appendix to estimate the extent of carbonation of shotcrete support applied to drifts in the repository during the monitoring and performance confirmation period 50 years prior to closure. This period would be the minimum time to which all shotcrete materials would be exposed to carbonation prior to closure.

The model is a relatively simple one in which it is assumed that the rate of carbonation is gas diffusion–controlled, with the effective diffusivity of CO_2 in the cementitious material controlled by the porosity of the carbonated zone through which the gas must migrate. The effective diffusivity is also described as an empirical function of the relative humidity, which affects the water content of the cementitious material. At high water contents, for example, there is relatively little of the pore space available through which the gas can diffuse. While CO_2 can diffuse in the aqueous phase, the diffusion coefficient is about 4 orders of magnitude slower than it is in the gas phase. The effective diffusivity also depends on the water–cement ratio of the cementitious material, because the water–cement ratio has a strong effect on the amount of capillary porosity developed in the cured cementitious material. The water referred to here is that used in preparation of the cementitious material and is not the water content of the pores of the resulting product.

The Papadakis equation is defined according to the following parameters:

- C (kilograms of cement per cubic meter)
- SF (kilograms of silica fume per cubic meter)
- W (kilograms of water per cubic meter)
- ρ_c, cement density (kilograms per cubic meter)
- ρ_{sf}, silica fume density (kilograms per cubic meter)
- ρ_w, water density (kilograms per cubic meter).

Papadakis (2000) shows that in the case of complete hydration and pozzolanic action (reaction with the silica fume), the amounts of CH, $C_3S_2H_3$ (C-S-H) (in kilograms per cubic meter of cement) and the total porosity of carbonated concrete is given as follows:

$$CH = 0.29\ C - 1.62\ SF \qquad \text{(Eq. D-5)}$$

$$\text{C-S-H} = 0.57\ C + 2.49\ SF \qquad \text{(Eq. D-6)}$$

$$\varepsilon_c = (W - 0.267\ C - 0.0278\ SF)/1000 \qquad \text{(Eq. D-7)}$$

For one-dimensional geometry, the evolution of the carbonation depth, x_c (meters), with time, t (seconds), is given by the analytical expression:

$$x_c = \sqrt{\frac{2D_{e,\mathrm{CO_2}}(\mathrm{CO_2}/100)t}{0.33CH + 0.214CSH}} \qquad \text{(Eq. D-8)}$$

where CO_2 is the CO_2 content (percent) in the ambient air at the concrete surface and $D_{e,\mathrm{CO_2}}$ is the effective diffusivity of CO_2 in carbonated cement (square meters per second). The effective diffusivity also depends on the ambient relative humidity according to the following empirical equation:

$$D_{e,CO_2} = A\left[\frac{\varepsilon_c}{C/\rho_c + SF/\rho_{SF} + W/\rho_W}\right]^a (1-RH/100)^b \qquad \text{(Eq. D-9)}$$

The optimal parameter values presented by Papadakis (2000) are 6.1×10^{-6} and 3 for A and a, respectively, and 2.2 for b. The parameter values for A, a, and b given above are strictly valid for $0.38 < W/(C + 2SF) < 0.58$.

Calculations based on the Papadakis (2000) carbonation model, updated to include the effects of silica fume, can be used to estimate the extent of carbonation of cementitious materials in the repository. The material likely to be most extensively carbonated is the shotcrete applied to provide ground support in the main access and ventilation drifts. This material currently has a design thickness of 10 cm (BSC 2004f), and it is assumed that the exposed face would be most prone to carbonation. It is also assumed that the availability of atmospheric CO_2 is unlimited (i.e., pCO_2 is not rate controlling). In Table D-5, the calculated depth of carbonation is given as a function of relative humidity, pCO_2, and temperature, which is accounted for by using an activation energy for gaseous diffusion of 27 kJ/mol in the Arrhenius equation. All calculations are carried out at pCO_2 of 3×10^{-4} bar, the accepted value for atmospheric CO_2 at 25°C. Minor pressure corrections for elevation have been omitted. The densities of cement (C) and silica fume (SF) used in the calculations are those cited by Papadakis (2000).

Table D-5. Shotcrete Carbonation Depth after 50 Years Using the Papadakis (2000) Carbonation Model

Temperature (°C)	W/(C+SF)	Relative Humidity (%)	Carbonation Depth (cm) SF(C+SF) = 6.4%	SF(C+SF) = 15%	SF(C+SF) = 25%
25	0.40	5	2.12	2.64	3.36
25	0.40	10	1.99	2.49	3.16
25	0.40	20	1.75	2.19	2.78
25	0.40	40	1.28	1.60	2.03
25	0.40	60	0.82	1.02	1.30
25	0.40	80	0.38	0.48	0.61
25	0.40	98	0.03	0.04	0.05
40	0.40	60	1.06	1.33	1.68
50	0.40	60	1.24	1.56	1.98
60	0.40	60	1.45	1.81	2.30
70	0.40	60	1.67	2.09	2.65
80	0.40	60	1.91	2.39	3.03
90	0.40	60	2.17	2.71	3.44

Source: DTN: LB0408CMATUZFT.002.

It should be noted that the Papadakis model assumes transport control on the rate of carbonation. Therefore, it does not adequately capture the potential switch in the rate-controlling mechanism, which occurs at low relative humidity. Because the rate of gas diffusion increases with increasing gas saturation (because decreasing relative humidity results in lower liquid

saturation), the Papadakis model will always predict the highest carbonation rates at the lowest relative humidity. However, carbonation rates should decrease at very low relative humidity, but the model does not capture this. Although at relative humidities approaching 100% the model predicts that the carbonation rate falls to zero, carbonation continues at a much slower rate, dictated by the diffusion of CO_2 through the liquid aqueous phase. The values given here, therefore, should be considered as maximum values for the very low relative humidity values.

The calculated depths of shotcrete carbonation are predicted to vary by over 2 orders of magnitude depending primarily on relative humidity. The possibility exists that the higher rates of carbonation could not be sustained because advective mass transport of CO_2 through the repository access drifts might be rate controlling. A simple mass-balance calculation demonstrates that this is not the case. In the following calculation, it is assumed that the shotcrete represents a substantial fraction of the reactive cementitious material in the repository and that only the exposed face of the shotcrete becomes carbonated at the maximum rate given in Table D-6 (i.e., 3.4 cm depth after 50 years). An approximation is also made that the carbonation rate is linear with time and that the volume fraction of the shotcrete due to portlandite is converted to calcite ($CaCO_3$). Elevation corrections for atmospheric pCO_2 are ignored. The approach assumes that all CO_2 is provided by the atmosphere through advective flow of air exclusively through the main access drift and that the air mass velocity in this drift determines whether such a velocity would be realistic in relation to natural convection. Values used in the calculation are given in Table D-6.

Table D-6. Parameters Used to Calculate Main Access Drift Velocity Required to Satisfy Shotcrete Carbonation Rates

Parameter	Units	Value	Reference
Carbonation depth	cm	3.4	This appendix.
Carbonation time	years	50	Assumed.
Fraction of shotcrete due to portlandite	–	0.056	This appendix.
Density of calcite	g/cm^3	2.710	Calculation from Table D-2.
Molecular weight of calcite	g/mol	100.09	Lide 2000, p. 4-50.
Density of portlandite	g/cm^3	2.26	Calculation from Table D-2.
Density of shotcrete	g/cm^3	2.425	Calculation from Table D-2.
Area of shotcrete associated with each emplacement drift	m^2	885	BSC 2004h.
Number of emplacement drifts	–	106	BSC 2004h.
CO_2 concentration in carbonated shotcrete	mol/m^3	1,821	This appendix.
Access drift diameter	m	7.62	BSC 2004h.

Source: DTN: LB0408CMATUZFT.002.

A calculation using the parameters given in Table D-6 shows that the air velocity in the main access drift required to satisfy maximum shotcrete carbonation rates is 5.17×10^{-3} m/s. This velocity is about 200 times slower than current forced ventilation rates in the Exploratory Studies Facility main drift. Therefore, forced ventilation rates prior to repository closure would be unlikely to control the rate of shotcrete carbonation.

Postclosure Conditions–Permanent closure of the repository is expected after approximately 100 years of atmospheric ventilation (BSC 2004m). Current plans are to backfill all access and ventilation drifts with pneumatically emplaced crushed tuff. Under these conditions, access of atmospheric CO_2 could be restricted. A simple application of Fick's first law of diffusion (see below) shows that the diffusive flux of atmospheric CO_2 to the repository through the fractures of the undisturbed host rock would be so small that such a mechanism would not account for any further carbonation of cementitious materials. It is also not clear whether sufficient CO_2 would be available within the repository host rocks to permit continued unrestricted carbonation of cementitious materials.

Given the quantity of cementitious materials remaining in the repository after closure, the quantity of CO_2 required for complete carbonation of the portlandite generated initially with shotcrete can be compared with what could be made available from the host rocks surrounding the repository. Table D-7 lists the parameters used in this calculation. The calculation ignores the presence of grout, which contributes only a minor quantity of Portland cement to the planned total inventory. It should also be emphasized that the calculation is simplistic in that it ignores CO_2 contributions due to calcite dissolution, aqueous phase equilibrium with respect to ambient pCO_2 in the coexisting gas phase, and kinetic and mass transfer constraints involved in degassing of matrix pore waters.

Table D-7. Parameters Used to Calculate the Availability of CO_2 within Yucca Mountain Pore Waters to Carbonate All Cementitious Materials within the Repository

Parameter	Units	Value	Reference
Type II cement in shotcrete	wt %	17.95	BSC 2004h.
Ca(OH)$_2$ generated in Type II cement	wt %	31	Calculated, this appendix.
Molecular weight Ca(OH)$_2$	g/mol	74.09	Lide 2000, p. 4-50.
Concentration of portlandite in shotcrete	mol/m^3	1,821	Calculated, this appendix.
Density of shotcrete	kg/m^3	2,425	Calculated from Table D-2.
Mass of shotcrete	tons	159,413	From Table D-1.
CO_2 required to react with Ca(OH)$_2$	mol	4.461×10^7	Calculated, this appendix.
Matrix porosity	–	0.164	Liu et al. 2003.
Saturation	–	0.61	Liu et al. 2003.
Water content in rock	kg/m^3	100	Calculated from Liu et al. 2003.
HCO$_3^-$ concentration in pore water	mg/L	110	DTN: GS951108312271.006.
Rock volume above repository horizon	km^3	2.23	BSC 2004h.
CO_2 in pore water	mol/m^3 rock	0.1792	Calculated, this appendix.
Total CO_2 in pore water	mol	4.001×10^8	Calculated, this appendix.

Source: DTN: LB0408CMATUZFT.002.

The results of this calculation, summarized in Table D-7, show that there would be an order of magnitude excess of CO_2 available to carbonate all of the cementitious materials. However, removal of all CO_2 from the pore waters to satisfy the requirements of carbonation would be impossible, as noted above, because thermodynamic back reactions would prevent complete stripping. The availability of CO_2 would be primarily dependent on CO_2 released by evaporation of pore water adjacent to the emplacement drifts. The extent to which CO_2 would be retained by

the pore waters and condensate elsewhere in the repository would depend on the depression of pCO_2 in the gaseous phase due to carbonation.

The maximum potential diffusive fluxes possible within the repository and whether they could limit the carbonation of cementitious materials can be gained through evaluation of the case of diffusion through a semi-infinite medium to a sink for the diffusing material. Crank (1975) gives an analytical solution for this case, where the initial concentration, C_0, of the diffusing substance is uniform throughout, and the interface is maintained at a concentration, C_1. The solution is:

$$C - C_1 / C_0 - C_1 = \text{erf}(x/2\sqrt{(Dt)}) \qquad\qquad \text{(Eq. D-10)}$$

For the special case where the surface concentration is zero, the total amount of diffusing substance, which has left the medium, is given by:

$$M_t = 2C_0 \sqrt{(Dt/\pi)} \qquad\qquad \text{(Eq. D-11)}$$

Equation D-10 permits calculation of the linear distribution of CO_2 in the fractures of the rock as a function of time, and Equation D-11 permits calculation of the depth to which concrete has been carbonated at various times following repository closure, assuming that carbonation is not rate controlling.

The capacity of the pore water to contain CO_2 exceeds that of the air in the fractures and unsaturated rock pores by a factor of 65, assuming the average bicarbonate concentration in pore waters is approximately 110 mg/L (Yang et al. 1996; DTN: GS951108312271.006) and the volume of aqueous phase per unit volume of rock exceeds the volume of air in the fractures by a factor of approximately 3.5. Thus, the preponderance of CO_2 is present initially in the pore water and not in the gas phase. It is assumed that 50% of all bicarbonate in the pore water is made available in the gas phase as CO_2 and that all pore and fracture space is occupied by the CO_2, the pore water having evaporated during the thermal period. The resulting concentration of CO_2 in the gaseous phase is 0.515 mol/m^3 (log(pCO_2) value of -2.0, or pCO_2 value of approximately 9,350 ppmV). This value is somewhat higher than the average concentration of CO_2 in the gaseous phase under dryout conditions. Therefore, the diffusion rates, calculated below, represent an upper limit. Table D-3 summarizes the parameters used in the calculation.

Figure D-5 shows the linear distance of host rock affected by the uptake of CO_2 by shotcrete, assuming one-dimensional geometry. In cylindrical or spherical coordinates, the distances are compressed in comparison, but, because of the complex nature of the geometry of the repository, representations in higher dimensions are not justified in this simple analysis.
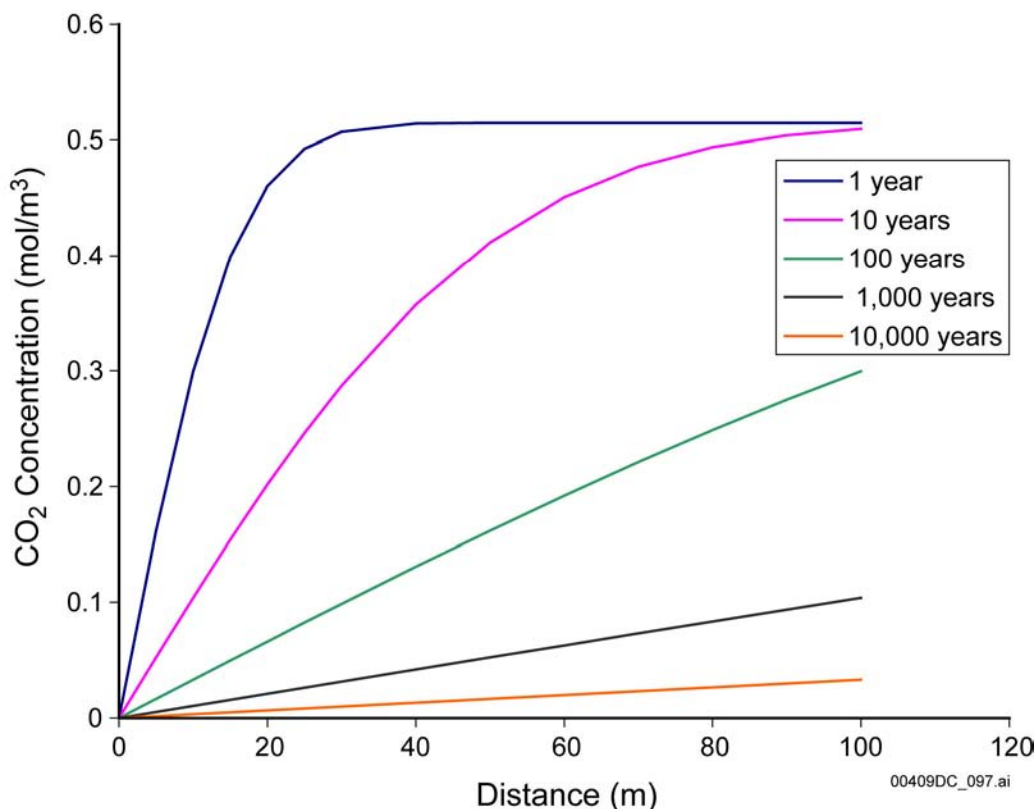
Source: DTN: LB0408CMATUZFT.002.

Figure D-5. Effective Distribution of CO_2 as a Function of Time and Distance from Carbonating Cementitious Material

Table D-8 shows that if the carbonation rate of cementitious materials were fast in relation to the diffusion of CO_2 through the rock fractures, all shotcrete would be completely carbonated before 1,000 years had elapsed, assuming that carbonation proceeds from both sides of the shotcrete that is 10 cm thick.

Table D-8. Depth to which Cementitious Material Would Be Carbonated, Assuming the Diffusive CO_2 Flux Would Be Rate Controlling

Time (years)	Carbonation Depth (cm)
1	0.267
10	0.843
100	2.67
200	3.31
1,000	8.43
10,000	26.7

Source: DTN: LB0408CMATUZFT.002.

The results summarized above are limited by the assumptions inherent in the calculations. Thus, it is assumed that the reaction rate is limited by the flux of CO_2, that the CO_2 diffusion coefficient at elevated temperatures is the same as that at 25°C, and that CO_2 equilibrium

between the aqueous (pore water) and gaseous (fracture) phase is always maintained. It should also be emphasized that the above analysis takes into account mass transport by gaseous phase diffusion alone. Advective transport through convection could also be operative. However, thermal-hydrologic-chemical modeling (BSC 2004h) suggests that CO_2 advective transport in the gaseous phase would be retarded by interaction with the aqueous phase, where pore waters or condensate exist beyond the region of dryout and would, therefore, be coupled with pore water percolation.

The above evaluation showing that the carbonation of shotcrete would be essentially complete within 1,000 years after repository closure presumes that the carbonation rate is not rate limiting. The extrapolation of the Papadakis model (Papadakis 2000) to temperatures in the vicinity of the boiling point of water allows a preliminary estimate to be made regarding the possibility that the carbonation rate could be sufficiently slow that the shotcrete would not be completely carbonated prior to rehydration. The calculations presented in Table D-9 show that the shotcrete formulated with Type II cement with 6.4 wt % silica fume would be completely carbonated in just over 100 years at a relative humidity of 80%. Extrapolation of the model to higher temperatures indicates even more rapid rates of carbonation. However, for reasons stated elsewhere in this section, the Papadakis model does not account for either boiling or dryout. The boiling of the aqueous phase in the pores of the cement would enhance gaseous phase diffusion of CO_2 into the cement, thus greatly accelerating carbonation in the presence of residual capillary water. Current estimates indicate that residual capillary water would persist to a temperature of about 120°C. The presence of dissolved (calcium or magnesium) chlorides in the shotcrete could stabilize the aqueous phase at still higher temperatures and enhance carbonation rates even further. In contrast, declining relative humidity with increasing temperature could inhibit carbonation because of the elimination of residual capillary or absorbed water that would otherwise act as a catalyst.

Table D-9. Shotcrete Carbonation Depth following Closure using the Papadakis (2000) Carbonation Model

Time (years)	Relative Humidity (%)	Carbonation Depth (cm)			
		90°C	100°C	120°C	140°C
50	40	10.70	(12.06)	(15.05)	Out of modeling bounds
	60	6.85	7.72	(11.76)	(11.76)
	80	3.19	3.60	5.49	5.49
	98	0.25	(0.29)	(0.36)	(0.44)
100	40	15.10	Out of modeling bounds	Out of modeling bounds	Out of modeling bounds
	60	9.68	10.92	(13.62)	(16.64)
	80	4.52	5.09	6.35	7.76
	98	0.36	(0.40)	(0.50)	(0.62)

Source: DTN: LB0408CMATUZFT.002.

NOTE: Numbers in parentheses are estimates for conditions outside the bounds of the Papadakis (2000) model. See text for discussion. pCO$_2$ = 0.30% or 3,000 ppmV.

Carbonation of all shotcrete is also constrained for the following reasons: (1) as the temperature rises in the repository, the C-H-S gel phase rapidly crystallizes (Shaw et al. 2002), which would

retard carbonation by back reactions favoring decarbonation; (2) the initial armoring of the shotcrete by precipitation of calcite in pores could inhibit further diffusive penetration of CO_2, and (3) some of the shotcrete would be located in regions where the mean temperature excursion would be limited, and, therefore, the kinetics of carbonation would be diminished.

Hardin (1998, p. 6-38) also noted that the rate of carbonation is dependent on a number of factors, including the advective aqueous flux of CO_2 dissolved in the pore water, release of CO_2 due to pore-water boiling, aqueous phase refluxing, temperature, relative humidity, the rate of diffusion of CO_2 into the cementitious material, and the nature and composition of the cementitious material. Extrapolated carbonation rates predicted by the Papadakis (2000) model above boiling temperatures, reported in this section, would indicate, however, that a 10-cm-thick shotcrete lining the main access and exhaust drifts would be completely carbonated within 1,000 years, provided that the reaction scheme defined by the Papadakis (2000) model would be applicable between boiling and temperatures as high as 170°C, at 85% relative humidity, and that the availability of CO_2 is not mass-transport limited.

Rehydration is predicted to occur in the waste packages around the peripheries of the waste package emplacement panels. It is assumed, for the purpose of discussion, that the contiguous main access and exhaust ventilation drifts are subject to the same corresponding dryout periods between 200 and 1,200 years after closure (Section D.4.3). Table D-10 shows the carbonation depth expected during the period following rehydration, during which it is assumed that the relative humidity is close to saturation (i.e., about 95%). The relative humidity is arbitrarily set, as the Papadakis equation ignores CO_2 diffusion through the aqueous phase filling pores, and therefore, 100% relative humidity would yield zero carbonation rates. At the minimum time of 200 years, the shotcrete would have been carbonated to a depth of about 1.5 cm on the exposed face prior to repository closure (see Table D-5), and about 3 cm from either side following closure (Table D-9). These sequential carbonation depths are not additive, but it can be assumed as a first approximation that about 50% of the shotcrete thickness will have been carbonated at the time that rehydration occurs. Thus, between about 500 and 5,000 years more time would be required for complete carbonation under conditions following rehydration. The presumption would be that further carbonation occurs in situ without the generation of an alkaline plume. Current knowledge does not permit such an interpretation without further study. Thus, it must be assumed as a conservative assumption that rehydration will lead to the formation of an alkaline plume. This scenario is evaluated in Section D.4.4.4.2.

Table D-10. Shotcrete Carbonation Depth following Rehydration at 95% Relative Humidity using the Papadakis (2000) Carbonation Model

Temperature (°C)	Carbonation Depth (cm)					
	After 200 years	After 500 years	After 1,000 years	After 3,000 years	After 7,000 years	After 10,000 years
90	1.39	2.20	3.11	5.39	8.23	9.83
80	1.23	1.94	2.74	4.74	7.25	8.66
70	1.07	1.69	2.40	4.15	6.34	7.58
60	0.93	1.47	2.08	2.64	5.50	6.57
50	0.80	1.26	1.79	3.10	4.73	5.65
40	0.68	1.08	1.52	2.64	4.03	4.82
30	0.57	0.91	1.28	2.22	3.40	4.06

Source: DTN: LB0408CMATUZFT.002.

NOTE: pCO_2 = 0.30% or 3,000 ppmV.

In the event that CO_2 were to become depleted, it can be shown that CO_2 transported from the atmosphere would occur primarily through pore-water advective transport. A simple application of Fick's first law of diffusion shows that the diffusive flux of atmospheric CO_2 into the repository through the fractures of the undisturbed host rock would be so small that such a mechanism would not account for any further carbonation of cementitious materials.

Fick's first law states:

$$F = D\, \partial C/\partial x \qquad \text{(Eq. D-12)}$$

where F is the flux in moles per square meters per second, C is the concentration in moles per cubic meter, x is the diffusive distance in meters, and D is the coefficient of diffusion in square meters per second. Assuming that cementitious material carbonation is fast in relation to CO_2 diffusion, that the steady-state concentration of CO_2 at the surface of the cementitious material is zero (i.e., CO_2 diffusion is rate controlling), and that the path length from the land surface to the repository interior is x, a finite difference approximation of Fick's first law can be taken to calculate the diffusive flux into the interior of the repository from the land surface:

$$F = \tau\phi D\Delta C/\Delta x \qquad \text{(Eq. D-13)}$$

where τ is the fracture tortuosity coefficient and ϕ is the fracture porosity. The values and sources of the parameters used in the calculation are given in Table D-11.

Table D-11. Parameters Used to Calculate the Diffusive CO_2 Flux from the Land Surface into the Repository

Parameter	Units	Value	Reference
Distance from the land surface to the interior of the repository, x□	m	200	Assumed.
CO_2 concentration in air	mol/m^3	0.01562	Calculated, this appendix.
Diffusion coefficient of CO_2 in air at 25°C	m^2/s	1.39×10^{-5}	Lackner et al. 1999.
Fracture tortuosity coefficient, τ	–	0.5	Liu et al. 2003.
Fracture porosity, ϕ	–	0.01	Assumed.
Diffusive CO_2 flux, F□	$mol/m^2 \cdot s$	5.4×10^{-12}	Calculated, this appendix.

Source: DTN: LB0408CMATUZFT.002.

The presumption in the above calculation is that diffusion of CO_2 occurs through the fractures of a dry impermeable rock. In fact, the vitroclastic rocks comprising the Yucca Mountain edifice are partially saturated (e.g., 61% in Table D-3) and have variable matrix porosities (e.g., 0.16 in Table D-3) (Liu et al. 2003). Thus, equilibration of CO_2 with the pore waters will take place locally at all points along the postulated 200-m diffusion path. The pore-water infiltration rate at Yucca Mountain is estimated to range between 1 and 5 mm/yr (Sonnenthal and Bodvarsson 1999). Thus, it can be shown that the aqueous phase advective flux of CO_2 to the repository horizon is between 1.8 and 9.0 $mol/m^2 \cdot yr$, or up to 50 times faster than by gaseous diffusion through the rock fractures.

To summarize, the bounding calculations presented in this section indicate that shotcrete support liners would be extensively if not completely carbonated prior to rehydration. During the period when dryout occurs, carbonation reaction rates are so high that the rate of carbonation would be limited only by the rate of diffusion of ambient gaseous CO_2 to the shotcrete support structures. Parts of the peripheries of the waste emplacement panels could rehydrate as soon as 200 years after dryout, and contiguous access and exhaust drifts could rehydrate at about the same time. Shotcrete in the drifts, which would have been exposed to periods as short as 200 years of dryout, would be incompletely carbonated prior to rehydration. Allowing credits for partial carbonation of the shotcrete prior to repository closure and prior to rehydration, it is estimated that up to 5,000 more years would be required for complete carbonation of the cooler parts of the repository. This duration is roughly of the same order of time observed for the carbonation of Roman pozzolanic concrete (Roy and Langton 1989), and suggests an upper bound for the time required for carbonation.

D.4.4.4 Leaching of Altered Cementitious Material

Leaching of cementitious materials will occur under three conditions:

- Random wetting as a result of episodic inflows of water via fast paths

- Transient condensation of evaporated pore water from the heated rock surrounding the emplacement

- Rehydration of the repository after thermal dissipation following heating due to radioactive decay.

D.4.4.4.1   Episodic Events Inducing Flow in Fractures

During episodic events when precipitation is very high, as occurs during intense localized summer thunderstorms or during winter storms and (or) subsequent snowmelt, transient surface flooding can occur with associated rapid downward advance of a fracture-saturated wetting front (BSC 2003c, Section 6.3.4). Localized flow could be enhanced by preferential infiltration due to topographic variability and the focusing of flow through transmissive faults intersecting the surface or shallow subsurface (Pruess 1998). Rapid gravitational migration of the inflowing water could also be facilitated by sheet flow (Tokunaga and Wan 1997). Such flows can migrate very rapidly under gravity. Pruess (1998) estimates that the average seepage velocities are on the order of 1 m/s.

Should episodic flow events occur in the future, it is expected that dryout surrounding the emplacement drifts will inhibit, or at least mitigate, their impact during the postclosure repository dryout period. In contrast to steady-state percolation through the pores of the rock matrix, where lateral plume spreading would be dominated by molecular diffusion (see Section D.4.4.4.2), preferential episodic flows would be limited to lateral spreading by hydrodynamic and capillary dispersion. The former process is minor, but the latter could be substantial, particularly in desiccated or highly unsaturated rocks (Pruess 1996). However, Pruess (1998) has shown through heterogeneous fracture flow simulations under the partially saturated conditions characteristic of the welded fractured tuffs at Yucca Mountain that gravitational effects tend to dominate capillary effects. Pruess (1998) also noted that fast flow could be generated by internal focusing mechanisms due to heterogeneities in the host rock, leading to enhanced flow velocities and flow funneling. The consequence of these mechanisms is that the resulting flow would be nearly vertical with almost no lateral dispersion. The simulated behavior has been observed in the field, although it is not necessarily universal. Focused episodic flows occurring at spatially distinct localities would, therefore, be unlikely to intersect. Furthermore, the rapid flow velocities and limited duration of such fracture flows would limit their ability both to leach significant alkaline components from cementitious materials or precipitate calcite and locally degrade the permeability of the fractures. Calcite precipitation would be limited and would spread out over the full thickness of the unsaturated zone, given the modeled rapid flow velocities in relation to calcite precipitation kinetics under subsurface conditions.

D.4.4.4.2   Steady-State Percolation of Pore Water through the Rock Matrix

Given the spatial separation of a failed waste container and shotcrete support structures in the main drift turnout intersections and in the exhaust drift intersections, the question arises as to the probability that leachate plumes from both might intersect and mix at depth. The likelihood that this would occur depends on the extent of lateral spreading of the plume due to transverse dispersion with increasing depth in the unsaturated zone. There are three mechanisms that could lead to plume lateral dispersion: hydrodynamic dispersion due to heterogeneities in the host rocks, molecular diffusion through the rock matrix, and capillary dispersion. The last process could occur to a significant degree only in the event of leaching of either cementitious material or the waste package by a focused plume percolating into the dryout zone surrounding the repository prior to rehydration, such as might occur during episodic events described in Section D.4.4.4. Rehydration of the repository horizon and underlying formations would be

accompanied by equilibration of capillary pressure, and, therefore, capillary dispersion would no longer be operative.

Transverse plume spreading due to intrinsic heterogeneities in the vitroclastic tuffs could be a significant factor in inducing lateral dispersion in a migrating plume. This process is essentially Fickian in nature and can be treated in the manner described by Pruess (1996). The effective transverse dispersivity, α_T, is

$$\alpha_T = \frac{1}{2}\frac{d}{dz}(\sigma_T^2) \qquad \text{(Eq. D-14)}$$

where σ_T^2 is the variance of the transverse distribution of solute concentration in the plume, and z is the vertical distance of migration. Consider a hydrologically unsaturated rock consisting of separate idealized cubic matrix blocks of length d, bounded by continuous fractures, such that each block is in contact with its neighbors. The contacts (asperities) represent only a fraction of the total surface area of the bounding fracture surfaces. It is assumed that the fracture surfaces represent impermeable capillary barriers, that the pore waters percolate under gravity, and that they only flow across blocks through the fracture asperities. Consider a point source contaminant originating in one block as the source of the contaminant plume and that this plume migrates vertically downward within the block. When the flow encounters the impermeable barrier at the bottom of the block, it is assumed to split into two separate equal flows at $x = +d_x/2$ and $x = -d_x/2$ in underlying contiguous blocks, where d_x is the horizontal dimension of the block. The increase in the variance due to this process, $\Delta\sigma_T^2$, is:

$$\Delta\sigma_T^2 = 1/2\{(+ d_x/2)^2 + (-d_x/2)^2\} = d_x^2/4 \qquad \text{(Eq. D-15)}$$

Given that the matrix blocks are assumed to be of uniform size, the impermeable barriers occur in the vertical direction with a separation, d_z, the vertical dimension of the block, then the transverse dispersivity can be expressed as:

$$\alpha_T = 1/2(\Omega/d_z)(d_x^2/4) \qquad \text{(Eq. D-16)}$$

where Ω is the probability of encountering a capillary barrier at the block intersection. If it is assumed that the asperities represent one-third of the block in contact, then $\Omega = 1 - 1/3 = 2/3$. Assuming that $d_z = d_x = 0.377$ m (Liu et al. 2003, Table 1), then $\alpha_T = 0.0314$ m.

The plume width, x, can be approximated by $(D_d t)^{1/2}$, where D_d is the dispersion coefficient and equals $\alpha_T v$, t is time, and v is the percolation velocity. Given that $z = vt$, x can be expressed as:

$$x = (\alpha_T z)^{1/2} \qquad \text{(Eq. D-17)}$$

The value of x, calculated at the 300-m depth of the water table below the repository horizon (BSC 2004k), is approximately 3.1 m.

Dispersivity arising from molecular diffusion, α_{md}, can be calculated from the effective molecular diffusion coefficient D_e and v:

$$\alpha_{md} = D_e/v \qquad\qquad\text{(Eq. D-18)}$$

Assuming an average molecular diffusion coefficient of 10^{-9} m^2/s (Sonnenthal and Bodvarsson 1999), a tortuosity factor of about 0.5 (Liu et al. 2003), and a porosity of 0.16 (Liu et al. 2003), D_e is 8×10^{-11} m^2/s. Assuming an infiltration rate of 5 mm/yr or 1.6×10^{-10} m/s gives a $\alpha_{md.}$ value approximately equal to 0.50 m. Dispersion due to molecular diffusion will, therefore, contribute overwhelmingly to plume lateral dispersion, and this effect will lead to a mean plume width of 24 m at the water table. The total estimated plume width at the water table 300 m below the repository horizon is the sum of the mean plume width due to molecular diffusion (24.5 m) and heterogeneity (3.1 m), or 27.6 m (see Figure D-5). These results are comparable with chloride lateral diffusion illustrated by Sonnenthal and Bodvarsson (1999).

An alkaline leachate plume could mix with a water-borne radionuclide plume from a failed waste package if the distance between the cementitious material and a failed waste package at the repository horizon is less than the plume width. The failure scenario of greatest concern is that which involves the failure of either of the outside waste packages in the emplacement drift. The end of the last waste package will be separated from the end of the turnout by a minimum horizontal distance of 1.5 m (BSC 2003d, Section 6.3). However, current plans involve the removal of all nonsupport concrete, including inverts, from the repository prior to closure (BSC 2003d; BSC 2004g). The 0.45 ton of grout associated with rock bolt supports will remain, but calculations elsewhere in this appendix (see Section D.4.4.3) indicate that this grout would be effectively carbonated prior to rehydration and would have negligible effect on repository performance. Therefore, the separation of the last emplaced waste package and the remaining committed cementitious support material (i.e., shotcrete) in the main access drift turnout intersection would be approximately 60 m (BSC 2004n) (Figure D-1). This separation would be sufficient to prevent the intersection of cementitious leachate plume with that of a plume transporting radionuclides from the last emplaced waste package if it were to fail.

The situation is somewhat different with respect to the first-emplaced waste package on the exhaust drift side, where a minimum standoff of 15 m would be maintained between the end of the first emplaced waste package and the centerline of the exhaust main (BSC 2003d, Section 6.3). Approximately 8.8 m of this distance would be shotcreted (BSC 2004i). Therefore, the separation between the start of an emplacement drift and the shotcreted intersection would be a little over 6 m. Thus, a potential exists for the intersection of cementitious leachate plume with a radionuclide-containing plume from the first-emplaced waste package. The nature and extent of predicted plume overlap from a hypothetical initiation of concurrent alkaline and radionuclide-bearing plumes is illustrated in Figure D-6. Note that the horizontal scale is exaggerated in relation to the vertical scale, creating a misleading impression that plume spreading is greater than is actually the case. The potential effects of this interaction are discussed below.
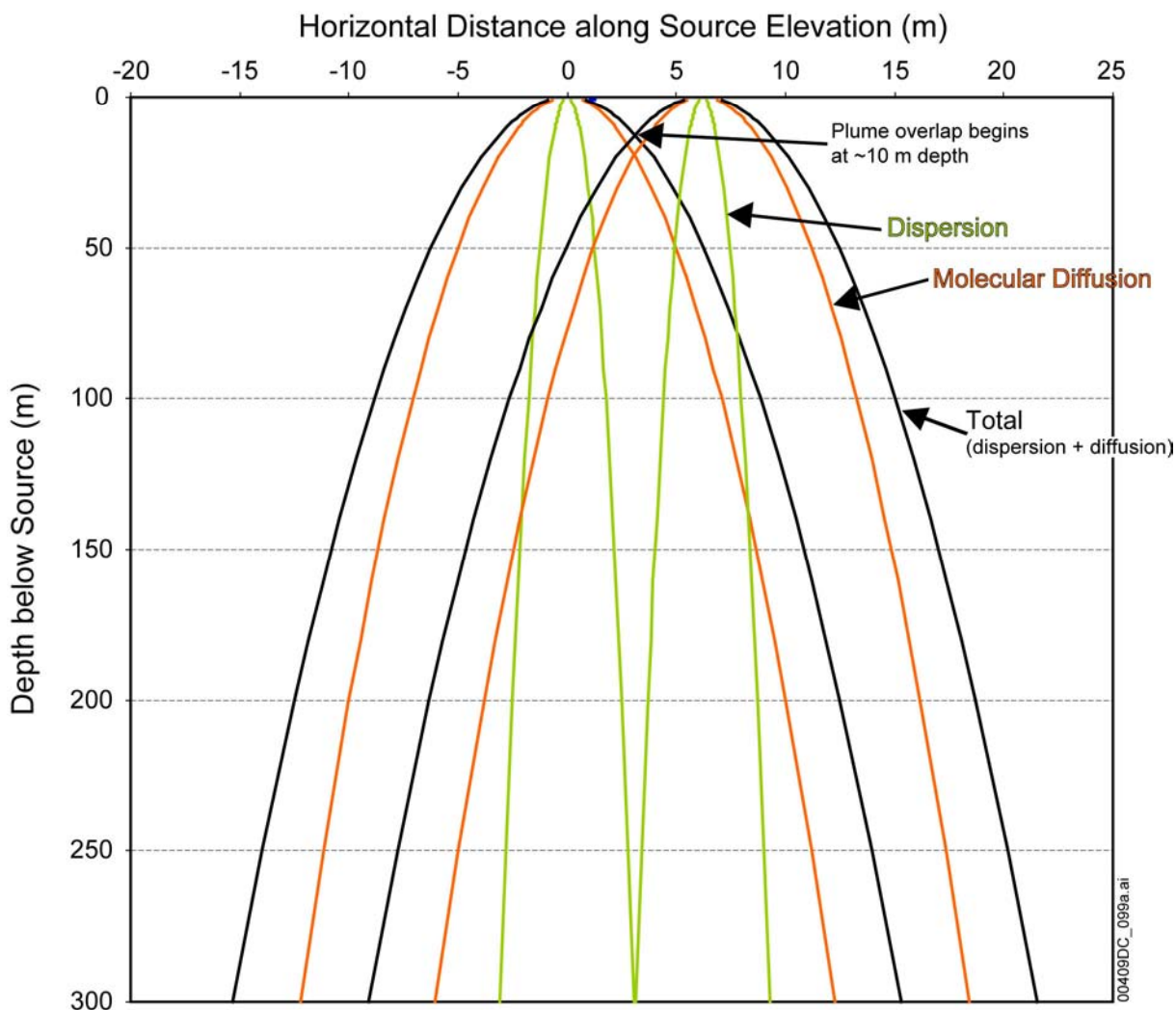
Source: DTN: LB0408CMATUZFT.003.

NOTE: Horizontal scale is exaggerated by a factor of approximately 7.5.

Figure D-6. Plume Spreading with Depth Due to Lateral Dispersion and Molecular Diffusion

D.4.4.4.3   Transient Condensation

Condensation of water vapor in the main drifts as a result of pore-water evaporation from host rocks surrounding the emplacement drifts will occur during the initial phase of heating after waste emplacement. This phenomenon arises because of transient temperature differences between the emplacement and main access and ventilation drifts when the latter will be cooler. The leaching of cementitious material by this condensate will take place under conditions when the cementitious material is still young and will be similar to those due to dewatering. The consequences will, therefore, be analogous to those described in Section D.4.4.1.

D.4.4.4.4   Rehydration

The composition and pH of the cementitious material leachate plume following rehydration of the repository would depend on the nature and extent of preceding recrystallization and carbonation under high pH (Hardin 1998). With total carbonation, the leachate plume composition would differ little from that of the ambient pore water (Hardin 1998, p. 6-28). The possible excess of sodium and potassium in the altered cementitious material (DTN: LL020805523125.002) might result in the transient release of $NaHCO_3$ (most potassium would be fixed in secondary illitic clay), and the pH could rise initially to more than 9, but this excursion is expected to be minimal in duration and, overall, influence only trace amounts of calcite likely to precipitate through interactions of the $NaHCO_3$ leachate with Ca^{2+} in the pore water. Therefore, if total carbonation of the cementitious material were to occur together with subsequent leaching, there would be no impact on repository performance or radionuclide migration. This condition could be achieved with respect to shotcrete support structures in the inner part of the repository, where the dryout period is about 1,000 years in duration (Section D.4.4.3).

Conditions would be somewhat different if only partial carbonation were to occur before rehydration, as would be expected in the peripheral parts of the repository (Section D.4.4.3). In this case, residual calcium silicates, such as gyrolite, xonotlite, tobermorite, and hillebrandite, could still be present (Hardin 1998, p. 6-37) (Figure D-3), depending on the amount of silica fume added to the shotcrete and the extent of reaction with the fine aggregate. In the presence of percolating pore water, the leachate composition could be elevated in calcium, and the pH could range between 10 and 12, depending on the chemical composition of the original Portland cement and the extent of subsequent interaction of the cement with the associated fine aggregate (Section D.4.4.2). The interaction of cementitious C-S-H phases with alkali feldspar in the fine aggregate of the shotcrete could also lead to modification of the resulting shotcrete phase assemblage, with NA_2O substituting in gyrolite, and Al_2O_3 substituting in tobermorite (Section D.4.4.2). These reactions could also modify the composition of the initial leachate. Studies to evaluate this phenomenon have yet to be undertaken.

In Table D-12, the chemical composition of the aqueous phase in equilibrium with binary two-phase assemblages in the system CaO-SiO_2-H_2O have been calculated at 25°C using EQ3 V 7.2b (Wolery 1992) and the associated Data0.dat database. The results are for illustrative purposes only, as the cementitious materials contain chemical components other than those employed to illustrate this simple system. Despite these limitations, the calculations clearly show the importance of the ultimate C/(C+S) ratio of the cementitious reaction product in minimizing the release of Ca^{2+} to the environment through leaching following rehydration.

Table D-12. Chemical Composition of Cementitious Materials Leachate as a Function of the Mineralogy after Hydrothermal Alteration

Phase Assemblage	Total SiO$_2$(aq) (mg/kg H$_2$O)	Total Ca^{2+} (mg/kg H$_2$O)	pH
Portlandite-hillebrandite	0.14	625	12.37
Hillebrandite-tobermorite-14A	0.20	559	12.33
Tobermorite-14A-gyrolite	18.4	16.9	10.74
Gyrolite-cristobalite(alpha)	51.9	12.8	10.09
Calcite[a]	-	43.9	7.62

Source: DTN: LB0408CMATUZFT.004; EQ3 Version 7.2b (Wolery 1992).

NOTE: [a]Assumed log(pCO$_2$) = 2.52 (3,000 ppmV).

Table D-12 shows that the reaction of the cement components of the shotcrete with silica fume and the fine aggregate could produce mineral assemblages such as tobermorite-14A-gyrolite or gyrolite-cristobalite(alpha). The coexisting aqueous phase at equilibrium with these mineral pairs differ in Ca^{2+} and SiO$_2$(aq) concentrations only incrementally from those of existing pore waters, and, therefore, a leachate from such mineral assemblages would not generate a deleterious alkaline plume.

Any alkaline leachate would be subject to reaction and neutralization by the ambient CO$_2$ in the gaseous phase filling the fractures in the host rock. The approximate rate of neutralization in the presence of elevated pCO$_2$ in the time period following rehydration can be estimated from experimental work and associated model simulations (DTNs: LL030211423125.005, LL030211523125.006). This work demonstrates that CO$_2$ uptake and neutralization at 25°C could take place in the field within a matter of weeks, a time period that is essentially instantaneous when considered within the context of repository timescales of interest. Such rapid rates of neutralization would suggest that plume neutralization would occur locally (i.e., within a few centimeters of the shotcrete interface). Field observations involving groundwater interactions with subsurface concrete structures corroborate these rapid reaction rates (Liu and He 1998). Ambient gaseous CO$_2$ uptake and aqueous phase carbonate diffusion rates would also suggest that much of the neutralization of the alkalinity and precipitation of calcite could occur within the pores of the shotcrete. However, additional modeling would be required to confirm this possibility. Therefore, it can be concluded that the generation of an alkaline plume following rehydration, which could affect radionuclide transport, would be extremely unlikely. If the cementitious material were to be incompletely carbonated, the leachate itself would be carbonated and the pH lowered to ambient pore-water values. The leaching of a partially carbonated cementitious material would, therefore, produce an outcome similar to that for a fully carbonated cementitious material, and the impact on radionuclide migration would be minor.

Even if an alkaline plume were to form, it would encounter elevated concentrations of CO$_2$ below the repository horizon. Dryout of the repository horizon would induce diffusive migration of CO$_2$ in the gaseous phase, which would be absorbed by groundwater and collect as a blanket beneath the repository horizon (CRWMS M&O 2000, pp. 79 to 81; DTN: LL030211423125.005), thereby providing added capacity for alkaline plume neutralization in the underlying unsaturated zone and inhibiting further plume migration. This blanket would,

however, be relevant primarily in neutralizing episodic fast flows, as discussed in Section D.4.4.4.1.

D.4.4.5   Precipitation of Secondary Calcite in Devitrified Tuff Host Rocks

One of the technical requirements of the response to ENFE 1.04 is an assessment of the potential effect of leaching of the emplaced cementitious materials and how the consequent precipitation of minerals within the host rock would impact the hydrologic properties of the unsaturated zone. Modification of the hydrologic regime could result in percolating pore water being diverted toward the waste packages in the emplacement drifts with undesired consequences in the event of a waste package failure. If alkaline plumes were to form due to incomplete carbonation, their neutralization would decrease the concentration of gas-phase CO_2 in the host-rock fractures and cause the precipitation of calcite in the rock pores and fractures below the repository horizon, with concomitant reduction of dissolved calcium. The plumes could also react with the vitroclastic tuffs of the host rock and precipitate secondary calcium aluminosilicates in the matrix pores and on fracture surfaces, causing further reduction in rock permeability, although this phenomenon is expected to be minor. As is discussed elsewhere in this appendix, the hydrologic impact would depend substantially on the extent to which the cementitious constituents are converted in situ into calcite during the period when the repository environment would have undergone dryout. Work done to date does not provide any quantitative predictions of the extent of carbonation during this period.

Given the uncertainties associated with estimates of the extent of cement carbonation during the dryout period prior to rehydration, it is instructive to consider a worst-case scenario in which all of the most highly reactive constituent (portlandite) that would be present initially in the shotcrete is leached at a specified location, such as a turnout intersection from the main access drift into one of the emplacement drifts or the exhaust side intersection from the emplacement drift, as illustrated in Figure D-1. At representative intersections, 665 m^2 and 220 m^2 of shotcrete, 0.1 m thick, or 66.5 m^3 and 22 m^3, will be applied, respectively, at these two intersections. It is assumed that the gross footprint of each turnout intersection is 36×10 m and 15×13 m, respectively, and that all of the initial portlandite, approximately 1,821 mol/m^3, contained in the cementitious materials would be dissolved, transported, and precipitated as calcite in the fractures immediately beneath these footprints, as would be predicted from laboratory experiments (DTN: LL030211423125.005).

If the calcite precipitates in the matrix (16.4 vol %; Liu et al. 2003) and in the fractures (1 vol %; estimated, this appendix) for a total of 17.4 vol %, then the total filled thickness in the rock below the turnout intersection would be 7.14 cm (Table D-13). Under these conditions, the rock would be rendered impermeable and all percolation would be diverted around this impermeable barrier. However, this calculation ignores completely the nature of the precipitation process in fractures in the unsaturated zone. Fractures are not of uniform width and contain numerous asperities. Localized precipitation at these asperities and irregular rimstone or calc-sinter deposition elsewhere within the fracture voids could result in the formation of a spongy tufa with a high porosity and low permeability. Very little of such material could reduce the transmissivity or totally seal the affected fractures after only minimal precipitation and divert the flow laterally, only to cause the process to be repeated in adjacent fractures. Thus, the hydrologic diversion of unsaturated zone groundwater flow around sealed regions below the shotcreted drifts could

become significant. It could be arbitrarily assumed that the calcite filled only the first centimeter of rock before lateral diversion took place, after which all further calcite precipitation took place to the same depth around the margins of the footprint. In this case, the affected area would be 2,571 m^2, and the margin would extend 13.4 m from the end of the shotcreted portion of the main access drift. This would place the margin about 49 m away from the first waste package. This would suggest that the hydrologic impact of calcite precipitation on the emplacement drift environment would be minimal.

Table D-13. Estimated Depth of Rock Voids Filled with Calcite Due to the Leaching of Portlandite from Shotcrete in a Main Access Drift Turnout Intersection

Parameter	Units	Value	Reference
Volume of shotcrete, main access drift intersection	m^3	66.5	BSC 2004h.
Assumed shotcrete footprint, main access drift intersection	m^2	360	This appendix.
Assumed shotcrete footprint, exhaust drift intersection	m^2	195	This appendix.
Volume of shotcrete, exhaust drift intersection	m^3	22.0	BSC 2004b.
Mass of portlandite in shotcrete	mol/m^3	1.821	This appendix.
Solubility of portlandite at 25°C	mol/kg H$_2$O	0.0156	EQ3/6 V.7.2b Data0.dat (Wolery 1992).
Equivalent volume of calcite	m^3	4.47	This appendix.
Density of calcite	g/cm^3	2.710	Calculation from Table D-2.
Molecular weight of calcite	g/mol	100.09	Lide 2000, p. 4-50.
Total void-space fraction in rock	–	0.174	Matrix volume from Liu et al. 2003. Fracture volume assumed.
Infiltration rate	mm/yr	1 to 5	Sonnenthal and Bodvarsson 1999.
Depth filled with calcite, main access drift intersection	cm	7.14	This appendix.
Depth filled with calcite, exhaust drift intersection	cm	4.36	This appendix.
Time to precipitate calcite	years	4,313 to 21,565	This appendix.

Source: DTNs: LB0408CMATUZFT.002, LB0408CMATUZFT.004.

Another aspect regarding alkaline plume neutralization is the time it would take to precipitate calcite in the rock pores and fractures. The infiltration rate at Yucca Mountain is estimated to range from 1 to 5 mm/yr (Sonnenthal and Bodvarsson 1999). Therefore, if the percolating pore water were to be saturated with respect to portlandite on contact with the cementitious materials at 25°C, it would contain approximately 0.0156 mol/kg H$_2$O·Ca(OH)$_2$(aq) (EQ3/6 V7.2b, Data0.dat; Wolery 1992). Mass-balance considerations show that this would lead to the deposition of between 5.62 and 28.1 mol/yr of calcite. Thus, the time required to leach all of the initial portlandite from the cementitious materials with essentially concurrent deposition in underlying pores of the host rock would be between 4,313 and 21,565 years. Because portlandite has retrograde solubility with temperature, leaching at higher temperatures would slow down the rate. The percolation rate following rehydration would be expected to be higher, thereby decreasing the overall time for precipitation of calcite due to plume neutralization. As noted elsewhere, the precipitation rate would likely be fast in relation to the leaching rate. The availability of CO$_2$ through diffusion would be expected to become rate controlling, because the

leaching rate of $Ca(OH)_2$ would be slow in relation to CO_2 gaseous diffusion rates (Section D.4.3.4).

Other aspects of the above process should also be considered, which would modify the distribution of precipitated calcite. Before advective transport, the alkaline leachate must diffuse out of the concrete, which would be shielded by a rind of precipitated calcite within the shotcrete pores. The leachate would be exposed to CO_2 during this process and would have a tendency to precipitate at or near the concrete air–water interface. Subsequently, unneutralized leachate would initially percolate mainly through the rock matrix under a presumed normal percolation flux. The rate of neutralization by CO_2 would depend largely on the liquid–gas interfacial area, but this interfacial area would be expected to be limited by fracture interfaces in the relatively small volume of affected rock beneath the turnout intersection. This could retard calcite precipitation and cause it to be distributed over a larger volume of rock underlying the footprint. However, quantitative calculations have not been performed to evaluate this possibility. As noted in Section D.4.3.5.1, episodic flows could rapidly leach and transport alkaline solutions from the shotcrete and distribute the precipitated calcite over a large volume of rock in a subvertical region beneath the footprint.

Given the possibility that complete carbonation of shotcrete and grout could occur in most of the repository, some consideration should also be given to the impact that the resulting mineralogy would have on the hydrology and radionuclide transport in this limiting case. The mineralogic composition of a completely carbonated cementitious material will depend, to a certain extent, on the original formulation of the cementitious material (i.e., the C/(S+C) ratio), as determined by the addition of silica fume and on the concentration of alumina and additives, such as gypsum (Nelson 1990). As noted in Section D.4.4.2, C-S-H gel could either alter directly to calcite after the substantial alteration of CH, or it could transform to calcite through intermediate secondary calcium silicates. Whichever path is taken, the resulting product would consist of calcite plus opaline silica. The remaining residual phases would consist dominantly of secondary and potassic or calcic clays, depending on the quantities of alumina and magnesia in the original cementitious material. A leachate from this mineral assemblage would not possess significant alkalinity, as shown in reaction progress simulations after 10,000 years (CRWMS M&O 1998, Figure 4-41) and would neither precipitate significant secondary calcite outside the cementitious material nor adversely affect radionuclide retardation (Section D.4.4.6).

D.4.4.6 Generation and Transport of Colloids from Grout

Another issue of concern regarding the emplacement of cementitious materials in the repository is the potential for colloidal particles to be generated and for these colloids to be advectively transported by groundwater and act as a substrate for radionuclide sorption or precipitation. This issue was raised in earlier publications (e.g., Hardin 1998, pp. 6-36, 6-59), citing supporting evidence by Ramsay et al. (1988). Such a scenario, while theoretically possible, is highly implausible for the following reasons:

- Significant release of colloids is plausible only from freshly prepared cementitious material before it has significantly recrystallized through exposure to elevated temperatures at high relative humidity. The colloidal C-S-H phase formed in the

cementitious material immediately after cement is mixed with water is a potential source of migrating colloids.

- During the time when mobile colloids could form and be transported, the ionic strength of the leachate is expected to be sufficiently high to destabilize the colloidal particles, causing them to aggregate or adhere to siliceous rock surfaces, thereby decreasing their concentration in solution to background levels.

- The effective diffusivity of colloidal particles into the rock matrix is many orders of magnitude lower than for molecular or ionic species. The advective transport of colloidal particles is restricted to episodic flow along transmissive faults under fast flow path conditions. Fast transport of colloidal particles is, therefore, severely restricted in volume and location within the repository. Therefore, lateral diffusion of colloids in a plume would be negligible, and the lateral spreading of colloids would be due to physical dispersion of the plume (Section D.4.4.4.2).

- During the period when colloids could be leached and transported from the grout, waste package failure is improbable. Therefore, the intersection of a leachate plume containing cementitious colloidal particles with a radionuclide-bearing leachate plume from a failed waste package is temporally improbable.

- The colloidal C-S-H phase formed in the grout during setting (the potential source of migrating colloids) is highly reactive and, thus, would be transformed to calcite or secondary C-S-H phases at the elevated temperatures, relative humidity, and $p\mathrm{CO_2}$ following repository closure (provided $\mathrm{CO_2}$ availability is not restricted).

- Any colloidal particles that survive aggregation or adhesion, as noted above, would be thermodynamically unstable in the ambient pore-water environment of the unsaturated zone, preferentially releasing calcium that precipitates as calcite under the calcite-saturated conditions present in the unsaturated zone at Yucca Mountain.

In order to substantiate the statements listed above, it is necessary to explain the characteristics of Portland cement, the principal reactive ingredient of shotcrete, and its behavior after contact with water. If recently set Portland cement is leached with distilled water, the CH readily dissolves to produce a highly alkaline solution with a pH in excess of 12, consisting primarily of dissolved $\mathrm{Ca(OH)_2}$, with minor concentrations of NaOH and KOH (DTN: LL020805523125.002; Wieland et al. 2004, p. 120). The leaching process can also mobilize colloidal C-S-H gel particles (Ramsay et al. 1988; Wieland and Spieler 2001). Wieland and Spieler (2001) measured particle sizes between 50 and 1,000 nm, but they assumed that the total population ranged in size to as low as 1 nm. Ramsay et al. (1988), however, observed particles between 2,000 to 5,000 nm in diameter, which aggregated (Ramsay et al. 1988, pp. 121, 123). Furthermore, they found evidence of particle growth (Ramsay et al. 1988, Figure 7b, pp. 122 and 123), reflecting Ostwald ripening (Steefel and Van Cappellen 1990). Wieland and Spieler (2001, p. 521) also determined that colloidal particle concentrations in solution were strongly dependent on ionic strength and that a leachate saturated with calcium hydroxide induces substantial colloidal aggregation, leading to a very low residual colloid concentration of about 0.01 mg/L. They showed that this concentration is equivalent to or less than the colloidal concentrations

found in natural groundwater (see also *Waste Form and In-Drift Colloids-Associated Radionuclide Concentrations: Abstraction and Summary* (BSC 2003a, p. 30)).

Because the concentration of produced cementitious colloidal particles would be at concentrations similar to those found to occur naturally in groundwater, their presence would be inconsequential except for the very high experimentally determined partition coefficients for uranium and neptunium on such particles (Hardin 1998, pp. 6-39 to 6-45). However, the capacity for these colloidal particles to be transported is limited to high permeability zones or open faults within Yucca Mountain and the coincidence of the positioning of emplaced grout within or immediately above such high permeability zones. Additionally, the capacity of these particles to transport uranium and neptunium depends on colocation of the colloids and radionuclides, which is unlikely. The findings of *Radionuclide Transport Models Under Ambient Conditions* (BSC 2003e, pp. 177 to 188, Attachments VI and VII) support this conclusion.

Leaching of the colloids from the grout would have to take place before the C-S-H colloid recrystallizes through thermal heating during the period of high relative humidity. This could only occur before dryout of the repository horizon, during or prior to emplacement of the waste packages. Thus, the release of colloids is temporally distinct from potential waste package failure.

The bases presented above, together with supporting documentation, lead to the conclusion that the release of colloidal particles from cementitious materials would be unlikely to affect repository performance or radionuclide migration.

D.4.5 Summary

Cementitious material (shotcrete and grout for rock bolt emplacement) is planned for use in the Yucca Mountain repository for ground support at the emplacement drift intersections with the main access drifts and the exhaust drifts. The retention of this material in the repository poses two concerns. The first is that the leaching of these cementitious materials will affect repository performance by modifying the hydrologic properties of the surrounding rock and diverting the flow of water entering the drifts. The second concern is that an alkaline plume resulting from leaching of this material could enhance radionuclide transport to the accessible environment, either through the complexation of radionuclides or through transport by pseudocolloids. Both concerns become relevant only after the repository environment rehydrates following a period of dryout due to heating caused by radioactive decay of the emplaced waste.

The first step in evaluating the concerns was to investigate the extent of chemical alteration of the shotcrete, formulated with Type II cement, prior to repository closure and during the postclosure dryout period. Chemical alteration of the cement component of the shotcrete would occur through recrystallization, reaction with silica fume and aggregate, and carbonation. The second step was to determine the consequences of this alteration on the formation of alkaline plumes caused by leaching the shotcrete following rehydration. The third and final step was to evaluate the potential impact of plume neutralization by CO_2 on the hydrology of the unsaturated zone, whether and where a shotcrete leachate plume would interact with a leachate waste plume from a failed waste package, and whether radionuclide migration would be affected.

Several important findings were obtained from the evaluation. The first was that recrystallization of the cement and its further reaction with silica fume additive and with the fine aggregate included in the shotcrete formulation would lead to the formation of a silica-rich calcium silicate hydrate assemblage. Carbonation of the cement component of the shotcrete would take place both before and after repository closure and simultaneously with recrystallization. Calculations indicate that carbonation would be substantial to complete, where the repository environment is hot enough that rehydration occurs after more than 1,000 years. Elsewhere, where rehydration occurs in less than 1,000 years, carbonation could be incomplete. During the dryout period, carbonation rates are limited by gaseous phase CO_2 diffusion through the host rocks, rather than by the carbonation reaction itself, which would be fast. Following rehydration, carbonation would continue at a reduced pace, the rate being limited by aqueous phase CO_2 diffusion into the pores of the shotcrete. Upon rehydration, the pore waters would leach the silica-rich calcium silicate hydrates, but their solubilities would be so low that calcium and silica concentrations would be comparable to those of ambient pore water, and the alkalinity would be low. Neutralization of this alkalinity would be very rapid, and, if any calcite were to precipitate, it would occur in the immediate vicinity or even within the pores of the shotcrete. The resulting plume would have a composition similar to that of the ambient pore water.

The proximity of shotcrete in the exhaust drift intersection to the nearest waste package in the emplacement drift indicates that a shotcrete leachate plume could intersect a radionuclide-bearing plume from the waste package below the repository horizon, but that this plume would have little or no impact on radionuclide migration. Because of the extensive recrystallization and modification of the mineralogy of the shotcrete and partial to complete carbonation, extensive precipitation of calcite in the pores of the host rock is unlikely, and, therefore, hydrologic modification of the unsaturated zone by the retention of ground support cementitious material is likewise considered unlikely.

D.5 REFERENCES

D.5.1 Documents Cited

BSC (Bechtel SAIC Company) 2001. *Repository Design, Waste Package Project 24-BWR Waste Package, Sheet 1 of 3, Sheet 2 of 3, and Sheet 3 of 3.* DWG-UDC-ME-000003 REV A. Las Vegas, Nevada: Bechtel SAIC Company. ACC: MOL.20020102.0173.

BSC 2003a. *Waste Form and In-Drift Colloids-Associated Radionuclide Concentrations: Abstraction and Summary.* MDL-EBS-PA-000004 REV 00 ICN 01. Las Vegas, Nevada: Bechtel SAIC Company. ACC: DOC.20031222.0012.

BSC 2003b. *Subsurface Geotechnical Parameters Report.* 800-K0C-WIS0-00400-000-00A. Las Vegas, Nevada: Bechtel SAIC Company. ACC: ENG.20040108.0001.

BSC 2003c. *Simulation of Net Infiltration for Modern and Potential Future Climates.* ANL-NBS-HS-000032 REV 00 ICN 02, with errata. Las Vegas, Nevada: Bechtel SAIC Company. ACC: MOL.20011119.0334; DOC.20031014.0004; DOC.20031015.0001.

BSC 2003d. *Underground Layout Configuration.* 800-P0C-MGR0-00100-000-00E. Las Vegas, Nevada: Bechtel SAIC Company. ACC: ENG.20031002.0007.

BSC 2003e. *Radionuclide Transport Models Under Ambient Conditions*. MDL-NBS-HS-000008 REV 01. Las Vegas, Nevada: Bechtel SAIC Company. ACC: DOC.20031201.0002.

BSC 2004a. *Engineered Barrier System Features, Events, and Processes.* ANL-WIS-PA-000002 REV 03 DRAFT A. Las Vegas, Nevada: Bechtel SAIC Company. ACC: MOL.20040721.0240.

BSC 2004b. *Closure and Sealing Preliminary Design Calculation.* 800-KMC-MGR0-00200-000-00A. Las Vegas, Nevada: Bechtel SAIC Company. ACC: ENG.20040113.0003.

BSC 2004c. *Features, Events, and Processes in UZ Flow and Transport.* ANL-NBS-MD-000001 REV 02. Las Vegas, Nevada: Bechtel SAIC Company. ACC: DOC.20040331.0002.

BSC 2004d. *Miscellaneous Waste-Form FEPs.* ANL-WIS-MD-000009 REV 01. Las Vegas, Nevada: Bechtel SAIC Company. ACC: DOC.20040421.0005.

BSC 2004e. *Engineered Barrier System: Physical and Chemical Environment Model*. ANL-EBS-MD-000033 REV 02. Las Vegas, Nevada: Bechtel SAIC Company. ACC: DOC.20040212.0004.

BSC 2004f. *Ground Control for Non-Emplacement Drifts for LA.* 800-KMC-88D0-00700-000-00A. Las Vegas, Nevada: Bechtel SAIC Company. ACC: ENG.20040302.0022.

BSC 2004g. *Subsurface Facility Description Document.* 800-3YD-MGR0-00100-000-004. Las Vegas, Nevada: Bechtel SAIC Company. ACC: ENG.20040630.0006.

BSC 2004h. *D&E/ PA/C IED Subsurface Facilities Committed Materials.* 800-IED-WIS0-00301-000-00B. Las Vegas, Nevada: Bechtel SAIC Company. ACC: ENG.20040318.0030.

BSC 2004i. *Turnout Drift Operations Configuration.* 800-KMC-SSD0-00100-000-00A. Las Vegas, Nevada: Bechtel SAIC Company. ACC: ENG.20040209.0010.

BSC 2004j. *Multiscale Thermohydrologic Model*. ANL-EBS-MD-000049 REV 01. Las Vegas, Nevada: Bechtel SAIC Company. ACC: DOC.20040301.0004.

BSC 2004k. *Mountain-Scale Coupled Processes (TH/THC/THM)*. MDL-NBS-HS-000007 REV 01, with errata. Las Vegas, Nevada: Bechtel SAIC Company. ACC: DOC.20031216.0003; DOC.20040211.0006.

BSC 2004l. *Drift-Scale Coupled Processes (DST and THC Seepage) Models*. MDL-NBS-HS-000001 REV 02, with errata. Las Vegas, Nevada: Bechtel SAIC Company. ACC: DOC.20030804.0004; DOC.20040219.0002; DOC.20040405.0005.

BSC 2004m. *D&E / PA/C IED Emplacement Drift Configuration and Environment*. 800-IED-MGR0-00201-000-00B. Las Vegas, Nevada: Bechtel SAIC Company. ACC: ENG.20040326.0001.

BSC 2004n. *Repository Subsurface Turnout Drift 1-8 Interface.* 800-KM0-SSD0-00301-000-00A. Las Vegas, Nevada: Bechtel SAIC Company. ACC: ENG.20040220.0009.

Crank, J. 1975. *The Mathematics of Diffusion*. 2nd Edition. Oxford, England: Clarendon Press. TIC: 9662.

CRWMS M&O 1998. "Near-Field Geochemical Environment." Chapter 4 of *Total System Performance Assessment-Viability Assessment (TSPA-VA) Analyses Technical Basis Document.* B00000000-01717-4301-00004 REV 00. Las Vegas, Nevada: CRWMS M&O. ACC: MOL.19980724.0393.

CRWMS M&O 2000. *Engineered Barrier System: Physical and Chemical Environment Model*. ANL-EBS-MD-000033 REV 01. Las Vegas, Nevada: CRWMS M&O. ACC: MOL.20001228.0081.

DOE (U.S. Department of Energy) 1998. *Total System Performance Assessment. Volume 3 of Viability Assessment of a Repository at Yucca Mountain*. DOE/RW-0508. Washington, D.C.: U.S. Department of Energy, Office of Civilian Radioactive Waste Management. ACC: MOL.19981007.0030.

Gaines, R.V.; Skinner, H.C.W.; Foord, E.E.; Mason, B.; and Rosenzweig, A. 1997. *Dana's New Mineralogy : The System of Mineralogy of James Dwight Dana and Edward Salisbury Dana.* 8th edition. New York, New York: Wiley-Interscience. TIC: 256455.

Hardin, E.L. 1998. *Near-Field/Altered-Zone Models Report*. UCRL-ID-129179 DR. Livermore, California: Lawrence Livermore National Laboratory. ACC: MOL.19980504.0577.

Hardin, E.L. 2001. "Subissue 1: Comments on Effects of Cementitious Materials." Slide presentation at U.S. Nuclear Regulatory Commission/U.S. Department of Energy Technical Exchange and Management Meeting on Evolution of the Near-Field Environment, January 9–12, 2001. ACC: MOL.20011017.0383.

Isu, N., Ishida, H., and Mitsuda, T. 1995. "Influence of Quartz Particle Size on the Chemical and Mechanical Properties of Autoclaved Aerated Concrete (I) Tobermorite Formation." *Cement and Concrete Research*, *25* (2), 243–248. New York, New York: Pergamon. TIC: 256452.

Kalousek, G.L., and Nelson, E.B. 1978. "Hydrothermal Reactions of Dicalcium Silicate and Silica." *Cement and Concrete Research*, *8*, 283–290. New York, New York: Elsevier Science Ltd. TIC: 256454.

Lackner, K.S.; Grimes, P.; and Ziock, H.-J. 1999. "Carbon Dioxide Extraction from Air: Is It an Option?" LA-UR-99-583. Los Alamos, New Mexico: Los Alamos National Laboratory. TIC: 256449.

Lide, D.R., ed. 2000. *CRC Handbook of Chemistry and Physics*. 81st Edition. Boca Raton, Florida: CRC Press. TIC: 253056.

Liu, H.-H.; Haukwa, C.B.; Ahlers, C.F.; Bodvarsson, G.S.; Flint, A.L.; and Guertal, W.B. 2003. "Modeling Flow and Transport in Unsaturated Fractured Rock: An Evaluation of the Continuum Approach." *Journal of Contaminant Hydrology, 62–63,* 173–188. New York, New York: Elsevier. TIC: 254205.

Liu, Z. and He, D. 1998. "Special Speleotherms in Cement-Grouting Tunnels and Their Implications of the Atmospheric CO_2 Sink." *Environmental Geology, 35* (4). Berlin, Germany; New York, New York: Springer-Verlag. TIC: 248998.

Meike, A. 1996. "Introduced (Man-Made) Materials." Chapter 6 of *Near-Field and Altered-Zone Environment Report*. Wilder, D.G., ed. UCRL-LR-124998, Volume II. Livermore, California: Lawrence Livermore National Laboratory. ACC: MOL.19961212.0122.

Meike, A. 1997. *A Discussion of the Relationship Between Repository Thermal History, Water Budget and the Evolution of Cementitious Materials*. Milestone SPGL1FM4. Livermore, California: Lawrence Livermore National Laboratory. ACC: MOL.19980114.0082.

Nelson, E.B., ed. 1990. *Well Cementing*. Developments in Petroleum Science, Volume 28. Amsterdam, The Netherlands: Elsevier. TIC: 256109.

Neville, A.M. 1996. *Properties of Concrete*. 4th Edition. New York, New York: John Wiley & Sons. TIC: 236567.

Papadakis, V.G. 2000. "Effect of Supplementary Cementing Materials on Concrete Resistance against Carbonation and Chloride Ingress." *Cement and Concrete Research*, *30*, 291–299. TIC: 256071.

Peterman, Z.E. and Cloke, P.L. 2002. "Geochemistry of Rock Units at the Potential Repository Level, Yucca Mountain, Nevada." *Applied Geochemistry*, *17*, 683–698. New York, New York: Pergamon. TIC: 254046.

Pruess, K. 1996. "Effective Parameters, Effective Processes: From Porous Flow Physics to *In Situ* Remediation Technology." *Groundwater and Subsurface Remediation: Research Strategies for In-Situ Technologies*. H. Kobus, B. Barczewski, and H.-P. Koschitzky, eds., 183–193. Berlin, Germany: Springer. TIC: 238489.

Pruess, K. 1998. "On Water Seepage and Fast Preferential Flow in Heterogeneous, Unsaturated Rock Fractures." *Journal of Contaminant Hydrology, 30,* 333–362. New York, New York: Elsevier. TIC: 238921.

Ramsay, J.D.F.; Avery, R.G.; and Russell, P.J. 1988. "Physical Characteristics and Sorption Behaviour of Colloids Generated from Cementitious Systems." *Radiochimica Acta*, *44/45*, 119–124. München, Germany: R. Oldenbourg Verlag. TIC: 226318.

Reamer, C.W. 2001. "U.S. Nuclear Regulatory Commission/U.S. Department of Energy Technical Exchange and Management Meeting on Evolution of the Near-Field Environment (January 9–12, 2001)." Letter from C.W. Reamer (NRC) to S. Brocoum (DOE/YMSCO), January 26, 2001, with enclosure. ACC: MOL.20010810.0033.

Rothstein, D.; Jeffrey, J.; Thomas, J.J.; Christensen, B.J.; Hamlin, M.; Jennings, H.M. 2002. "Solubility Behavior of Ca-, S-, Al-, and Si-bearing Solid Phases in Portland Cement Pore Solutions as a Function of Hydration Time." *Cement and Concrete Research*, *32*, 1663–1671. New York, New York: Elsevier. TIC: 253818.

Roy, D.M. and Langton, C.A. 1989. *Studies of Ancient Concrete as Analogs of Cementitious Sealing Materials for a Repository in Tuff.* LA-11527-MS. Los Alamos, New Mexico: Los Alamos National Laboratory. ACC: HQX.19890608.0033.

Shaw, S.; Clark, S.M.; and Henderson, C.M.B. 2000. "Hydrothermal Formation of the Calcium Silicate Hydrates, Tobermorite ($Ca_5Si_6O_{16}(OH)_2 \cdot 4H_2O$) and Xonotlite ($Ca_6Si_6O_{17}(OH)_2$): an In Situ Synchrotron Study." *Chemical Geology*, *167* (1–2), 129–140. Amsterdam, The Netherlands; New York, New York: Elsevier. TIC: 252352.

Shaw, S.C.; Henderson, M.B.; and Clark, S.M. 2002. "In-Situ Synchrotron Study of the Kinetics, Thermodynamics, and Reaction Mechanisms of the Hydrothermal Crystallization of Gyrolite, $Ca_{16}Si_{24}O_{60}(OH)_8 \cdot 14H_2O$." *American Mineralogist*, *87*, 533–541. Washington, D.C.: Mineralogical Society of America. TIC: 253336.

Sonnenthal, E.L. and Bodvarsson, G.S. 1999. "Constraints on the Hydrology of the Unsaturated Zone at Yucca Mountain, NV from Three-Dimensional Models of Chloride and Strontium Geochemistry." *Journal of Contaminant Hydrology*, 38, 107–156. New York, New York: Elsevier. TIC: 249840.

Steefel, C.I. and Van Cappellen, P. 1990. "A New Kinetic Approach to Modeling Water-Rock Interaction: The Role of Nucleation, Precursors, and Ostwald Ripening." *Geochimica et Cosmochimica Acta*, *54*, (10), 2657–2677. New York, New York: Pergamon. TIC: 240813.

Stevula, L. and Petrovic, J. 1983. "Formation of an Intermediate C-S-H Phase during the Hydrothermal Synthesis of Gyrolite." *Cement and Concrete Research*, *13*, 684–688. New York, New York: Elsevier Science Ltd. TIC: 256453.

Tennis, P.D. 1999. "Portland Cement Characteristics–1998." *Concrete Technology Today, 20,* (2), 1–7. S. Kosmatka, ed. Skokie, Illinois: Portland Cement Association. TIC: 256269.

Tokunaga, T.K. and Wan, J. 1997. "Water Film Flow along Fracture Surfaces of Porous Rock." *Water Resources Research*, *33*, (6), 1287-1295. Washington, D.C.: American Geophysical Union. TIC: 242739.

Wieland, E. and Spieler, P. 2001. "Colloids in the Mortar Backfill of a Cementitious Repository for Radioactive Waste." *Waste Management*, *21*, (6), 511–523. New York, New York: Elsevier. TIC: 251666.

Wieland, E.; Tits, J.; and Bradbury, M.H. 2004. "The Potential Effect of Cementitious Colloids on Radionuclide Mobilization in a Repository for Radioactive Waste." *Applied Geochemistry*, *19*, 119–135. TIC: 256073.

Wolery, T.J. 1992. *EQ3/6, A Software Package for Geochemical Modeling of Aqueous Systems: Package Overview and Installation Guide (Version 7.0).* UCRL-MA-110662, Part I. Livermore, California: Lawrence Livermore National Laboratory. TIC: 205087.

Yang, I.C.; Rattray, G.W.; and Yu, P. 1996. *Interpretation of Chemical and Isotopic Data from Boreholes in the Unsaturated Zone at Yucca Mountain, Nevada.* Water-Resources Investigations Report 96-4058. Denver, Colorado: U.S. Geological Survey. ACC: MOL.19980528.0216.

Younker, J.L. 1996. "Status/Summary Report for Fiscal Year 1996 Activities within the Performance Assessment Overview Study on the Consequences of Cementitious Materials." Letter from J.L. Younker (CRWMS M&O) to S.J. Brocoum (DOE/YMSCO), September 30, 1996, LV.PA.DCS.09/96-038, with attachments. ACC: MOL.19971016.0202; MOL.19971016.0203.

Ziegler, J.D. 2003. Transmittal of Report Technical Basis Document No. 5: In-Drift Chemical Environment Addressing 15 Key Technical Issue (KTI) Agreements. Letter from J.D. Ziegler (DOE/ORD) to Chief, High-Level Waste Branch, DWM/NMSS (NRC), November 25, 2003, 1126039633, with enclosure. ACC: MOL.20040206.0348.

D.5.2 Data, Listed by Data Tracking Number

GS951108312271.006. Interpretations of Chemical and Isotopic Data from Boreholes in the Unsaturated Zone at Yucca Mountain Nevada. Submittal date: 09/13/2001.

LB0408CMATUZFT.001. Hydrothermal Recrystallization–Supporting Calculations. Submittal date: In progress.

LB0408CMATUZFT.002. Carbonation–Papadakis Model Calculations for Carbonation Distances. Submittal date: In progress.

LB0408CMATUZFT.003. Leaching of Altered Cementitious Materials–Estimates of Molecular Diffusion/Dispersion in Cementitious Material Transport. Submittal date: In progress.

LB0408CMATUZFT.004. Leaching of Altered Cementitious Materials–EQ3/6 Simulations for Cementitious Material Transport. Submittal date: In progress.

LL020711323125.001. Pre-Test Calculations for Grout Carbonation Experiments. Submittal date: 08/13/2002.

LL020805523125.002. Experimental Studies of Cement Grout-Water Chemical Interaction. Submittal date: 08/28/2002.

LL030211423125.005. Cementitious Grout-Seepage Water Interaction. Submittal date: 02/02/2004.

LL030211523125.006. EQ3/6 Modeling of Grout-Reacted Liquid Carbonation Experiments. Submittal date: 07/01/2003.

INTENTIONALLY LEFT BLANK